A Fluorescence Spectroscopic Approach to Studying Nanoparticle Chemical Environments, Architecture, and Assembly

by

Anthony J. Berardi

A dissertation submitted in partial fulfillment
of the requirements for the degree of
Doctor of Philosophy
(Macromolecular Science and Engineering)
in the University of Michigan
2024

Doctoral Committee:

Professor Joerg Lahann, Chair
Professor Julie Biteen
Professor Jinsang Kim
Assistant Professor Abdon Pena-Francesch

Anthony J. Berardi

aberardi@umich.edu

ORCID iD: 0000-0002-0442-6274

For my grandparents, Antonio Berardi, Josephine Berardi, Giuseppe Caico, and Rosa Caico.

Acknowledgements

This dissertation would not exist without the unwavering support, encouragement, and love of my parents, Domenico and Marialuisa Berardi. Thank you for instilling in me a curiosity and passion for knowledge. My brother and sister, Matthew and Gabriella, have been my lifelong companions. Thank you for the laughs, bickering, and love. My aunt, Rosanna Berardi, and my uncles, Francesco and Angelo Caico, have been unwavering in their support my whole life. Thank you for building Erector sets, Legos, and K'NEX with me. I think those skills translated. Finally, I'd like to thank my grandparents, Antonio and Josephine Berardi, and Giuseppe and Rosa Caico, for bringing their families to the United States to create better lives and opportunities and instilling in me the value of hard work, respect, and most importantly, love.

My fiancé, Samantha, has witnessed firsthand the rollercoaster of emotions, stress, and uncertainty that inevitably accompany the pursuit of a doctoral degree. Thank you for your love, friendship, and the joy you bring to my life every day. Our dogs, Winston and Willow, have stolen my heart and soul. Thank you, dawgs, for reminding me that life is beautiful and for schooling me daily in patience and fun.

Thank you, Prof. Joerg Lahann, my PhD advisor, for allowing me the independence to follow my curiosity for the past five years. Your leadership, scientific rigor, and excitement for innovative ideas inspires me to continually refine my thinking and strive for impact. Thank you, Dr. Jeffery Raymond, my closest mentor, for your unceasing scientific insights and friendship; this dissertation certainly would not exist without your ideas and expertise in seemingly anything and

everything. Thank you for the generous gift of your time and knowledge. Thank you to my friends and colleagues in the Lahann Lab: Albert Chang, Joshua Flint, Dr. Jason Gregory, Jihyun (John) Kim, Do Hoon (Chris) Kim, Prof. Yeongun Ko, Dr. Ava Mauser, Dr. Dylan Neale, Dr. Deliris Ortiz-Ortiz, Arit Patra, Dr. Daniel Quevedo, Dr. Michael Triebwasser, Fjorela Xhyliu, Dr. Yao Yao, Julio Zelaya, and Dr. Xiaoyang Zhong. Time spent with all of you, both in and out of the lab, has been so much fun. I'd also like to thank my undergraduate trainee, Sonja Francisco, for her enthusiasm and dedication in the lab, and her significant contribution to the data presented in Chapter 2 of this dissertation.

I would not have pursued a doctoral degree in Macromolecular Science and Engineering without the support of my earliest scientific mentors. Thank you, Matthew Hellerer, my high school chemistry teacher at St. Joseph's Collegiate Institute in Buffalo, NY, for being my first point of contact with the chemical sciences. I cannot understate how big of an impact your enthusiasm for science, learning, and discipline has made on my life and the lives of so many other students. Thank you, Dr. Jeremy Steinbacher, my undergraduate research advisor at Canisius College in Buffalo, NY, for your mentorship and friendship over the last nine years. I learned more in the four years working in your lab than anywhere else; the technical skills you taught me have been crucial to the work reported in this dissertation. Thank you, Profs. Philip Sheridan, Steve Szczepankiewicz, Timothy Gregg, Mary O'Sullivan, Mariusz Kozik, and Peter Schaber, my undergraduate chemistry professors at Canisius College, for the valuable gift of knowledge and inspiring me to pursue a career in chemical research.

I'd like to thank the members of my dissertation committee for their scientific insights and mentorship. Thank you, Prof. Jinsang Kim, director of the Macromolecular Science and Engineering program, for admitting me to pursue my PhD at the University of Michigan, for your

support and dedication to me and all of the other Macro students, and for your contagious enthusiasm for large molecules. Thank you, Prof. Abdon Pena-Francesch, for your thoughtful and kind presence over the last few years. I am grateful for both our scientific and casual conversations. Thank you, Prof. Julie Biteen, for your scientific wisdom as it pertains to physical chemistry and optics and for your kindness and support for my work.

I'd like to thank a few other special people in my life for their friendship, support, and the great times we've had and will continue to have: Dr. W. Benton Swanson, Marko Spiric, Ivana Spiric, Filippo Gentile, Joshua Canavan, Canio Marasco, Lillian Caico, Claire Caico, Elizabeth Caico, Salvatore Falsone, Jack Falsone, Sabrina Caico, Theresa Caico, Cecelia Kinane, Dr. Luis E. Martinetti, and Luis B. Martinetti.

Finally, I'd like to acknowledge the National Science Foundation and the University of Michigan Rackham Graduate School for awarding me a Graduate Research Fellowship (DGE 1841052) and a Rackham Merit Fellowship, respectively, which fully funded my stipend and tuition during my doctoral studies.

Table of Contents

List of Tables

List of Figures

List of Appendices

Abstract

Three decades of intense research in nanomedicine have yielded few clinical outcomes, particularly in targeted gene delivery. Beyond regulatory challenges, the scarcity of FDA-approved nanoformulated gene therapies (only three as of writing) can be attributed to several technical issues: 1) the complex, multidimensional chemical and materials design space of nanoparticle delivery systems makes it difficult to determine the appropriate nanoparticle physicochemical characteristics for therapeutic applications, 2) successful therapeutic payload delivery to target sites requires nanoparticles to navigate complex biological environments and barriers, and 3) current analytical tools provide limited insight into nanoparticle interactions with these biological environments. Thus, new methods are needed to study nanoparticle-environment interactions to better inform nanomedicine design. This dissertation focuses on time-resolved fluorescence spectroscopy (TRFS) to study therapeutically relevant nanoparticles, including their formulation, interactions, architecture, and assembly.

In Chapter 2, a photoreactive electrohydrodynamic (EHD) jetting process was developed to prepare synthetic protein nanoparticles, achieving a four-order magnitude improvement in processing and purification time. This process utilized a fluorescent, small molecule photocrosslinker with two photoreactive benzophenone-containing arms extending from a dithiomaleimide core. The photocrosslinker stabilized protein nanoparticles and served as an intrinsic molecular reporter for formulation monitoring using TRFS, providing insights into

nanoparticle stability and architecture inaccessible to state-of-the-art techniques like scanning electron microscopy and dynamic light scattering.

In Chapter 3, the fluorescent, small molecule photocrosslinker's design was refined to enhance reactivity, as two variants were developed for preparing nanoparticles from both protein and non-protein materials, specifically synthetic polymers. One crosslinker contained benzophenone moieties with four reactive arms based on the same dithiomaleimide core as in Chapter 2, while the second variant contained methacrylate reactive groups. Three distinct nanoparticle types – protein nanoparticles, polymer nanogels, and block copolymer micelles – were prepared using the refined crosslinkers. Each nanoparticle type could discern minute changes in interparticle chemical environments, as measured by TRFS, with protein nanoparticles exhibiting the greatest sensitivity across an order of magnitude. Encapsulation of the small molecule drug paclitaxel in protein nanoparticles induced characteristic changes in fluorescence lifetime profiles based on the drug encapsulation mode.

Finally, a heterobifunctional reversible addition–fragmentation chain-transfer (RAFT) system was developed for the controlled polymerization of methacrylic monomers, enabling orthogonal end group conjugations post-polymerization. This versatile system was used to synthesize a variety of linear, monodisperse polymers with different chemical characters, confirming functionality through the conjugation of two different small molecule fluorescent probes to the functional end groups. An amphiphilic block copolymer was synthesized, fluorescent end group conjugated, and self-assembled into micelles. TRFS was used to probe micelle assembly by measuring the fluorescence lifetime of both end groups simultaneously, as well as the micelle system's interaction with 5 nm silver nanoparticles. Self-reporting nanoparticles, such as the ones developed in this dissertation, will be critical for unraveling nanoparticle stability and

nanoparticle-drug interactions informing the future development of rationally engineered nanoparticle-based drug carriers.

Chapter 1 – Introduction

1.1 Nanomedicine

The targeted delivery of therapeutic cargoes is one of the most pressing and studied topics in the pharmaceutical and biotechnological fields. In the early 1900s, German physician Paul Ehrlich popularized the concept of the "magic bullet" – defined as the ability for a therapeutic compound to navigate through the body following administration and home specifically to the site of disease or infection without negatively affecting otherwise healthy tissue.[1] The idea of the "magic bullet" has manifested in modern times by the nanomedicine field, which, broadly, has used nanoparticles as vehicles to encapsulate and carry therapeutic cargoes, like small molecules, nucleic acids, and proteins, through the bloodstream and to the site of disease. A nanoparticle is a particle of matter with a diameter of 1-500 nm that can be composed of a variety of material substrates, including metals, polymers, proteins, and lipids.[2] Nanoparticles have been proposed to outperform traditional small molecule and biologic drugs in a variety of ways, including through cargo protection, controlled cargo release, extended circulation time, and improved cell- and tissue-specific targeting.[3] While scientists, clinicians, and engineers have made progress toward Ehrlich's postulated idea over the century since, major questions still remain to be addressed in the field of targeted drug delivery, all of which center upon understanding how specific delivery vehicles, often synthetic nanoparticles or viruses, encapsulate therapeutic cargo, interact with various tissues and complex biological fluids as they travel throughout the body, and are taken up and trafficked by cells.[4,5]

There are approximately 40 FDA-approved nanomedicines used in the clinic, composed of a variety of nanomaterials, encapsulating a variety of therapeutic cargoes, and prescribed for a variety of disease indications and applications. These nanomedicines fall into four broad categories of therapeutic application: 1) cancer, 2) iron replacement, 3) imaging, and 4) vaccines, anesthetics, fungal treatments, and macular degeneration.[6–8] Over last 20 years, the field of gene therapy has become a major focus of the nanomedicine community, with the aim of using nanoparticles to encapsulate nucleic acids, like DNA and RNA, and other gene editing machinery in nanoparticles for delivery to cells.[9–11]

The "central dogma" of molecular biology states that a sequence of base pairs of DNA composing a gene are transcribed into a strand of messenger RNA (mRNA) which is translated into a protein. Proteins are responsible for almost all function within a cell, from catalysis to molecular transport to providing cellular and tissue structure.[12] Depending on the type of gene therapeutic payload encapsulated in nanotherapeutics, different genetic manipulations can be performed on target cells, like the introduction of an exogenous gene or the silencing or deletion of an existing, problematic gene, ultimately with the goal of altering the cell's ability to express those genes into proteins.[9] Gene therapeutic approaches have wide implications in treating cancer, genetic diseases, infectious diseases, and any other indication where the overexpression or underexpression of a gene is implicated in a specific pathology.[13]

The first gene therapy was FDA-approved in 2003 and, since then, the vast majority of FDA approvals in this space have been for viral therapies. A viral gene therapy is composed of an adeno-associated virus (AAV) or a lentivirus particle that is engineered to encapsulate several types of cargo: 1) a transgene and, optionally, promoters and regulatory sequences, 2) small interfering RNA (siRNA), 3) clustered regularly interspaced short palindromic repeat-associated

protein 9 (CRISPR-Cas9) components, and 4) other regulatory machinery and sequences.[14–16] While viral vectors are highly efficient at entering cells and delivering their cargo, they are often highly immunogenic, have a limited cargo capacity, may unintentionally disrupt endogenous genes leading to insertional mutagenesis, and are complex and expensive to manufacture at scale.[9,11,17] Non-viral vectors, namely synthetic nanoparticles, are currently being widely studied as alternative delivery vehicles for gene therapeutic payloads to overcome the major drawbacks of viral delivery systems. Since 2000, at least 8,000 new publications per year were published with the key words "gene therapy" and 30,000 new gene therapy reports were published in 2023 alone (**Figure 1.1**).[18] Despite over three decades of academic and industrial research into non-viral delivery systems, however, there are only two FDA-approved non-viral gene therapies: 1) patisiran (Onpattro®) – an siRNA-containing lipid nanoparticle (LNP) that silences the expression of misfolded transthyretin (TTR) proteins in patients with TTR-mediated amyloidosis (hATTR), 2) givosiran (Givlaari®) – an N-acetylgalactosamine (GalNAc) conjugated siRNA that silences the expression of aminolevulinic acid synthase 1 (ALAS1) mRNA in patients with acute hepatic porphyria (AHP), and 3) the COVID-19 mRNA vaccines.[19–21]

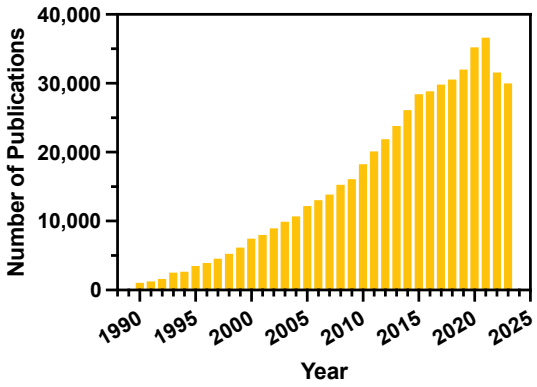

Figure 1.1: PubMed search for "gene therapy."

Targeting a nanoparticle delivery system to a specific cell type without eliciting an undesirable immune response, before the administered dose is cleared by the excretory system,

and without the nanoparticle itself degrading is a complex spatiotemporal challenge requiring the consideration of a wide range of biological barriers and how they might interact on a molecular level with the delivery system. Nanocarriers are generally designed on a [supra]molecular level to encapsulate as much payload per particle as possible, protect the payload from premature degradation or release, disguise the system from immune system recognition, circulate for long periods of time, bind only to target cells, and release the payload only when the carrier has reached the desired intercellular environment. Because this is such a difficult engineering challenge with many variables, both on the biological barrier side and the nanoparticle design side, the rest of this chapter will focus non-exhaustively on some of the most important biological and materials design considerations, as well as molecular and instrumental tools, for engineering effective drug carriers.

1.2 Design, cellular, and systemic barriers to overcome for optimal nanoparticle transport and cargo delivery

1.2.1 Biological barriers to nanoparticle-based drug delivery

Clinically speaking, nanoparticle treatments are generally administered intravenously. Following administration, nanoparticles circulate throughout the vasculature, encountering immune cells, like macrophages, and serum proteins until they are either cleared by the excretory system or extravasated through the endothelial cells that line vasculature and into the extracellular matrix, where they can bind to and be internalized by target cells (**Figure 1.2**). Nanoparticles can enter target cells through a variety of internalization processes, namely endocytosis, phagocytosis, membrane fusion, and direct penetration. The vast majority of cellular uptake of nanoparticles occurs through endocytosis, of which there are several varieties: 1) clathrin-mediated endocytosis, 2) caveolae-mediated endocytosis, 3) macropinocytosis, and 4) receptor-mediated endocytosis.[22,23]

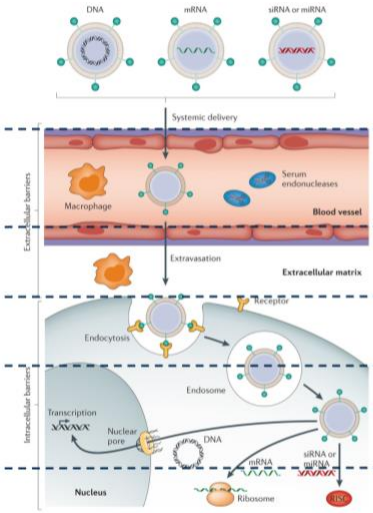

Process	Cargo Type	Challenges
Circulation	All	Immune cells, premature clearance, endonucleases
Extravasation	All	Tissue- and pathology-specific permeability
Endocytosis	All	Tissue- and pathology-specific permeability
Endosomal escape	All	↓ pH with ↑ time, time-dependent content lysis
Nuclear entry	pDNA, CRISPR RNPs	Two lipid bylayer membranes governed by selective nuclear pores

Figure 1.2: High-level overview of nanoparticle transport process.[11]

Regardless of the mode of endocytosis, a nanoparticle binding event at the cell membrane and subsequent signaling prompts the membrane to surround and engulf the particle in question, pulling it into the cytosol in a vesicle, known as an endosome.[22] Once internalized into the cell in the form of an endosome, the nanocarrier must escape and release its payload into the cytosol. Over time, endosomes are progressively acidified until they age and become lysosomes. Lysosomes are organelles responsible for degrading any intercellular waste, exhibit a pH of approximately 4.5-5, and contain a variety of enzymes that will destroy the contents of the lysosome. If a nanocarrier does not escape the endosome before it ages to a lysosome, it will be disposed of and no longer able to perform its therapeutic function.[23]

Depending on the type of gene therapeutic cargo encapsulated in the nanocarrier, escape from the endosome and into the cytosol might be the final destination, or it may have to undergo further trafficking to the nucleus to perform its function. If the payload is mRNA or siRNA, their mechanism of action is performed in the cytosol, either through translation into protein by a ribosome or through interaction with the RNA-induced silencing complex (RISC), respectively. If

the payload is DNA or gene editing machinery like a CRISPR-Cas9 ribonucleoprotein complex, they must migrate through nuclear pores and into the nucleus to perform their functions.[11]

1.2.2 Non-viral nanocarrier design considerations

In a 2020 review in *Nature Nanotechnology* regarding a framework for delivery system design, Poon and coworkers posit the following seven questions as critical to address for engineers designing nanotherapeutics: 1) Where is the delivery target?; 2) What is the cargo or active agent that needs to be delivered to the target location?; 3) Where is the site of administration?; 4) What are the specific organs, tissues, and cells encountered along the delivery pathway?; 5) What are the interactions between the nanoparticle carrier and the body in each of these biological environments along the delivery pathway?; 6) What strategies are available to overcome the barriers at each step in the delivery pathway?; and 7) How will any administered components leave the disease site and be excreted from the body?[24] These questions succinctly highlight the highly complex biological pathway that nanoparticles must traverse in order to arrive at the desired target location.

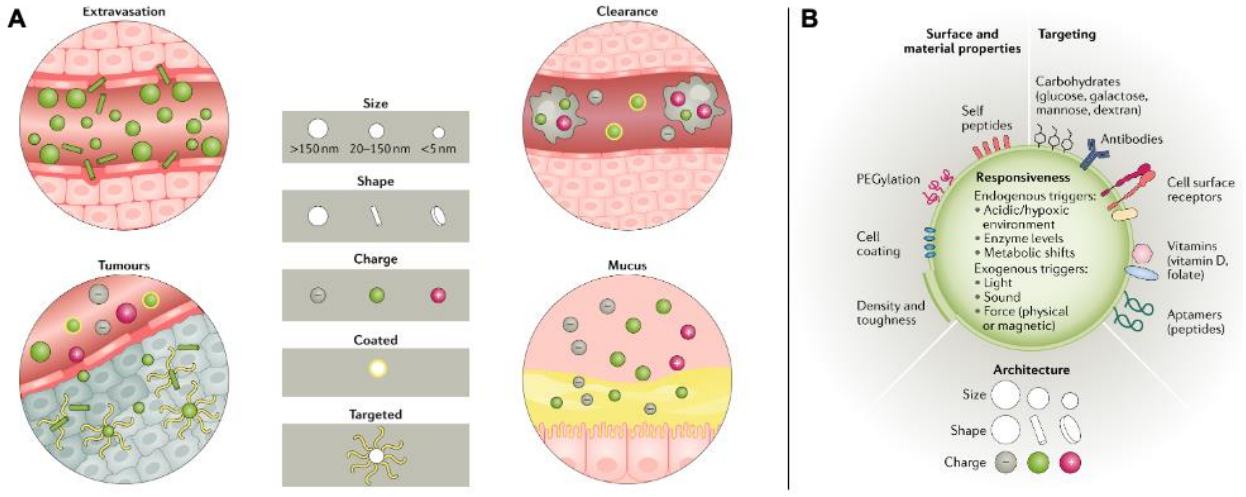

Figure 1.3: (A) The impact of five high-level nanoparticle design considerations on biological function, (B) specific nanomaterial properties and their impact on biological function.[25]

Bioengineers have developed a toolbox of general nanoparticle design principles to address these major seven questions, broadly grouped into five main categories: size, shape, surface charge, surface chemistry, and targeting capability, each of which impact nanoparticle biodistribution following administration (**Figure 1.3A**).[25]

1.2.2.1 Size

Nanoparticle size can be engineered to guide *in vivo* distribution. Generally speaking, nanoparticles smaller than 10 nm in diameter are rapidly cleared by the kidneys after administration, while particles larger than 200 nm will adsorb opsonin proteins on their surface as they circulate in the blood stream, triggering phagocytes in the mononuclear phagocyte system (MPS) to bind and clear them.[26,27] However, these general size effects can be altered by the specific material of which the nanoparticle is composed and the specific chemistry at the surface.

1.2.2.2 Coating

Coating the surface of nanoparticles with the hydrophilic polymer polyethylene glycol (PEG), often referred to as "PEGylation", is the most popular strategy to engineer particles with "stealth" properties that resist opsonin adsorption and therefore MPS clearance, as well as interparticle aggregation. However, not all PEG is created equally, as the molecular weight, molecular conformation (linear vs. branched), and surface density on the nanoparticle all alter biodistribution.[28] In addition to PEG, zwitterionic polymers and ligands that contain both positive and negative charges, resulting in an overall neutral charge, have been used to increase *in vivo* circulation and resist MPS clearance.[29]

1.2.2.3 Shape

Nanoparticle shape has been shown to be a major factor affecting cellular uptake, *in vivo* biodistribution, and hemorheological dynamics during flow through vasculature. For example, it has been demonstrated that the tumbling dynamics and behavior in blood flow of disc-like particles allows them to interact more favorably with the walls of the vasculature than spherical particles, resulting in greater adhesion to endothelial cells and more subsequent extravasation.[27] Rod- and filament-like polymer micelles have been shown to exhibit significantly greater circulation times than spherical micelles due to their ability to align with blood flow in the vasculature.[30] The curvature and aspect ratio of particles, additionally, have been shown to have a major influence on uptake (more specifically, on phagocytosis) as spherical particles are taken up faster than more ellipsoidal particles.[31] Even within these observations there exist contradictions and competing forces. A rod-like particle circulates for longer in the vasculature than a spherical particle, but experiences much slower cellular internalization. Therefore, the choice of shape for a nanoparticle system is not straightforward and tradeoffs must be made depending on which properties are most important to accomplish successful delivery.

1.2.2.4 Charge

The surface charge of a nanoparticle, often referred to as the zeta potential, is the voltage difference between the solvent in which a colloid is suspended and the stationary layer of solvent associated with the suspended particles, generally measured in millivolts (mV). In the absence of an active targeting mechanism, nanoparticle surface charge is a major determining factor that predicts cellular uptake. In general, the more positively charged a nanoparticle, the better it is internalized.[27,29] This phenomenon has been demonstrated across a variety of nanoparticle types, including lipid,[32] gold,[33] and polymer[34] nanoparticles, among others, and is due to the ability for

positively charged moieties to interact with the negatively charged phospholipid cell membrane and negatively charged groups, like sialic acid, bound to the membrane.[29] Charge is also an important factor that influences the ability for a nanoparticle to complex with negatively charged gene therapeutic payloads. In the case of lipid nanoparticles, ionizable lipids with nitrogen-containing functional groups, which are protonated under acidic conditions, are used to form stable complexes with nucleic acids, like mRNA or siRNA, and enhance endosomal escape (see **1.4.1** for more). However, lipid nanoparticles will ideally have a neutral surface charge to avoid clearance by the MPS.[35] Like shape, tradeoffs must be made when engineering a nanoparticle delivery system's surface charge; the more positively charged the particle, the better it will be internalized into cells, but the more quickly it will be cleared by the MPS due to the ready adsorption of opsonin and other serum proteins.

1.2.2.5 Targeting

The nanoparticle properties discussed up until this point all rely on passive methods, like charge-charge interactions or stealth properties, to affect delivery outcomes. Historically, much of the drug delivery field has exploited the so-called enhanced permeability and retention (EPR) effect for targeting tumors, specifically. EPR theory states that when nanoparticles are administered systemically to an organism with a tumor, the particles will accumulate specifically in tumors by crossing the tumor endothelial barrier through enlarged intercellular junctions that are a consequence of cancer pathology. The particles are retained in the tumor due to an increase in pressure created by poor lymphatic drainage.[36] However, in a 2016 meta-analysis of 223 papers that contained the key words "nanoparticle delivery" published from 2005-2015, Chan and coworkers determined that a median of 0.7% of administered nanoparticles were delivered to solid tumors.[37] More effective targeting has been achieved using *active* targeting mechanisms through

the conjugation of small molecules, peptides, antibodies, antibody fragments, and DNA aptamers to the surface of nanoparticles which bind specifically to cell surface receptors or other binding motifs.[38,39]

1.3 Gene therapeutic cargo for nanoparticles

The introduction of plasmid DNA (pDNA), mRNA, and CRISPR-Cas9 ribonucleoprotein (RNP) complexes into cells with nanoparticles can be used to introduce a new gene, while small interfering RNA (siRNA), microRNA (miRNA), base editors, and CRISPR-Cas9 RNPs can be used to silence, mutate, or delete an existing gene. Each of these gene therapeutic payloads function through their interaction with different cellular machinery that play various mechanistic roles in controlling gene expression, explainable in a straightforward manner by the so-called "central dogma" of molecular biology (DNA genes are transcribed to mRNA by RNA polymerase which is translated into proteins by ribosomes).[12]

1.3.1 pDNA

pDNA is a circular strand of DNA constructed through the ligation of a desired gene of interest at a restriction site. These circular vectors are commonly used in cloning and protein production through delivery to bacteria, like *E. coli*, or yeast to prompt those cells to produce the protein corresponding to the ligated gene. They are used similarly as gene therapies through their encapsulation into nanoparticles and delivery to target cells to *prompt those cells to produce a desired protein*.[40,41] After release into the cytosol, pDNA must travel to the nucleus and pass through the nuclear membrane through pores. Once in the nucleus, it is transcribed into mRNA by RNA polymerase II, exported to ribosomes in the cytosol, and translated into the protein of interest. Nuclear entry of pDNA can be enhanced by the inclusion of a nuclear localization signal in the

plasmid's base pair sequence. Nuclear entry may also happen during the mitotic disassembly of the nuclear envelope during the process of cell division, but this will only occur within a population of actively dividing cells. The expression of protein from pDNA is transient, meaning protein will only be expressed as long as the pDNA is present in the cell at sufficient quantities. More pDNA must be administered to prompt continued therapeutic effect.

1.3.2 mRNA

mRNA is a linear, single stranded RNA molecule that is endogenously produced by the transcription of DNA sequences in the nucleus, exported into the cytosol, and translated into protein by ribosomes.[42–44] It is a more attractive therapeutic alternative to pDNA because it does not require the extra steps of nuclear entry, transcription, cytosolic export, and translation.[45] Once the nanoparticle containing the mRNA escapes the endosome and the payload is released into the cytosol, it can immediately translocate to ribosomes to *prompt protein production*. Like pDNA, mRNA expression is transient.

1.3.3 CRISPR-Cas9 RNP

The CRISPR system can either *permanently* delete a gene or *insert* a new gene into a cell's genome.[46–48] A CRISPR-Cas9 RNP is a protein-nucleic acid complex involving a guide RNA (gRNA) and a Cas9 enzyme. The gRNA directs the complex to a specific genomic DNA sequence and Cas9 makes a double-stranded break at that target site. The cell must then repair the DNA breakage, either through non-homologous end joining (NHEJ), which results in gene deletion, or homology-directed repair (HDR), which results in the insertion of a new gene in the presence of a donor DNA template. CRISPR-Cas9 systems can be delivered to cells either as a complete protein-

nucleic acid complex or through the co-delivery of a plasmid encoding for the Cas9 protein and a gRNA. CRISPR-Cas9 systems must enter the nucleus like pDNA to perform their function.

1.3.4 Base editors

Base editors are an emerging class of genetic technologies built using Cas9 enzymes that allow for the *conversion of one DNA base pair to another*.[49] For example, cytosine base editors convert C-G pairs to T-A pairs while adenine base editors convert A-T pairs to G-C pairs. Base editors are composed of a Cas9 enzyme that has been catalytically impaired and fused to a deaminase. They do not induce a double-stranded break and have fewer off-target effects than Cas9, but can only be used to correct DNA point mutations.[50]

1.3.5 siRNA

siRNA is a small double stranded RNA molecule that operates through the process of RNA interference (RNAi) to *silence the expression of a gene*.[51–53] siRNA performs its mechanism of action in the cytosol where it is incorporated into the RNA-induced silencing complex (RISC), which separates the two siRNA strands. The guide strand of siRNA is paired with its complementary mRNA sequence in the cytoplasm. Upon binding, RISC degrades the target mRNA, resulting in a silencing in that mRNA's ability to get translated to protein. siRNA expression is transient. Gene silencing only happens as long as siRNA is present at high enough levels in the cytoplasm.

1.3.6 miRNA

Like siRNA, miRNA is involved in RNAi through interaction with RISC.[11,35] miRNA is a double stranded RNA molecule that binds to RISC, is separated, and the guide strand is used to bind complementary mRNAs for degradation. miRNA expression is transient.

1.4 Materials for nanoparticles

Nanoparticles have been synthesized from a wide variety of materials, including metals, organometallic components, polymers, lipids, and proteins.[25] Thus, nanoparticle preparation and the resulting nanoparticle properties are controlled entirely by their specific chemistries. Inorganic nanoparticles are generally rigid, stiff, and non-degradable, as a consequence of the rigidity and stability of their composite inorganic lattice molecular structures.[2] On the other hand, organic nanoparticles, composed of lipids, polymers, proteins, and other organic molecules and macromolecules, are much more flexible and can be engineered to be degradable, again, as a consequence of their carbon-based molecular structures. While inorganic nanoparticles, like gold and silica nanoparticles, have been explored as carriers for therapeutics, organic nanoparticles have been studied to a considerably higher degree and are the most clinically relevant category of nanoparticles for their compositional diversity and modularity and ease of synthesis.[43,54–56]

1.4.1 Lipids

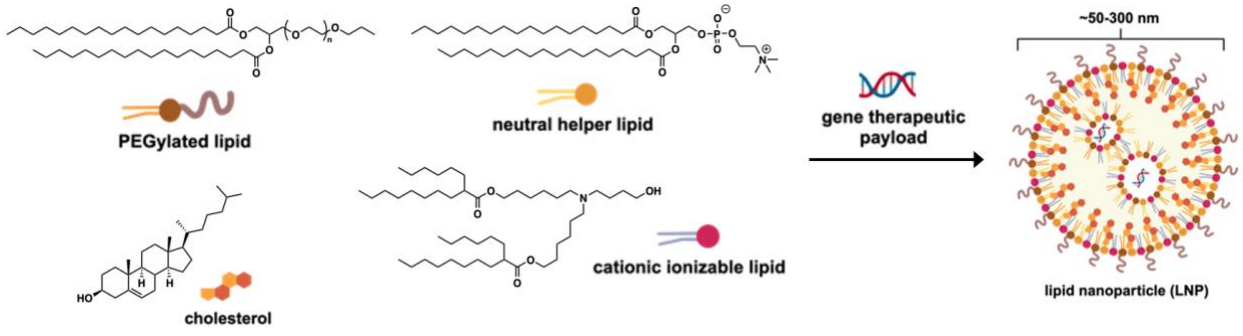

Figure 1.4: Common molecular components of lipid nanoparticles (LNPs).

Lipids are a group of bioorganic molecules involved in energy storage, signaling, and structural functions in cells, like composing the cell membrane and other intercellular membranes.[12] Lipids are generally hydrophobic or amphiphilic, due to the presence of aliphatic hydrocarbon chains and sometimes polar, charged head groups. Lipids can be used to prepare a

variety of nanoparticles, including liposomes and lipid nanoparticles (LNPs).[57] The difference between these two varieties is due to differences in preparation method and nanostructure. Liposomes are generally composed of phospholipids and cholesterol and exhibit a spherical, lipid bilayer structure, similar to that of cell membranes. They are prepared either through the sonication of a thin film of lipid components in a suitable solvent or by extrusion through a size cutoff membrane.[58] LNPs are less ordered in structure (**Figure 1.4**) and prepared either by manually mixing lipid components together by vigorous pipetting or through more controlled mixing via microfluidic devices. LNPs for gene therapy are composed generally of a PEGylated lipid which provides stealth properties (see **1.2.2.2**), a neutral helper lipid, like 1,2-dioleoyl-sn-glycero-3-phosphoethanolamine (DOPE), cholesterol which provides rigidity, and a cationic ionizable lipid which is protonated at certain pHs and allows for the complexation with anionic nucleic acids and nucleic acid complexes.[25,43,59] LNPs compose the only FDA approved nanoformulated gene therapies to date (as of spring 2024).[19,21] The main strategy for engineering complexation and targeting efficacy is to alter the ionizable lipid in LNP formulations. A broad spectrum of ionizable lipids have been synthesized and screened, containing different lipid chain compositions, chain lengths, and, most importantly, ionizable head groups. Generally, head groups contain amines of varying chemical character.[60–63]

1.4.2 Polymers

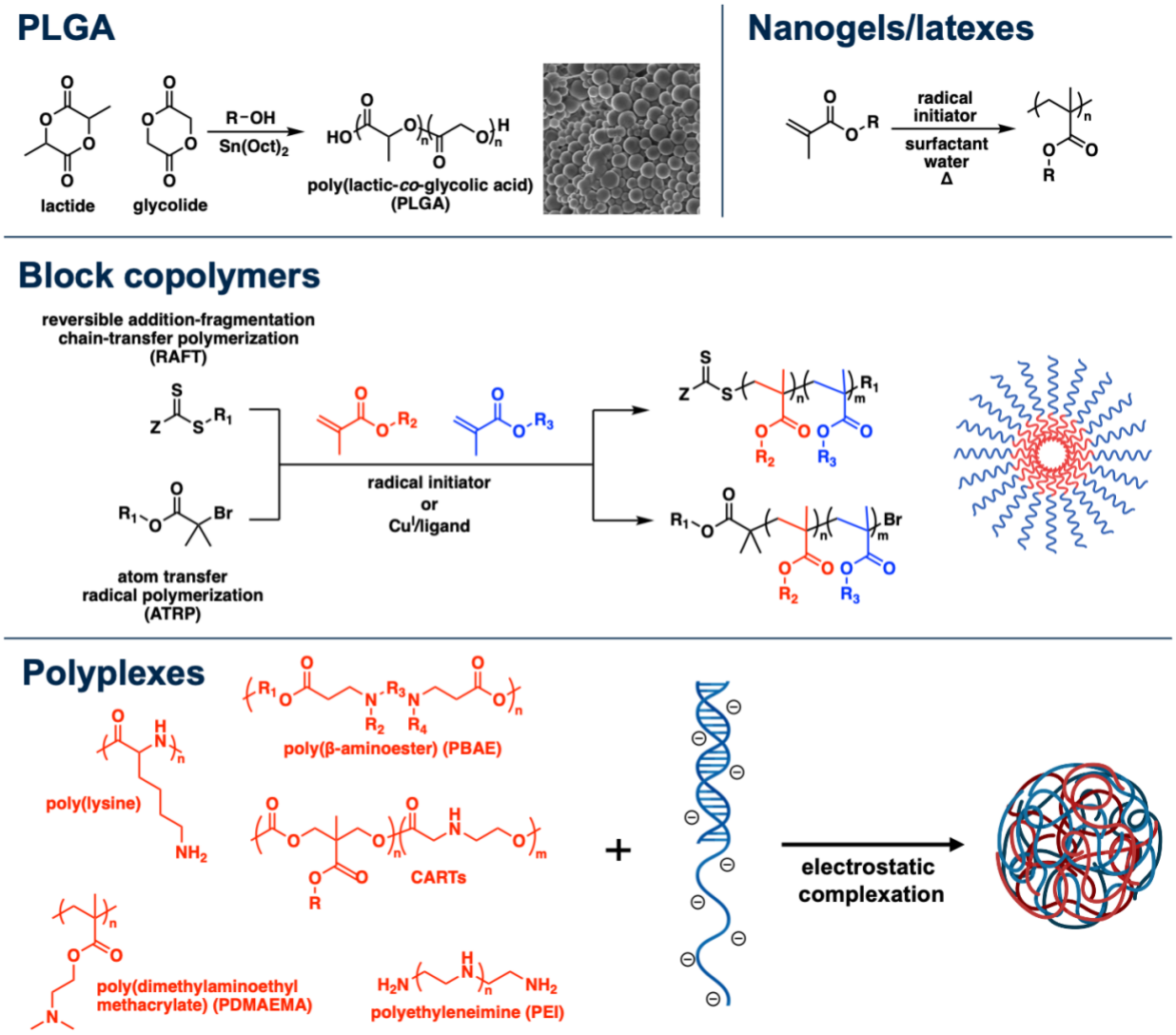

Figure 1.5: Examples of several common polymer chemistries used to prepare nanoparticles.

Synthetic polymers compose another large category of materials for the preparation of organic nanoparticles. A robust toolkit of synthetic polymer chemistries exists for the preparation of polymers for nanomedicine applications.[64,65] Perhaps the most widely used, clinically relevant polymer is poly(lactic-*co*-glycolic acid) (PLGA) (**Figure 1.5 PLGA**).[66,67] PLGA is generally prepared through the ring opening polymerization of the cyclic dimers of lactic acid and glycolic acid with a hydroxyl-bearing initiator in the presence of the tin (II) 2-ethylhexanoate (Sn(II)Oct)

catalyst. PLGA is a biocompatible and biodegradable polymer that hydrolyzes via its polyester linkages used in a variety of medical devices, from tubing to controlled release implants to nanoparticles.[68] It's generally not employed in gene therapy nanomedicine applications due to its neutral charge, but PLGA nanoparticles have been used widely to encapsulate small molecule therapeutics.

Polymer nanogels are spherical, crosslinked nanoparticles generally prepared through the radical emulsion polymerization of an unsaturated monomer, like an acrylate, methacrylate, acrylamide, methacrylamide, or vinyl ether with a crosslinker (**Figure 1.5 Nanogels/latexes**).[69,70] This type of polymerization is generally performed in surfactant-containing water, where the monomers and crosslinkers partition into surfactant micelles. When a radical initiator is added to the mixture, it polymerizes the monomers and crosslinkers contained within the micelles, forming a spherical nanogel with a network-like structure. Nanogels are generally employed for the encapsulation and delivery of small molecule therapeutics.[71,72]

Controlled radical polymerization (CRP) methods, like reversible addition– fragmentation chain-transfer (RAFT) polymerization and atom transfer radical polymerization (ATRP), are commonly used to synthesize highly monodisperse, linear polymers from unsaturated monomers with end group chemistries defined by their corresponding chain transfer agents (CTAs) and initiators, respectively.[73–77] RAFT and ATRP are "living" polymerization techniques and their resulting polymers can be reinitiated after synthesis and chain extended with other monomers to synthesize well-defined block copolymers (**Figure 1.5 Block copolymers**).[77–83] In the drug delivery and nanomedicine space, amphiphilic block copolymers, containing hydrophobic and hydrophilic blocks are often used to prepare polymer micelle nanoparticles by self-assembly in a selective solvent, like water, which prompts the aggregation of hydrophobic blocks and solvation

of hydrophobic blocks. Block copolymer micelle nanoparticles have been used for the delivery of a wide variety of therapeutic modalities, including small molecules, nucleic acids, and proteins.[84–86] Cationic monomers, like dimethylaminoethyl methacrylate (DMAEMA), are commonly used to synthesize block copolymers used in nanomedicine because they electrostatically complex well with anionic nucleic acids.[87,88]

Charged, cationic polymers represent another large category of polymers used in for the synthesis of polyplexes, or electrostatically-driven complexes of cationic polymers with anionic nucleic acids (**Figure 1.5 Polyplexes**).[89,90] Poly(ethyleneimine) (PEI) was the first charged polymer used for this purpose, synthesized from the ring opening polymerization of aziridine. It exists in both linear and branched forms and a large amount of work has been published regarding the impacts of architecture, molecular weight, and formulation parameters on ultimate delivery success.[91,92] PEI is toxic in large doses so the field has moved away from it as a delivery vehicle. Since then, a number of cationic polymer systems have emerged as alternatives to PEI. Poly(β-aminoesters) (PBAEs) are a category of cationic polymers synthesized by the polymerization of diacrylates with diamines.[93,94] Their characteristic ester backbone linkages provide them with biodegradable properties and much effort has been dedicated to discerning the impact of different R-group chemistries on complexation and delivery efficacy.[95] A notable polymeric system developed by the Waymouth group at Stanford University called charge-altering reversible transporters (CARTs) has gained recent attention for its efficacy in delivering mRNA and self-immolating backbone structure.[96] Despite the extensive research efforts in this space, however, there are currently no FDA-approved polymer nanoparticles for gene therapy applications. There are several polymer nanoparticle systems approved for small molecule delivery.

1.4.3 Proteins

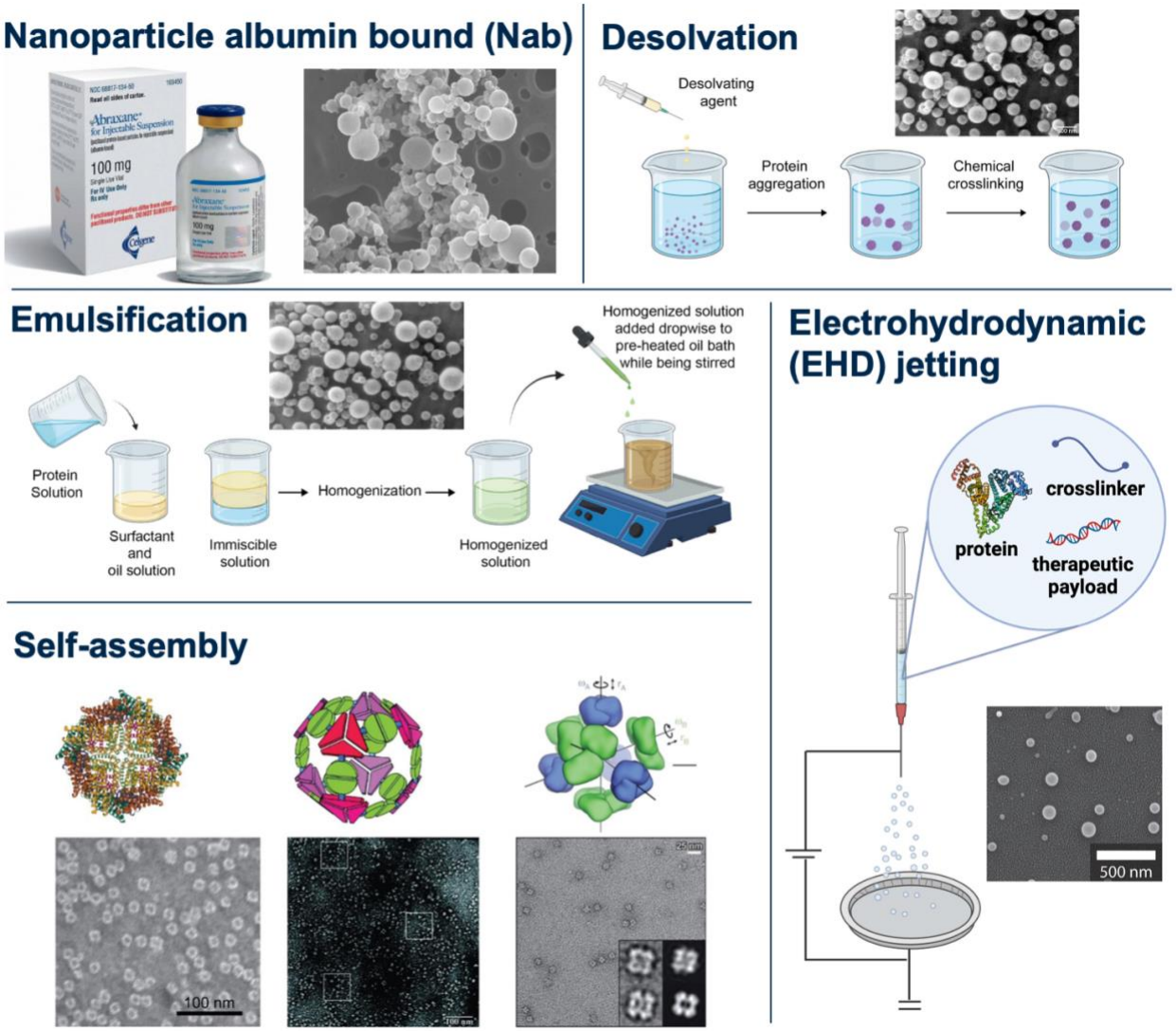

Figure 1.6: Five common protein nanoparticle preparation methods.

Proteins represent the third major class of organic substrates used to construct nanoparticles.[54,97,98] They are the least advanced with regard to technology development and no protein nanoparticles are FDA-approved for gene therapies. Abraxane®, or nanoparticle albumin bound (Nab) paclitaxel, a high-pressure homogenized blend of albumin and small molecule anti-cancer drug paclitaxel, is approved for the treatment of breast cancer, lung cancer, and others (**Figure 1.6 Nanopartcle albumin bound (Nab)**).[99] Several techniques are available for the

preparation of protein nanoparticles, including desolvation, emulsification, and self-assembly. Desolvation involves the slow addition of a desolvating agent, often ethanol or other organic solvents, to a stirring solution of dissolved protein to prompt the formation of aggregates, followed by chemical crosslinking using multifunctional molecules like glutaraldehyde (**Figure 1.6 Desolvation**).[100,101] Emulsification is a solution-based process, similar to desolvation, but involves the formation of a stable emulsion of immiscible solutions of protein in water and surfactant in an organic solvent.[54] The emulsion suspension is added dropwise to a hot oil bath, prompting protein denaturation, aggregation, and stabilization. Because desolvation and emulsification require the use of denaturing solvents and/or elevated temperatures, protein secondary and tertiary structures are often not preserved and the processes are not compatible with delicate nucleic acid cargo. Thus, any intrinsic protein function is generally not preserved and the composite proteins are used merely for their structural capacity.

Self-assembly is an emerging technique for the synthesis of protein nanoparticles, requiring the *de novo* computational design and expression of new proteins that, in solution, assemble into highly ordered nanostructures (**Figure 1.6 Self-assembly**).[102,103] Despite the precision of this technique in its ability to produce uniform nanoparticles with engineered function and tissue specificity, it is expensive and computationally intense, and engineering bacterial strains to express the new proteins is not trivial.

Electrohydrodynamic (EHD) jetting is an emerging technique for the synthesis of protein nanoparticles, pioneered by the Lahann group at the University of Michigan. EHD jetting is similar to electrospraying and involves the dissolution of a structural macromolecule (synthetic polymer, protein) and a crosslinker in a suitable solvent (**Figure 1.6 Electrohydrodynamic (EHD) jetting**).[104–106] The solution is drawn into a syringe and flown downward toward a grounded

collection surface at a constant rate. A voltage is applied to the needle of the syringe, inducing an electric field between the needle and the collection surface. As the solution enters the electric field, the solvent evaporates and the macromolecular components and crosslinkers nanoaggregate in flight toward the collection surface. What results is a crosslinked nanoparticle with a network-like architecture, composed of macromolecules randomly joined together by crosslinks. This process has been used to produce synthetic polymer micro- and nanoparticles, and recently, protein nanoparticles.[104,107] EHD jetting allows for separate control over physical and chemical properties; the physical properties of the resulting nanoparticles, like size and shape, are controllable by the processing parameters associated with EHD jetting (voltage, flow rate, solvent selection), while the chemical properties of the resulting nanoparticles, like zeta potential, crosslinking density, and chemical composition, are controllable by the specific macromolecular and crosslinking components included in the jetting solution and their relative stoichiometries.[108,109]

While quite nascent in their stage of development regarding preparation methods and clinical significance, proteins represent a high-potential category of material substrates for nanoparticle synthesis. Proteins are highly complex biomacromolecules with sophisticated functions, ranging from catalysis to cellular scaffolding, all dependent on the several orders of complexity associated with amino acid sequences and macromolecular structure (primary, secondary, tertiary structure).[12]

1.5 Chemistry used to construct nanoparticles

1.5.1 Non-specific chemistries

The chemical toolbox of nanoparticle synthesis generally involves a set of chemical coupling and degradation reactions, referred to colloquially as "bioconjugate chemistry."[110] Often, these bioconjugate chemistries take advantage of intrinsic functional groups found on

biomacromolecules, like proteins and nucleic acids, the most common of which are amines, thiols, alcohols, and carboxylic acids (**Figure 1.7**). These reactions are used to crosslink macromolecules into nanoparticles, ligate payloads to nanoparticles, or label nanoparticles with reporters, like fluorescent dyes or radionuclides. Amines are nucleophiles, and will perform substitution reactions with electrophiles under slightly basic conditions, like N-hydroxysuccinimide esters (NHS esters), pentafluorophenyl esters (PFP esters), aldehydes, isocyanates, and epoxides (**Figure 1.7A**). Thiols are also nucleophiles and will perform thiol-ene Michael additions with maleimides and other alkene-containing species like [meth]acrylates, as well as redox reactions with disulfides (**Figure 1.7B**). Carboxylic acids are electrophiles, and will undergo nucleophilic attack from nucleophiles like amines and alcohols in the presence of suitable coupling reagents (often carbodiimides) to form amides and esters, respectively (**Figure 1.7C**).

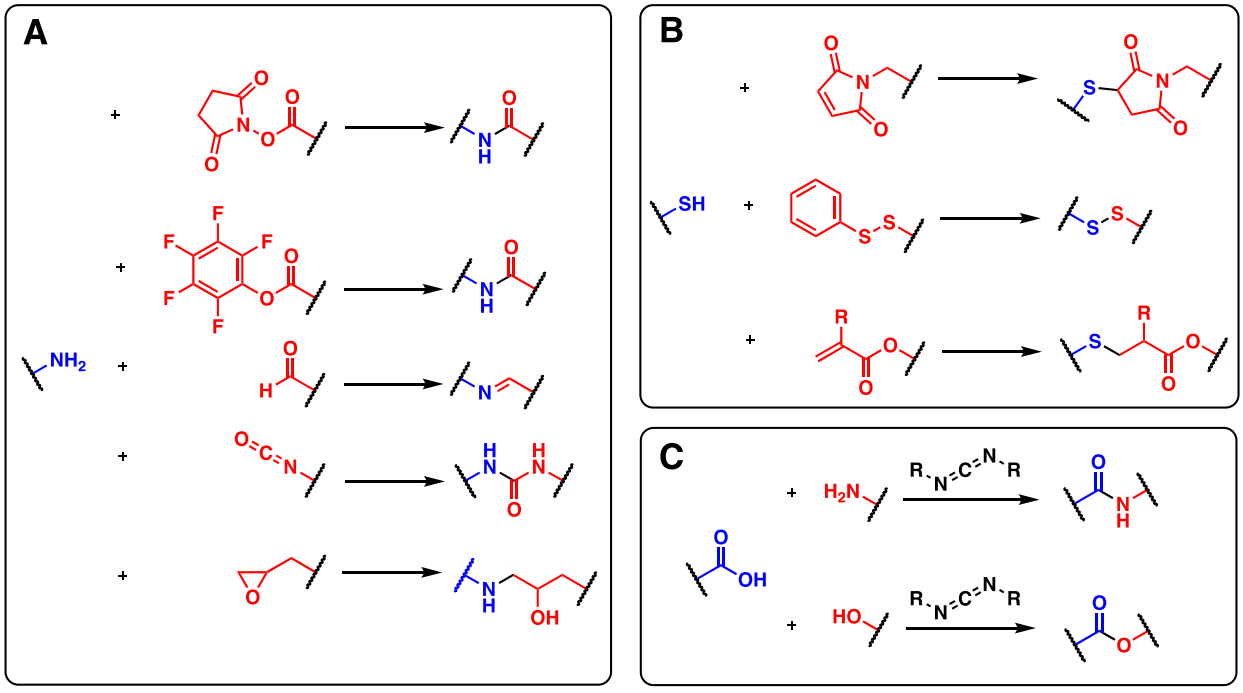

Figure 1.7: Bioconjugate chemistries involving intrinsic protein residues. A) Amines, B) thiols, and C) carboxylic acids. The chemistries illustrated in this figure are non-exhaustive.

1.5.2 Bioorthogonal, specific chemistries

The chemistries outlined in **Figure 1.7** are all non-specific. For example, every carboxylic acid present in a reaction mixture will react with every amine available at the defined stoichiometry. Since biomacromolecular species contain tens to hundreds of these functional groups per molecule, these reactions are either performed in excess or dearth with respect to a specific functional group. So, an experimentalist can say, for example, that they modified 10 available carboxylic acids on a target protein with an amine-containing ligand to form new amide bonds between the two, but cannot say specifically which amino acid residues were modified. In some cases, however, the ability to ligate to or crosslink a macromolecule at a specific location is desired. Bioorthogonal, specific chemical reactions were developed for this purpose (**Figure 1.8**). Bioorthogonal chemistries involve the introduction of a functional group at a defined site in a [bio]macromolecule, like at a specific amino acid residue, that is biologically exogenous. That is to say, it is not naturally-occurring and therefore does not have any intrinsic reactivity with other endogenous functional groups. The "click" reaction, which won the 2022 Nobel Prize in chemistry, is one such example of a biorthogonal chemical reaction (**Figure 1.8A**).[111,112] Click reactions are cyclization reactions that take place between azides and alkynes to form 5-membered triazole heterocycles. This reaction can be performed with an azide and a linear, terminal alkyne in the presence of a Cu^{1} catalyst, or between an azide and a strained alkyne without a catalyst, like the dibenzocyclooctyne (DBCO) shown in the bottom half of **Figure 1.8A**.[113] Another example of a biorthogonal chemistry is the Diels-Alder reaction, which involves the formation of a 6-membered ring between a diene and a dienophile, like a maleimide (**Figure 1.8B**).[114]

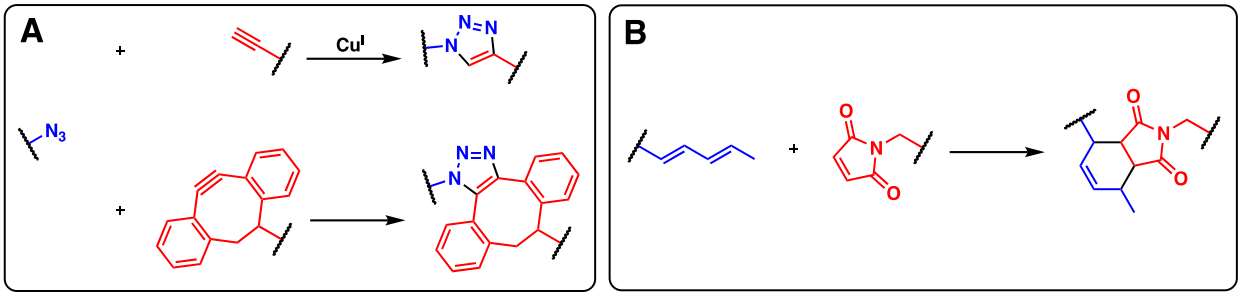

Figure 1.8: Bioorthogonal, specific chemistries. A) Azide-alkyne click reactions and B) Diels-Alder reactions.

1.5.3 Photoreactions

The drawback to the chemistries previously mentioned in this section is that they begin occuring spontaneously as soon as both reactants are added to the same reaction vessel. Often, it is desirable to initiate a reaction at a specific time or only in a specific location. Photoreactions are employed for this purpose, and generally require the irradiation of a sample with ultraviolet (UV) light to initiate the reaction.[110] Benzophenone and diazirine moieties are common photoreactive functional groups which react through the abstraction of hydrogen atoms on a macromolecular substrate.[115,116] Aryl azides are a third common photoreactive moiety that reacts through a nucleophilic attack from an amine and subsequent ring expansion (**Figure 1.9**).[117] While not as ubiquitous as the other chemistries mentioned in this section, photoreactions are used extensively in preparing polymers (via photopolymerizations) and in the mass spectrometric analysis of substrate-ligand binding.

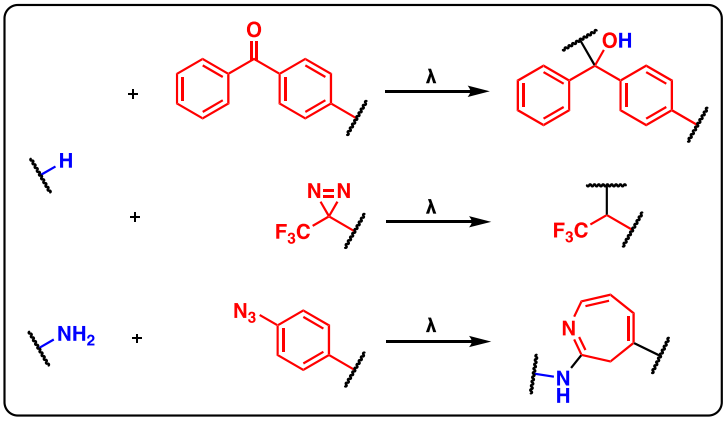

Figure 1.9: Photochemical reactions commonly employed in bioconjugate applications.

1.5.4 Stimuli-responsive chemistries

Nanoparticles engineered for nanomedicine applications are often engineered with degradability in mind; it is desirable for a nanoparticle to degrade and release its payload at the target biological site. This is generally accomplished through the use of stimuli-responsive linkers that are engineered into the nanoparticle network.[118,119] Disulfides are perhaps the most widely used functional groups for this purpose, as they are cleaved into two thiols under reducing conditions (**Figure 1.10**). It is generally accepted that a cell's cytosol is a slightly reducing environment and therefore, when a nanoparticle reaches the cytosol, the disulfide bonds holding the nanoparticle together will reduce to release the encapsulated payload.[120] Ketals/acetals, hydrazones, and esters are other common functional groups found in degradable nanoparticles and are all cleavable through acid-catalyzed hydrolysis (**Figure 1.10**).[121,122] Most nanoparticles enter cells through an endocytic uptake mechanism. Endosomes exhibit an acidic pH (~5.5) and thus, nanoparticles bound with acid responsive linkers will cleave and release their payload once in the endosome. Peptide linkers are less common in degradable nanoparticle systems than the aforementioned linkers and are more predominantly found in antibody-drug conjugates, the most common of which is the valine-citrulline (Val-Cit) linker (**Figure 1.10, bottom**).[123] Peptide linkers

are more selective than the reducible or acid-sensitive linkers in that they will generally only cleave in the presence of an enzyme that selects for that specific peptide sequence. The Val-Cit linker is selectively cleaved by cathepsin, a cytosolic proteinase.

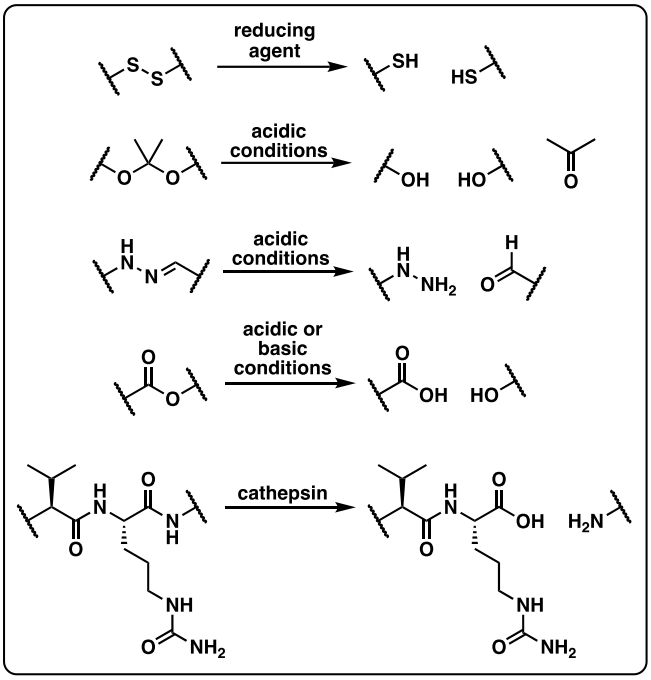

Figure 1.10: Common cleavable linkers used in drug delivery applications.

1.6 Methods for the study of nanoparticle design

1.6.1 Instrumentation

There are six main state-of-the-art instrumental techniques used to characterize nanoparticles for nanomedicine applications: dynamic light scattering (DLS), nanoparticle tracking analysis (NTA), electron microscopy, atomic force microscopy (AFM), Fourier transform-infrared (FT-IR) spectroscopy, and UV-vis spectroscopy. Each of these instrumental techniques are used to study both physical and chemical properties of nanoparticles.[124]

DLS and NTA are both solution-based methods used to measure the hydrodynamic diameter (D_h) and polydispersity index (PDI) of a suspension of nanoparticles.[125,126] The PDI

describes how narrow the nanoparticle population's D_h is – PDIs close to 0 are the most monodisperse and PDIs greater than 0.4 are generally considered polydisperse. DLS is a light scattering-based method and DLS instruments are often able to measure the zeta potential of a nanoparticle population. NTA is a camera-based method and cannot measure zeta potential, but can measure the concentration of nanoparticles in a given sample, reported in number of nanoparticles per unit volume.

Electron microscopy can be subdivided into two categories: transmission electron microscopy (TEM) and scanning electron microscopy (SEM). Both techniques provide nanometer-level resolution inaccessible to optical microscopy techniques, but TEM creates images by detecting the electrons that pass through a sample, while SEM detects electrons that are reflected from a sample.[127–130] Both types of electron microscopy can be used in conjunction with energy dispersive X-ray spectroscopy (EDX) and electron energy loss spectroscopy (EELS), which are spectroscopic methods for identifying the elemental composition of a sample.[131] TEM and SEM both provide size and morphology information about a nanoparticle sample and the images can be quantified using image analysis protocols. AFM is another technique for imaging nanoparticle samples, but rather than using electrons, uses a mechanical cantilever that rasters over the surface of the sample to detect texture which is compiled into an image.[132] AFM gives size and morphological information about a nanoparticle sample similar to TEM and SEM, but can additionally provide data on nanomechanical properties using nanoindentation techniques.

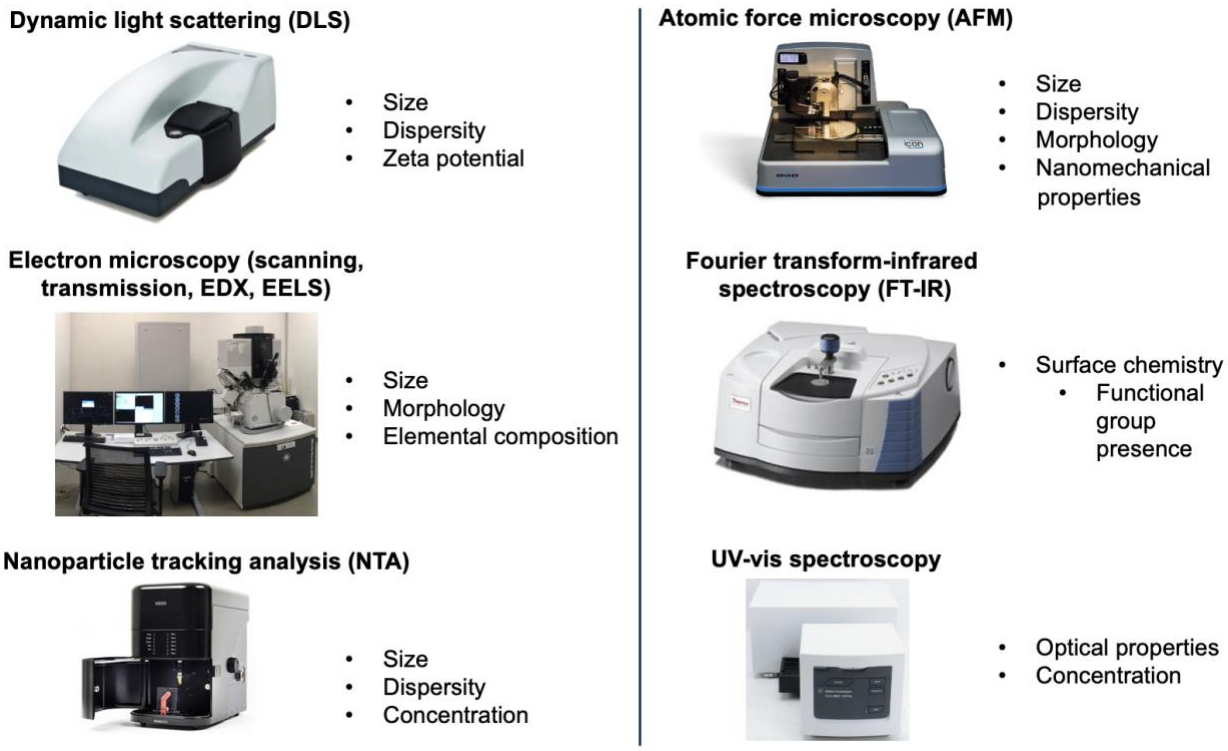

Figure 1.11: Instrumental techniques for studying nanoparticles.

In addition to the physical properties measurable by DLS, NTA, electron microscopy, and AFM, chemical properties of nanoparticles can be measured using FT-IR and UV-vis spectroscopy.[133,134] FT-IR is commonly employed to measure the presence of characteristic functional groups present on the surface of nanoparticles, while UV-vis can be used to analyze the optical properties of a sample by measuring the absorption of photons across the UV and visible regions of the electromagnetic spectrum. UV-vis can additionally be used to measure the concentration of nanoparticles suspended in a sample, but requires the sample to absorb photons in the UV-vis regime, which not all nanoparticle types do, and requires the development of a standard curve against which the sample is measured.[135]

The state-of-the-art techniques for the direct characterization of nanoparticles mainly provide data regarding the size, morphology, and surface chemistry of samples. *These techniques are severely limited in their ability to characterize nanoparticle-environment or nanoparticle-*

biological interactions in situ. A major limitation in the study of nanoparticles for nanomedicine applications lies in the difficulty of measuring how all of the design considerations (material selection, payload selection, chemistry, physical properties) ultimately influence a particular system's success, or lack thereof, in a biological therapeutic context.

1.6.2 Fluorescence spectroscopy

Fluorescence spectroscopy is an instrumental method that undergirds many of the ubiquitous bioanalytical techniques used in cell and molecular biology, physiology, and biochemistry, including but not limited to fluorescence microscopy, flow cytometry, plate-based assays, and DNA sequencing.[136] It always involves the labelling of a biomolecular or cellular species of interest with a fluorescent dye (also referred to as a fluorophore, chromophore, or dye). Fluorophores are usually small molecules with large, π-conjugated ring systems that, upon excitation with photons of a defined wavelength, will emit photons at a slightly longer wavelength.[137] The molecular structure of a fluorophore dictates the specific wavelengths at which it can be excited and emit light. For instance, the fluorophore fluorescein isothiocyanate (FITC) is excited at 495 nm and emits light at 519 nm (green), while the fluorophore sulforhodamine 101 acid chloride (Texas Red) is excited at 589 nm and emits light at 615 nm (red). The distance between the peak excitation wavelength and emission wavelength of a fluorophore is called the Stokes Shift. The process of excitation and fluorescence emission is often illustrated by a Jablonski diagram (**Figure 1.12A**).[136]

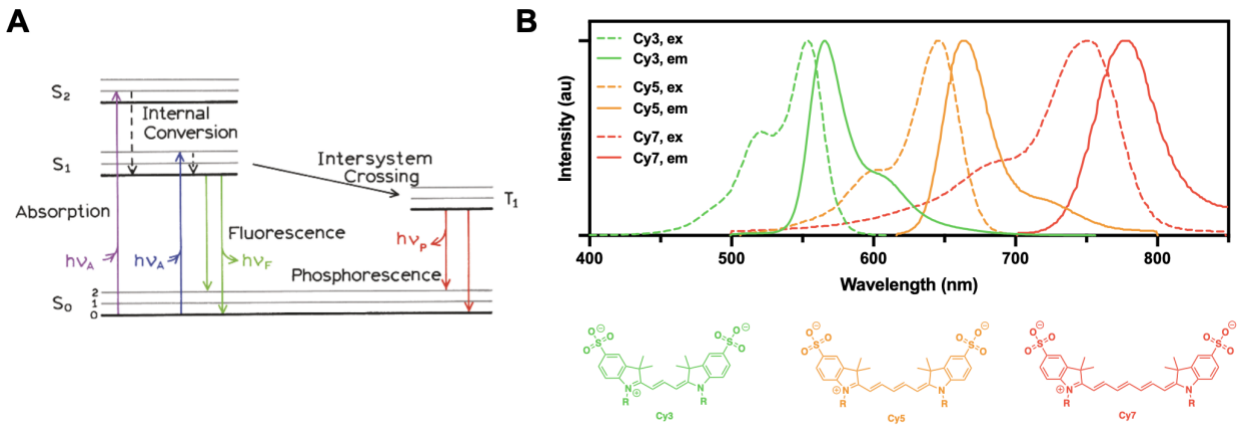

Figure 1.12: (A) A Jablonski diagram and (B) steady-state fluorescence excitation and emission spectra of the cyanine family of fluorescent dyes.

A typical Jablonski diagram illustrates the singlet ground, first, and second electronic states (S_0, S_1, and S_2) and the triplet first electronic state (T_1) of a general molecular species (**Figure 1.12A**). When the molecule is given energy in the form of photons, it is absorbed and excited to a vibrational energy level greater than that of the ground state, usually S_1 or S_2.[136] If a molecule is excited to a vibrational level greater than S_1, the molecule *generally* quickly relaxes to S_1 (on the order of 10^{-12} seconds). From there, the molecule can relax back to the ground state, S_0 via three pathways: 1) non-radiative decay, 2) fluorescence emission, or 3) phosphorescence emission. In the case of non-radiative decay, the absorbed energy dissipates in the form of heat and no photons are emitted. In the case of fluorescence emission, a form of radiative decay, the molecule in its S_1 state returns to S_0 via the emission of photons.[136] In the case of phosphorescence emission, another form of radiative decay, the molecule in its S_1 state must first undergo a conversion of spin to the first triplet state, T_1, via a process called intersystem crossing. From there, the molecule can relax to the ground state via phosphorescence by the emission of photons. Fluorescence and phosphorescence occur on different time scales; fluorescence generally occurs on the order of 10^{-8} seconds while phosphorescence occurs many orders of magnitude more slowly, from 10^{-3} to 10^{3}

seconds, and the specific decay pathway that a molecular species takes is chemical structure dependent.[136]

1.6.2.1 Steady-state fluorescence spectroscopy

Almost all bioanalytical techniques, like those mentioned in the previous section, employ the steady-state fluorescence spectroscopic detection of fluorophores. Steady-state fluorescence spectroscopy detects the average intensity of emission of a fluorophore when excited at a particular wavelength. Fluorophores do not emit photons at a single wavelength. Rather, photons are emitted across a range of wavelengths. The average emission intensities of a fluorophore can be plotted with respect to wavelength to create an emission spectrum, illustrated in **Figure 1.12B** as the solid green, orange, and red lines. The emission spectrum of a fluorophore is independent of excitation wavelength, as long as that excitation wavelength falls within the excitation band. The excitation spectrum of a fluorophore can be acquired by measuring the emission intensity at a single wavelength as a function of excitation wavelength. These average intensity values can be plotted with respect to wavelength to create an excitation spectrum, illustrated in **Figure 1.12B** as the dashed green, orange, and red lines. It is important to note that the excitation spectrum of a fluorophore is *not* the same as the absorption spectrum. Absorption spectroscopy (often referred to as UV-vis spectroscopy) involves the irradiation of a sample with light, generally in the UV and visible regime, and measures the difference in intensity of incident light from the intensity of light that passes through the sample.

Steady-state fluorescence spectroscopy is useful for microscopists who wish to observe where a fluorophore is located spatially, for example in a slice of tissue or within a cell. It is useful in flow cytometry for the selective labelling and detection of populations of cells, in plate-based assays for the selective labelling and detection of ligands or substrates, and in gel electrophoresis

for the selective labelling of nucleic acids and proteins. It does not, however, allow the user to measure the *lifetime* of a fluorescent species.

1.6.2.2 Time-resolved fluorescence spectroscopy and fluorescence lifetime

Fluorescence lifetime is defined as the average time a fluorophore spends in its excited state when given energy in the form of photons of a particular wavelength.[136] The lifetime of a small molecule fluorophore dissolved in a good solvent is generally between 1 and 10 ns.[138] While steady-state fluorescence spectroscopy is a useful tool to label biomolecular species and detect them on a spatial level, for instance, with microscopy, time-resolved fluorescence spectroscopy (TRFS) can be used to provide more nuanced information about an emissive species' local environment.[138] Fluorescence lifetime is: 1) a state function independent of instrumental conditions like the wavelength of excitation or exposure duration, 2) independent of fluorescence intensity or fluorophore concentration, and 3) sensitive to internal molecular structural factors and external environmental factors like temperature, polarity, and the presence of a quenching species.

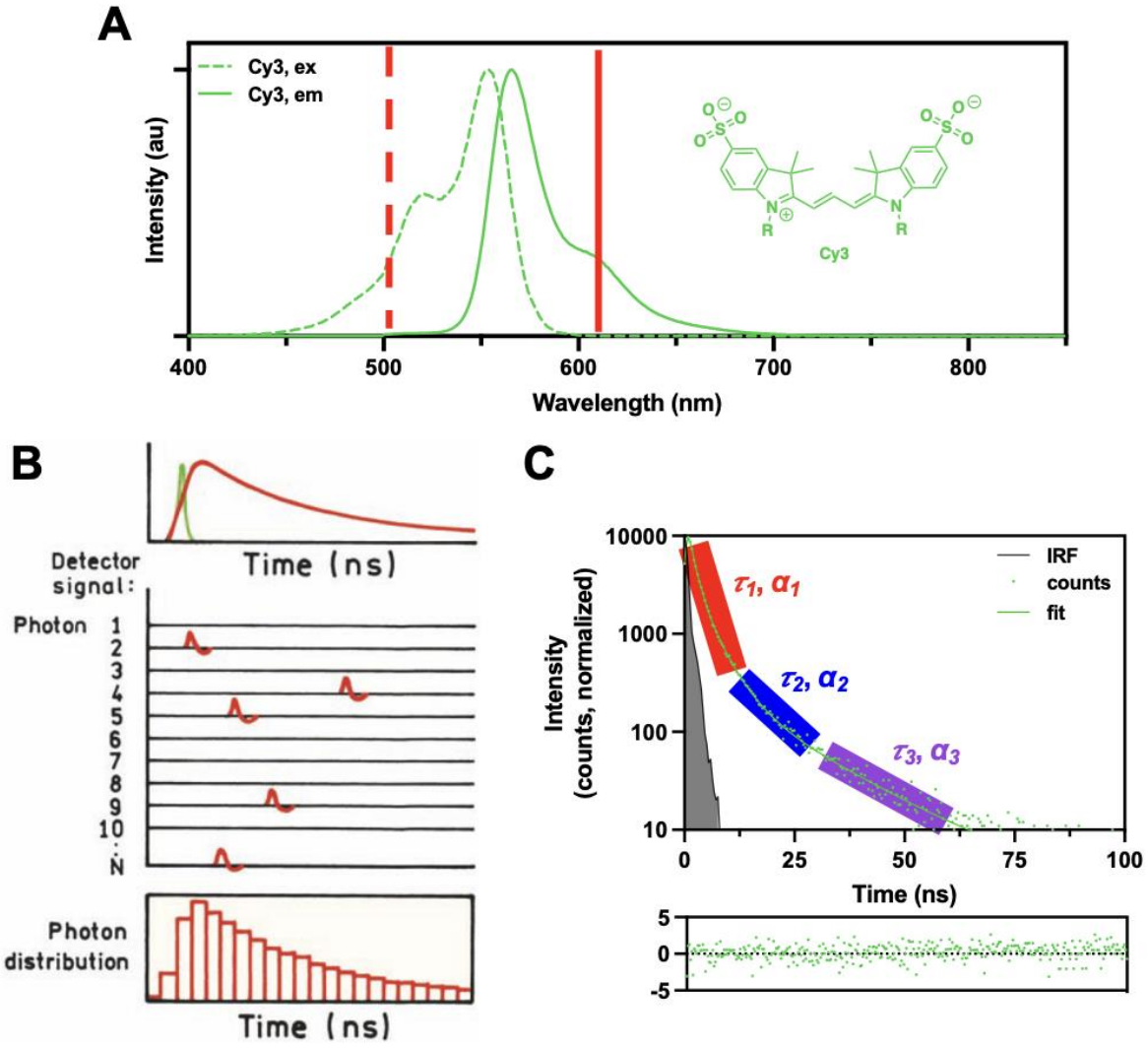

Figure 1.13: (A) Steady-state fluorescence excitation (green dashed) and emission (green solid) spectra for Cy3 dissolved in THF. The red dashed and solid lines indicate the excitation and emission wavelengths used in a time-resolved fluorescence spectroscopy experiment, respectively; (B) a general scheme illustrating the process of single photon counting at a chosen emission wavelength with respect to time after a fluorophore is given an excitation pulse (green); (C) fluorescence lifetime decay curve of Cy3 measured at an emission wavelength of 625 nm when excited at 500 nm with a ps diode laser (individual points on decay curve represent photon counts and solid line represents third order exponential decay fit with fit residuals plotted below).

On a practical level, TRFS involves exciting a fluorophore at one given wavelength and measuring the time it takes for individual photons to be emitted at a chosen wavelength of detection, shown in **Figure 1.13A** as the dashed and solid red lines overlaid on the excitation and emission spectra of Cy3. If a fluorophore is given an excitation pulse at time zero, the photons emitted after that excitation pulse are collected until they are no longer being emitted. The

distribution of photons and their intensity with respect to time can then be plotted to obtain a decay curve (**Figure 1.13B**). **Figure 1.13C** illustrates the lifetime curve obtained by measuring the decay of Cy3 dissolved in THF, excited at 500 nm and measured at 625 nm. The individual points plotted on this curve can be thought of as individual photons being counted and the solid fit line is a third order exponential decay function that has been fitted to the raw data, shown in **Equation 1.1**:[136]

$$I(t) = \alpha_1 e^{(-\frac{t}{\tau_1})} + \alpha_2 e^{(-\frac{t}{\tau_2})} + \alpha_3 e^{(-\frac{t}{\tau_3})} \quad (1.1)$$

Each component of the decay function describes a different segment of the overall decay, where τ_1 and α_1 describe the early portion of the decay, τ_2 and α_2 describe the intermediate portion of the decay, and τ_3 and α_3 describe the tail. The τ values are the component lifetimes and the α values can be thought of as the weights for that term in the function. The τ and α values can be extracted from the fit to calculate a τ_{av}, or the average fluorescence lifetime for that specific molecular species dissolved in the chosen solvent, according to the weighted average formula shown in **Equation 1.2**:[136]

$$\tau_{av} = \frac{\alpha_1\tau_1^2 + \alpha_2\tau_2^2 + \alpha_3\tau_3^2}{\alpha_1\tau_1 + \alpha_2\tau_2 + \alpha_3\tau_3} \quad (1.2)$$

Several internal and external factors modulate the fluorescence lifetime of an emissive species. *External* factors like Förster resonance energy transfer (FRET), Dexter electron transfer (DET), dynamic quenching, photon reabsorption, and the formation of excimers all affect the fluorescence lifetime of a fluorophore.[138] These modes of fluorescence lifetime modulation are not relevant to the work discussed in this dissertation and therefore will not be discussed here in any more detail. *Internal* factors, like internal rotation, temperature, viscosity, polarity, and excited state electron and proton transfer (ESET/ESPT) affect the fluorescence lifetime of a fluorophore. One of the major pathways to dissipate the energy of an excited fluorophore and shunt its decay toward non-radiative modes is through rotation of the parts of the molecule participating in

emission. An increase in internal rotation thus results in a decrease in lifetime.[138] It follows, then, that any process that increases or decreases a fluorophore's ability to rotate will consequently decrease or increase the fluorophore's lifetime, respectively. For example, lowering the temperature or increasing the viscosity of the system will constrain the internal rotation of a molecule, resulting in an increase in lifetime. Fluorescence lifetime also depends on the polarity of the system, with the general trend of decreasing lifetime with increasing polarity.[139] Finally, reversible changes in the distribution of electrons or protons associated with a molecule's excited state can play a role in modulating lifetime.[138] In ESET, electrons from the molecule in its excited state travel from the donor site to an acceptor site, resulting in a non-fluorescent species that relaxes to the ground state via non-radiative decay. ESPT is a similar process, only involving protons and generally occurring between two molecules, rather within the same molecule. These transfer processes are critical for the function of conducting polymers and fluorescent-based metal sensors. *In the context of materials and, more specifically, nanoparticles, these processes manifest when a fluorophore is embedded within a material's matrix – increasing its lifetime compared to the free fluorophore dissolved in a good solvent (**Figure* **1.14***).*[140] *This principle, combined with the other internal factors that influence fluorescence lifetime, particularly polarity, describes many of the systems developed in this dissertation.*

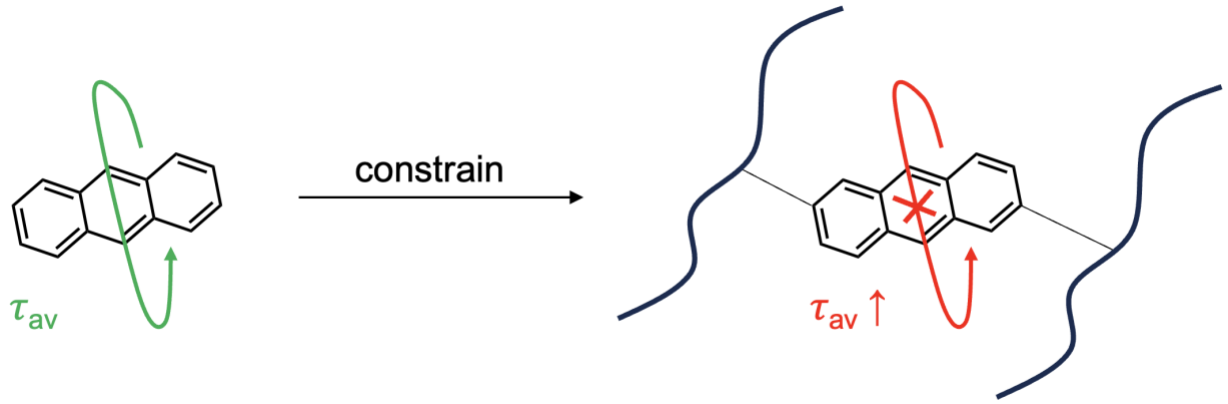

Figure 1.14: A fluorescent anthracene molecule constrained in a polymeric or nanoparticulate matrix exhibits a longer fluorescence lifetime than its dissolved counterpart.

1.6.3 Rational nanoparticle design vs. unbiased screening approaches

Nanoparticle formulations for drug delivery applications are traditionally optimized in the academic literature by low-throughput empirical methods where several rationally designed materials are synthesized in batches, individually purified, and screened for biological effect *in vivo*. The formulation that most closely matches the desired therapeutic effect is then selected and examined in greater detail. While a tried-and-true method, manual optimization of a small selection of formulations neglects the physicochemical complexity of multi-component, high-dimensional nanomaterials whose design often hinges on a delicate balance between covalent, ionic, and Van der Waals interactions. High-throughput approaches to nanoparticle optimization have emerged in the last 10 years as laboratory automation has become cheaper and more accessible.[141–143]

Generally, these studies involve synthesizing and purifying large numbers (>100) of chemically distinct nanoparticle formulations, screening their biological effect *in vitro* in parallel, and selecting a few top-performing candidates to test *in vivo*. While effective at identifying potential nanoparticle formulation candidates for a specific application or disease pathology, these studies often neglect detailed characterization of the nanoparticle libraries, resulting in the identification of hit formulations without uncovering underlying structure-property relationships

to inform future formulation and experimentation.[61,62] The vast majority of characterization performed is limited to the study of hydrodynamic diameter and zeta potential via DLS measurements. These measurements are straightforward to perform in a high throughput context, especially if done using a DLS instrument that accommodates well plates. However, by only measuring diameter and zeta potential, these studies neglect the investigation of any of the complex nanomaterial-environment and nanomaterial-payload interactions that affect biological outcomes. What results, as a consequence, is the publication of a large number of studies employing unbiased, high throughput screening approaches to nanoparticle formulation development *without providing clear information regarding which physicochemical properties of the nanoparticles studied resulted in success, and most importantly, the mechanism by which those properties influence biological outcomes.* Of note, particularly pertaining to the technology described in this dissertation, TRFS can be performed in a high throughput context.

Some pioneering works by the Langer and Anderson groups in the early 2010s employed high-throughput approaches to generate non-viral siRNA vector libraries of cationic lipidoid nanoparticles, cationic core-shell polymer nanoparticles, and microfluidically-synthesized cationic lipid nanoparticle libraries, in addition to polymer-based vectors for small molecule anticancer payloads.[144–147] While high quality studies, these first high-throughput NP publications lacked much in the way of elucidating structure-activity relationships; they merely sought to identify hit materials for the application at hand.

A 2019 study by Mirkin and coworkers demonstrated that, in a well-defined design space, ML algorithms could be deployed to uncover non-linear structural phenomenon for spherical nucleic acid NPs synthesized in a combinatorial fashion.[148] A 2020 publication by Reineke and coworkers surveyed a library of 43 statistical copolymers for use as CRISPR-Cas9 RNP non-viral

vectors.[88] The authors characterized nine physicochemical properties of each polymer, screened them for toxicity, gene editing efficiency, and cellular uptake and used random forest classifiers to map the influence of those properties on their three biological outputs. It was found that editing efficiency is dependent on hydrophobicity-associated parameters like *clogP* and n_{Hill} while toxicity and uptake are dependent on polyplex diameter and cationicity-associated parameters like pKa and ζ-potential. A recent publication from Leibfarth and coworkers demonstrated utility in combining flow polymer synthesis with ML analysis to discover fluorinated copolymers that exhibit high signal intensity and high aqueous solubility for ^{19}F MRI applications.[149]

Pioneering works by Dahlman and coworkers, beginning with their seminal paper published in 2017 in *Proceedings of the National Academy of Science*, have reported methods for foregoing the *in vitro* parallel screen of lipid nanoparticles prior to *in vivo* testing with a DNA barcoding approach to formulation study.[60] There is a large body of literature that suggests that *in vitro* identification of hit formulations do not necessarily translate to *in vivo* success because of the increased complexity associated with *in vivo* nano-bio interactions.[61,63] The Dahlman group synthesizes libraries of lipid nanoparticles using a microfluidic method and labels each formulation with a unique DNA barcode. All the nanoparticle formulations are pooled together and injected into a single mouse. After some time, the mouse is sacrificed, the organs and tissues are removed and disaggregated, cellular DNA is extracted, and the DNA is subjected to polymerase chain reaction (PCR) analysis for the presence of any of the barcodes. With this method, the researchers are able to track the biological fate of each formulation. Despite the utility of this method, the Dahlman group only characterizes the hydrodynamic diameters of each formulation.

1.7 Conclusions

This chapter detailed an overview of the characteristics that one must consider when engineering a new nanoparticle drug delivery system on several length scales, including the atomic and molecular scale features of nanoparticle components, the materials that those molecules compose, the complex biological barriers that a nanoparticle must overcome to successfully deliver a therapeutic payload, and the methods available for the characterization of nanoparticles. After surveying this large engineering design space regarding nanoparticle synthesis and deployment, I've drawn three major conclusions:

1. The deployment of a successful nanoparticle delivery system requires several length scales of coordination – from the atomic level all the way to the organism level.
2. Rationally engineering nanoparticle delivery systems in such a large and multidimensional chemical/materials design space is a historically challenging endeavor, with an extremely low rate of clinical translation.
3. State-of-the-art analytical tools provide limited insight into materials properties and material-biology interactions.

Therefore, I hypothesize that **TRFS, coupled with the rational molecular design of self-reporting nanoparticle structural components, will provide nuanced characterization data with respect to nanomaterial-environment and nanomaterial-payload interactions inaccessible to state-of-the-art methods.** This dissertation aims to address some of the shortcomings of the nanoparticle drug delivery field by developing new molecular tools and nanoparticle fabrication methods that allow for the study of formulations using TRFS.

Chapter 2 – Synthetic Protein Nanoparticles via Photoreactive Electrohydrodynamic Jetting

2.1 Authors and Contributions

This chapter contains text and data from a manuscript under review as of the time of writing as:

Synthetic Protein Nanoparticles via Photoreactive Electrohydrodynamic Jetting

Anthony J. Berardi,* Sonja D. Francisco,* Albert Chang, Julio C. Zelaya, Jeffery E. Raymond, Joerg Lahann (**denotes equal contribution*)

Macromolecular Rapid Communications

2.2 Abstract

Protein nanoparticles are an attractive class of materials for nanomedicine applications due to the intrinsic biocompatibility, biodegradability, and intrinsic functionality of their constituent proteins. Despite the clinical success of select protein nanoparticles, this class of nanocarriers remains understudied and underdeveloped compared to lipid and polymer nanoparticles due to challenges related to formulation optimization, large design space, and their structural complexity. In this work, we introduce a modular strategy for protein nanoparticle preparation based on the concept of photoreactive jetting. The process relies on continuous UV irradiation during electrohydrodynamic (EHD) jetting of protein solutions that contain a homobifunctional photocrosslinker. The resulting protein nanoparticles exhibit nanogel-like architectures comprised of proteins that are linked via synthetic moieties. Compared to conventional protein nanoparticles,

this method reduced nanoparticle processing times to minutes, rather than hours to days. The inclusion of an emissive structural motif as the molecular scaffold of the photocrosslinker was used to study the supramolecular architecture of the stable nanoparticles via time-resolved fluorescence spectroscopy.

2.3 Introduction

Nanoparticles are attractive vehicles for therapeutics due to their large payload capacity, ability to stabilize otherwise insoluble small molecule drugs, improved biodistribution, and low off-target toxicity.[25] To date, the majority of clinically approved nanoparticles are composed of either lipids or polymers.[55] These systems feature molecular building blocks that are versatile and easy to formulate, but suffer from low degrees of cell and tissue-specificity. Proteins have been widely studied as intrinsic therapeutic agents, in the form of monoclonal antibodies (mAbs) and antibody-drug conjugates (ADCs).[150,151] Other protein therapeutics act as carriers for small molecule drugs and nucleic acids for gene therapy.[152] Protein nanoparticles (PNP) have been fabricated through several methods, including nanoparticle albumin-bound (Nab) processing,[153] emulsification,[98,154] desolvation,[97,155] and self-assembly.[54] Nab technology has been extensively used clinically to prepare Nab-paclitaxel (Abraxane®), an albumin-based sPNP loaded with paclitaxel for the treatment of metastatic breast cancer.[99] The Nab process involves high-pressure homogenization of aqueous and organic solutions of proteins and small molecule drugs at high shear rates, resulting in nanoparticles with small molecules buried in the hydrophobic domains of their composite proteins.[54,99] The emulsification and desolvation processes involve the addition of an aqueous protein solution to either a surfactant-containing oil phase or antisolvent, respectively, resulting in the formation of stable nanoparticles via thermodynamic and entropic forces; the resulting nanoparticles are then either thermally or chemical crosslinked.[54,97,98,153,154] While highly

scalable, these processes suffer from a lack of modularity and versatility, as solution and processing parameters need to be optimized for every formulation. Self-assembly is an attractive method to produce highly controlled, designer nanomaterials, but requires the de novo design of individual protein components. This process is computationally intense, both difficult and expensive to execute experimentally, and not compatible with native proteins.[156–158] None of the aforementioned preparation methods are amenable to high throughput screening workflows, which have been extensively employed for the discovery of lipid and polymer nanoparticles but have yet to be deployed for protein nanoparticle formulation discovery.

Synthetic protein nanoparticles (sPNPs)[54] are a class of therapeutic drug carriers that combine the intrinsic features of proteins with the engineering precision and manufacturability observed in synthetic polymer and lipid nanoparticles. Recently, sPNPs have been prepared via electrohydrodynamic (EHD) jetting.[106] This method involves dilute solutions of protein, therapeutic cargo, and a crosslinker that are atomized using high electrical fields. The process results in stable nanoparticles with low polydispersity that are collected as a solid powder from the collection substrate.[104,106,159] sPNPs exhibit a network-like architecture, with individual proteins joined together by crosslinkers and therapeutic molecules interspersed throughout the network. Protein nanoparticles produced with this method have displayed therapeutic utility in treating glioblastoma, melanoma, and lung inflammation in murine models.[152,160–162]

Previous studies used homobifunctional crosslinkers based on an NHS ester-oligo(ethylene glycol)-NHS ester (NHS-OEG-NHS) architecture to stabilize protein nanoparticles with EHD jetting.[106,152,159,160] Following EHD jetting, the collection surfaces on which nanoparticles were deposited were incubated at 37 °C for several days to ensure complete conversion of the NHS groups. While effective in stabilizing sPNPs, the use of the NHS-OEG-NHS crosslinkers comes

with its own set of challenges, including batch-to-batch variability in the linkers, the need for additional purification steps, and sluggish reaction kinetics of the solid-state crosslinking reaction.

2.4 Methods

2.4.1 Materials

All reagents and solvents were purchased from Sigma Aldrich and used without further purification. UltraPure water was purchased from Invitrogen. Silica gel flash chromatography was performed using SiliCycle SiliaFlash P60 silica gel. Thin-layer chromatography was performed on Supelco TLC plates (pre-coated with a 250 μm layer of a silica gel 60 matrix with fluorescent indicator F254) and visualized with a UV hand lamp (254 nm and 365 nm) and potassium permanganate stain.

2.4.2 Nuclear Magnetic Resonance (NMR) Spectroscopy

NMR spectra were recorded on a Bruker Avance Neo spectrometer operating at 500 MHz. Samples were dissolved in $CDCl_3$ for analysis. Chemical shift was referenced to the solvent residual peak at 7.26 ppm and 77.16 ppm for ^{1}H spectra and ^{13}C spectra, respectively.

2.4.3 Liquid Chromatography – Mass Spectrometry (LC-MS)

Small molecule mass spectra were recorded on an Agilent 6230 ESI-TOF HPLC-MS in positive ion mode with a manual injection valve and no column in series before the detector. Samples were dissolved at millimolar concentrations in HPLC-grade acetonitrile prior to analysis.

2.4.4 Steady-state Fluorescence Spectroscopy

Steady-state excitation and emission spectra (2D and 3D) of small molecules and nanoparticles were recorded on a Horiba FluoroMax Plus spectrofluorometer equipped with a 150

W xenon arc lamp, Czerny-Turner monochromaters, an R928P photomultiplier tube capable of detection from 185-850 nm, and reference photodiode for monitoring lamp output. Excitation and emission slit widths were set to 4 nm. **2** was measured in DMSO, nanoparticle samples were measured in UltraPure water, and all measurements were performed in quartz cuvettes.

2.4.5 Time-Correlated Single Photon Counting (TCSPC)

Fluorescence lifetime measurements of **2** and nanoparticles were acquired on a Horiba FluoroMax Plus spectrofluorometer with a Horiba NanoLED 390 nm solid state diode laser (<1.4 ns pulse duration) driven by NanoLED NL-C2 Pulsed Diode Controller and DeltaHub DH-HT TCSPC Controller modules. Sample measurements were recorded at 535 nm with a 1 MHz laser repetition rate, measurement range of 200 ns, 950 V detector bias, and histogram set to 512. The instrument response function (IRF) was determined from the scattering signal of a suspension of Ludox HS-40 silica at 370 nm. Measurements were performed in quartz cuvettes.

2.4.6 Scanning Electron Microscopy (SEM)

SEM images were acquired on a Thermo Fisher Nova 200 Nanolab SEM/FIB microscope operating at a voltage of 17 kV, a current of 0.14 nA, and a dwell time of 10 μs. Samples were prepared by placing a silicon wafer on the collection pans during the EHD jetting process to collect spraying nanoparticles directly onto the wafer surface. Wafers were adhered onto a stub with double sided copper tape and gold sputter coated for 40 seconds prior to imaging.

2.4.7 Dynamic Light Scattering (DLS)

Nanoparticle size and zeta potential measurements were performed on a Malvern Zetasizer Nano ZSP equipped with a 633 nm 4mW He-Ne laser at an angle of 173°. All samples were equilibrated to ambient temperature before measurement. Particle size and zeta potential were

analyzed with the provided Nano DTS software package. Size measurements were recorded in disposable low volume cuvettes and zeta potential measurements were recorded in Malvern folded capillary disposable cuvettes.

2.4.8 Synthesis of 1

The synthesis of **1** was conducted according to previously published reports.[163] In a typical synthesis, 2,3-dibromomaleimide (1 g, 3.92 mmol, 1 eq.) and sodium acetate (0.81 g, 9.81 mmol, 2.5 eq.) were added to a 50 mL round bottom flask and dissolved in 20 mL of methanol with stirring. The flask was sealed with a septum and 2-mercaptoethanol (0.69 mL, 9.81 mmol, 2.5 eq.) was added dropwise via syringe. Upon addition, the reaction mixture turned immediately to a bright yellow color. After stirring at room temperature for 2 hours, the reaction mixture was poured into a separatory funnel and diluted 3x with water. The mixture was extracted 7-9x with ethyl acetate. The organic layer was collected, dried over sodium sulfate, and evaporated. The resulting crude residue was purified by standard phase flash chromatography with a 2-15% methanol gradient in dichloromethane.

HRMS (ESI-TOF): calc'd for $[M+ACN+Na]^+$ 313.02, found 313.95.

^{1}H NMR (500 MHz, $CDCl_3$): δ 3.32 (t, J = 7.6 Hz, 6H), 3.58 (q, J = 7.5, 7.0 Hz, 4H), 4.95 (br, 2H)

2.4.9 Synthesis of 2

In a dark room, **1** (1g, 4.02 mmol, 1 eq.), 4-benzoylbenzoic acid (2.72 g, 12.05 mmol, 3 eq.) and 4-dimethlaminopyridine (49 mg, 0.40 mmol, 0.10 eq.) were added to a 50 mL round bottom flask and dissolved in 20 mL of tetrahydrofuran. The flask sealed with a septum, chilled in an ice bath, and diisopropylcarbodiimide (1.89 mL, 12.05 mmol, 3 eq.) was added dropwise via syringe. The temperature was allowed to come to room temperature. After overnight reaction, the

mixture was filtered and concentrated under reduced pressure. The resulting residue was purified with standard phase flash chromatography in 20% ethyl acetate in toluene. All purification was performed in the dark and the product was always stored in an amber vial wrapped in aluminum foil in the dark.

HRMS (ESI-TOF): calc'd for $[M+Na]^+$ 688.11, found 688.11.

^1H NMR (500 MHz, $CDCl_3$): δ 3.65 (t, *J* = 5.8 Hz, 4H), 4.51 (t, *J* = 5.8 Hz, 4H), 7.51-7.62 (m, 4H), 7.63-7.85 (m, 10H), 8.03 (d, *J* = 8.4 Hz, 4H)

2.4.10 Preparation of synthetic protein nanoparticles by EHD jetting

All sPNPs were prepared via electrohydrodynamic jetting. Human serum albumin (HSA) (5 mg) and **2** (at various % w/w relative to HSA) were dissolved in 1 mL of a 20% v/v methanol in UltraPure water solution with vortexing and gentle bath sonication, being careful to keep the room dark and the sample shielded from light so as not to prematurely trigger a benzophenone photoreaction. The solution was drawn into a 1 mL syringe fitted with a 10 G blunt-tipped needle and wrapped in aluminum foil and electrical tape to shield the solution from ambient light. The solution was flown downward with a syringe pump toward an aluminum collection pan (15 cm diameter) at a flow rate of 0.1 mL/hr, situated 8 cm above the collection pan. A voltage of 6-10 kV was applied to the syringe needle and the collection pan was grounded. Two UV lamps (Everbeam, 365 nm, 50 W) were positioned orthogonal to each other and directed toward the electrospray. The lamps were run for the duration of the jetting process (**Figure 2.6**, **Figure 2.7**). Each formulation was jetted for 30 minutes onto a single collection pan. 1 mL of UltraPure water was pipetted over the pan surface to collect the resulting nanoparticles. The resulting nanoparticle suspensions were analyzed without any further processing for all solution-state measurements.

2.5 Results and Discussion

In this communication, we describe a novel protein nanoparticle fabrication method using photoreactive EHD jetting. This strategy is based on the recognition that during EHD jetting, the surface area of the atomized fluid increases approximately three orders of magnitude, opening the door for ultrafast photoreactions. By replacing the conventional homobifunctional linkers' NHS ester groups with photoreactive moieties, nanoparticle crosslinking was completed in situ, i.e., without the need for additional post-processing. This resulted in a fabrication method amenable to high-throughput workflows and therefore minimized unnecessary processing and purification steps. The process introduced in this study employed spatiotemporal, light-mediated crosslinking that only occurred during the EHD jetting process itself, reduced post-jetting crosslinking, processing, and purification time to about 1 minute (a four order of magnitude improvement in time over previously reported methods) and dramatically increased sPNP yield. Briefly, a solution composed of human serum albumin (HSA) and homobifunctional, photoreactive crosslinker **2** was prepared in a 20% v/v mixture of methanol in water. The solution was drawn into a syringe and accelerated downward through an electric field toward a collection surface. 365 nm UV lamps were directed over the jetting path, effectively crosslinking the proteins into nanoparticles as they travelled from the syringe tip to the collection surface while solvent evaporated (**Figure 2.1**, **Figure 2.6**, **Figure 2.7**).

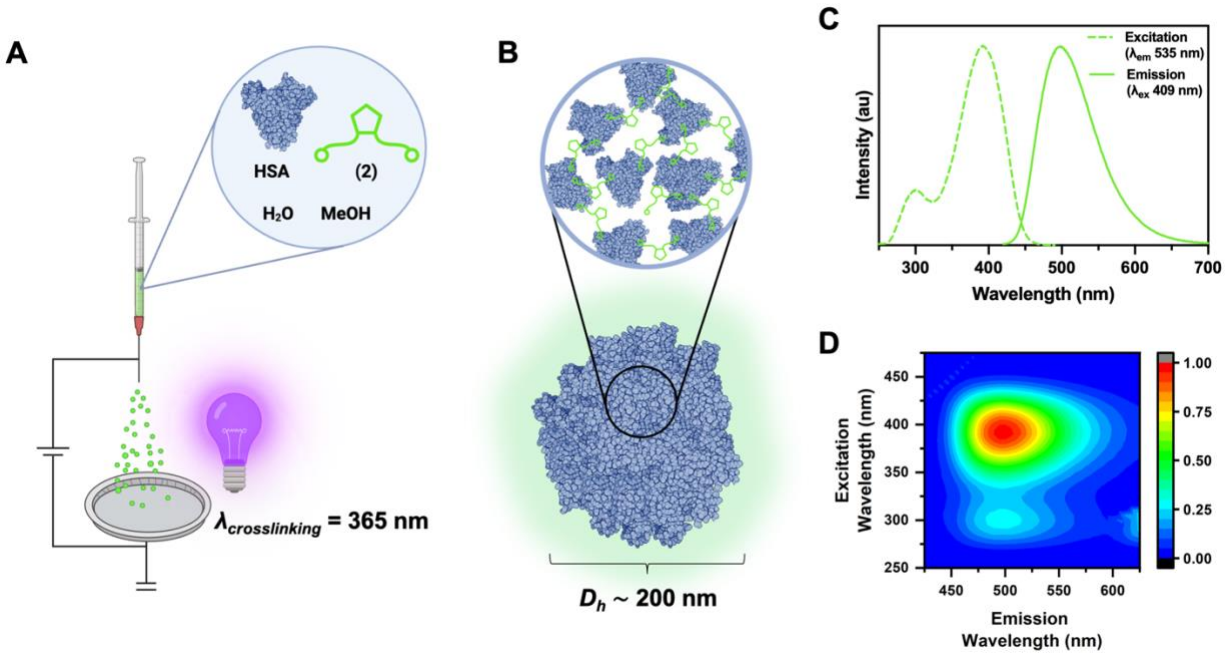

Figure 2.1: (A) Schematic overview of continuous synthetic protein nanoparticle fabrication and crosslinking process via electrohydrodynamic jetting, (B) proposed nanoparticle structure, (C) excitation and emission spectra of crosslinker **2**, and (D) 3D excitation-emission spectrum of crosslinker **2**.

2.5.1 Synthesis and Design of Photocrosslinker 2

Photocrosslinker **2** is based on a dithiomaleimide scaffold with two benzophenone-containing arms capable of undergoing photoreactions with nearby macromolecules through a carbonyl-centered radical produced upon UV irradiation.[115,164] **2** was synthesized in a two-step process, first through the reaction of 2-mercaptoethanol with 2,3-dibromomaleimide to produce **1**, and then by coupling the resulting dihydroxyl-bearing synthetic intermediate with 4-benzoylbenzoic acid to produce **2** (**Figure 2.2**). A dithiomaleimide scaffold was chosen as the basis for this crosslinker for its intrinsic, broadband fluorescence in the 450-650 nm regime (**Figure 2.1C-D**), resulting in a molecule that was photoreactive and stabilizing toward biomacromolecules. Additionally, intrinsic bright emission allowed for self-reporting via downstream fluorescence detection methods.[163,165,166]

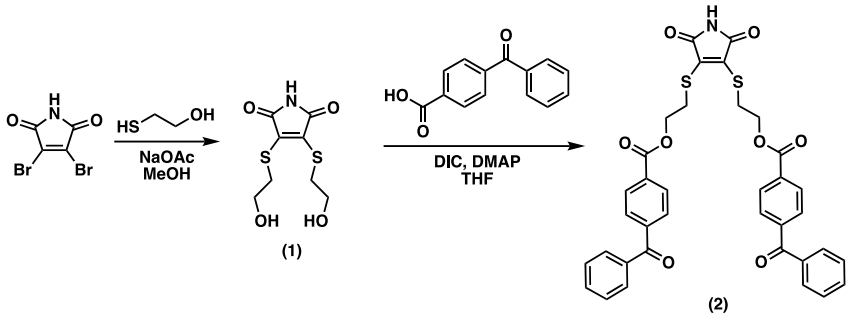

Figure 2.2: Synthetic strategy to prepare crosslinker **2**.

2.5.2 Dry-State sPNP Physical Characterization with SEM

Following preliminary experimentation which confirmed that the inclusion of a homobifunctional photocrosslinker and UV lamps in the EHD jetting process would lead to stable sPNPs, we sought to understand the influence that the stoichiometry of photocrosslinker **2** in the pre-jetting solution would have on resulting nanoparticle physical properties. To investigate this premise, eight sPNP formulations with differing amounts of 2 relative to HSA were EHD jetted, in the range of 0-5% w/w. A summary of all formulations is listed in **Table 1**. From the analysis of SEM images of silicon wafers placed on the collection surface during EHD jetting, it was determined that all eight formulations resulted in the deposition of spherical sPNPs, characteristically similar to those produced in previous investigations (**Figure 2.3A**).[106,152,159,160,162] All formulations, including the formulation with no crosslinker (black), resulted in sPNPs with diameters around 200 nm and circularities greater than 0.8, via SEM image analysis (**Figure 2.3B-C**, **Table 2.1**, **Figure 2.8**). The images shown are of a single batch of sPNPs; three batches were independently produced to investigate the consistency of this process and no significant batch-to-batch variability was observed.

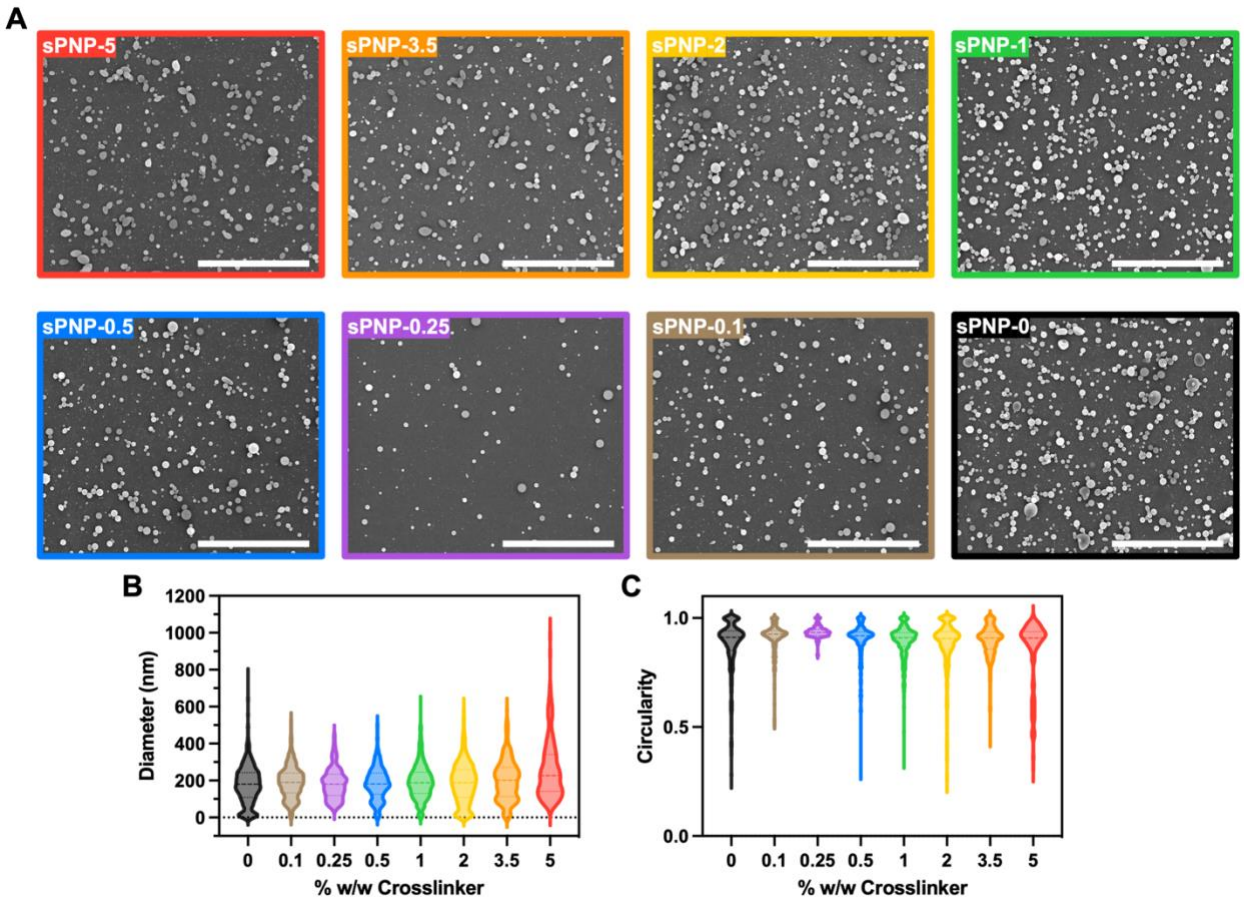

Figure 2.3: SEM images (A), distributions of diameters (B), and distributions of circularity (C) of synthetic protein nanoparticles formulated at eight different weight percentages of crosslinker 2 relative to HSA. Diameter and circularity distributions were calculated from image analysis of at least 200 individual nanoparticles (Scale bar = 5 μm).

2.5.3 Hydrated-State sPNP Physicochemical Characterization with DLS

Next, sPNPs were collected from the collection surfaces after EHD jetting by pipetting 1 mL of water over the area of the surface and analyzed by a variety of solution-based techniques (**Figure 2.6**). To assess how well the suspended sPNPs, in a hydrated environment, retained their previous dry-state shape, hydrodynamic diameters were measured with dynamic light scattering (DLS). The transition from 0.25% to 0.1% w/w crosslinker relative to HSA in the formulation resulted in a precipitous decrease in hydrodynamic diameter. At % w/w ≥ 0.25%, DLS peak diameters in the 130-230 nm range were recorded, suggesting the presence of stable nanoparticles,

while at % w/w ≤ 0.1%, DLS peak diameters in the 1-10 nm range were recorded, suggesting a predominating presence of free HSA protein (**Figure 2.4A-B**, **Table 2.1**). While SEM images of either **sPNP-0.1** or **sPNP-0** confirmed the successful preparation of sPNPs, these nanoparticles were not stable in aqueous solutions indicating that the concentration of crosslinker was too low. All samples, regardless of their supramolecular architecture, displayed mildly negative zeta potentials of approximately -10 mV with no trend as a function of crosslinker stoichiometry (**Figure 2.4C**), consistent with previous studies of HSA-based sPNP surface charge. When plotted with respect to the weight percentage of crosslinker in each formulation, DLS peak diameter and polydispersity (PDI) displayed inverse trends. Diameter rapidly increased and plateaued around 200 nm by 0.5% w/w, while PDI decreased from around 0.6 for low % w/w formulations and plateaued to approximately 0.2 as the amount of crosslinker increased (**Figure 2.4D**, **Table 2.1**). These results suggest that for 1% w/w crosslinker or greater, sPNPs produced by photoreactive EHD jetting were well-controlled and monodisperse with diameters in the 200 nm range. The DLS traces shown are of a single batch of sPNPs; three independent batches were produced and no significant batch-to-batch variability was observed (**Figure 2.9**). Additionally, DLS analysis confirmed that both photocrosslinker **2** and UV light were required to prepare stable sPNPs (**Figure 2.10**).

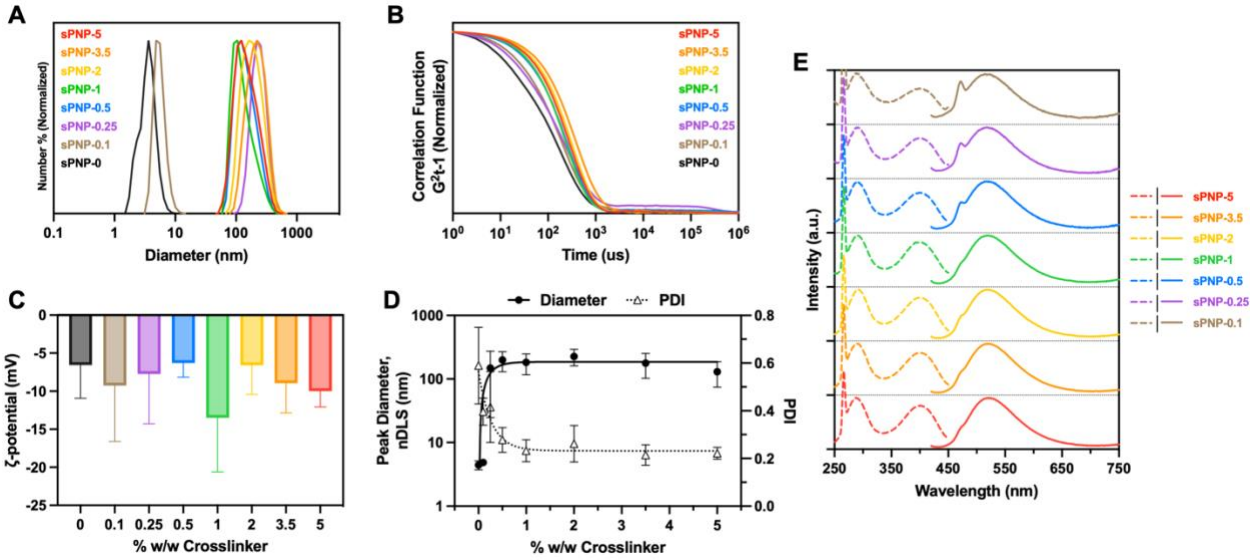

Figure 2.4: (A) Number-based DLS size distributions, (B) DLS correlation functions, and (C) zeta potential measurements for synthetic protein nanoparticles formulated at 8 different weight percentages of crosslinker 2 relative to HSA. (D) Number-based DLS peak diameter and PDI plotted with respect to the weight percentage of crosslinker in each formulation, and (E) steady-state excitation (dashed lines) and emission (solid lines) spectra for all formulations. Size distribution and correlation function data are shown for one representative batch of nanoparticles. Error bars in (C) and (D) represent standard deviation from the mean of three independently produced nanoparticle batches. λ_{em}=535 nm for all excitation spectra, λ_{ex}=405 nm for all emission spectra, and all spectra were acquired with a 4 nm slit width.

			Dry-State Physical Properties		Hydrated-State Physical Properties		
	% w/w Crosslinker	**Crosslinker: HSA molar ratio**	**Mean Diameter (nm)**	**Mean Circularity**	**Peak Diameter, nDLS (nm)**	**PDI**	**ζ-potential (mV)**
sPNP-5	5	4.96	262.2	0.840	130.3	0.222	-9.98
sPNP-3.5	3.5	3.47	202.0	0.892	177.1	0.214	-8.95
sPNP-2	2	1.99	187.6	0.870	226.3	0.262	-6.60
sPNP-1	1	0.992	193.4	0.888	182.0	0.233	-13.49
sPNP-0.5	0.5	0.496	184.3	0.891	199.0	0.277	-6.30
sPNP-0.25	0.25	0.248	184.1	0.936	148.5	0.415	-7.73
sPNP-0.1	0.1	0.0992	192.5	0.912	4.9	0.396	-9.27
sPNP-0	0	0	180.4	0.874	4.4	0.589	-6.56

Table 2.1: Physical property values for synthetic protein nanoparticles of 8 different weight percentages of crosslinker **2** relative to HSA. Dry-state and hydrated-state properties were obtained from SEM and DLS characterization, respectively.

2.5.4 Time-Resolved Fluorescence Spectroscopy Provides Insight Into sPNP Formulation Parameters Inaccessible to SEM and DLS

With the exception of **sPNP-0** (no photocrosslinker), all formulations exhibited broadband fluorescence emission from 450-650 nm when excited at 405 nm and two excitation peaks in the 250-450 nm regime when emission was monitored at 535 nm (**Figure 2.4E**), as a result of the inclusion of photocrosslinker **2**. No clear differences in λ_{max} were detectable for either steady-state excitation or emission spectra between any of the formulations studied. However, based on previous studies in our group and others, we hypothesized that the particle formulations might exhibit differences in their fluorescence lifetimes. This might be due differences in internal gelation states, solvation states, and physical stress on the crosslinkers based on the local environments in the sPNPs, implying that fluorescence lifetime data may provide additional information about the architecture of each formulation.[165,167] Time-correlated single photon counting (TCSPC) was employed to measure nanoparticle fluorescence lifetimes, and the measured photon counts appeared to bin to two paths of decay in a fashion analogous to the peak diameters recorded via DLS analysis plotted in **Figure 2.4A-B** (**Figure 2.5A, inset**). **Equation 2.1** was used to fit the raw photon counts composing the decays to a third-order exponential decay function:

$$I(t) = a_1 e^{\left(-\frac{t}{\tau_1}\right)} + a_2 e^{\left(-\frac{t}{\tau_2}\right)} + a_3 e^{\left(-\frac{t}{\tau_3}\right)} \quad (2.1)$$

where τ_n are the component lifetimes of each term and α_n represent the amplitude weights associated with each component lifetime. The τ_n and α_n values extracted from fitting for each sPNP formulation are summarized in **Table 2.2**.

All three component lifetimes, τ_1, τ_2, and τ_3, increased as a function of crosslinker stoichiometry in sPNP formulations and plateaued between 1 and 2% w/w crosslinker, in

accordance with a one-phase association function (**Figure 2.5B**, **Table 2.2**). Interestingly, while all component lifetimes increased asymptotically with respect to crosslinker stoichiometry, the component lifetime weights, α_n, remained constant for each individual decay component (**Figure 2.5C**, **Table 2.2**). It is generally accepted that the shortest component lifetime, τ_1, describes the intrinsic emission of a fluorophore as impacted by solvent effects and non-radiative decay processes. Longer component lifetimes, τ_2 and τ_3, are often attributed to secondary decay processes associated with environmental, electronic, or physical factors beyond solvation, such as fluorophore-fluorophore and fluorophore-substrate interactions.[136,138,168] These assignments have been made in other systems utilizing dithiomaleimide fluorophores extensively.[165–168]

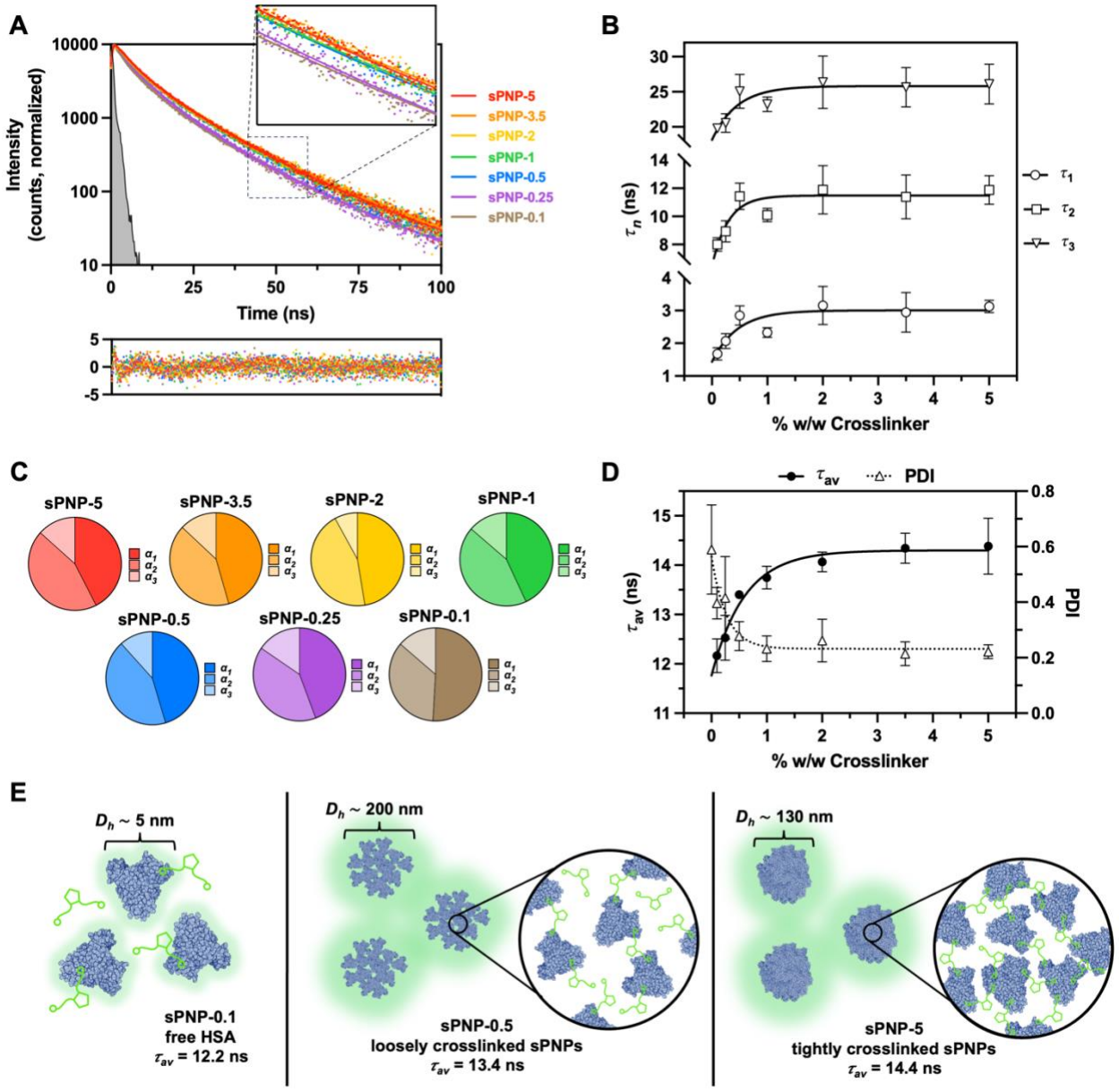

Figure 2.5: (A) Fluorescence lifetime decays fitted to third-order exponential decay functions (top) and fit residuals (bottom), (B) individual component lifetimes (τ_1, τ_2, τ_3) plotted with respect to the weight percentage of crosslinker in each formulation, (C) amplitude weights (α_1, α_2, α_3) corresponding to each component lifetime, τ_n, plotted as parts of a whole, (D) average fluorescence lifetime (τ_{av}) and PDI plotted with respect to the weight percentage of crosslinker in each synthetic protein nanoparticle formulation, and (E) proposed sPNP supramolecular architectures as a function of weight percentage crosslinker in each formulation. (Error bars in (B) and (D) represent standard deviation from the mean of three independently produced nanoparticle batches.)

Extracting τ_n and α_n terms from the exponential decay deconvolution process, an average fluorescence lifetime, τ_{av}, was calculated for each measurement according to **Equation 2.2**:[136]

$$\tau_{av} = \frac{\alpha_1\tau_1^2+\alpha_2\tau_2^2+\alpha_3\tau_3^2}{\alpha_1\tau_1+\alpha_2\tau_2+\alpha_3\tau_3} \quad (2.2)$$

Taken together, the individual component lifetimes and their weights were used to calculate an average fluorescence lifetime for each sPNP sample, and the corresponding τ_{av} values were plotted with respect to % w/w crosslinker (**Figure 2.5D**). An asymptotically increasing trend in τ_{av} was observed in the range of 12-14 ns with increasing % w/w crosslinker, comparable and inverse to the trends in sPNP diameter and PDI, respectively, described previously. All sPNP formulations exhibited longer τ_{av} values than **2** dissolved in water (τ_{av} = 11.9 ns, **Figure 2.11**), indicating that the EHD jetting/photocrosslinking process resulted in crosslinkers covalently bound to HSA proteins, regardless of the crosslinker amount. As % w/w crosslinker increased and stable particles began to form, the molecular rotation and solvent relaxation events of **2** decrease, resulting in an increase in the observed τ_{av}.

	τ_1 (ns)	τ_2 (ns)	τ_3 (ns)	α_1	α_2	α_3	τ_{av} (ns)
sPNP-5	3.13	11.9	26.1	0.461	0.440	0.100	14.4
sPNP-3.5	2.95	11.4	25.6	0.458	0.435	0.107	14.3
sPNP-2	3.15	11.9	26.3	0.470	0.436	0.0934	14.1
sPNP-1	2.33	10.1	23.2	0.450	0.424	0.126	13.7
sPNP-0.5	2.85	11.4	25.1	0.479	0.434	0.0868	13.4
sPNP-0.25	2.07	8.94	20.5	0.453	0.408	0.140	12.5
sPNP-0.1	1.68	8.00	19.8	0.490	0.372	0.139	12.2

Table 2.2: Fluorescence lifetime kinetic data for all synthetic protein nanoparticle formulations. Values are derived from third-order exponential decay fits generated from raw photon counts. Amplitudes (α_n) are normalized to 1. Full decay curves, fits, and plots of values can be found in Figure 2.5.

We speculate that a sol-gel transition occurred across the inflection points of the plots of peak diameter, PDI, and τ_{av} (**Figure 2.4D**, **Figure 2.5D**) with respect to crosslinker weight percentage.[169] Below the observed transition regime of about 0.1-1% w/w crosslinker, most of the protein and crosslinkers were either unreacted or in an oligomeric state (**Figure 2.5E**, left). Only above the 0.1-1% w/w crosslinker transition regime did the macromolecular components of the EHD jetting solution begin to fully polymerize, crosslinking and resulting in stable nanoparticles that no longer dissolved into their constituents (**Figure 2.5E**, middle, right). The DLS data suggest

an abrupt transition point between 0.1 and 0.25% w/w crosslinker, where particles formed above 0.1% w/w and did not form below 0.25% w/w. The fluorescence lifetime analysis, on the other hand, provide a more nuanced mechanistic insight into nanoparticle formation. The observed transition is not as abrupt, as lifetimes gradually increased with respect to crosslinker concentration until they plateaued between 1-2% w/w as the local environment around individual **2** crosslinks stabilized. Therefore, we suggest that the critical crosslinker concentration required to form stable sPNPs via photoreactive EHD jetting is approximately 2% w/w relative to protein (**sPNP-2**), corresponding roughly to 2 molar equivalents of crosslinker for every 1 molar equivalent of protein (**Table 2.1**). Notably, this process did not employ a photosensitizer; the benzophenone moieties act as the crosslinker. Additionally, the high surface area of the nanoparticles promoted faster crosslinking than what would be expected from similar crosslinking reactions in a bulk phase.

2.6 Conclusion

In this study, we produced synthetic protein nanoparticles via a photoreactive electrohydrodynamic jetting process and employed a fluorescent, benzophenone-based crosslinker to stabilize the resulting particles. Engineering an emissive dithiomaleimide moiety into the crosslinker backbone allowed us to probe for the optimal crosslinker concentration to result in stable nanoparticles with time-correlated single photon counting, which was found to be 2% w/w relative to protein. This method provides access to molecular information inaccessible to state-of-the-art physical characterization techniques like scanning electron microscopy and dynamic light scattering. In addition to the implementation of an alternative analytical method to probe nanoparticle architecture, the process of protein nanoparticle production via EHD jetting was significantly improved, decreasing processing and purification time to approximately one minute, an improvement in efficiency by four orders of magnitude. Future work is needed to adapt this

photoreactive electrohydrodynamic jetting process to high throughput screening workflows to generate protein nanoparticle libraries – work that we believe will significantly impact the field of nanomedicine, resulting in improved and more streamlined clinical translation.

2.7 Supplementary Figures

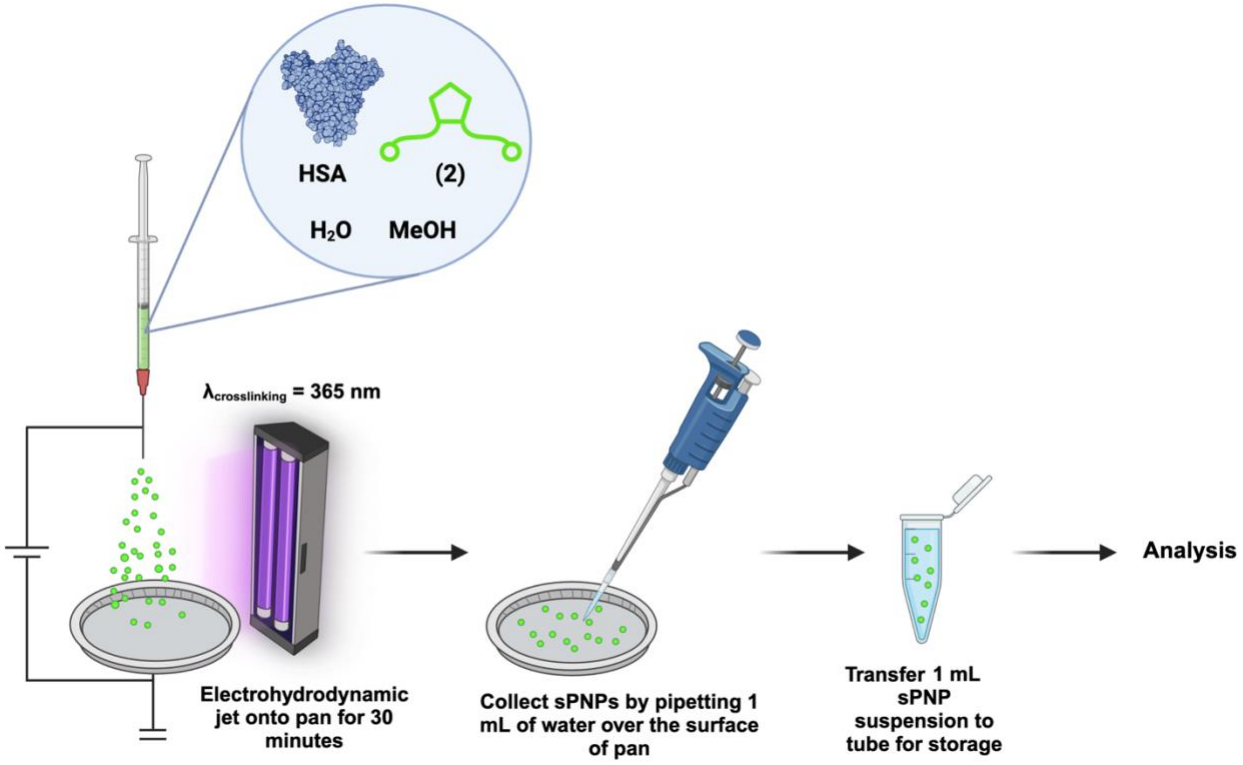

Figure 2.6: Overview of continuous sPNP crosslinking/production process. A solution containing protein, crosslinker, and solvent are flown toward a grounded collection pan while the spray is irradiated with 365 nm light. After 30 minutes of electrohydrodynamic jetting, the sPNPs are liberated from the collection pan by gently pipetting over the surface with 1 mL of water. The resulting sPNP suspension is transferred to a storage tube for analysis.

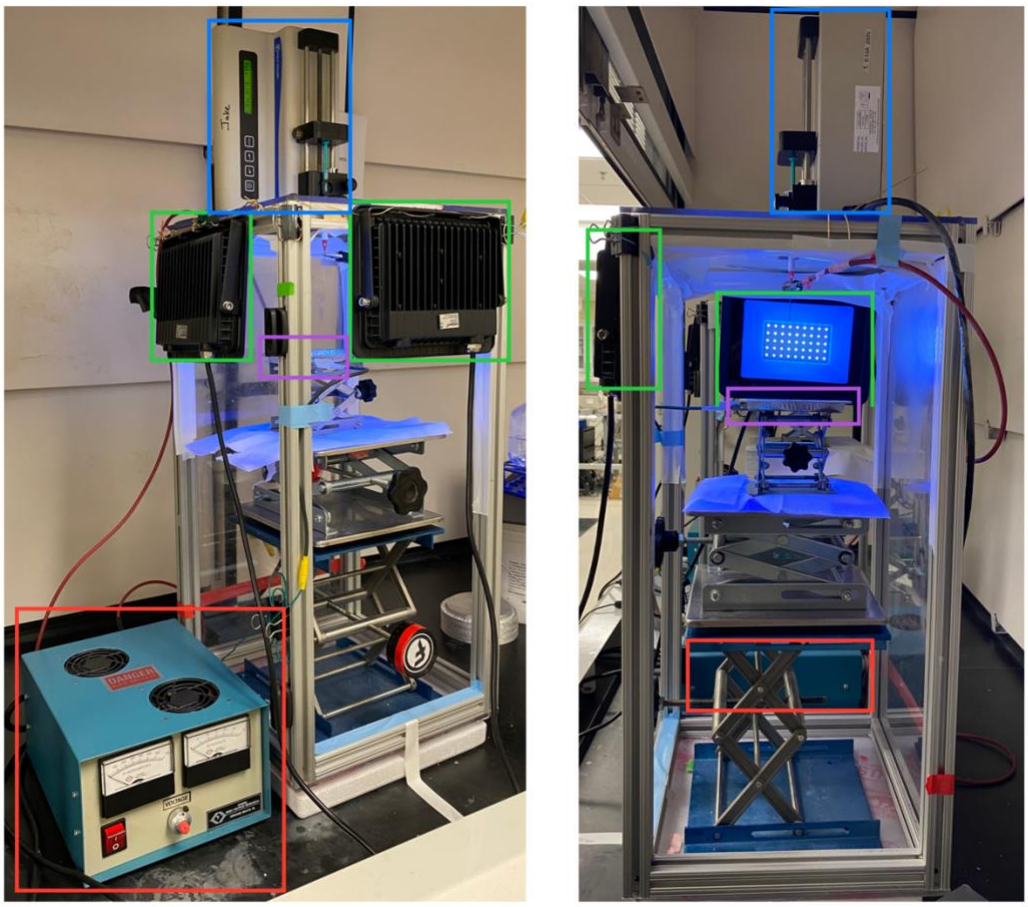

Figure 2.7: Diagram of the continuous EHD jetting/crosslinking setup. Front view (left) and right side view (right). Red = power supply, blue = syringe pump, green = UV lamps, purple = collection pan.

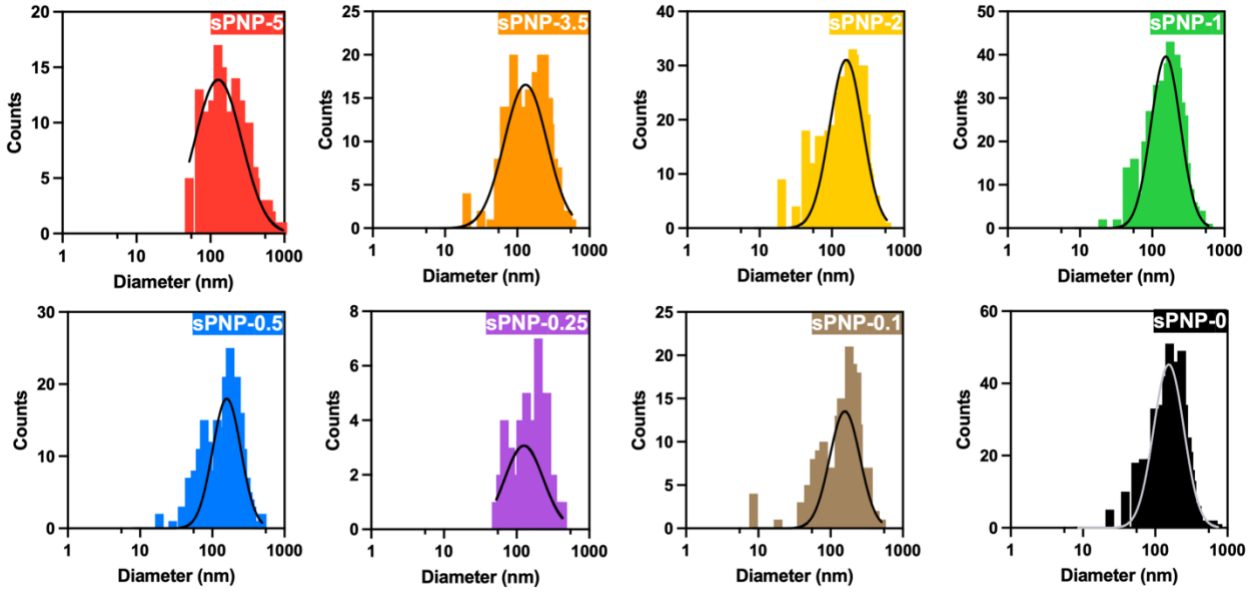

Figure 2.8: Supplemental to **Figure 2.3**. Lognormal fitting of diameter histograms calculated from SEM image analysis. This data was generated from images presented in Figure 2. At least 200 individual nanoparticle counts were analyzed for each sample.

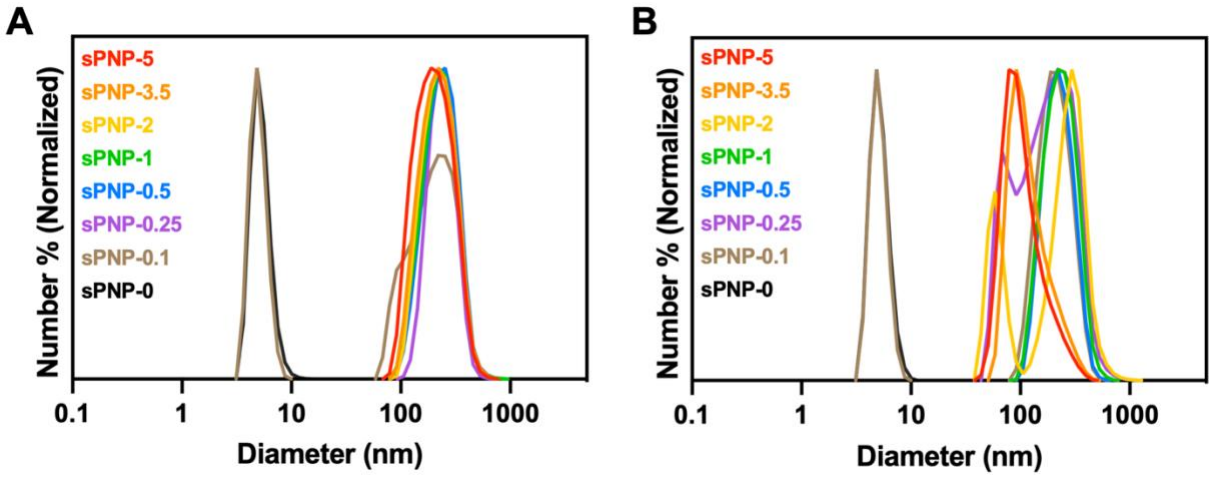

Figure 2.9: Number-based DLS size distributions for batch 2 (A) and batch 3 (B).

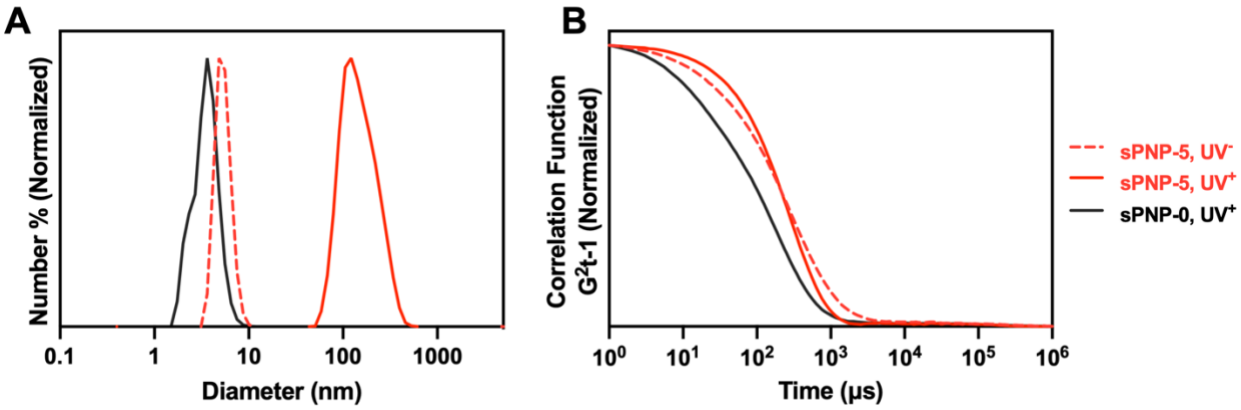

Figure 2.10: (A) DLS traces and (B) correlation functions for samples with 5 wt% crosslinker treated either with or without UV during EHD jetting (red) and 0 wt% crosslinker treated with UV. Only the sample with crosslinker and UV results in stable sPNPs.

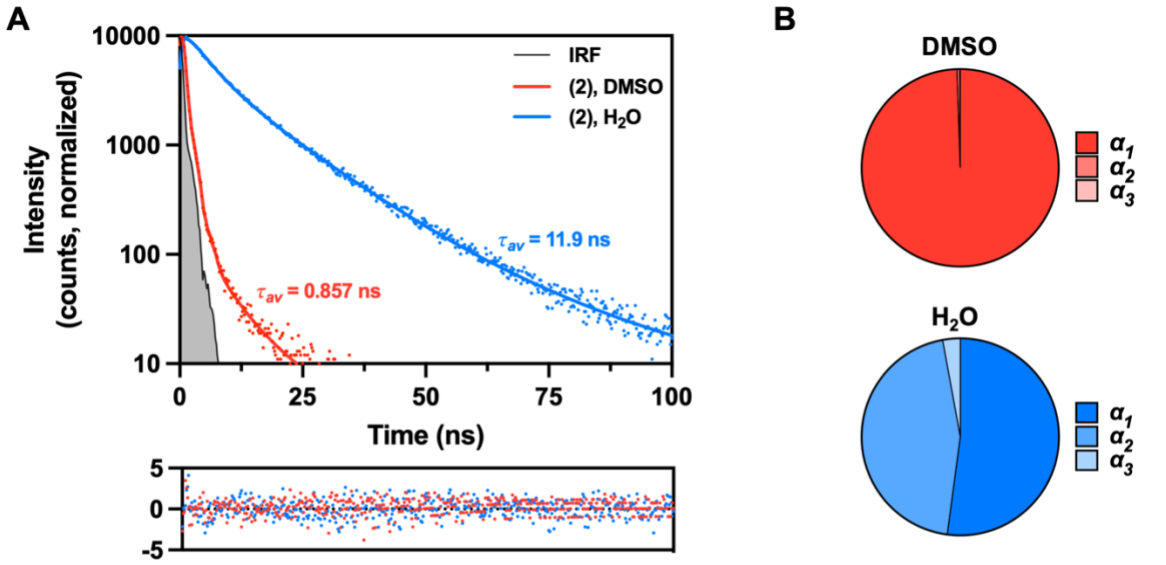

C

	τ_1 (ns)	τ_2 (ns)	τ_3 (ns)	α_1	α_2	α_3	τ_{av} (ns)
(2), DMSO	0.414	3.86	12.1	0.995	0.00434	0.000963	0.857
(2), H_2O	4.15	12.5	28.7	0.521	0.450	0.0287	11.9

Figure 2.11: (A) Fluorescence lifetime decays fitted to third order exponential decay functions (top) and fit residuals (bottom), (B) α value weights corresponding to each component lifetime plotted as parts of whole, and (C) corresponding kinetic data for crosslinker **2** in DMSO and water. **2** exhibits an ultra-fast lifetime in DMSO, a good solvent. In water, a poor solvent for **2**, its lifetime is an order of magnitude higher. However, it is still slower than all the lifetimes recorded for sPNP formulations – indicating that the longer lifetimes observed for sPNP formulations are, indeed, attributable to **2**'s interaction with the stabilizing nanoparticle matrix.

Chapter 3 – Self-Reporting Therapeutic Protein Nanoparticles

3.1 Authors and Contributions

This chapter contains text and data from the following accepted manuscript:

Self-Reporting Therapeutic Protein Nanoparticles

Anthony J. Berardi, Jeffery E. Raymond, Albert Chang, Ava K. Mauser, Joerg Lahann

ACS Applied Materials & Interfaces

3.2 Abstract

We present a modular strategy to synthesize nanoparticle sensors equipped with emissive molecular reporters capable of discerning minute changes in interparticle chemical environments based on fluorescence lifetime analysis. Three types of nanoparticles were synthesized with the aid of tailor-made molecular reporters and it was found that protein nanoparticles exhibited greater sensitivity to changes in the core environment than polymer nanogels and block copolymer micelles. Encapsulation of the hydrophobic small-molecule drug paclitaxel (PTX) in self-reporting protein nanoparticles induced characteristic changes in fluorescence lifetime profiles, detected via time-resolved fluorescence spectroscopy. Depending on the mode of drug encapsulation, self-reporting protein nanoparticles revealed pronounced differences in their fluorescence lifetime signatures, which correlated with burst- vs. diffusion-controlled release profiles. Self-reporting nanoparticles, such as the ones developed here, will be critical for unraveling nanoparticle stability

and nanoparticle-drug interactions informing the future development of rationally engineered nanoparticle-based drug carriers.

3.3 Introduction

In nanomedicine, nanoparticles are used as vehicles to deliver therapeutic payloads and as contrast agents for imaging.[25,170] Considerable attention has thus been directed toward *in situ* monitoring to provide insight into physicochemical processes underlying complex phenomena, for example during the rational formulation of nanoparticles[168,171,172] or to elucidate biological mechanisms of uptake or potency.[173] Protein nanoparticles (PNPs) are an emerging class of nanocarriers that exhibit advantages over lipid, polymer, and inorganic nanoparticles, due to the diversity in their component building blocks, conjugation capabilities, biodegradability, and low immunogenicity.[54,152,162] Despite the recent encouraging success of nanoparticle-based therapeutic delivery systems in the clinic,[6–8] several barriers to the clinical translation of PNPs still exist, most notably in site-specific targeting, biological barrier transport, and efficient payload delivery.[24,174–176] PNPs offer an engineering design space that is considerably larger, potentially more versatile, and more complex than incumbent lipid or polymer nanoparticles due to the biochemical, structural, and functional complexity inherent to their composite proteins. Concomitantly, their functional properties, including nanomaterial-drug interaction, payload release kinetics and dynamics, and stability, are complex and remain understudied.[54] High-throughput nanoparticle library screens have emerged as promising methods to identify lead formulations with desired properties, however, such unbiased approaches have so far fallen short in generating foundational knowledge related to structure-property relationships in PNPs.[60,88,143,177,178] Therefore, new real-time monitoring methods are needed to better inform parameterization in high throughput screening experiments and clinical translation.[24,37]

Small molecule fluorophores are ubiquitous tools deployed across a wide range of scientific disciplines, including drug discovery, cell and tissue imaging, analyte detection, single-molecule experimentation, and labeling, which all employ fluorescence spectroscopy or microscopy detection methods.[136] The steady-state excitation and emission spectra of a fluorophore are chemical structure-dependent and can probe the molecular environment within nanoparticles. For instance, pairs of fluorophores known to engage in Förster resonance energy transfer (FRET) are often conjugated to interacting macromolecules or nanomaterials to probe their proximity to one another and thus serve as molecular reporters.[110,179] These steady-state fluorescence methods, however, are dependent on the local concentration of fluorophores employed and the fluorophores are often designed on a molecular level with application specificity in mind, for example, to report on pH or redox environments.[180,181]

Fluorescence lifetime imaging microscopy (FLIM) and time-resolved fluorescence spectroscopy are alternative methods to infer knowledge about the molecular environment within nanoparticles. Importantly, the fluorescence lifetime of an emissive species is concentration-independent and is highly sensitive to changes in local physicochemical environments, such as temperature, polarity, viscosity, and the presence of external quenchers.[136,138,182,183] In addition, fluorophores do not have to be designed *de novo* for a given application. Small molecule fluorophores exhibit short average fluorescence lifetimes (τ_{av}<3 ns) in good solvents and longer lifetimes (τ_{av}>3 ns) in bad solvents.[184] When immobilized and prohibited from free rotation in solvent, for instance, when bound to a nanoparticle, imbedded in a bulk material, or dissolved in a viscous liquid, fluorescence lifetimes of fluorophores increase compared to their well-solvated counterparts.[172,173,185] This phenomenon has been used to monitor polymer micelle assembly and

solvation, silica nanoparticle solvation, polymer micelle disassembly *in vitro*, and pH using quantum dots *in vitro*.

Dithiomaleimides (DTMs), along with their amine-substituted counterparts, diaminomaleimides (DAMs), are an emerging class of compact, non-conjugated fluorophores that can be synthesized via conjugate addition reactions in a straightforward manner from halide-substituted maleimides and thiols or amines, respectively.[186–188] DTMs and DAMs have tunable emissive properties based on the nature of their substituent groups (e.g., alkyl vs. aromatic)[186,187,189] and have been shown to exhibit solvatochromism.[188] Due to their modular nature and straightforward preparation, DTMs and DAMs have been implemented across a wide range of molecular engineering and nanomaterial applications, including protein engineering,[190–192] polymer labeling,[163,193,194] block copolymer micelles,[167] and nanogels,[140,166] as both structural components and fluorescent reporters. Fluorescence lifetime has been used to characterize some of these systems, either through distinguishing the assembly state of a polymer micelle,[165] confirming that a DTM had been immobilized in a material,[140] or in FRET-based barcoding systems.[166]

In this chapter, we describe the design and synthesis of three different self-reporting nanoparticles of distinct material composition and supramolecular architecture, enabled by the use of reactive, emissive molecular reporters as crosslinking components. Deploying the molecular reporters as both structural and sensing components allowed for direct monitoring by time-resolved fluorescence spectroscopy of how the nanoparticles responded to differences in external and internal chemical environments caused by exposure to solvent or drug encapsulation.

3.4 Methods

3.4.1 Materials

All solvents and reagents were purchased from Sigma Aldrich and used without further purification unless otherwise specified. Silica gel flash chromatography was performed using SiliCycle SiliaFlash P60 silica gel. Thin-layer chromatography was performed on Supelco TLC plates (pre-coated with a 250 μm layer of silica gel 60 matrix with fluorescent indicator F254) and visualized with a UV hand lamp (254 nm and 365 nm) and potassium permanganate stain.

3.4.2 Nuclear Magnetic Resonance (NMR) Spectroscopy

NMR spectra were recorded on either a Varian MR400 spectrometer at 400 MHz or a Bruker Avance Neo spectrometer at 500 MHz. All samples were dissolved in either $CDCl_3$ or DMSO-d_6. Chemical shift for ^1H spectra was referenced to the solvent residual peak at 7.26 ppm for samples acquired in $CDCl_3$ or the solvent residual peak 2.50 ppm for samples acquired in DMSO-d_6. Chemical shift for ^{13}C spectra was referenced to the solvent residual peak at 77.16 ppm for samples acquired in $CDCl_3$ or the solvent residual peak 39.52 ppm for samples acquired in DMSO-d_6.

3.4.3 Liquid Chromatography – Mass Spectrometry (LC-MS)

Small molecule mass spectra were recorded on an Agilent 6230 ESI-TOF HPLC-MS in positive ion mode with a manual injection valve and no column in series before the detector. Samples were dissolved at millimolar concentrations in HPLC-grade acetonitrile prior to analysis.

3.4.4 Steady-state Fluorescence Spectroscopy

Steady-state excitation and emission spectra (2D and 3D) of small molecules and nanoparticles were recorded on a Horiba FluoroMax Plus spectrofluorometer equipped with a 150 W xenon arc

lamp, Czerny-Turner monochromaters, an R928P photomultiplier tube capable of detection from 185-850 nm, and reference photodiode for monitoring lamp output. Excitation and emission slit widths were set to 1 nm. Small molecule samples were measured in DMSO, nanoparticle samples were measured in UltraPure water, and both were performed in quartz cuvettes.

3.4.5 Time-Correlated Single Photon Counting (TCSPC)

Fluorescence lifetime measurements of small molecules and nanoparticles were acquired on a Horiba FluoroMax Plus spectrofluorometer with a Horiba NanoLED 390 nm solid state diode laser (<1.4 ns pulse duration) driven by NanoLED NL-C2 Pulsed Diode Controller and DeltaHub DH-HT TCSPC Controller modules. Sample measurements were recorded at 535 nm with a 1 MHz laser repetition rate, measurement range of 200 ns, 950 V detector bias, and histogram set to 512. The instrument response function (IRF) was determined from the scattering signal of a suspension of Ludox HS-40 silica at 370 nm. Measurements were performed in quartz cuvettes. Prior to the measurement of nanoparticle samples, 50 uL aliquots of stock nanoparticle suspensions were added to vials, freeze dried, and resuspended in the solvent of choice. Small molecule samples were measured at 1 μM in the solvent of choice.

3.4.6 Size Exclusion Chromatography (SEC)

SEC measurements were performed with THF as the eluent at 40 °C on a Shimadzu system equipped with an autosampler, refractive index detector, and photodiode array detector. The stationary phase was composed of a Phenomenex Phenogel 10 um Linear(2), 300x7.8mm column and calibrated with linear polystyrene standards of molecular weights ranging from 1,000,000 g/mol to 92 g/mol.

3.4.7 Scanning Electron Microscopy (SEM)

SEM images were acquired on a Thermo Fisher Nova 200 Nanolab SEM/FIB microscope operating at a voltage of 17 kV, a current of 0.14 nA, and a dwell time of 10 μs. Samples for **sPNP** were prepared by placing a silicon wafer on the collection pans during the EHD jetting process and spraying nanoparticles directly onto the wafer surface. Samples for **NG** and **MC** were prepared by drop casting suspensions of respective nanoparticles in water onto silicon wafers and drying overnight in a dessicator under house vaccum. Wafers were adhered onto a stub with double sided copper tape and gold sputter coated for 40 seconds prior to imaging.

3.4.8 Dynamic Light Scattering (DLS)

Nanoparticle size measurements were performed on a Malvern Zetasizer Nano ZSP at an angle of 173° with a 4mW He-Ne laser at 633 nm. All samples were equilibrated to ambient temperature before measurement. Particle size and zeta potential were analyzed with the provided Nano DTS software package. Measurements were recorded in Malvern folded capillary disposable cuvettes.

3.4.9 Data Analysis

All NMR spectra were analyzed and plotted with MestReNova v14. Steady-state emission spectra, excitation spectra, 3D emission-excitation spectra, SEC traces, and DLS traces were analyzed with Microsoft Excel and plotted with OriginPro. TCSPC fluorescence lifetime decay traces were fitted to third order exponential decays with the Horiba EzTime software package and plotted with OriginPro. All other plots were generated with OriginPro. SEM micrographs were analyzed using Fiji. Some schematic diagrams and illustrations were created with BioRender.com.

3.4.10 Small Molecule, Polymer, and Nanoparticle Synthetic Details

3.4.10.1 Synthesis of 1

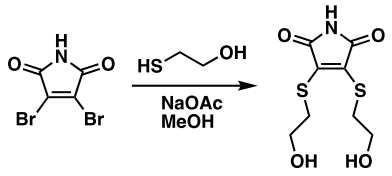

(1)

The synthesis of **1** was conducted according to a previously published report. In a typical batch, 2,3-dibromomaleimide (1 g, 3.92 mmol, 1 eq.) and sodium acetate (0.81 g, 9.81 mmol, 2.5 eq.) were added to a 50 mL round bottom flask and dissolved in 20 mL of methanol with stirring. The flask was sealed with a septum and 2-mercaptoethanol (0.69 mL, 9.81 mmol, 2.5 eq.) was added dropwise via syringe. Upon addition, the reaction mixture turned immediately to a bright yellow color. After stirring at room temperature for 2 hours, the reaction mixture was poured into a separatory funnel and diluted 3x with water. The mixture was extracted 7-9x with ethyl acetate. The organic layer was collected, dried over sodium sulfate, and evaporated. The resulting crude residue was purified by standard phase flash chromatography with a 2-15% methanol gradient in dichloromethane.

HRMS (ESI-TOF): calc'd for $[M+ACN+Na]^+$ 313.02, found 313.95.

^{1}H NMR (400 MHz, DMSO-d_6): δ 3.32 (t, *J* = 7.6 Hz, 6H), 3.58 (q, *J* = 7.5, 7.0 Hz, 4H), 4.95 (br, 2H)

3.4.10.2 Synthesis of 2a

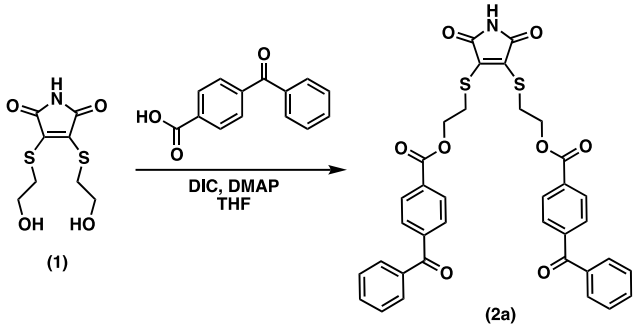

1 (1 g, 4.02 mmol, 1 eq.), 4-benzoylbenzoic acid (2.72 g, 12.05 mmol, 3 eq.), and 4-dimethlaminopyridine (49 mg, 0.40 mmol, 0.10 eq.) were added to a 50 mL round bottom flask and dissolved in 20 mL of tetrahydrofuran. The flask sealed with a septum, chilled in an ice bath, and diisopropylcarbodiimide (1.89 mL, 12.05 mmol, 3 eq.) was added dropwise via syringe. The temperature was allowed to come to room temperature. After overnight reaction, the mixture was filtered and concentrated under reduced pressure. The resulting residue was purified with standard phase flash chromatography in 20% ethyl acetate in toluene.

HRMS (ESI-TOF): calc'd for $[M+Na]^+$ 688.11, found 688.11.

^{1}H NMR (500 MHz, DMSO-d_6): δ 3.65 (t, *J* = 5.8 Hz, 4H), 4.51 (t, *J* = 5.8 Hz, 4H), 7.51-7.62 (m, 4H), 7.63-7.85 (m, 10H), 8.03 (d, *J* = 8.4 Hz, 4H)

3.4.10.3 Synthesis of 2b

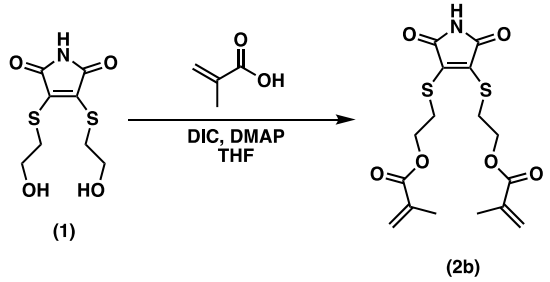

1 (1 g, 4.02 mmol, 1 eq.), methacrylic acid (0.847 mL, 10.04 mmol, 2.5 eq.), and 4-dimethlaminopyridine (49 mg, 0.40 mmol, 0.10 eq.) were added to a 50 mL round bottom flask

and dissolved in 20 mL of tetrahydrofuran. The flask sealed with a septum, chilled in an ice bath, and diisopropylcarbodiimide (1.57 mL, 10.04 mmol, 2.5 eq.) was added dropwise via syringe. The temperature was allowed to come to room temperature. After overnight reaction, the mixture was filtered and concentrated under reduced pressure. The resulting residue was purified with standard phase flash chromatography in 20% ethyl acetate in toluene.

Methacrylate functional group installation was performed via the acid-alcohol coupling of **1** with methacrylic acid instead of the field standard of a base-catalyzed nucleophilic attack of methacryloyl chloride with an alcohol. We found that the maleimide nitrogen was quite reactive to acid chlorides, in addition to the hydroxyl groups, and sought to keep that site unreacted for downstream activation without having to introduce protecting groups.

HRMS (ESI-TOF): calc'd for $[M+Na]^+$ 408.06, found 408.05.

^{1}H NMR (500 MHz, $CDCl_3$): δ 1.93 (s, 6H), 3.60 (t, *J* = 6.2 Hz, 4H), 4.38 (t, *J* = 6.2 Hz, 4H), 5.59 (s, 2H), 6.10 (s, 2H)

3.4.10.4 Synthesis of 3a

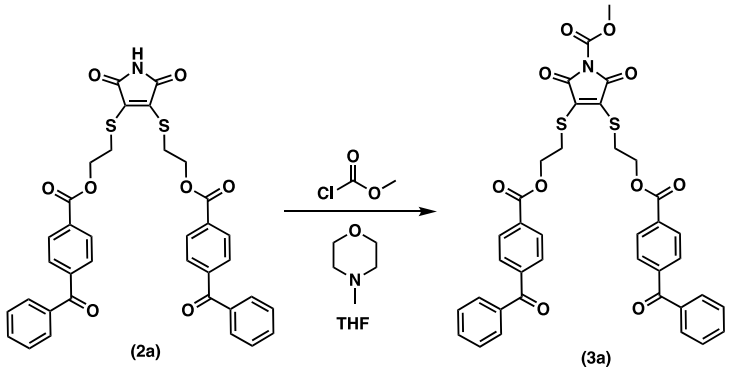

2a (0.404 g, 0.61 mmol, 1 eq.) was dissolved in 10 mL of anhydrous THF and added to a flame dried 50 mL round bottom flask and kept under a nitrogen atmosphere. N-methylmorpholine (0.134 mL, 1.22 mmol, 2 eq.) were added to the flask via syringe and the reaction mixture was allowed to stir at room temperature for 15 min. Methyl chloroformate (0.094 mL, 1.22 mmol, 2

eq.) was added to the flask via syringe and the reaction mixture was stirred for 1 hr. The reaction was quenched by the addition of 100 mL of dichloromethane and extracted 3x with water. The organic layer was collected, dried over sodium sulfate, and evaporated. The crude residue was analyzed without further purification.

HRMS (ESI-TOF): calc'd for $[M+Na]^+$ 746.76, found 746.70

^{1}H NMR (500 MHz, $CDCl_3$): δ 3.74 (t, *J* = 6.0 Hz, 4H), 4.62 (t, *J* = 6.0 Hz, 4H), 7.56 (dt, *J* = 58.1, 7.5 Hz, 6H), 7.81 (td, *J* = 8.5, 1.7 Hz, 8H), 8.11 (d, *J* = 8.4 Hz, 4H)

3.4.10.5 Synthesis of 3b

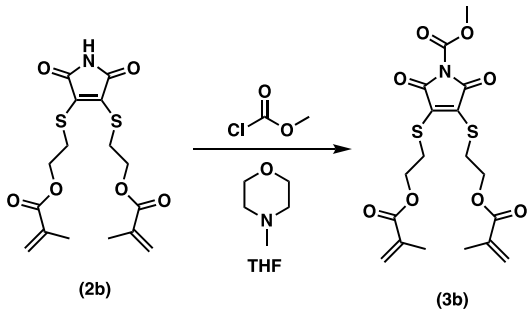

2b (0.303 g, 0.79 mmol, 1 eq.) was dissolved in 10 mL of anhydrous THF and added to a flame dried 50 mL round bottom flask and kept under a nitrogen atmosphere. N-methylmorpholine (0.73 mL, 1.57 mmol, 2 eq.) were added to the flask via syringe and the reaction mixture was allowed to stir at room temperature for 15 min. Methyl chloroformate (0.12 mL, 1.57 mmol, 2 eq.) was added to the flask via syringe and the reaction mixture was stirred for 1 hr. The reaction was quenched by the addition of 100 mL of dichloromethane and extracted 3x with water. The organic layer was collected, dried over sodium sulfate, and evaporated. The crude residue was analyzed without further purification.

HRMS (ESI-TOF): calc'd for $[M+Na]^+$ 466.06, found 466.06.

^{1}H NMR (500 MHz, $CDCl_3$): δ 1.93 (s, 6H), 3.65 (t, *J* = 6.1 Hz, 4H), 3.97 (s, 3H), 4.39 (t, *J* = 6.1 Hz, 4H), 5.59 (s, 2H), 6.09 (s, 2H)

3.4.10.6 Synthesis of 4a

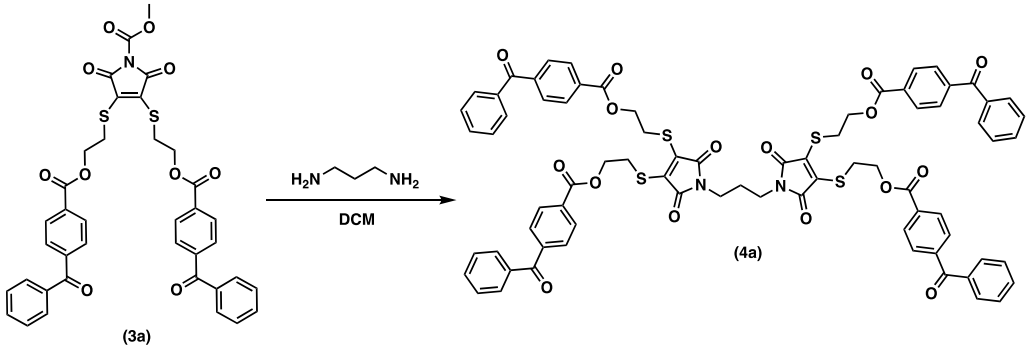

3a (0.45 g, 0.622 mmol, 2 eq.) and 1,3-diaminopropane (26.2 μL, 0.311 mmol, 1 eq.) were dissolved in dichloromethane and stirred overnight at room temperature. The dichloromethane was evaporated and the crude residue was purified with standard phase flash chromatography in 20% ethyl acetate in toluene.

HRMS (ESI-TOF): calc'd for $[M+Na]^+$ 1394.52, found 1394.26.

^{1}H NMR (500 MHz, $CDCl_3$): δ 1.86 (quint, *J* = 7.1 Hz, 2H), 3.42 (t, *J* = 7.2 Hz, 4H), 3.69 (t, *J* = 6.3 Hz, 8H), 4.59 (t, *J* = 6.2 Hz, 8H), 7.42-7.67 (m, 12H), 7.72-7.88 (m, 16H), 8.03-8.19 (m, 8H)

3.4.10.7 Synthesis of 4b

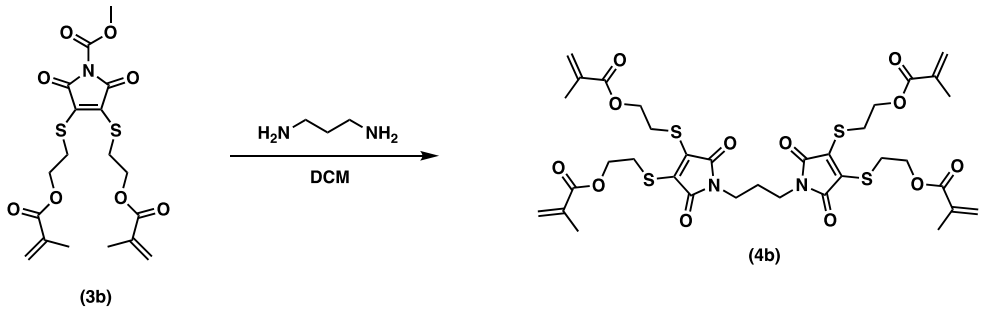

3b (0.28 g, 0.627 mmol, 2 eq.) and 1,3-diaminopropane (26.4 μL, 0.313 mmol, 1 eq.) were dissolved in dichloromethane and stirred overnight at room temperature. The dichloromethane was

evaporated and the crude residue was purified with standard phase flash chromatography in 15% ethyl acetate in toluene.

HRMS (ESI-TOF): calc'd for $[M+Na]^+$ 833.15, found 833.15.

^{1}H NMR (500 MHz, $CDCl_3$): δ 0.77-0.92 (m, 2H), 1.93 (s, 12H), 3.51 (t, *J* = 7.1 Hz, 4H), 3.59 (t, *J* = 6.2 Hz, 8H), 4.38 (t, *J* = 6.2 Hz, 8H), 5.58 (s, 4H), 6.10 (s, 4H)

3.4.10.8 sPNP (synthetic protein nanoparticle) preparation

sPNP was prepared via electrohydrodynamic (EHD) jetting. Human serum albumin (5 mg) and **4a** (0.25 mg) were dissolved in 1 mL of a 20 v/v% DMSO in UltraPure water solution with vortexing and bath sonication. The solution was flown downward via a syringe pump toward an aluminum collection pan (15 cm diameter) at a rate of 0.1 mL/hr through a syringe fitted with a 10 G blunt-tipped needle. The tip of the syringe needle was situated 15 cm above the collection pan. A voltage of 10 kV was applied from the syringe needle to the collection pan. Collection pans were changed every 30 min until 8 pans were accumulated. Each pan was placed in a Fisherbrand UV Crosslinker and irradiated at 368 nm at maximum power for 30 s. 4 mL of UltraPure water were used to collect the resulting nanoparticles from the pan surfaces using gentle agitation from a plastic razor blade. The resulting suspension was probe sonicated at 5 A for 30 s and centrifuged for 5 min at 4000 rpm. The resulting supernatant was distributed into 2 mL centrifuge tubes and centrifuged for 1 hr at 21000 rpm. The supernatant was discarded and the resulting pellets were resuspended in 500 uL of UltraPure water. **sPNP** was characterized by SEM, DLS, steady-state absorption, excitation, and emission spectroscopy, and TSCPC.

3.4.10.9 NG (crosslinked nanogel) preparation

Sodium dodecyl sulfate (SDS) (1.25 mg), 2-hydroxyethyl methacrylate (HEMA) (46.7 uL, 384 μmol), **4b** (2.5 mg, 3.09 μmol, 5 wt% relative to HEMA), and a few granules of 1,3,5-trioxane

were dissolved in 5 mL of UltraPure water in a 5 mL round bottom flask. A 100 μL t_0 aliquot was withdrawn for later NMR analysis, the flask was sealed with a septum, and purged with nitrogen for 30 minutes with stirring. After purging, the mixture was heated to 70 °C in an oil bath and 25 uL of a degassed, aqueous solution containing potassium persulfate (1.25 mg) was injected in one portion via syringe. The mixture was allowed to stir while heating for 3 hours. The flask was opened to atmosphere and a 100 μL t_f aliquot was withdrawn for later NMR analysis. SDS and unreacted HEMA were removed by two wash cycles consisting of centrifugation at 4000 RPM for 10 minutes and resuspension in UltraPure water. **NG** was characterized by SEM, DLS, steady-state absorption, excitation, and emission spectroscopy, and TSCPC.

3.4.10.10 MC (core-crosslinked micelle) preparation

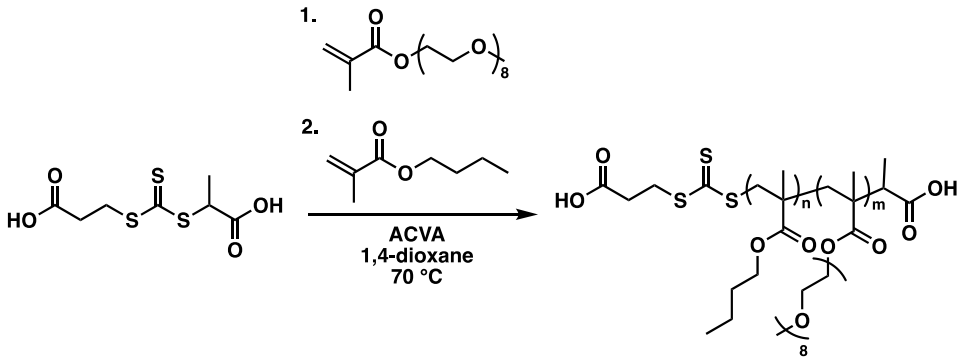

Synthesis of poly(PEGMA) homopolymer via RAFT polymerization

Polyethylene glycol methyl ether methacrylate (PEGMA, average M_n 500) (2 mL, 4.32 mmol, 50 eq.), 2-[[(2-carboxyethyl)sulfanylthiocarbonyl]-sulfanyl]propanoic acid (22.0 mg, 86.4 μmol, 1 eq.), 4,4′-azobis(4-cyanovaleric acid) (ACVA) (2.42 mg, 8.64 μmol, 0.1 eq.), and a few granules of 1,3,5-trioxane were added to a 20 mL Schlenk flask equipped with a stir bar and dissolved in 20 mL of 1,4-dioxane. A 100 μL t_0 aliquot was withdrawn for later NMR analysis and the flask was sealed with a rubber septum. The reaction mixture was purged with nitrogen for 30 minutes with stirring. After purging, the flask was heated to 70 °C and stirred overnight. The flask

was opened to atmosphere and a 100 μL t_f aliquot was withdrawn for later NMR analysis. Poly(PEGMA) homopolymer was isolated by three repetitions of a wash cycle consisting of precipitation into cold hexane with stirring, decanting the hexane supernatant, and redissolution of the resulting polymer in tetrahydrofuran. The final polymer was dried following washing and characterized via NMR and SEC.

Monomer conversion = 80%; *degree of polymerization (m)* = 40; $M_{n,\,NMR}$ = 20,254 g/mol; $M_{n,\,SEC}$ = 24,314 g/mol; $M_{w,\,SEC}$ = 31,004; $Đ_{SEC}$ = 1.28

Synthesis of poly(BMA-b-PEGMA) diblock copolymer via RAFT polymerization

Butyl methacrylate (BMA) (0.25 mL, 1.57 mmol, 50 eq.), poly(PEGMA) macroCTA (0.636 g, 31.4 μmol, 1 eq.), ACVA (0.88 mg, 3.14 μmol, 0.1 eq.), and a few granules of 1,3,5-trioxane were added to a 10 mL Schlenk flask equipped with a stir bar and dissolved in 10 mL of 1,4-dioxane. A 100 μL t_0 aliquot was withdrawn for later NMR analysis and the flask was sealed with a rubber septum. The reaction mixture was purged with nitrogen for 30 minutes with stirring. After purging, the flask was heated to 70 °C and stirred overnight. The flask was opened to atmosphere and a 100 μL t_f aliquot was withdrawn for later NMR analysis. Poly(BMA-b-PEGMA) diblock copolymer was isolated by three repetitions of a wash cycle consisting of precipitation into cold hexane with stirring, decanting the hexane supernatant, and redissolution of the resulting polymer in tetrahydrofuran. The final polymer was dried following washing and characterized via NMR and SEC.

Monomer conversion = 90%; *degree of polymerization (n)* = 45; $M_{n,\,NMR}$ = 26,653 g/mol; $M_{n,\,SEC}$ = 27,982 g/mol; $M_{w,\,SEC}$ = 33,274; $Đ_{SEC}$ = 1.19

	Degree of polymerization	$M_{n,\ NMR}$ (g/mol)	$M_{n,\ SEC}$ (g/mol)	$M_{w,\ SEC}$ (g/mol)	$Đ_{SEC}$
Poly(PEGMA)	40	20,254	24,314	31,004	1.28
Poly(BMA-b-PEGMA)	95	26,653	27,982	33,274	1.19

Table 3.1: Block copolymer characterization - summary table.

MC preparation from poly(BMA-b-PEGMA) diblock copolymer

Poly(BMA-b-PEGMA) diblock copolymer (50 mg, 1.87 μmol, 1 eq.) and **4b** (4.6 mg, 5.63 μmol, 3 eq.) were dissolved in 1 mL of DMSO in a 5 mL round bottom flask. ACVA (0.053 mg, 0.187 μmol, 0.1 eq.) dissolved in 4 mL of UltraPure water was added to the flask dropwise with stirring. The mixture was purged with nitrogen for 30 minutes with stirring. After purging, the flask was submerged in a 70 °C an oil bath and stirred for 5 hours. Following micelle self-assembly and crosslinking, the reaction mixture was diluted with 5 mL of water and dialyzed against 1 L of deionized water for 3 days with a 10 kDa cutoff membrane to remove DMSO. **MC** was characterized by SEM, DLS, steady-state absorption, excitation, and emission spectroscopy, and TSCPC.

3.4.10.11 Calculation of monomer conversion via NMR analysis

The monomer conversions for the preparation of **NG** and syntheses of poly(PEGMA) homopolymer and poly(BMA-b-PEGMA) diblock copolymer were calculated by the observation of the decrease in methacrylate resonance integrals in the ^{1}H NMR spectra of t_0 and t_f aliquots withdrawn before and after polymerization, relative to the signal from an included internal standard of 1,3,5-trioxane (**Figure C.3**). Briefly, 400 uL of DMSO-d_6 was added to the t_0 and t_f 100 μL aliquots and ^{1}H NMR spectra were acquired of both. Chemical shift was normalized to the TMS peak at 0.0 ppm. The singlet at 5.1 ppm (corresponding to 1,3,5-trioxane's methylene peak)

was assigned a normalized integral of 100.0. The two characteristic singlets resulting from unreacted methacrylate monomer terminal alkene groups (between 5.0 and 6.0 ppm) were integrated relative to the 1,3,5-trioxane singlet. The following equation was used to calculate the monomer conversion:

$$\%\ monomer\ conversion = \frac{I_{t_f} - I_{t_0}}{I_{t_f}} \cdot 100\%$$

where I_{t_0} is the average integral of monomer terminal alkene singlets for the t_0 sample and I_{t_f} is the average integral of monomer terminal alkene singlets for the t_f sample. For poly(PEGMA) homopolymer and poly(BMA-b-PEGMA) diblock copolymer samples, the calculated monomer conversion value was used to calculate the number average molecular weight, $M_{n,\,NMR}$, using the following equation:

$$M_{n,NMR} = MW_{CTA} + MW_{monomer}(\%\ monomer\ conversion \cdot DP_{target})$$

where MW_{CTA} is the molecular weight of the chain transfer agent (CTA), 2-[[(2-carboxyethyl)sulfanylthiocarbonyl]-sulfanyl]propanoic acid (254 g/mol), $MW_{monomer}$ is the molecular weight of the methacrylic monomer used, *% monomer conversion* is the calculated monomer conversion, and DP_{target} is the target degree of polymerization (50 in both cases). In the case of the poly(BMA-b-PEGMA) diblock copolymer, the CTA employed was poly(PEGMA) homopolymer as a macroCTA and thus MW_{CTA} = 20,254 g/mol. This method for calculating M_n via ^{1}H NMR with a 1,3,5-trioxane internal standard is generalizable for all controlled polymerization techniques involving the chain growth polymerization of vinylic monomers, including atom transfer radical polymerization (ATRP), nitroxide-mediated polymerization (NMP), and reversible addition-fragmentation chain-transfer polymerization (RAFT) where it can be assumed that dispersity values ($Đ$) approach 1.

3.4.10.12 PTX sPNP and Nab-PTX sPNP preparation

PTX sPNP and **Nab-PTX sPNP** were prepared in the exact same manner as **sPNP**, differing only in the composition of the pre-jetting solution. For **PTX sPNP**, the pre-jetting solution was prepared by dissolving human serum albumin (5 mg), **4a** (0.25 mg), and paclitaxel (0.5 mg) in 1 mL of a 20 v/v% DMSO in UltraPure water. For **Nab-PTX sPNP**, the pre-jetting solution was prepared by dissolving Nab-paclitaxel (5 mg) and **4a** (0.25 mg) in 1 mL of a 20 v/v% DMSO in UltraPure water. Nab-paclitaxel was produced using high-pressure homogenization. Briefly, paclitaxel (30 mg) was dissolved in 550 μL of chloroform at 37 °C. 5 mL of chloroform was added to 35 mL of distilled water in a 50 mL tube and vortexed. The resulting top phase of water saturated with chloroform was removed and 30 mL were added to 300 mg of human serum albumin. The human serum albumin and paclitaxel solutions were combined, tip sonicated at 50 A for 1 minute, and high pressure homogenized with an Avestin EmulsiFlex-B15 for 7 cycles at 24,000 psi. The resulting sample was frozen and lyophilized, resulting in Nab-paclitaxel with a theoretical loading of 10 wt% paclitaxel relative to human serum albumin.

3.5 Results and Discussion

3.5.1 Design Approach to Self-Reporting Nanoparticle Synthesis

We sought to develop a nanoparticle synthetic strategy based on a versatile crosslinker platform applicable across a variety of material substrates. We hypothesized that incorporating a reporting fluorescent moiety in the crosslinker backbone would result in stable, emissive nanoparticles. The fluorescence of the nanoparticle crosslinkers enables monitoring of emission lifetime variations with time-resolved fluorescence spectroscopy in response to changes in the interparticle milieu, like mechanical force, polarity alterations, or the presence of an exogenous molecular species (**Figure 3.1A**).

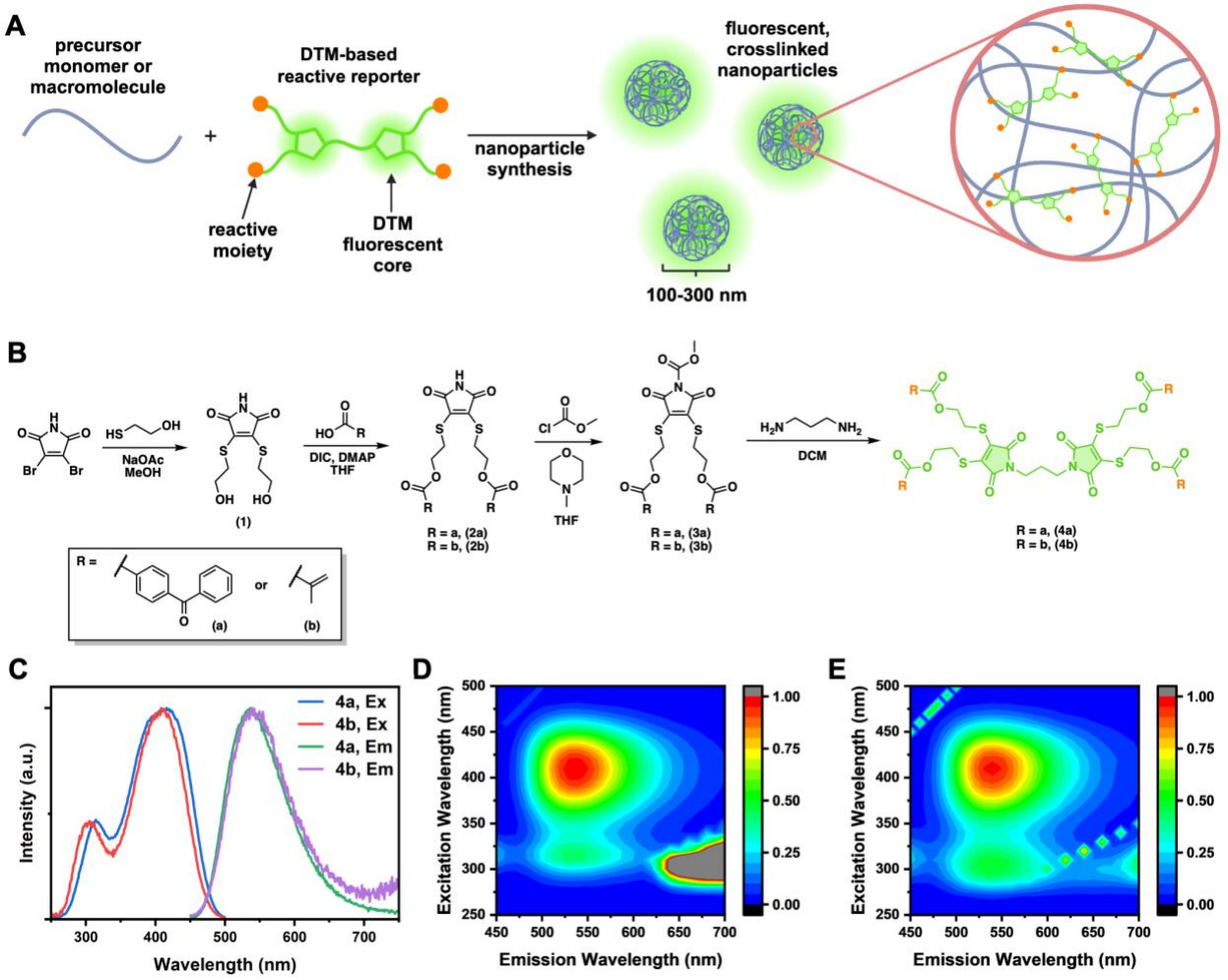

Figure 3.1: Synthesis and photophysical properties of DTM-based reactive reporters. (A) Framework for crosslinked, fluorescent nanoparticle fabrication, (B) synthesis of four-arm DTM-based emissive reactive reporters, (C) 2D excitation and emission spectra of **4a** and **4b** (λ_{em} = 535 nm for excitation spectra, λ_{ex} = 415 nm for emission spectra), and 3D excitation-emission spectra for **4a** (D) and **4b** (E).

3.5.2 Synthesis and Steady-State Photophysical Characterization of Molecular Reporters

This study is focused on the synthesis and application of two small molecule crosslinking reporters based on a modular scaffold consisting of four main variables: 1) valency, 2) reactive chemistry, 3) arm composition, and 4) bridge composition (**Figure 3.1B**). In principle, a vast number of chemically distinct reporters is achievable within this design space. A dithiomaleimide moiety was chosen as the core for this molecular architecture for its intrinsic fluorescence, relative stability to photobleaching, and ease of functionalization. Arm composition can be tuned by

choosing an appropriate linear, heterobifunctional linker containing an α-terminal thiol and an ω-terminal hydroxyl. In the first step of the generalized reaction, primary thiols react with 2,3-dibromomaleimide to form a substituted dithiomaleimide with two pendant hydroxyl groups (**1**). From there, reactive moieties containing a carboxylic acid can be coupled to the two primary hydroxyls in a straightforward manner using carbodiimide-mediated chemistry to yield the two-arm linkers **2a** and **2b**. The linkers' valency can be extended to four by coupling to itself in a two-step process, first by activating the imide nitrogen on the dithiomaleimide ring with methyl chloroformate, forming a carbamate (**3a**, **3b**), and finally through substitution reaction with a linear diamino linker. For our purposes, we chose β-mercaptoethanol as the α-thiol-ω-hydroxyl linker, 4-benzoylbenzoic acid and methacrylic acid as the reactive carboxylic acids, and 1,3-diaminopropane the linear diamino linker, generating two four-arm linkers, **4a** and **4b**, with benzophenone and methacrylic reactive groups, respectively. Benzophenone moieties can be activated with 365 nm light to form a tertiary radical centered at the diphenyl ketone carbon, which will abstract hydrogen atoms from nearby macromolecules. Methacrylates are ubiquitously employed as the reactive moieties of monomers in chain growth polymerizations.

Following synthesis, reporting crosslinkers **4a** and **4b** were characterized by steady-state fluorescence spectroscopy in DMSO. In accordance with previous reports, both reporters exhibit broadband emission from ~450-700 nm when excited at 415 nm, characteristic of molecules containing a DTM moiety. Additionally, both reporters displayed two excitation bands, one near 300 nm and one near 400 nm, when emission intensity is monitored at 535 nm (**Figure 3.1C**). Plots of 3D excitation-emission spectra reveal that both excitation bands result in emission with maxima at 535 nm, in accordance with Kasha's rule (**Figure 3.1D-E**).[136] Exact excitation and emission maxima values are listed in **Table 3.3**.

3.5.3 Chemical Environment-Dependent Fluorescence Lifetime Characterization of Molecular Reporters

Prior to nanoparticle synthesis, we sought to understand how the fluorescence lifetimes of neat solutions of **4a** and **4b** might be modulated by local chemical environments. 1 μM solutions of **4a** and **4b** were prepared in six solvents that represent a wide range of dielectric constants and refractive indices (**Table 3.2**), and time-correlated single photon counting (TCSPC) was used to measure fluorescence lifetime decays. A solid state nanoLED diode laser (390 nm, <1.4 ns pulse duration) was the excitation source for all samples while monitoring emission decay at 535 nm. Fluorescence lifetime decays were fit to third-order exponential decay functions, shown in **Equation 3.1**, below, and plotted in **Figure 3.6A-B**.

$$I(t) = \alpha_1 e^{(-\frac{t}{\tau_1})} + \alpha_2 e^{(-\frac{t}{\tau_2})} + \alpha_3 e^{(-\frac{t}{\tau_3})} \quad (3.1)$$

From **Equation 3.1**, τ and α component values can be used to calculate the average fluorescence lifetime of each sample, according to **Equation 3.2** and **Equation 3.3**,

$$\tau_{av,I} = \frac{\alpha_1\tau_1^2+\alpha_2\tau_2^2+\alpha_3\tau_3^2}{\alpha_1\tau_1+\alpha_2\tau_2+\alpha_3\tau_3} \quad (3.2)$$

$$\tau_{av,A} = \frac{\alpha_1\tau_1+\alpha_2\tau_2+\alpha_3\tau_3}{\alpha_1+\alpha_2+\alpha_3} \quad (3.3)$$

where $\tau_{av,\,I}$ is the intensity-weighted average fluorescence lifetime and $\tau_{av,\,A}$ is the amplitude-weighted average fluorescence lifetime. A complete list of all τ_n, α_n, $\tau_{av,\,I}$, and $\tau_{av,\,A}$ values for decays plotted in **Figure 3.3** and **Figure 3.6** are listed in **Table 3.5**. Component lifetimes and amplitudes are plotted in **Figure 3.7**. For conciseness, all τ_{av} values discussed in the main text are $\tau_{av,\,I}$ values.[195]

While fluorescence lifetime is an intrinsic property of all emitting species, its decay profile is modulated by a variety of internal factors, like the ability of the molecule to rotate freely in an

excited state, undergo intersystem crossing, or undergo excited state electron/proton transfer, as well as external factors, such as temperature, viscosity, and polarity.[138] Berezin et al. studied the effect of solvent polarity on several near-IR polymethine fluorescent probes using solvent orientation polarizability (SOP, Δf) as a metric to express polarity.[139] SOP is a dimensionless expression of solvent polarity that takes dielectric constant (ε) and refractive index (n) into account, detailed in **Equation 3.4**.[136]

$$\Delta f = \frac{\varepsilon - 1}{2\varepsilon + 1} - \frac{n^2 - 1}{2n^2 + 1} \tag{3.4}$$

SOP values for solvents used in this study are listed in **Table 3.2**: Numerical descriptors for solvents employed in this chapter., along with their ε and n values. A wide range of average fluorescence lifetimes for both **4a** and **4b** were measured across six solvents studied, plotted with respect to SOP in **Figure 3.6** and listed in **Table 3.5**. **4a** gave a τ_{av} range of 2.01-6.30 ns, while **4b** gave a τ_{av} range of 0.83-8.63 ns, indicating that the fluorescence lifetimes of both sensor molecules are SOP-dependent, with a general trend of increasing lifetime with decreasing SOP (**Figure 3.6C**). Both **4a** and **4b** display their shortest lifetimes in DMSO, where τ_{av} = 2.01 ns and 0.83 ns, respectively. In every solvent except for DMSO, **4a**'s second lifetime component, τ_2 was the dominant decay component, whereas **4b**'s dominant decay component was τ_1, evidenced by the amplitude weights of each component lifetime (**Figure 3.7D**). This suggests that **4b** more strongly interacts with solvents of a wide range of SOPs compared to **4a**, explainable by **4a**'s steric bulk in the form of four highly aromatic benzophenone moieties which are more difficult to solubilize in polar solvents than methacrylic moieties.

solvent	ε	n	Δf
toluene	2.38	1.50	0.013
ether	4.33	1.35	0.167
tetrahydrofuran (THF)	7.58	1.41	0.210
dichloromethane (DCM)	8.93	1.42	0.217
dimethyl sulfoxide (DMSO)	46.7	1.48	0.263
methanol	32.7	1.33	0.309
water	80.1	1.33	0.320

Table 3.2: Numerical descriptors for solvents employed in this chapter.

3.5.4 Nanoparticle Synthesis and Physical Characterization

Three compositionally and architecturally distinct nanoparticle types were prepared using **4a** and **4b**. Synthetic protein nanoparticles (**sPNP**) were prepared via electrohydrodynamic (EHD) jetting of **4a** with human serum albumin (HSA) (**Figure 3.2A**). EHD jetting is a technique that involves the laminar flow of a macromolecule-containing solution through an electric field toward a grounded collection surface. EHD jetting provides nanoscale control over anisotropy, size, shape, and composition, and has been used to prepare nanoparticles composed of synthetic polymers and proteins, along with Janus varieties of both.[106,159,196,197] Following EHD jetting, the deposited nanoparticles were exposed to 365 nm light to initiate benzophenone crosslinking through **4a** and collected into water. The resulting **sPNP** feature a gel-like structure, with individual HSA proteins linked via **4a** in a network structure (**Figure 3.2A**). **sPNP** were uniformly spherical in shape (**Figure 3.2D**) and displayed a Z-average hydrodynamic diameter (D_h) of 243.9 nm and polydispersity (PDI) of 0.160, measured by dynamic light scattering (DLS) (**Figure 3.2G**).

Crosslinked nanogels (**NG**) were synthesized via emulsion polymerization of 2-hydroxyethyl methacrylate (HEMA) in surfactant-containing water with 5 wt% **4b** relative to monomer (**Figure 3.2B**). Dithiomaleimides have been incorporated into polymethyl methacrylate (PMMA) nanogels as fluorescent reporters, but never as both a fluorescent reporter and

crosslinker. **NG** were less spherical in shape than **sPNP** in the dry state (**Figure 3.2E**) and displayed a similar D_h of 221.4 nm and PDI of 0.024 via DLS (**Figure 3.2H**).

Core-crosslinked block copolymer micelles (**MC**) were synthesized using a 26 kDa block copolymer of butyl methacrylate (BMA) and polyethylene glycol methacrylate (PEGMA) (poly(BMA_{45}-b-$PEGMA_{40}$)) prepared via RAFT polymerization. The block copolymer was dissolved in DMSO and water was added dropwise with stirring to prompt micelle self-assembly. The polymer was designed such that the RAFT-active trithiocarbonate moiety aggregates in the hydrophobic core of the micelle at the end of the BMA block. 3 equivalents of **4b** relative to the block copolymer were added to the suspension of **MC**, along with a water-soluble radical initiator, and the mixture was heated above the initiator's decomposition temperature to reinitiate RAFT polymerization in the micelle cores, effectively core-crosslinking the nanostructures (**Figure 3.2C**).[198] The resulting nanoparticles are spherical in nature (**Figure 3.2F**), but smaller than both **sPNP** and **NG** in both the dry and hydrated states, with a D_h of 201.7 nm and PDI of 0.239 via DLS (**Figure 3.2I**). The Z-average D_h, PDI, and ζ-potential of each nanoparticle formulation is listed in **Table 3.3**.

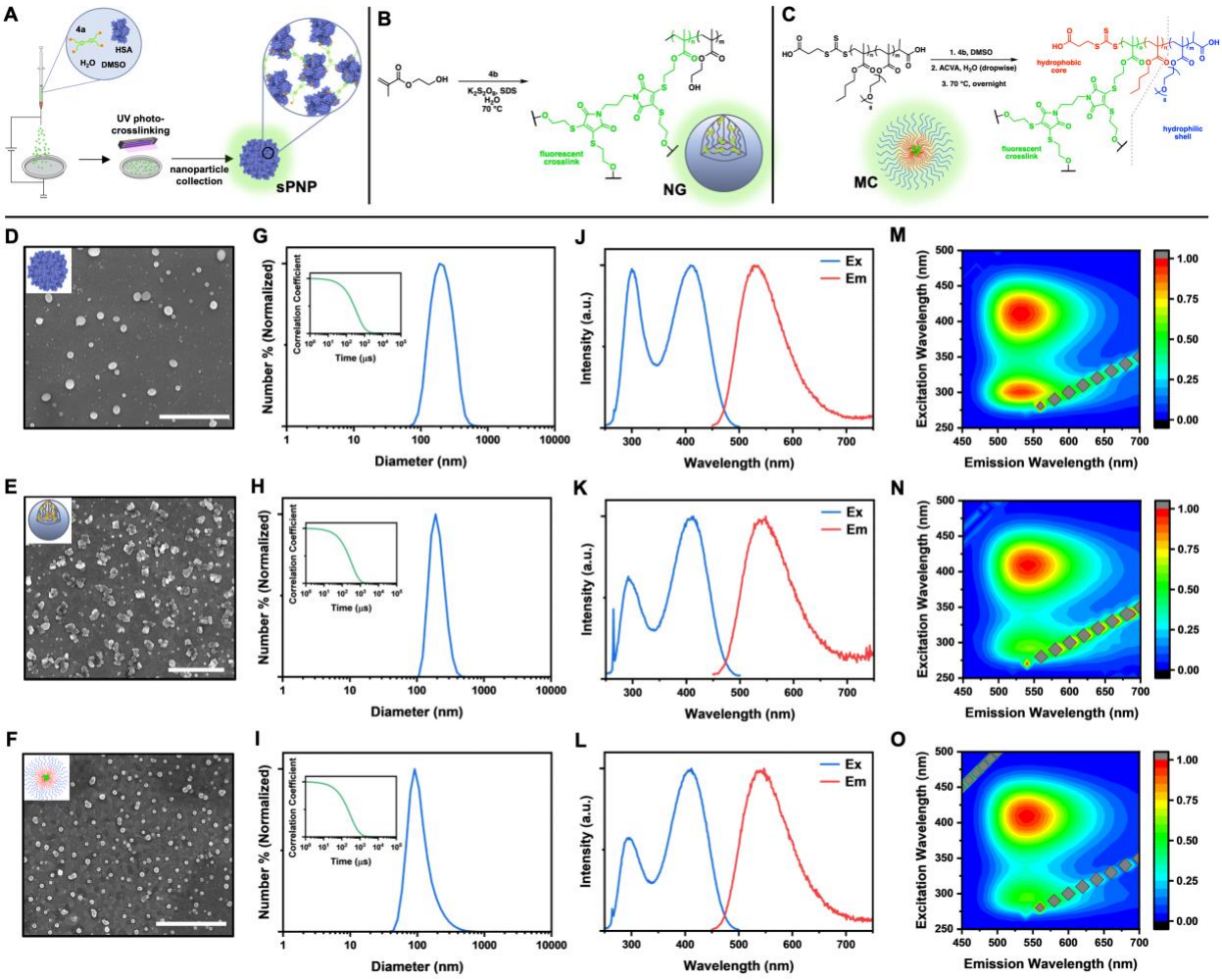

Figure 3.2: Nanoparticles were prepared using reactive reporters **4a** and **4b** as crosslinkers. (A, B, C) Synthetic schemes, (D, E, F) SEM micrographs, (G, H, I) DLS traces with inset correlation functions, (J, K, L) 2D excitation and emission spectra (λ_{em} = 535 nm for excitation spectra, λ_{ex} = 415 for emission spectra), and (M, N, O) 3D excitation-emission plots of **sPNP**, **NG**, and **MC**, respectively. (SEM image scale bar = 2 μm.)

3.5.5 Nanoparticle Steady-State Photophysical Characterization

Following preparation, **sPNP**, **NG**, and **MC** nanoparticles were characterized by steady-state fluorescence spectroscopy in water to determine the extent to which reactive reporters **4a** and **4b** had imbued emissivity to the resulting materials. In all three cases, the nanoparticles exhibit broadband emission from ~490-700 nm when excited at 415 nm, the same emission band that **4a** and **4b** exhibit. Additionally, all three nanoparticle samples display the same two excitation bands as the small molecule precursors near 300 nm and 400 nm when emission intensity is monitored

at 535 nm (**Figure 3.2J-L**). Despite almost identical excitation and emission bands to **4a** and **4b** **(Figure 3.1C)**, $\lambda_{max,\ ex}$ and $\lambda_{max,\ em}$ of nanoparticle samples did display slight shifts compared to their small molecule precursors. The $\lambda_{max,\ em}$ of **sPNP** exhibited a hypsochromic shift of 13 nm and $\lambda_{max,\ ex}$ exhibited a bathochromic shift of 8 nm compared to **4a**. The $\lambda_{max,\ em}$ of **NG** exhibited a bathochromic shift of 9 nm and $\lambda_{max,\ ex}$ exhibited a bathochromic shift of 5 nm compared to **4b**. The $\lambda_{max,\ em}$ of **MC** exhibited a bathochromic shift of 8 nm and $\lambda_{max,\ ex}$ exhibited a bathochromic shift of 4 nm compared to **4b** (**Table 3.3**). Despite the shifts in maxima, however, all nanoparticles were imparted with broadband emissivity after crosslinking with reporters **4a** and **4b**.

	$\lambda_{max,\ ex}$ (nm)[a]	$\lambda_{max,\ em}$ (nm)[b]	D_h (nm)[c]	PDI	ζ-potential (mV)
4a	416	540	-	-	-
4b	408	539	-	-	-
sPNP	409	527	243.9	0.160	-31.8
NG	413	548	221.4	0.024	-35.0
MC	412	547	201.7	0.239	-17.0

Table 3.3: Steady-state photophysical and physical values for reporters and nanoparticles. ([a]λ_{em} = 535 nm; [b]λ_{ex} = 415 nm; [c]D_h is the Z-average hydrodynamic diameter measured by DLS.)

3.5.6 Chemical Environment-Dependent Fluorescence Lifetime Characterization of Nanoparticles.

Solvent polarity and the ability for molecular rotation are important external factors that modulate the fluorescence lifetime of fluorophores.[138] Lower solubility and prevention of molecular rotation result in a decrease in non-radiative decay processes and a longer fluorescence lifetime.[136,138] Thus, we expected each of the three synthesized nanoparticle species to exhibit longer average fluorescence lifetimes with less variability than the small molecule sensors alone when measured in seven solvents of different orientation polarizability, as embedding **4a** and **4b** into nanostructures should constrain their molecular rotation and have solvent-shielding effects. While an increase in fluorescence lifetime compared to free reporter was universally observed for **sPNP**, **NG**, and **MC** samples, we discovered that **sPNP** exhibited a particularly strong response to

changes in their chemical environment, demonstrated by the ~20 ns difference in τ_{av} in DMSO (5.70 ns) versus DCM (25.92 ns) (**Figure 3.3A**, **Table 3.5**). **NG** and **MC** were less sensitive to SOP than **sPNP**, with τ_{av} ranges of 6.29-11.29 ns and 6.83-11.69 ns, respectively (**Figure 3.3B-C**, **Table 3.5**, **Figure 3.7**).

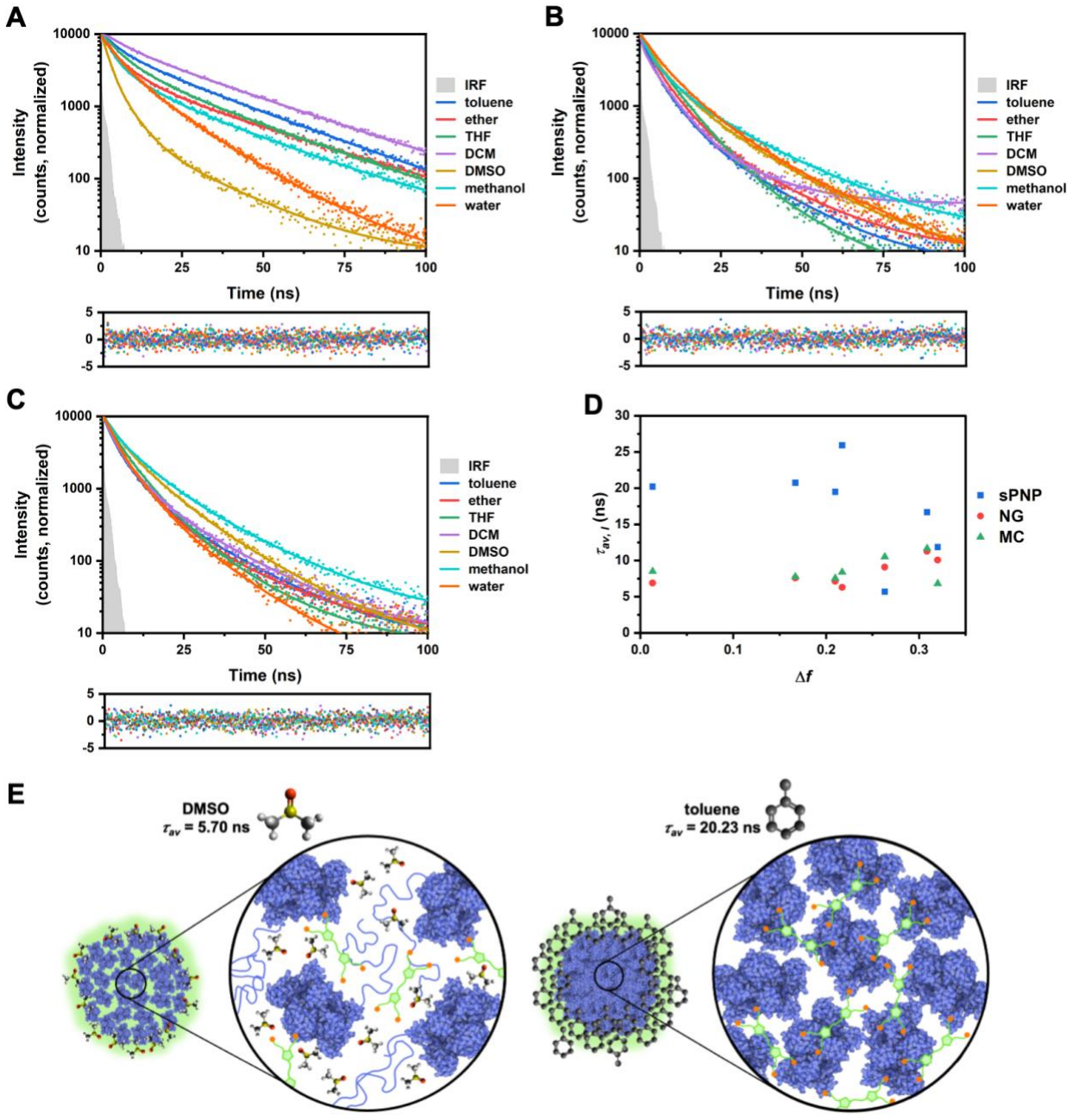

Figure 3.3: Nanoparticles exhibit chemical environment-dependent fluorescence lifetime decays. Fluorescence lifetime decay curves (top) for **sPNP** (A), **NG** (B), and **MC** (C) in various solvents fitted to third order exponential decay functions with residuals (bottom), (D) intensity-weighted average fluorescence lifetimes with respect to solvent orientation polarizability (SOP, Δf), and (E) proposed external and internal structures of **sPNP** in DMSO and toluene.

For **sPNP** in polar solvents (DMSO, methanol, water), fluorescence lifetime decay was dominated by the first decay component, τ_1, contributing greater than 50% of amplitude weights (α_1) to the average fluorescence lifetime. In less polar solvents (toluene, ether, THF, DCM),

however, the first lifetime decay component was diminished in **sPNP**, with amplitude weights favoring second and third decay components τ_2 and τ_3 (**Table 3.5**, **Figure 3.7**). **NG** and **MC** samples displayed considerably less fluctuation in the first decay component weight, α_1, than **sPNPs**. For both **NG** and **MC** samples and across all solvents surveyed, α_1's fraction of all three decay component weights never deviated outside the range of 45-75% of the whole and exhibited no trend with respect to SOP. The lack of trend and high percentage α_1 weights indicate that the poly(HEMA) and poly(BMA_{45}-b-$PEGMA_{40}$) polymers of which **NG** and **MC** are composed, respectively, do not respond significantly differently across different SOP chemical environments. We thus hypothesized that the fluorescence lifetime sensitivity of **sPNP** across SOPs is attributed to the amphiphilic nature of their constituent proteins. In DMSO, **sPNP** showed an increase of τ_{av} from 2.01 ns to 5.70 ns, indicating ordering and rigidification in the local environment of reporter **4a** when immobilized in the nanoparticle matrix. Interestingly, **sPNP** in DMSO exhibits a faster τ_{av} than **4a** dissolved in toluene, THF, and DCM, indicating that DMSO's ability to penetrate **sPNP** and solvate the local milieu proximal to **4a** is better even than pure small molecule **4a** in other organic solvents (**Table 3.5**). Globular proteins, such as HSA, are known to be tolerant to denaturation in up to 30 v/v% DMSO in water.[199] Above that threshold, proteins begin to unfold and denature, but the amphiphilic polypeptide chains of which they are composed still remain solvated in the amphiphilic environment of DMSO.[200] We hypothesize that in pure DMSO, **sPNP** exhibits a loosely packed structure owing to both the partial denaturation of the composite HSA proteins, illustrated in **Figure 3.3E** as blue unraveled strands, and the penetration of DMSO solvent molecules into the interior of the particle, increasing the solvation and decreasing the rigidification of the **sPNP** core.

sPNP exhibits considerably longer lifetimes in less polar organic solvents as the local protein-based material environment changes. For example, in toluene, **sPNP** has a τ_{av} of 20.23 ns. Toluene is a hydrophobic, highly aromatic solvent. When proteins are folded into a 3D conformation, only hydrophilic residues are presented on their surface, accessible to their native biological solvent of water. We hypothesize that the large increase in τ_{av} in toluene is attributed to the highly unfavorable interaction of toluene with **sPNP**'s composite protein material; HSA's hydrophilic surface residues prefer to interact with other HSA molecules composing the **sPNP** rather than toluene, driving solvent out from the interior of the particle, consequently reducing solvation and increasing rigidification around internal **4a** reporters (**Figure 3.3E**).

3.5.7 Effect of Binary Solvent Mixtures of DMSO and Toluene on Fluorescence Lifetime of Nanoparticles

DMSO and toluene have highly disparate SOP values (0.263 and 0.013, respectively) while being fully miscible. We hypothesized that a binary mixture of DMSO and toluene would result in a chemical environment with an SOP between that of both pure solvents and therefore should result in an **sPNP** fluorescence lifetime between 5.70 ns and 20.23 ns, corresponding to pure DMSO and toluene, respectively. To test this hypothesis, we measured the fluorescence lifetime of **sPNP** in a 1:1 mixture of DMSO:toluene and plotted the lifetime decay traces and component τ and α values from the third-order exponential decay fits with respect to the lifetime data acquired previously in pure solvents (**Figure 3.4**). We also performed the same experiment and analyses for **NG** and **MC** samples.

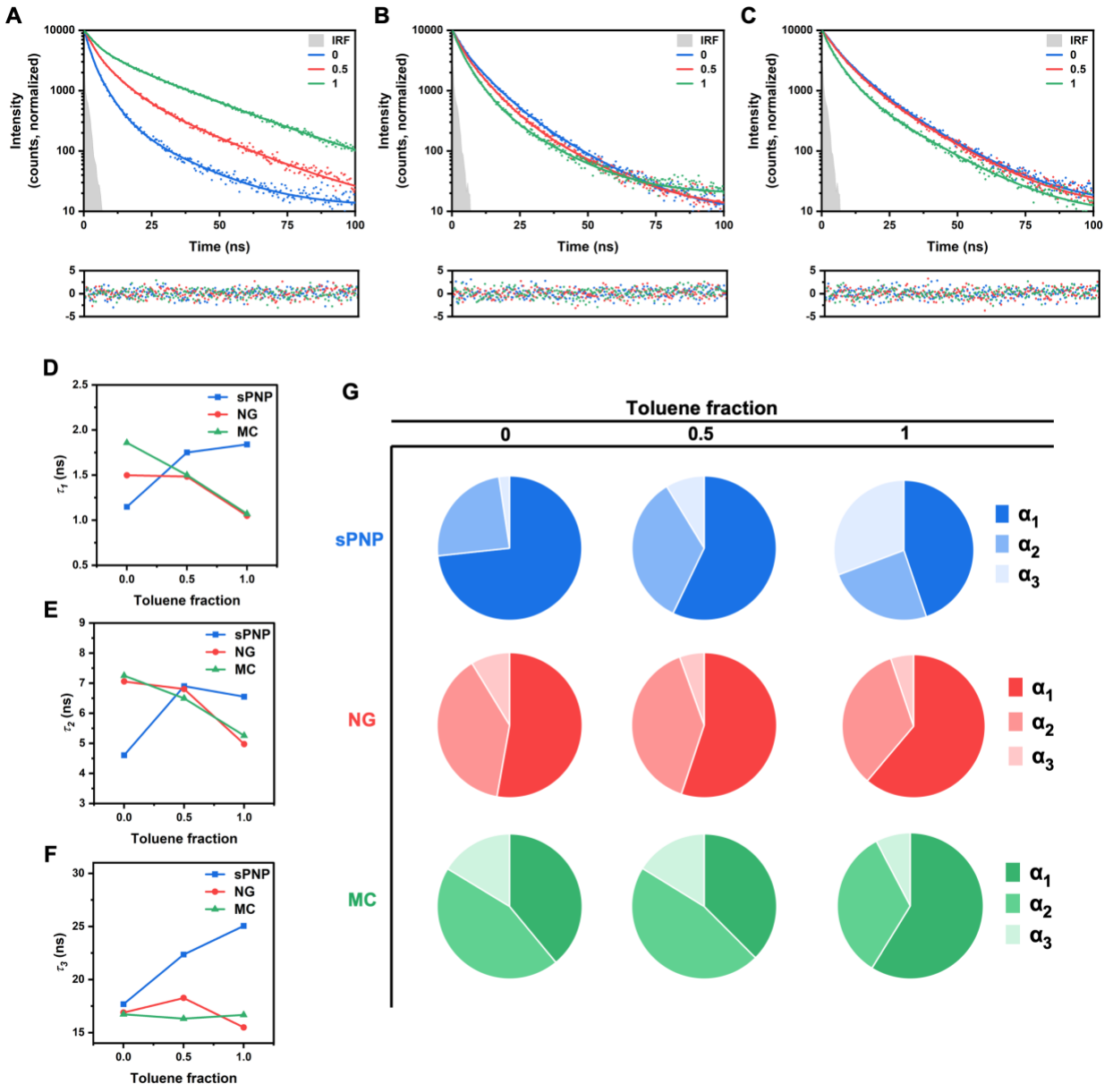

Figure 3.4: Nanoparticle fluorescence lifetimes reflect changes to solvent orientation polarizability in binary mixtures of DMSO and toluene. Fluorescence lifetime decay curves of **sPNP** (A), **NG** (B), and **MC** (C). τ_1 (D), τ_2 (E), and τ_3 (F) plotted with respect to solvent toluene fraction, and (G) amplitudes α_1, α_2, and α_3 expressed as fractions of a whole and arranged with respect to toluene fraction.

When the toluene fraction in DMSO was 0.5, **sPNP** exhibited a τ_{av} of 11.60 ns, placing it between the lifetimes observed in pure DMSO and pure toluene environments (**Figure 3.4A, Table 3.4**). Component lifetimes τ_1, τ_2, and τ_3 did not change meaningfully as the toluene fraction in DMSO was modulated from 0 to 0.5 to 1 (**Figure 3.4D-F**, **Table 3.4**). However, the amplitudes

associated with those component lifetimes shifted drastically. In a pure DMSO environment, average fluorescence lifetime for sPNP is dominated by τ_1, with α_1 accounting for ~74% of all amplitude weights. In 0.5 toluene fraction, α_1 decreased to ~57% of amplitude weights, and even further to ~45% in pure toluene (**Figure 3.4G**, **Table 3.4**). The first lifetime component in a multi-component decay is associated with fluorophore-to-solvent quenching processes and the decrease in corresponding α_1 values indicate that fluorescent **4a** linkages in the internal network structure of **sPNP** are transitioning from a relatively strong interaction with solvent to a weak one during the chemical environment transition from DMSO to toluene. The **NG** and **MC** nanoparticles also demonstrate dynamic fluorescence lifetime responses to binary mixtures of DMSO and toluene, but to a lesser degree than **sPNP**. **NG** exhibits a τ_{av} of 9.08 ns in pure DMSO, 8.39 ns in 1:1 DMSO:toluene, and 6.90 ns in pure toluene. **MC** exhibits a τ_{av} of 10.53 ns in pure DMSO, 10.22 ns in 1:1 DMSO:toluene, and 8.51 ns in pure toluene (**Table 3.4**). This trend indicates that **4b**, the crosslinking reporter for both **NG** and **MC**, is better solvated in toluene than DMSO when immobilized in those respective nanoparticles, a trend that is opposite to the one observed for **sPNP**. We attribute this behavior to differences in how each nanoparticle's composite material allows solvents of varying polarity to penetrate. In sum, we've shown that **sPNP** exhibits robust differences in fluorescence lifetime as a result of changing SOP, both in unary solvents spanning a range of SOPs, and in binary mixtures of solvents of disparate polarities. **NG** and **MC** also exhibit fluorescence lifetime differences as a consequence of SOP, but to a much lesser degree.

	DMSO: toluene	τ_1 (ns)	τ_2 (ns)	τ_3 (ns)	α_1	α_2	α_3	$\tau_{av,\,I}$ (ns)
	0:1	1.15	4.60	17.68	0.733	0.243	0.0238	5.70
sPNP	1:1	1.75	6.90	22.35	0.571	0.342	0.0871	11.60
	1:0	1.84	6.55	25.05	0.448	0.245	0.307	20.23
	0:1	1.50	7.06	16.89	0.528	0.385	0.0873	9.08
NG	1:1	1.48	6.80	18.26	0.551	0.394	0.0550	8.39
	1:0	1.05	4.97	15.49	0.612	0.336	0.0523	6.90
	0:1	1.86	7.25	16.72	0.390	0.447	0.163	10.53
MC	1:1	1.50	6.50	16.32	0.375	0.463	0.162	10.22
	1:0	1.07	5.26	16.67	0.588	0.335	0.0768	8.51

Table 3.4: Fluorescence lifetime kinetic values for nanoparticles in DMSO, 1:1 DMSO:toluene, and toluene for third-order exponential decay fits.

3.5.8 Mode of Drug Encapsulation Impacts Fluorescence Lifetime Decay

After establishing **sPNP**'s exceptional ability to discern its chemical environment using fluorescence lifetime measurements, we sought to understand how the encapsulation of a small molecule drug might modulate the kinetics of fluorescence lifetime decays. We chose paclitaxel (PTX) for its widespread clinical use.[99] PTX is a hydrophobic drug typically formulated with polyethoxylated castor oil as the vehicle for intravenous administration, which has been reported to lead to negative side effects.[99] Nanoparticle-bound albumin-PTX (Nab-PTX) is a clinically-used form of PTX prepared by high pressure homogenization, resulting in HSA aggregates with PTX embedded in protein hydrophobic domains.[99] We thus compared PTX-loaded **sPNP** that were prepared by either EHD jetting a simple mixture of free PTX with HSA or Nab-PTX, which we hypothesized would lead to differences in fluorescence lifetime compared to unloaded nanoparticles, due to PTX's availability, or lack thereof, to interact with reactive reporter **4a**. Two **sPNP** formulations, **PTX sPNP** and **Nab-PTX sPNP**, were synthesized as illustrated in **Figure 3.5A** and **Figure 3.5D**. **PTX sPNP** were prepared by first mixing free PTX, HSA, **4a**, and solvent, followed by EHD jetting of the mixture. The preparation of **Nab-PTX sPNP** followed an analog procedure with the exception that Nab-PTX was included in the jetting solution in place of free PTX and HSA. Both formulations contained equal amounts of PTX (10 wt% relative to HSA).

Following fabrication and collection, each formulation was resuspended in seven different solvents as shown in **Figure 3.3**, and fluorescence lifetime decay profiles were measured after 2 minutes of equilibration (**Figure 3.5B** and **Figure 3.5E**). Kinetic values of the third-order exponential decay fit, plots of τ_{av} vs. SOP, and pie charts displaying α values for these samples can be found in **Table 3.6** and **Figure 3.8**.

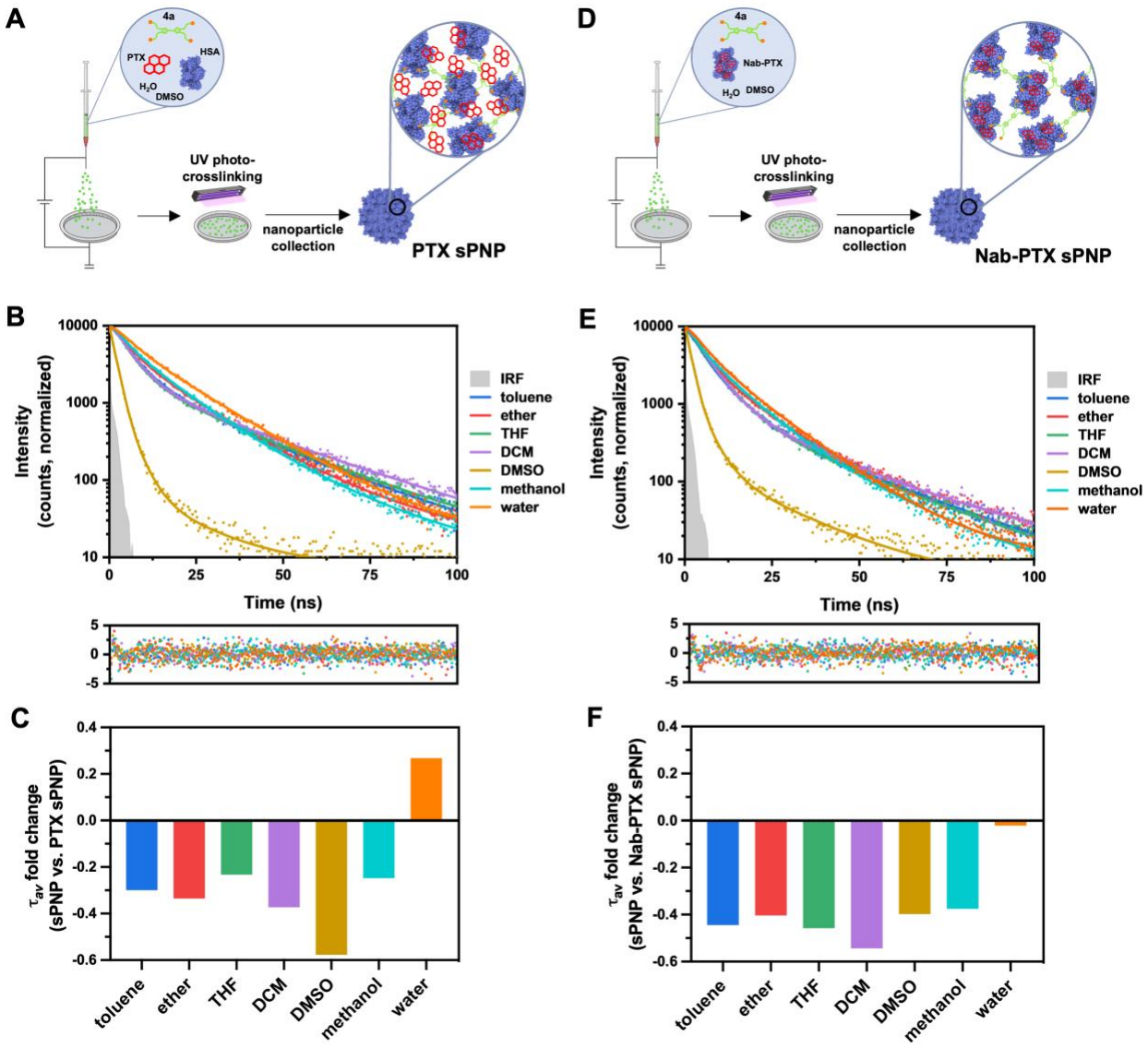

Figure 3.5: **sPNP** crosslinked with **4a** can sense the loading configuration of hydrophobic drug, paclitaxel. (A) Fabrication and proposed structure of **PTX sPNP**, (B) fluorescence lifetime decay curves for **PTX sPNP** in various solvents, (C) plot of the fold change in τ_{av} of **sPNP** compared to **PTX sPNP**, (D) fabrication and proposed structure of **Nab-PTX sPNP**, (E) fluorescence lifetime decay curves for **Nab-PTX sPNP** in various solvents, (F) plot of the fold change in τ_{av} of **sPNP** compared to **Nab-PTX sPNP**.

Compared to their drug-free **sPNP** counterparts, both **PTX sPNP** and **Nab-PTX sPNP** exhibited a decrease in τ_{av} across all organic solvents (**Figure 3.5C** and **Figure 3.5F**), regardless of the specific mode of PTX encapsulation. The influx of solvent into the **sPNP** cores creates a more solvent-like environment around reporter **4a**, resulting in a decrease in τ_{av}, a consequence of the fact that emitted photons are more quickly quenched. However, differing phenomena are observed when the nanoparticles are suspended in water. In the case of **PTX sPNP**, an increase in τ_{av} is observed relative to **sPNP**, whereas τ_{av} measured for **Nab-PTX sPNP** remains almost identical to that measured for drug-free **sPNPs**. These differences in τ_{av} can be attributed to the distinct internal environments of the nanoparticles as a result of how homogenously PTX is distributed in the nanoparticle cores. These results suggest that the local distribution of PTX molecules within **PTX sPNP** is highly heterogeneous, presumably due to phase segregation during particle preparation. When **PTX sPNP** are resuspended in water, the highly hydrophobic PTX molecules increase the overall hydrophobicity of the **sPNP** cores, shielding the water molecules from entering the nanoparticle and thereby creating a less solvent-rich environment. The result is a measurable increase in τ_{av}. In contrast, **Nab-PTX sPNP** are characterized by a more homogenous distribution of PTX molecules throughout the nanoparticle due to high-pressure homogenization. Therefore, water molecules interact with the core of **Nab-PTX sPNP** similar to drug-free **sPNP**, resulting in negligible changes in τ_{av}. This experiment demonstrates that the use of reactive reporter **4a** to stabilize **sPNP** not only imbues external chemical environmental sensing, but also allows for the direct monitoring of critical formulation differences that might result in fundamental differences in their drug delivery responses.

3.6 Conclusion

We developed a self-reporting nanoparticle synthetic strategy, enabled through crosslinking with fluorescent molecular reporters applicable across several types of material substrates. Two tetravalent reporters, **4a** and **4b**, were synthesized, equipped with benzophenone and methacrylate reactive moieties, respectively. **4a** and **4b** exhibit emission maxima around 535 nm and fluorescence lifetime differences in seven different solvents, but generally τ_{av} clustered around 4 ns. The reporters were deployed as crosslinkers in three nanoparticle systems and self-reporting protein nanoparticles (**sPNP**) exhibited enhanced fluorescence lifetime differences of an order of magnitude across chemical environments compared to polymer nanogels (**NG**) and block copolymer micelles (**MC**), specifically with regard to intraparticle properties, such as solvent environment and drug loading distributions. The results in this study regarding drug loading distributions corroborate the premise that the loading configuration of paclitaxel in protein nanoparticles impacts its release profile; particles loaded with Nab-paclitaxel follow diffusion-dominated drug release kinetics that are seven times slower than the burst release observed for blended particles.[201] In sum, this work demonstrates that DTM-based reporters can perceive even minute changes in the chemical environment of therapeutic nanoparticles, a feature that we believe to be especially important for the study of protein-based nanomedicines, in particular, as their internal nanoenvironments are considerably more complex and difficult to predict than lipid and polymer nanoparticles.

This system is applicable to a range of nanomedicine applications where *in situ* reporters are desired to probe dynamic nanomaterial and biochemical environments. Specifically, this system, in conjunction with fluorescence lifetime imaging microscopy, has the potential to provide valuable spatiotemporal information regarding the various stages of nanoparticle delivery,

including cellular uptake, endocytosis, payload release, and degradation, by detecting cellular microenvironment differences at each stage. More broadly, this work establishes the utility of time-resolved fluorescence spectroscopy as a complement to traditional nanoparticle characterization techniques, like dynamic light scattering, for its ability to discern nanoparticle-environment and nanoparticle-cargo interactions; properties that we believe will be important for the advancement of protein-based materials and the nanomedicine field generally.

3.7 Supplementary Figures and Tables

3.7.1 Supplementary Figures and Tables Referenced in Chapter 3

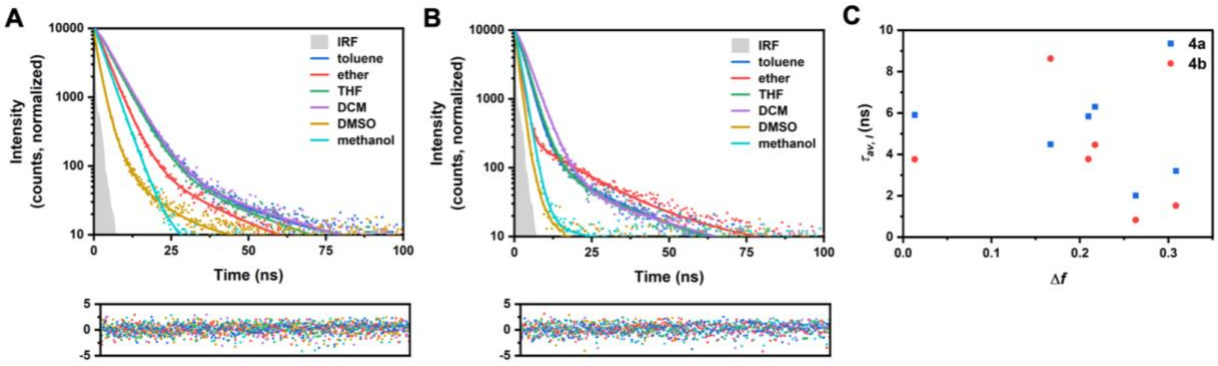

Figure 3.6: Supplemental to **Figure 3.1**. Fluorescence lifetime decays of **4a** and **4b** in various solvents. Fluorescence lifetime decay curves for **4a** (A) and **4b** (B) in various solvents fitted to third order exponential decay functions with residuals for fits plotted below, and (C) plots of intensity-weighted average fluorescence lifetimes with respect to solvent orientation polarizability.

	Solvent	τ_1 (ns)	τ_2 (ns)	τ_3 (ns)	α_1	α_2	α_3	$\tau_{av,\ I}$ (ns)	$\tau_{av,\ A}$ (ns)
4a	toluene	1.43	5.15	20.27	0.123	0.862	0.0142	5.91	4.91
	ether	1.44	3.90	19.51	0.303	0.687	0.00997	4.49	3.31
	THF	2.61	5.03	23.34	0.142	0.847	0.0113	5.84	4.89
	DCM	2.10	5.20	25.96	0.0134	0.975	0.0112	6.30	5.39
	DMSO	1.00	2.67	10.68	0.857	0.136	0.00680	2.01	1.29
	methanol	1.03	3.43	27.22	0.394	0.606	0.000630	3.21	2.50
4b	toluene	2.27	5.44	21.69	0.961	0.0309	0.00765	3.76	2.52
	ether	1.07	14.86	97.25	0.988	0.0113	0.000810	8.63	1.30
	THF	2.38	3.94	22.08	0.879	0.114	0.00703	3.78	2.70
	DCM	3.12	4.39	28.94	0.823	0.172	0.00496	4.46	3.46
	DMSO	0.71	3.48	-	0.991	0.00897	-	0.83	0.73
	methanol	1.15	2.24	24.72	0.914	0.0853	0.000440	1.52	1.26
sPNP	toluene	1.84	6.55	25.05	0.448	0.245	0.307	20.23	10.12
	ether	1.95	7.32	30.13	0.519	0.307	0.174	20.75	8.50
	THF	2.69	8.17	26.75	0.386	0.355	0.259	19.50	10.87
	DCM	5.27	12.01	28.72	0.279	0.112	0.610	25.92	20.32
	DMSO	1.15	4.60	17.68	0.733	0.243	0.0238	5.70	2.38
	methanol	1.85	6.86	25.23	0.610	0.238	0.152	16.70	6.60
	water	4.79	11.64	20.01	0.513	0.373	0.113	11.87	9.07
NG	toluene	1.05	4.97	15.49	0.612	0.336	0.0524	6.90	3.12
	ether	1.48	5.99	17.59	0.557	0.393	0.0498	7.58	4.06
	THF	1.75	6.99	17.10	0.488	0.481	0.0301	7.15	4.74
	DCM	0.63	5.67	15.76	0.785	0.192	0.0231	6.29	1.95
	DMSO	1.50	7.06	16.89	0.528	0.385	0.0873	9.08	4.98
	methanol	1.27	6.55	19.60	0.646	0.255	0.0991	11.29	4.43
	water	1.62	7.02	17.54	0.416	0.465	0.120	10.08	6.04
MC	toluene	1.07	5.26	16.67	0.588	0.335	0.0767	8.51	3.67
	ether	1.48	6.29	18.64	0.595	0.361	0.0435	7.74	3.97
	THF	1.51	6.66	16.19	0.491	0.457	0.0519	7.56	4.63
	DCM	1.17	5.41	17.08	0.619	0.312	0.0689	8.39	3.59
	DMSO	1.86	7.25	16.72	0.390	0.447	0.163	10.53	6.69
	methanol	1.50	7.88	19.21	0.510	0.361	0.129	11.69	6.09
	water	1.73	5.88	14.56	0.533	0.405	0.0618	6.83	4.20

Table 3.5: Supplemental to **Figure 3.3** and **Figure 3.6**. Fluorescence lifetime kinetic data for **4a**, **4b**, **sPNP**, **NG**, and **MC** in various solvents, values. Values are derived from third order exponential decay fits generated from raw data. Amplitudes are normalized to 1. Full decay curves and fits are shown in **Figure 3.3** and **Figure 3.6**.

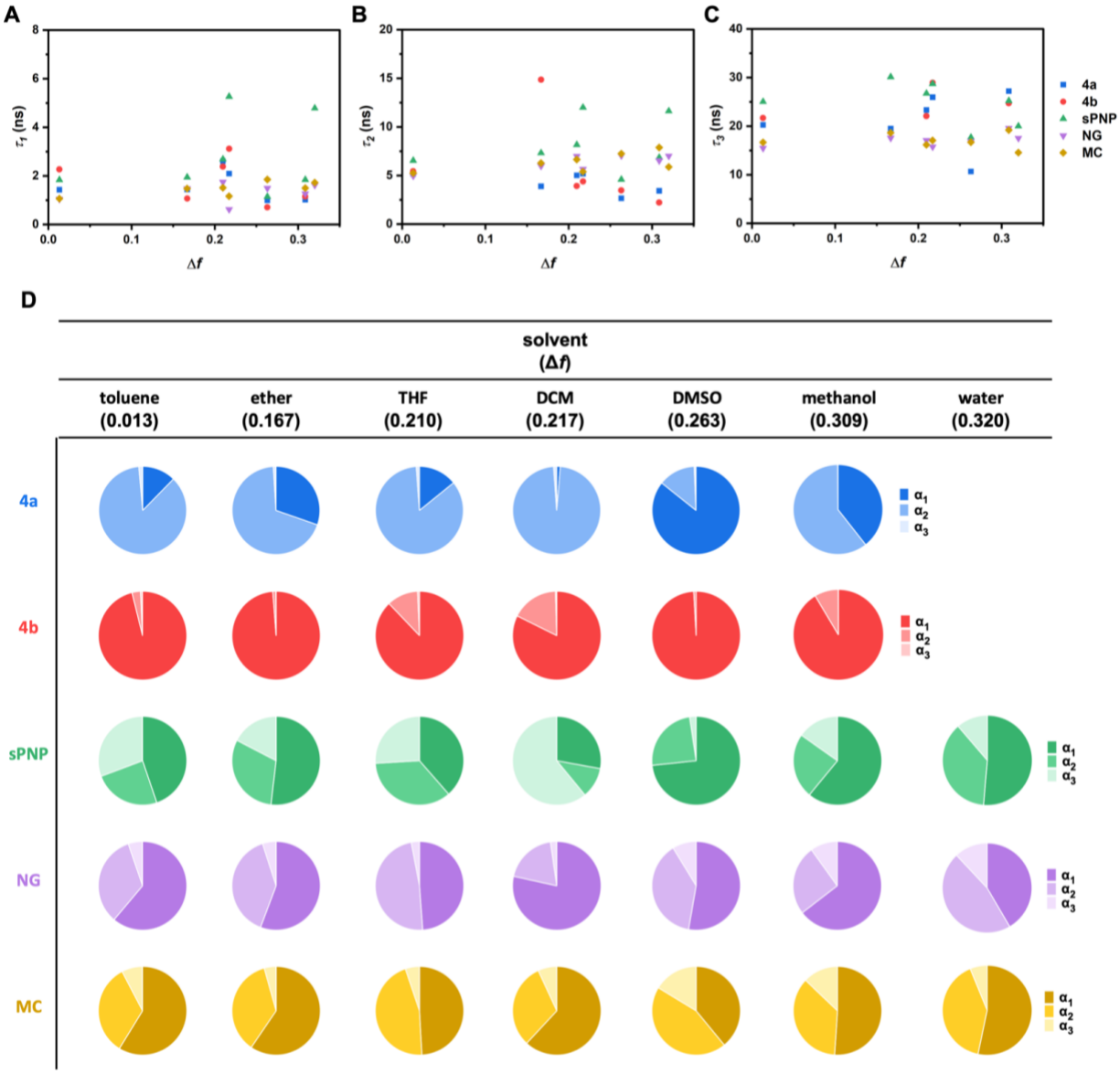

Figure 3.7: Supplemental to **Figure 3.3**, **Figure 3.6**, and **Table 3.5**. Fluorescence lifetime kinetic data for **4a**, **4b**, **sPNP**, **NG**, and **MC** in various solvents, plots. (A) τ_1, (B) τ_2, and (C) τ_3 values, plotted with respect to solvent orientation polarizability, and (D) pie charts displaying α_1, α_2, and α_3 values as parts of a whole.

	Solvent	τ_1 (ns)	τ_2 (ns)	τ_3 (ns)	α_1	α_2	α_3	$\tau_{av,\ I}$ (ns)	$\tau_{av,\ A}$ (ns)
PTX sPNP	toluene	4.18	11.2	26.0	0.684	0.202	0.115	14.2	8.093
	ether	4.10	14.1	38.6	0.546	0.433	0.020	13.8	9.150
	THF	4.37	18.0	34.2	0.799	0.158	0.043	15.0	7.807
	DCM	4.58	11.8	29.7	0.773	0.110	0.117	16.2	8.332
	DMSO	1.22	3.40	16.1	0.884	0.1122	0.00413	2.41	1.527
	methanol	3.31	11.7	23.6	0.423	0.507	0.070	12.6	8.967
	water	5.26	15.4	54.9	0.395	0.597	0.008	15.1	11.717
Nab-PTX sPNP	toluene	3.13	7.41	25.3	0.497	0.433	0.0697	11.2	6.531
	ether	3.15	10.3	34.0	0.591	0.375	0.0340	12.4	6.900
	THF	2.71	6.73	24.0	0.379	0.551	0.0693	10.6	6.398
	DCM	4.92	14.4	34.5	0.858	0.110	0.0319	11.8	6.906
	DMSO	1.16	3.85	19.2	0.896	0.096	0.00725	3.43	1.547
	methanol	2.14	8.79	20.2	0.444	0.481	0.0750	10.4	6.692
	water	4.70	13.0	64.8	0.554	0.443	0.00291	11.6	8.547

Table 3.6: Supplemental to **Figure 3.5**. Fluorescence lifetime kinetic data for **PTX sPNP** and **Nab-PTX sPNP** in various solvents, values. Values are derived from third order exponential decay fits generated from raw data. Amplitudes are normalized to 1. Full decay curves and fits are shown in **Figure 3.5**.

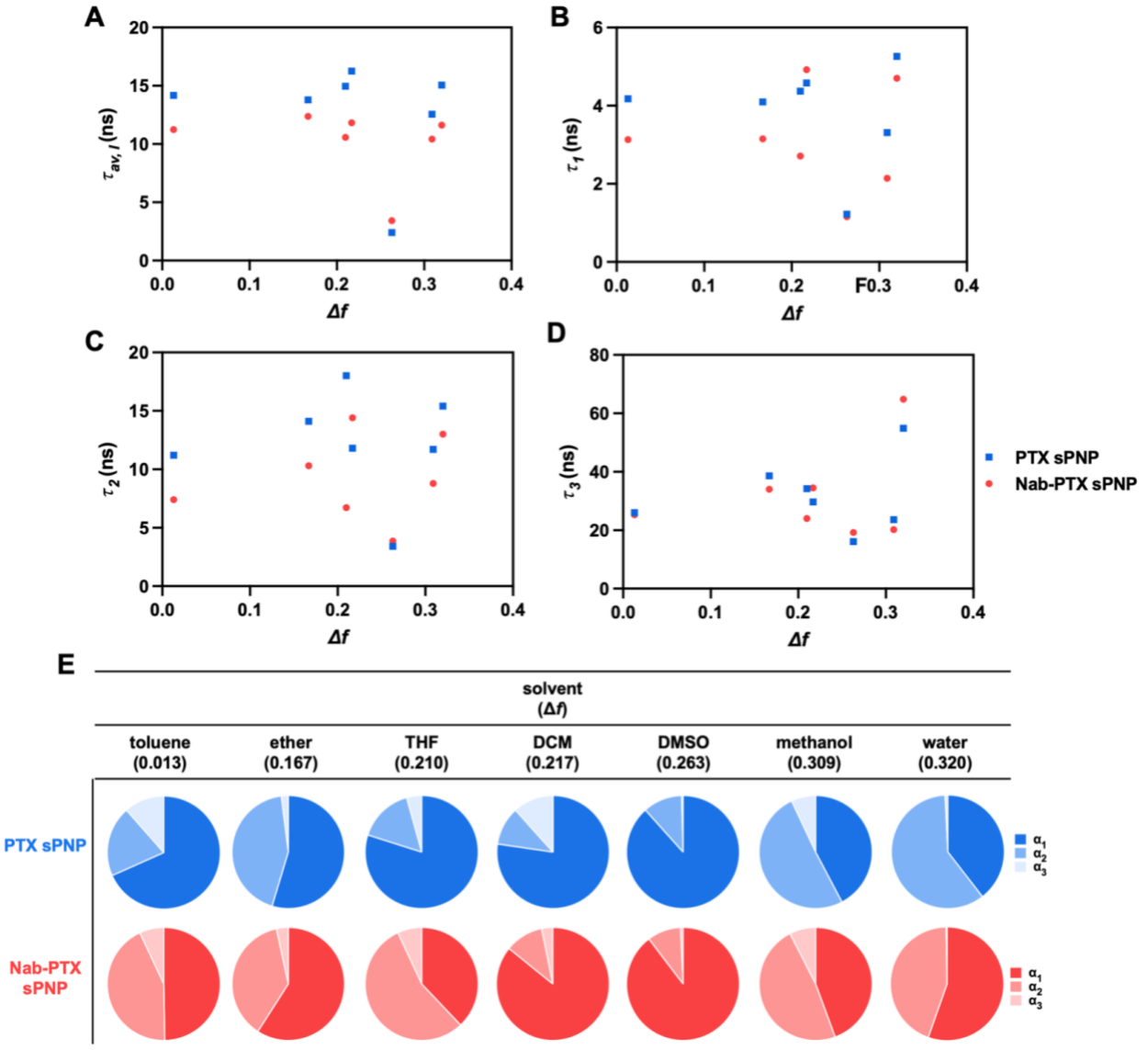

Figure 3.8: Supplemental to **Figure 3.5** and **Table 3.6**. Fluorescence lifetime kinetic data for **PTX sPNP** and **Nab-PTX sPNP** in various solvents, plots. Intensity-weighted average fluorescence lifetime (A), τ_1 (B), τ_2 (C), and τ_3 (D) values plotted with respect to solvent orientation polarizability, and (E) pie charts displaying α_1, α_2, and α_3 values as parts of a whole.

See Appendix C for NMR spectra of all compounds and additional supplementary figures not explicitly referenced in this chapter.

Chapter 4 – A Heterobifunctional RAFT System and its Application in Self-Reporting Micelles

4.1 Authors and Contributions

This chapter contains text and data in preparation for publication as:

A Heterobifunctional RAFT System and its Application in Self-Reporting Micelles

Anthony J. Berardi, Yeongun Ko, Jeffery E. Raymond, Joerg Lahann

4.2 Abstract

In this chapter, we developed a heterobifunctional RAFT system to synthesize linear methacrylate-based polymers that can undergo Hetero-Diels–Alder (HDA) and conjugate addition (CA) reactions at their respective chain ends immediately following polymerization. This system was enabled by the design of a chain transfer agent (CTA) with a diethoxyphosphoryl Z group, activating the dithioester's thiocarbonyl as a dienophile, and a dibromomaleimide-containing R group, capable of engaging in conjugate addition reactions with thiol-containing ligands following polymerization. The synthesized CTA was used to polymerize hydrophobic, hydrophilic, and fluorinated methacrylic monomers, all of which exhibit low polydispersities and react according to pseudo first-order kinetics. A homopolymer of triethylene glycol methyl ether methacrylate was used as a model substrate to study end group HDA and CA reactions, characterized by ^{1}H NMR and a dual-color fluorescence spectroscopic approach. Next, an amphiphilic, diblock copolymer was synthesized and functionalized at both end groups and characterized in a similar manner to

the homopolymer. The diblock copolymer was subsequently used to prepare micellar nanostructures. The dual-color end group labelling strategy provided insight into block copolymer assembly state across five binary THF/water solutions of varying volume ratios via time-resolved fluorescence spectroscopy, complementary to dynamic light scattering characterization. Finally, we used time-resolved fluorescence spectroscopy to detect the core internalization and shell association of hydrophobic and hydrophilic silver nanoparticles, respectively.

4.3 Introduction

Controlled, living polymerization techniques have fundamentally changed the field of polymer science, enabling the precision synthesis of a wide range of monodisperse polymers of diverse monomer composition, multiblock architecture, macromolecular topology, and end group functionality.[79,202] Nitroxide-mediated polymerization (NMP),[203] atom transfer radical polymerization (ATRP),[80] and reversible addition–fragmentation chain transfer (RAFT) polymerization[78] are the most widely used methods to produce controlled, living polymers. All three of these methods have been used to prepare telechelic polymers with end group functionality for post-polymerization chain end functionalization. However, access to bifunctional polymers by NMP and ATRP immediately following polymerization is challenging due to the specific chemistry of their respective initiator systems, and requires post-polymerization end functional group installation, increasing synthetic complexity and contributing to yield loss.[204–206] RAFT polymerization, on the other hand, can be used to prepare α,ω-heterotelechelic polymer conjugates immediately following polymerization by manipulating the Z and R group chemistries of its requisite chain transfer agents (CTAs).[207–210] To date, however, very few α,ω-heterotelechelic RAFT systems have been reported that incorporate two orthogonal end group chemistries for

immediate post-polymerization functionalization and do not require multiple transformation steps before the final ligand of interest can be conjugated.[211–217]

Heterotelechelic polymers, and heterobifunctional molecules in general, are widely applicable across a range of bioconjugate, surface modification, nanomaterial, and biotechnological applications.[218–222] Hetero-Diels–Alder (HDA) cycloadditions have emerged as a promising strategy to conjugate diene-labelled compounds to the intrinsic thiocarbonyl RAFT polymer end group by engineering the CTA's Z group to possess electron donating character.[223–228] These conjugation reactions, developed by Barner-Kowolik and coworkers, can be performed in organic and aqueous media and have been used to conjugate small molecules, microparticles, synthetic polymers, and proteins to RAFT polymers. Additionally, over the last decade, dithiomaleimides (DTMs) have emerged as versatile, fluorescent scaffold moieties that have been used as both structural and reporting components across a number of macromolecular and nanomaterial applications, like protein engineering,[190–192,229] polymer labelling,[163,193,194] block copolymer nanoparticles,[167] and nanogels.[140,166] O'Reilly and coworkers reported a straightforward procedure to synthesize dibromomaleimide (DBM)-end functional RAFT polymers from a DBM-containing CTA that can undergo conjugate additions with thiols to give a fluorescent DTM polymer adduct.[165,193] While both of these RAFT polymer end group modification schemes have seen independent success to perform monofunctional end group conjugations to RAFT polymers, neither have been implemented in either homo- or heterobifunctional RAFT systems. Additionally, both of these end group modification strategies are reversible, as HDA cycloaddition products can degrade at elevated temperature and DTMs can undergo exchange reactions with excess thiols or in the presence of reducing agents. This approach

unlocks the potential for synthesis of dual stimuli-responsive materials in a RAFT system that combines both end group chemistries.[230,231]

In this report, we sought to design a new α,ω-heterotelechelic RAFT system capable of orthogonal end group reactions performable immediately following polymer synthesis without the need for post-polymerization functional group manipulation or installation. To accomplish this, we designed a CTA that incorporates functional groups that can perform both HDA and CA reactions following the polymerization of methacrylic monomers and do not interfere with the kinetics of RAFT polymerization. In addition to the polymerization of several commercially available methacrylic monomers and characterization of end group conjugations to a triethylene glycol methyl ether methacrylate-based homopolymer, we synthesized an amphiphilic block copolymer from which we fabricated self-assembling polymer nanoparticles with the ability to detect the presence of an exogenous metal nanosilver species in a dose-dependent manner. This new system is widely applicable across drug delivery, surface chemistry, and biotechnological applications, like proteolysis targeting chimeras (PROTACs), where orthogonal molecular heterobifunctionality are beneficial.

4.4 Methods

4.4.1 Materials

All solvents and reagents were purchased from Sigma Aldrich and used without further purification unless otherwise specified. Aminomethylcoumarin acetic acid was purchased from Lumiprobe. 4 nm C18 silver nanospheres were purchased from NanoXact. All methacrylic monomers were de-inhibited by filtration through a plug of basic alumina immediately prior to use. Silica gel flash chromatography was performed using SiliCycle SiliaFlash P60 silica gel. Thin-layer chromatography was performed on Supelco TLC plates (pre-coated with a 250 μm layer of

silica gel 60 matrix with fluorescent indicator F254) and visualized with a UV hand lamp (254 nm and 365 nm) and potassium permanganate stain.

4.4.2 Nuclear Magnetic Resonance (NMR) Spectroscopy

NMR spectra were recorded on either a Varian MR400 spectrometer at 400 MHz or a Bruker Avance Neo spectrometer at 500 MHz. All samples were dissolved in $CDCl_3$ or DMSO-d_6; chemical shift was referenced to the solvent residual peak at 7.26 ppm or 2.50 ppm, respectively.

4.4.3 Liquid Chromatography – Mass Spectrometry (LC-MS)

Small molecule mass spectra were recorded on an Agilent 6230 ESI-TOF HPLC-MS in positive ion mode with a manual injection valve and no column in series before the detector. Samples were dissolved at millimolar concentrations in HPLC-grade acetonitrile prior to analysis.

4.4.4 Steady-state Fluorescence Spectroscopy

Steady-state excitation and emission spectra of small molecules and nanoparticles were recorded on a Horiba FluoroMax Plus spectrofluorometer equipped with a 150 W xenon arc lamp, Czerny-Turner monochromaters, an R928P photomultiplier tube capable of detection from 185-850 nm, and reference photodiode for monitoring lamp output.

4.4.5 Time-Correlated Single Photon Counting (TCSPC)

TCSPC measurements of small molecules, polymers, and micelles were acquired on a Horiba FluoroMax Plus spectrofluorometer with a Horiba NanoLED 390 nm solid state diode laser (<1.4 ns pulse duration) driven by NanoLED NL-C2 Pulsed Diode Controller and DeltaHub DH-HT TCSPC Controller modules. Sample measurements were recorded at either 425 nm or 600 nm with a 1 MHz laser repetition rate, measurement range of 100 ns, 950 V detector bias, and histogram

set to 512. The instrument response function (IRF) was determined from the scattering signal of a suspension of Ludox HS-40 silica at 370 nm. Measurements were performed in quartz cuvettes.

4.4.6 Size Exclusion Chromatography (SEC)

SEC measurements were performed with THF as the eluent at 40 °C on a Shimadzu LC system equipped with an autosampler, refractive index detector, and photodiode array detector. The stationary phase was composed of a Phenomenex Phenogel 10 um Linear(2), 300x7.8mm column and calibrated with linear polystyrene standards of molecular weights ranging from 1,000,000 g/mol to 92 g/mol. Molecular weight distributions and polydispersity indices were determined from chromatograms using the provided LCsolution software package.

4.4.7 Dynamic Light Scattering (DLS)

Nanoparticle size measurements were performed on a Malvern Zetasizer Nano ZSP at an angle of 173° with a 4mW He-Ne laser at 633 nm. All samples were equilibrated to ambient temperature before measurement. Particle size and zeta potential were analyzed with the provided Nano DTS software package. Measurements were recorded in Malvern folded capillary disposable cuvettes.

4.4.8 Data Analysis

All NMR spectra were analyzed and plotted with MestReNova v14. Steady-state emission spectra, excitation spectra, SEC traces, and DLS traces were analyzed with Microsoft Excel and plotted with GraphPad Prism 11. TCSPC fluorescence lifetime decay traces were fitted with the Horiba EzTime software package and plotted with GraphPad Prism 11. All other plots were generated with GraphPad Prism 11. All chemical structures were generated with ChemDraw 20.

4.4.9 Small Molecule, Polymer, and Micelle Synthetic Details

4.4.9.1 Synthesis of 1

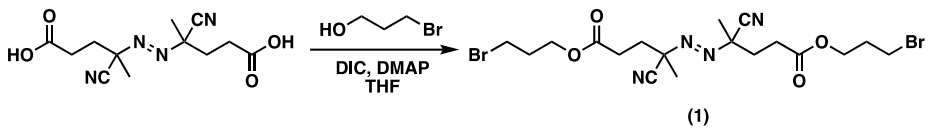

(1)

4,4-azobis(4-cyanovaleric acid) (4.00 g, 14.3 mmol, 1 eq.), 3-bromo-1-propanol (2.84 mL, 31.4 mmol, 2.2 eq.), and 4-dimethylaminopyridine (0.174 g, 1.43 mmol, 0.1 eq.) were added to a round bottom flask and dissolved in 75 mL of THF with stirring. The flask was chilled in an ice bath and N,N'-diisopropylcarbodiimide (4.92 mL, 31.4 mmol, 2.2 eq.) was added dropwise via syringe. The reaction was allowed to come to room temperature and stirred overnight. THF was removed by rotary evaporation and the resulting crude was redissolved in dichloromethane, then extracted 2x with a saturated aqueous solution of sodium bicarbonate, 1x with 1M HCl, and 1x with brine. The organic layer was collected, dried over sodium sulfate, and removed via rotary evaporation. The resulting crude was purified by normal phase flash chromatography in 6:4 hexane:ethyl acetate. The resulting product was a clear oil. Yield: 2.92 g.

HRMS (ESI-TOF): calc'd for $[M+K-2H]^-$ 556.96, found 556.99

^{1}H NMR (500 MHz, $CDCl_3$): δ 1.70 (d, *J* = 27.5 Hz, 6H), 2.19 (quint, *J* = 3.8 Hz, 4H), 2.45 (m, 8H), 3.46 (t, *J* = 4.0 Hz, 4H), 4.26 (qd, *J* = 6.2, 3.8 Hz, 4H)

4.4.9.2 Synthesis of 2

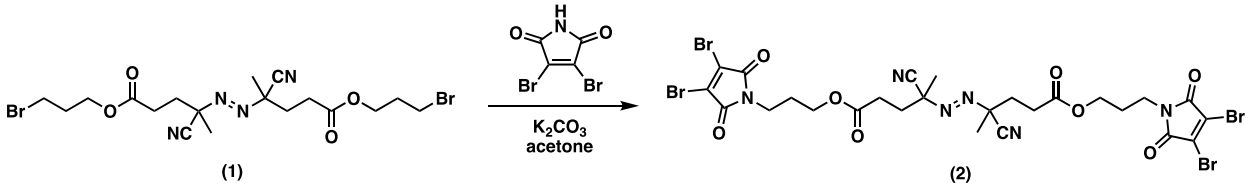

(1) (2)

2,3-dibromomaleimide (3.15 g, 12.3 mmol, 2.2 eq.) and potassium carbonate (2.92 g, 12.3 mmol, 2.2 eq.) were dissolved in 50 mL of acetone with stirring. 1 (2.92 g, 5.61 mmol, 1 eq.) was dissolved in a minimal amount of acetone and added to the stirring flask in one portion. The

reaction mixture was stirred for 48 hours at room temperature. Acetone was removed by rotary evaporation and the resulting crude was redissolved in ethyl acetate, then extracted 3x with brine. The organic layer was collected, dried over sodium sulfate, and removed via rotary evaporation. The resulting crude was purified normal phase flash chromatography in 6.5:3.5 hexane:ethyl acetate. The resulting product was a yellow oil. Yield: 1.10 g.

^{1}H NMR (500 MHz, $CDCl_3$): δ 1.71 (dd, *J* = 28.5, 3.3 Hz, 6H), 2.19 (m, 4H), 2.44 (m, 8H), 3.46 (t, *J* = 6.5 Hz, 4H), 4.26 (t, *J* = 6.2 Hz, 4H)

4.4.9.3 Synthesis of 3

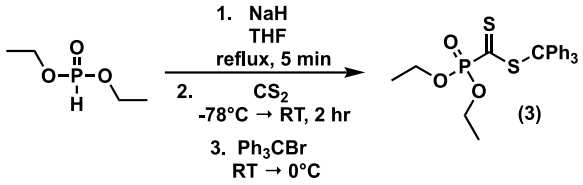

The procedure for the synthesis of 3 was adapted and refined from a previous report.[232] NaH (0.753 g, 31.36 mmol) was added to a round bottom flask with 40 mL of dry THF. Diethyl phosphite (4 mL, 31.05 mmol) in 5 mL of dry THF was added dropwise to the same flask under inert conditions. The reaction refluxed for 10 minutes without any added heat and with stirring. The flask was then chilled to -78 °C in a dry ice/acetone bath. Carbon disulfide (4.015 mL, 66.75 mmol) was added dropwise to the chilled flask via syringe. The reaction was allowed to come to room temperature and stir for 2 hours. During this time, the reaction mixture turned a turbid, dark orange color. The flask was chilled in an ice bath, opened to atmosphere, and bromotriphenylmethane (10.136 g, 31.36 mmol) was added to the reaction mixture in one portion. The flask was allowed to come to room temperature and stir for 3 hours. The reaction mixture turned a violet color during this time. Following reaction, the mixture was filtered to remove insoluble particles, THF was removed by

rotary evaporation, and the resulting viscous, violet material was purified by normal phase flash chromatography in diethyl ether. The final product is a vibrant violet crystalline material.

HRMS (ESI-TOF): calc'd for $[M+H]^+$ 457.10, found $[C_{19}H_{15}]^\bullet$ 243.12

^{1}H NMR (500 MHz, DMSO-d_6): δ 1.32 (t, J = 7.0 Hz, 6H), 4.05-4.26 (m, 4H), 7.11-7.38 (m, 15H)

4.4.9.4 Synthesis of 4

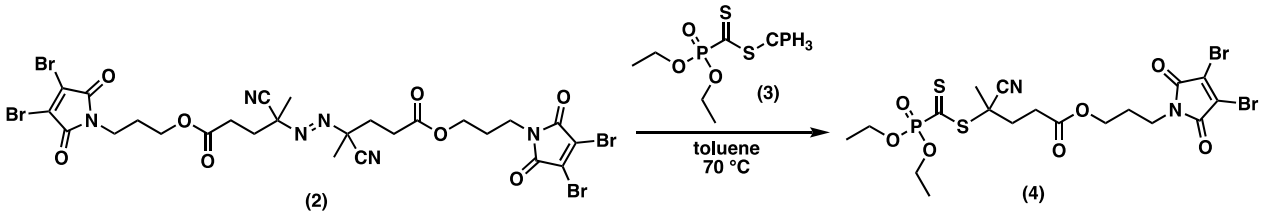

2 (1.10 g, 1.27 mmol, 1 eq.) and 3 (0.578 g, 1.27 mmol, 1 eq.) were added to a 25 mL Schlenk flask and dissolved in 20 mL of toluene. The flask was sealed and deoxygenated with three freeze-pump-thaw cycles. The flask was heated to 70 °C and stirred overnight. The reaction mixture was then allowed to come to room temperature and the toluene was removed by rotary evaporation. The resulting crude was immediately purified by normal phase flash chromatography in 4:6 hexane:ethyl acetate. The final product is a vibrant magenta oil. Yield: 0.400 g.

HRMS (ESI-TOF): calc'd for $[M+H]^+$ 632.91, found 632.91

^{1}H NMR (500 MHz, $CDCl_3$): δ 1.38 (td, *J* = 6.2, 2.9 Hz, 6H), 1.86 (s, 3H), 2.19 (quint, *J* = 6.3 Hz, 2H), 2.42 (m, 2H), 2.63 (m, 2H), 3.47 (t, *J* = 6.4 Hz, 2H), 4.25 (m, 6H)

4.4.9.5 Synthesis of 5

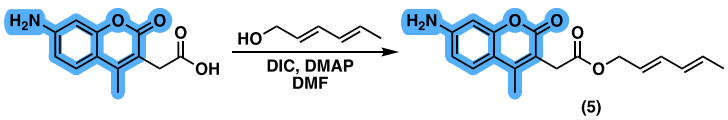

Aminomethylcoumarin acetic acid (0.100 g, 0.429 mmol, 1 eq.), *trans*,*trans*-2,4-hexadien-1-ol (63 mg, 0.643 mmol, 1.5 eq.), and 4-dimethylaminopyridine (7.8 mg, 0.0643 mmol, 0.1 eq.) were

added to a 20 mL round bottom flask and dissolved in DMF with stirring. The flask was chilled in an ice bath and N,N'-diisopropylcarbodiimide (0.100 mL, 0.643 mmol, 1.5 eq.) was added dropwise. The reaction was allowed to come to room temperature and stirred overnight. The reaction mixture was poured into a separatory funnel, along with 30 mL of dichloromethane, and extracted 5x with water and 1x with brine. The organic layer was collected, dried over sodium sulfate, and dichloromethane was removed by rotary evaporation. The resulting crude was purified by normal phase flash chromatography in 5% methanol in dichloromethane. The resulting product is a white solid.

HRMS (ESI-TOF): calc'd for $[M+Na]^+$ 336.12, found 336.12

^{1}H NMR (500 MHz, $CDCl_3$): δ 1.75 (d, *J* = 6.7 Hz, 3H), 2.33 (s, 2H), 4.11 (s, 2H), 4.61 (d, *J* = 6.6 Hz, 2H), 5.68 (ddt, *J* = 49.2, 14.3, 6.7 Hz, 2H), 6.15 (dt, *J* = 99.2 Hz, 18.5 Hz, 2H), 6.56 (m, 2H), 7.40 (d, *J* = 8.5 Hz, 1H)

Steady-state fluorescence (THF): $\lambda_{max,\,ex}$ = 346 nm (λ_{ex} 435 nm), $\lambda_{max,\,em}$ = 420 nm (λ_{ex} 348 nm)

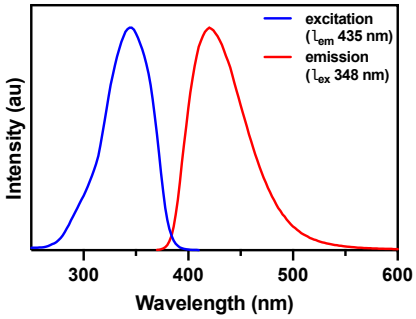

4.4.9.6 Synthesis of 6

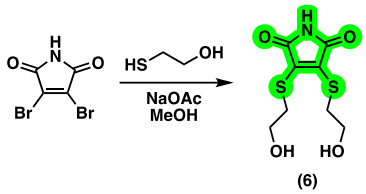

(6)

2,3-dibromomaleimide (1 g, 3.92 mmol, 1 eq.) and sodium acetate (0.81 g, 9.81 mmol, 2.5 eq.) were added to a 50 mL round bottom flask and dissolved in 20 mL of methanol with stirring. The flask was sealed with a septum and 2-mercaptoethanol (0.69 mL, 9.81 mmol, 2.5 eq.) was added dropwise via syringe. Upon addition, the reaction mixture turned immediately to a bright yellow color. After stirring at room temperature for 2 hours, the reaction mixture was poured into a separatory funnel and diluted 3x with water. The mixture was extracted 7-9x with ethyl acetate. The organic layer was collected, dried over sodium sulfate, and evaporated. The resulting crude residue was purified by standard phase flash chromatography with a 2-15% methanol gradient in dichloromethane.

HRMS (ESI-TOF): calc'd for [M+ACN+Na]+ 313.02, found 313.95.

^{1}H NMR (500 MHz, $CDCl_3$): δ 3.32 (t, J = 7.6 Hz, 6H), 3.58 (q, J = 7.5, 7.0 Hz, 4H), 4.95 (br, 2H)

Steady-state fluorescence (THF): $\lambda_{max,\,ex}$ = 399 nm (λ_{ex} 510 nm), $\lambda_{max,\,em}$ = 512 nm (λ_{ex} 400 nm)

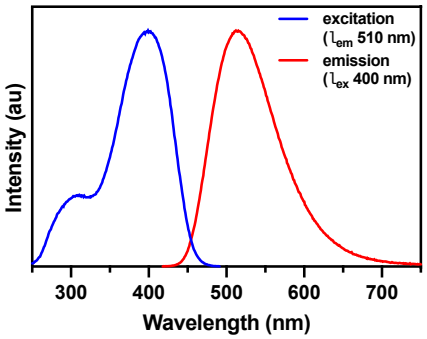

4.4.9.7 Synthesis of all polymers (P1, P2, P3, P4) in Figure 4.2

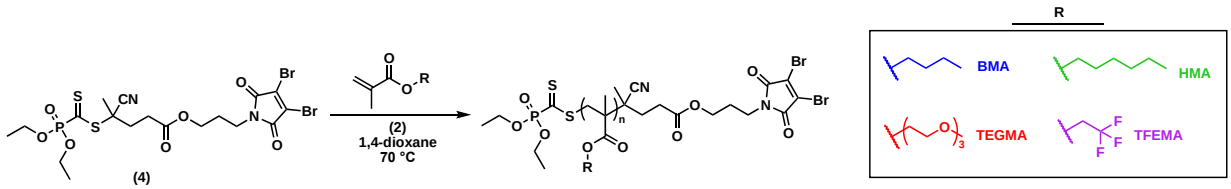

4 (10.0 mg, 15.7 µmol, 1 eq.), 2 (1.37 mg, 1.57 µmol, 0.1 eq.), and a methacrylic monomer (788 µmol, 50 eq.) were added to a 5 mL Schlenk flask and dissolved in 3 mL of 1,4-dioxane. A few granules of 1,3,5-trioxane were added to the reaction mixture for use as an internal ^{1}H NMR standard. A 100 µL aliquot was taken and reserved for later NMR analysis. The flask was sealed and the mixture was purged with nitrogen gas for 30 minutes. The flask was heated in an oil bath at 70 °C for 14 hours. The flask was removed from the oil bath, opened to atmosphere, and allowed to come to room temperature. A 100 µl aliquot was taken and reserved for later NMR analysis. Polymers were isolated by repeated precipitation into a suitable, chilled antisolvent (either hexane or methanol in all cases), redissolved in a suitable good solvent, transferred to a tared vial, and dried by rotary evaporation. The resulting purified polymers were analyzed by NMR and SEC.

Monomer abbreviations:

BMA – n-butyl methacrylate (MW = 142.20 g/mol, D = 0.984 g/mL)

TEGMA – triethylene glycol methyl ether methacrylate (MW = 232.27 g/mol, D = 1.027 g/mL)

HMA – hexyl methacrylate (MW = 170.25 g/mol, D = 0.863 g/mL)

TFEMA – trifluroethanol methacrylate (MW = 168.11, D = 1.181 g/mL)

Polymer abbreviations:

P1 – poly(BMA)

P2 – poly(TEGMA)

P3 – poly(HMA)

P4 – poly(TFEMA)

4.4.9.8 Method for the analysis of RAFT polymerization kinetics and $M_{n,\,NMR}$ via ^{1}H NMR analysis

Kinetics for the RAFT polymerization of BMA and TEGMA were calculated by observing the decrease in methacrylate resonance integrals in the ^{1}H NMR spectra of 100 μL aliquots withdrawn from the reaction mixture at defined time points, relative to the signal from an included internal standard of 1,3,5-trioxane (**Figure 4.2**). An aliquot was withdrawn before polymerization initiation (t_0) and at 1 hour increments until 6 hours had passed ($t_1 - t_7$). 400 μL of DMSO-d_6 was added to each 100 μL aliquot and ^{1}H NMR spectra were acquired for all samples. Chemical shift was normalized to the TMS peak at 0.0 ppm. For each spectrum, the singlet at 5.1 ppm (corresponding to 1,3,5-trioxane's methylene peak) was assigned a normalized integral of 100.0. The two characteristic singlets resulting from unreacted methacrylate monomer terminal alkene groups (between 5.0 and 6.0 ppm) were integrated relative to the 1,3,5-trioxane singlet. The following equation was used to calculate the monomer conversion at each defined time point:

$$\%\ monomer\ conversion = \frac{I_{t_n} - I_{t_0}}{I_{t_n}} \cdot 100\%$$

where I_{t_0} is the average integral of monomer terminal alkene singlets for the t_0 sample and I_{t_n} is the average integral of monomer terminal alkene singlets for the sample in question (t_n). The calculated % monomer conversion for each sample was plotted with respect to time to yield **Figure 4.2B**. The following expression was used to calculate y-values for the first-order kinetic plot seen in **Figure 4.2C**:

$$\ln\left(\frac{I_{t_0}}{I_{t_n}}\right)$$

To calculate $M_{n,\,NMR}$ values for the four polymers recorded in Table 1, the following equation was used:

$$M_{n,NMR} = MW_{CTA} + MW_{monomer}(\%\ monomer\ conversion \cdot DP_{target})$$

where MW_{CTA} is the molecular weight of chain transfer agent 4 (634 g/mol), $MW_{monomer}$ is the molecular weight of the methacrylic monomer used, *% monomer conversion* is the calculated monomer conversion at t_f, and DP_{target} is the targeted degree of polymerization (100 in all cases). This method for calculating M_n via ^{1}H NMR with a 1,3,5-trioxane internal standard is generalizable for all controlled polymerization techniques involving the chain growth polymerization of vinylic monomers, including atom transfer radical polymerization (ATRP), nitroxide-mediated polymerization (NMP), and reversible addition-fragmentation chain-transfer polymerization (RAFT) where it can be assumed that polydispersity values ($Đ$) approach 1.

4.4.9.9 Synthesis of P5 – hetero-Diels–Alder (HDA) end group reaction to P2 homopolymer

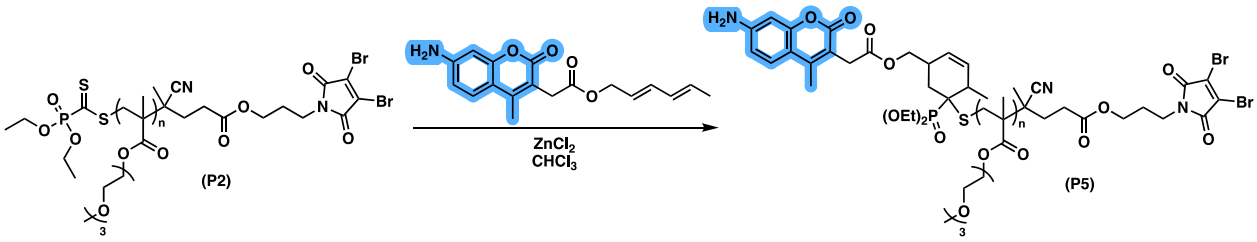

P2 (20 mg, $M_{n,\,NMR}$ = 18,127 g/mol, 0.0110 mmol, 1 eq.), 5 (0.41 mg, 0.0132 mmol, 1.2 eq.), and $ZnCl_2$ (0.18 mg, 0.0132 mmol, 1.2 eq.) were added to a vial and dissolved in 4 mL of chloroform. The vial was stirred overnight at 50 °C. Following reaction, the chloroform was removed via rotary evaporation and the crude was redissolved in 1 mL of DMSO. The polymer was purified by centrifugation 5x through a 5 mL spin column packed with Sephadex G-10 (swollen for at least 1 hr in DMSO).[233] The resulting polymer in DMSO was dialyzed against acetone with a 1 kDa

membrane and dried via rotary evaporation. Fluorescent polymer conjugate P5 was analyzed by ^{1}H NMR and fluorescence spectroscopy.

4.4.9.10 Synthesis of P6 – conjugate addition (CA) end group reaction to P2 homopolymer

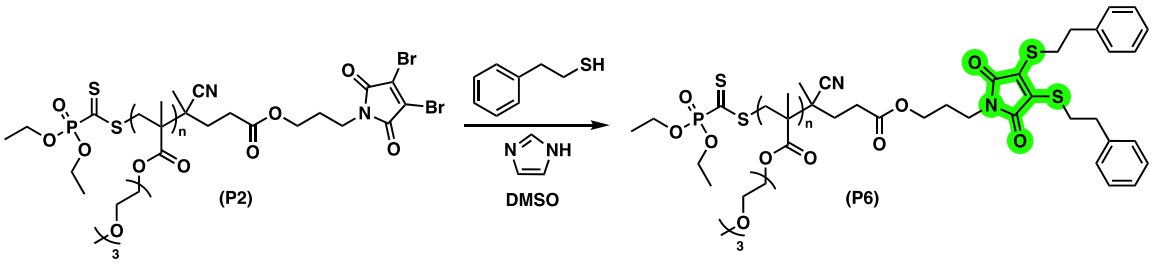

P2 (20 mg, $M_{n,\,NMR}$ = 18,127 g/mol, 0.0110 mmol, 1 eq.) and imidazole (9.0 µL, 20 mg/mL stock solution, 0.0265 mmol, 2.4 eq.) were added to a vial and dissolved in 4 mL of DMSO. Phenylethyl mercaptan (18.3 µL, 20 mg/mL stock solution, 0.0265 mmol, 2.4 eq) was added to the vial and the reaction was stirred overnight at room temperature. Following reaction, the polymer was purified by centrifugation 5x through a 5 mL spin column packed with Sephadex G-10 (swollen for at least 1 hr in DMSO).[233] The resulting polymer in DMSO was dialyzed against acetone with a 1 kDa membrane and dried via rotary evaporation. Fluorescent polymer conjugate P6 was analyzed by ^{1}H NMR and fluorescence spectroscopy.

4.4.9.11 Synthesis of diblock copolymer P7 – RAFT chain extension of P2 with BMA

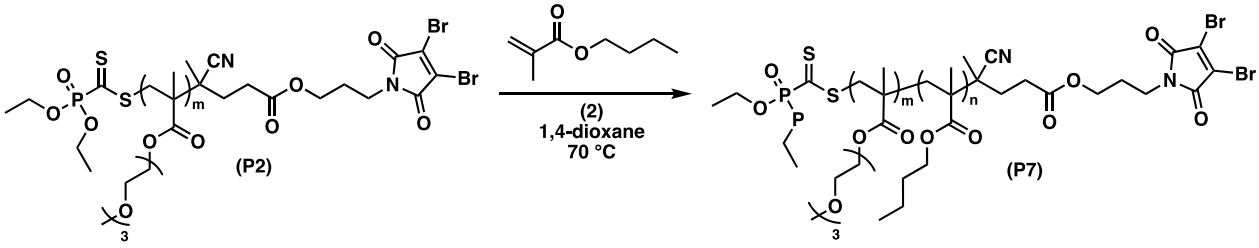

P2 (60 mg, $M_{n,\,NMR}$ = 18,127 g/mol, 0.0331 mmol, 1 eq.), BMA (53 µL, 0.331 mmol, 100 eq.), and 2 (0.0927 mg, 3.31 µmol, 0.1 eq.) were added to a 4 mL vial and dissolved in 1 mL of 1,4-dioxane. A few granules of 1,3,5-trioxane were added to the reaction mixture for use as an internal ^{1}H NMR

standard. A 50 µL aliquot was taken and reserved for later NMR analysis. The vial was sealed with a septum and the mixture was purged with nitrogen gas for 30 minutes. The flask was heated in an oil bath at 70 °C for 14 hours. The flask was removed from the oil bath, opened to atmosphere, and allowed to come to room temperature. A 50 µl aliquot was taken and reserved for later NMR analysis. The resulting diblock copolymer was isolated by precipitation into cold hexane, redissolved in THF, transferred to a tared vial, and dried by rotary evaporation. Resulting diblock copolymer P7 was analyzed by NMR and SEC.

$M_{n,\,NMR}$ = 24,280; $M_{n,\,SEC}$ = 24,267; $M_{w,\,SEC}$ = 33,808; $Đ$ = 1.39; m = 75; n = 43

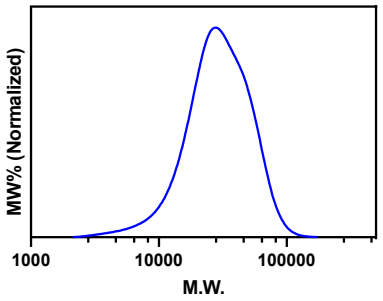

4.4.9.12 Synthesis of P8 – orthogonal hetero-Diels–Alder and conjugate addition reactions to P7

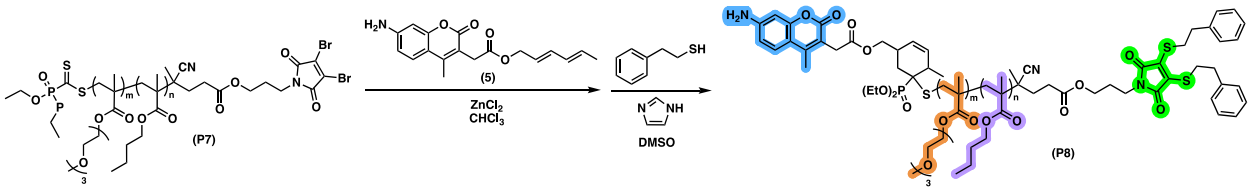

HDA and CA reactions were performed sequentially in an identical fashion to the procedures outlined above for homopolymers. Sephadex and dialysis purification was performed after each step as described above.[233] The resulting fluorescent copolymer was analyzed by fluorescence spectroscopy to confirm fluorescent end group presence (**Figure 4.3**).

4.4.9.13 Polymer micelle preparation from P8

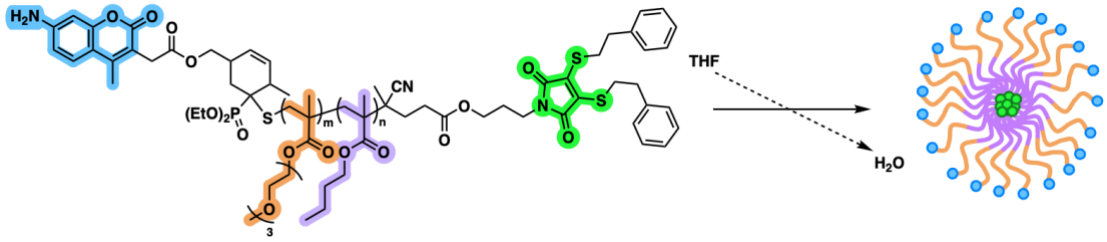

End group-conjugated pTEGMA-b-pBMA diblock copolymer was dissolved in THF at a concentration of 20 mg/mL). 50 uL of polymer solution in THF was added dropwise to 1 mL of UltraPure water stirring vigorously in a 4 mL vial. The resulting suspension of micelles was allowed to stir for at least an hour and bath sonicated prior to use. Polymer micelles were characterized by DLS and fluorescence spectroscopy (**Figure 4.3**).

4.5 Results and Discussion

Inspired by the work of both Barner-Kowolik and coworkers[223–225,227,228] and O'Reilly and coworkers,[165,193,194] we designed a RAFT chain transfer agent (CTA) **4** with a diethoxyphosphoryl Z group and dithiomaleimide R group. The diethoxyphosphoryl Z group is capable of activating the thiocarbonyl as a hetero-dienophile in a hetero-Diels–Alder (HDA) reaction with a diene post-RAFT polymerization and the dibromomaleimide R group is capable of engaging in CA reactions with thiols resulting in fluorescent DTMs pre- and post-RAFT polymerization (**Figure 4.1**). The synthesis of CTA **4** was completed in three steps, starting from 4,4-azobiscyanovaleric acid (ACVA), a common water-soluble radical initiator. ACVA was first esterified with 3-bromo-1-propanol to give dibromo compound **1**, which was then substituted at the primary bromides with dibromomaleimide to give **2**. The final CTA was isolated following the radical exchange of **2** with triphenylmethyl diethoxyphosphoryldithioformate (**3**).[232]

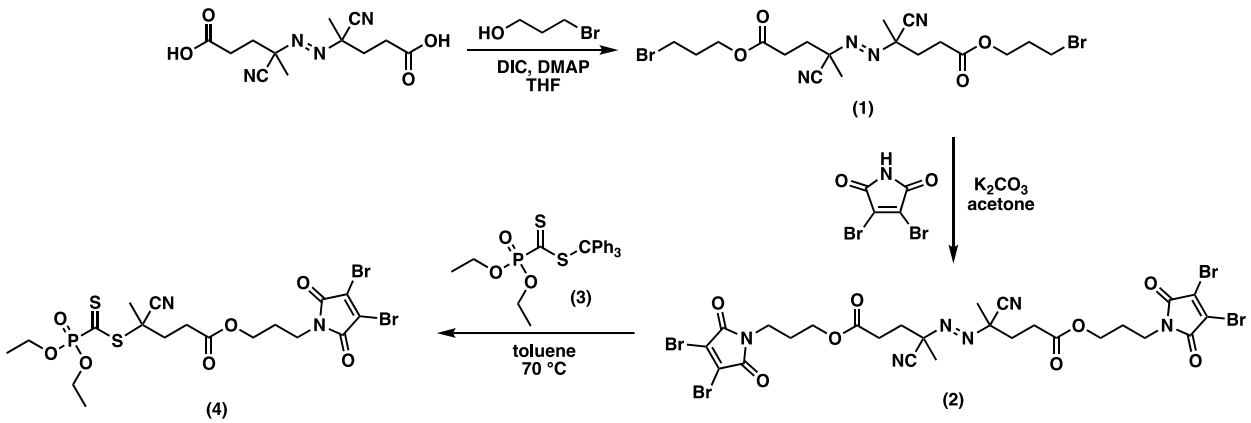

Figure 4.1: Three-step synthesis of heterobifunctional RAFT agent capable of performing orthogonal hetero-Diels–Alder and conjugate addition reactions post-polymerization.

Following the synthesis of CTA **4**, several commercially available methacrylic monomers were RAFT polymerized in 1,4-dioxane at 70 °C, with **2** as the thermal radical initiator to prevent any end group loss during polymerization (**Figure 4.2A**). The RAFT polymerization of two hydrophobic monomers (n-butyl methacrylate (BMA) and hexyl methacrylate (HMA)), one hydrophilic monomer (triethylene glycol methyl ether methacrylate (TEGMA)), and one fluorinated monomer (trifluoroethyl methacrylate (TFEMA)) all resulted in low-dispersity polymers ($Đ < 1.2$) and achieved at least 60% conversion after 16 hours of reaction (**Figure 4.2D**, **Table 4.1**). The polymerization kinetics of BMA and TEGMA were monitored by ^{1}H NMR spectroscopy for the first six hours of reaction relative to an internal 1,3,5-trioxane internal standard and both reactions followed pseudo-first order kinetics, characteristic of RAFT polymerization (**Figure 4.2B**, **C**).

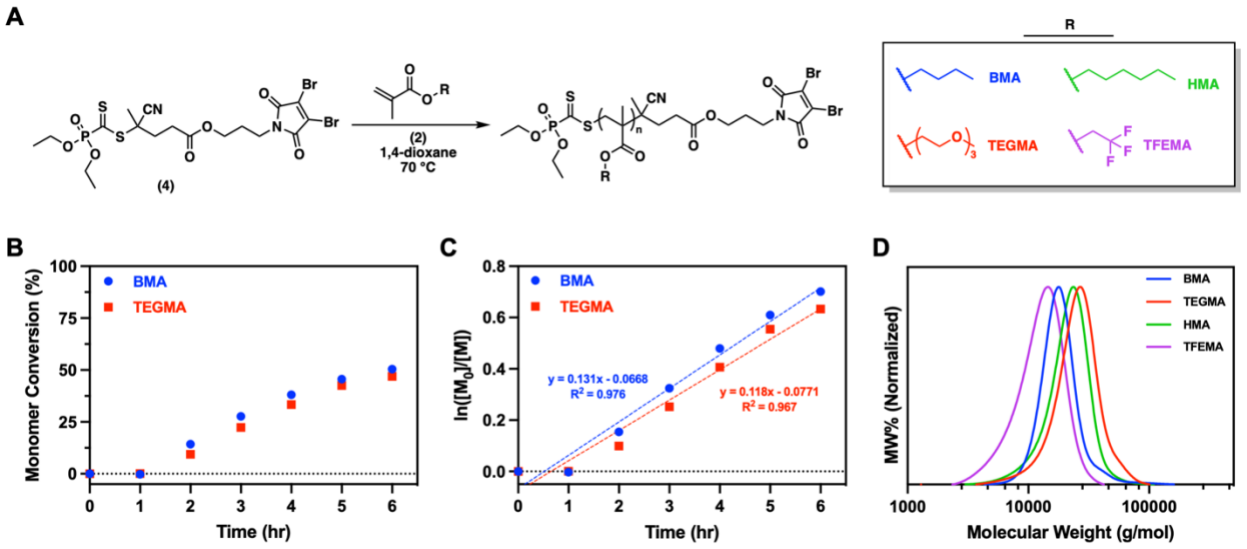

Figure 4.2: (A) RAFT polymerization of four diverse methacrylate monomers, (B) monomer conversion vs. time and (C) first order kinetic plot for BMA and TEGMA RAFT polymerization, and (D) molecular weight distributions for all polymers synthesized, measured by SEC.

	Monomer	Reaction time (hr)	Monomer Conversion (%)	$M_{n,\ NMR}$	$M_{n,\ GPC}$	$M_{w,\ GPC}$	$Đ$
P1	BMA	16	60	9,174	17,122	19,755	1.15
P2	TEGMA	16	75	18,127	22,766	27,443	1.20
P3	HMA	16	68	12,138	19,477	23,111	1.18
P4	TFEMA	16	60	10,826	11,305	13,736	1.21

Table 4.1: Molecular weight distribution characterization data for polymers synthesized in **Figure 4.1**.

We developed a dual-color fluorescence strategy to assess the ability of polymers synthesized using CTA **4** to undergo orthogonal end group reactions. The CA of thiols or amines to the dibromomaleimide end of the polymer is fluorogenic and results in an emissive adduct with broadband emission from ~500-700 nm ($\lambda_{max,\ ex}$ = 410 nm, $\lambda_{max,\ em}$ = 530 nm).[193,194] To probe HDA reactions to the opposite end of polymers we sought to select a fluorescent dye that would emit in the blue or red regimes that could be readily functionalized with a diene. Aminomethylcoumarin acetic acid (AMCA), a blue dye with $\lambda_{max,\ ex}$ = 348 nm and $\lambda_{max,\ em}$ = 435 nm, was selected for this purpose and esterified to the diene-functional version fit for our purpose with 2,4-hexadien-1-ol to

give **5**. **P2**, the 18 kDa poly(TEGMA) synthesized for **Figure 4.2** was chosen as the polymer substrate to probe end group reactions.

An HDA reaction between **P2** and **5** was performed in chloroform with a catalytic amount of $ZnCl_2$ and purified by gel filtration through Sephadex followed by dialysis. In parallel, a CA reaction between **P2** and phenylethyl mercaptan was performed in DMSO, mediated by imidazole as a base catalyst, purified identically to the HDA reaction (**Figure 4.3A**). Phenylethyl mercaptan was chosen as the thiol-containing ligand for this experiment for its aromatic functional group, detectable by ^{1}H NMR in the aromatic region from 6.5-8 ppm and away from the characteristic downfield resonances of **P2**. Both the HDA and CA reaction products, **P5** and **P6**, respectively, were characterized by ^{1}H NMR spectroscopy, steady-state fluorescence spectroscopy, and time-resolved fluorescence spectroscopy (**Figure 4.3B**-**F**). In both cases, the appearance of aromatic proton peaks corresponding to those labelled in red (**Figure 4.3A**, **B**) was observed in the NMR spectra of purified polymer conjugates. Additionally, each polymer exhibited fluorescence emission as a consequence of the addition of an emissive end group moiety resulting from conjugation. The HDA conjugation of **5** to **P2** imbued the resulting conjugate **P5** with blue emission ($\lambda_{max,\ em}$ = 405 nm). The fluorogenic CA of phenylethyl mercaptan to **P2** resulted in conjugate **P6** exhibiting green emission characteristic of a dithiomaleimide moiety ($\lambda_{max,\ em}$ = 535 nm) (**Figure 4.3D**).

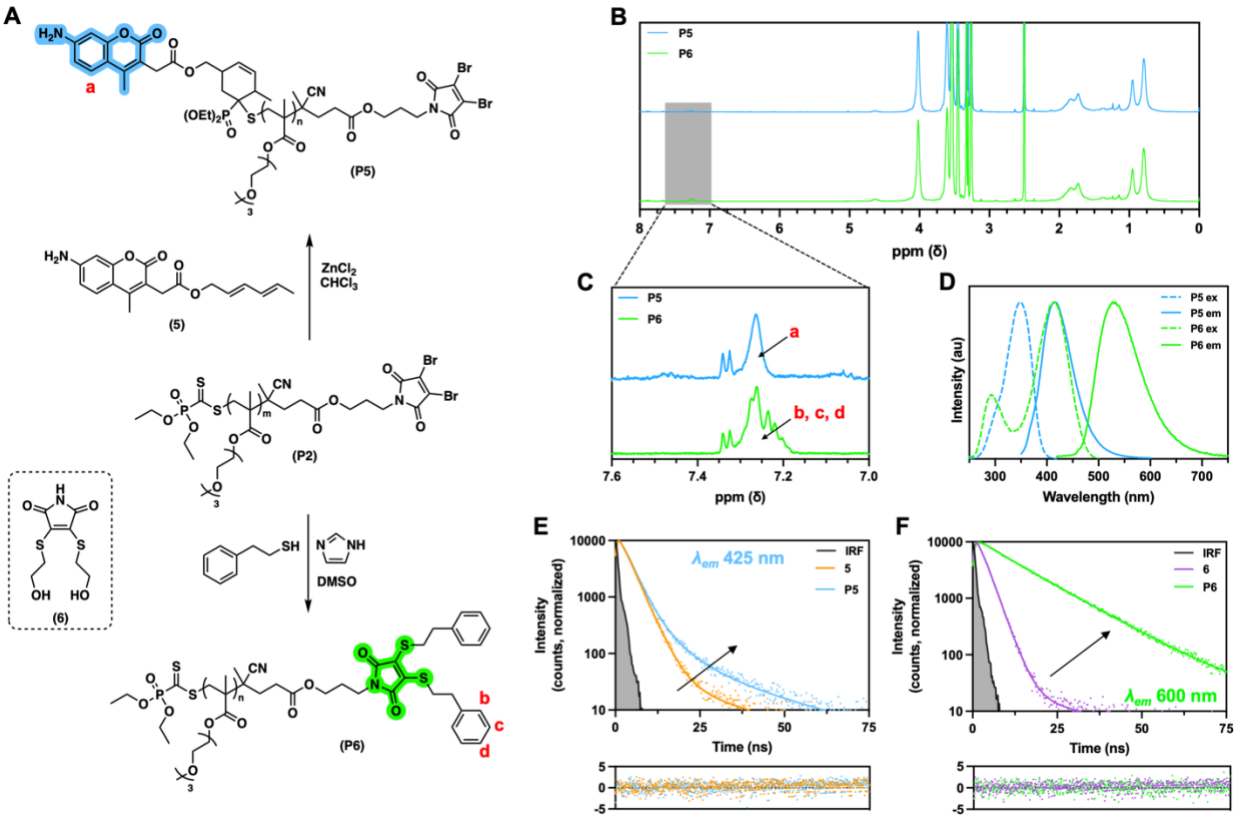

Figure 4.3: (A) Orthogonal hetero-Diels–Alder and conjugate addition end group reactions with AMCA-diene and phenylethyl mercaptan, respectively, (B) full ^{1}H NMR spectra of end group reaction products, (C) aromatic region of ^{1}H NMR spectra of end group reaction products, (D) steady-state excitation and emission spectra of end group reaction products, (E) fluorescence lifetime decays of **5** and **P5** with exponential decay fit residuals shown below, and (F) fluorescence lifetime decays of **6** and **P6** with exponential decay fit residuals shown below. λ_{em} = 425 nm and λ_{ex} = 325 nm for steady-state excitation and emission spectra of **P5**. λ_{em} = 535 nm and λ_{ex} = 405 nm for steady-state excitation and emission spectra of **P6**. Fluorescence lifetime decays were measured at λ_{em} = 425 nm and λ_{em} = 600 nm in (E) and (F), respectively. All samples were dissolved in THF prior to fluorescence analysis.

We employed time-resolved fluorescence spectroscopy to corroborate evidence of polymer end group conjugation from ^{1}H NMR and steady-state fluorescence measurements. **Equation 4.1** was used to fit the raw photon counts composing the decays to a third-order exponential decay function:

$$I(t) = a_1 e^{\left(-\frac{t}{\tau_1}\right)} + a_2 e^{\left(-\frac{t}{\tau_2}\right)} + a_3 e^{\left(-\frac{t}{\tau_3}\right)} \quad (4.1)$$

where τ_n are the component lifetimes of each term and α_n represent the amplitude weights associated with each component lifetime.[136]l The τ_n and α_n values extracted from fitting for each end group and % v/v THF/H_2O are summarized in **Table 4.2**. τ_n and α_n terms from the exponential

decay deconvolution process were used to calculate an average fluorescence lifetime, τ_{av}, for each measurement according to **Equation 4.2**:[136]

$$\tau_{av} = \frac{\alpha_1\tau_1^2+\alpha_2\tau_2^2+\alpha_3\tau_3^2}{\alpha_1\tau_1+\alpha_2\tau_2+\alpha_3\tau_3} \quad (4.2)$$

The fluorescence lifetime of an emissive species is known to increase when bound to a macromolecule or immobilized in a material matrix, such as a nanoparticle.[138] Compared to free **5** dissolved in THF, a good solvent, the HDA polymer conjugate, **P5**, exhibits a shift to a longer fluorescence lifetime, suggesting that the reaction occurred and **5** is covalently bound to **P6** (**Figure 4.3E**). Similarly, compared to analogous dihydroxyethyl-functionalized dithiomaleimide **6** dissolved in THF, CA polymer conjugate **P6** exhibits a shift to a longer fluorescence lifetime (**Figure 4.3F**).

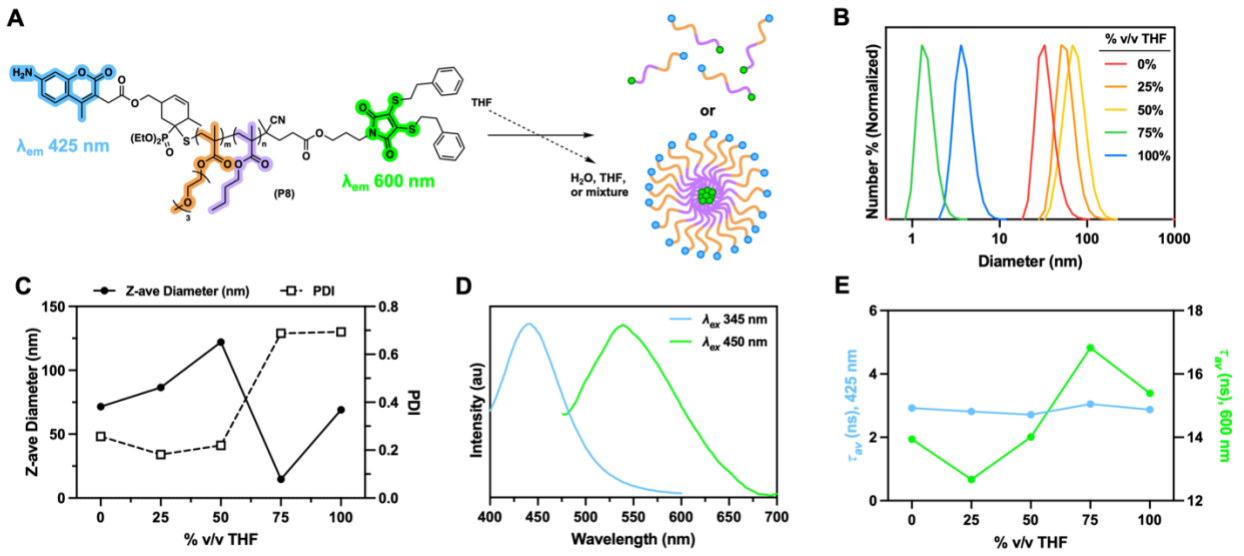

Figure 4.4: (A) End group-conjugated, amphiphilic, diblock copolymer micelle formation as a function of THF concentration, (B) DLS traces of polymer micelles in varying % v/v THF/H_2O, (C) Z-ave diameter and PDI of polymer micelles as a function of % v/v THF/H_2O, (D) steady-state emission spectra of end group-conjugated, amphiphilic, diblock copolymer micelles in H_2O, and (E) average fluorescence lifetime of polymer micelles as a function of % v/v THF/H_2O. Fluorescence lifetime decays were measured at λ_{em} = 425 nm and λ_{em} = 600 nm to probe the hetero-Diels–Alder and conjugate addition polymer ends, respectively.

After confirming the ability for heterobifunctional **P2** synthesized with CTA **4** to undergo both HDA and CA end group reactions, we sought to extend the utility of this system to a

nanomaterial context. Unmodified **P2** was chain extended via RAFT polymerization with BMA to synthesize amphiphilic diblock copolymer **P7**. Sequential HDA and CA reactions were performed on **P7** with **5** and phenylethyl mercaptan, respectively, to yield dual-color diblock copolymer **P8**. Since both end groups of **P8** are emissive at different wavelengths, we hypothesized that they could be simultaneously and independently probed with time-resolved fluorescence spectroscopy to give insight into how the amphiphilic polymer might behave and assemble in a selective environment (**Figure 4.4A**).

We prepared five binary solutions of THF and water, with pure THF being the least selective due to **P8**'s complete solubility, and pure water being the most selective due to **P8**'s amphiphilic nature. **P8** was resuspended in 0, 25, 50, 75, and 100% v/v THF/water and DLS measurements were recorded for all five samples (**Figure 4.4B**). In 0% v/v THF, 75 nm particles were observed with a highly monodisperse PDI value of 0.2. At 25 and 50% v/v THF, particle Z-average diameter increased to 85 and 125 nm, respectively, while PDI remained constant around 0.2. We hypothesize that as the volume fraction of THF increases, the hydrophobic BMA block becomes better solvated and less compact, increasing the particle diameter, but not necessarily the PDI, as the population size distribution remains consistent. However, between 50 and 75% v/v THF, a major transition was observed as **P8** decreased in Z-average diameter to 14 nm while PDI increased to 0.7, corresponding to a breakdown of the micellar particle architecture and a transition to a unimeric state. In 100% v/v THF, a slight size increase was observed, while PDI stayed constant at 0.7, indicating a reorganization to an oligomeric, but not micellar, state.

λ_{em} (nm)	% v/v THF/H_2O	τ_1 (ns)	τ_2 (ns)	τ_3 (ns)	α_1	α_2	α_3	τ_{av} (ns)
425	0	0.408	3.71	7.48	0.831	0.157	0.0116	2.92
	25	0.375	3.64	6.79	0.840	0.148	0.0122	2.82
	50	0.405	3.75	9.56	0.837	0.160	0.00240	2.71
	75	0.684	3.55	11.1	0.598	0.399	0.00286	3.05
	100	1.05	3.22	15.0	0.468	0.530	0.00169	2.88
600	0	0.779	5.52	28.4	0.711	0.244	0.0452	13.9
	25	0.650	5.03	29.5	0.761	0.210	0.0283	12.7
	50	0.700	4.78	32.9	0.755	0.218	0.0269	14.0
	75	1.17	5.30	36.6	0.656	0.302	0.0419	16.8
	100	1.55	6.94	33.6	0.618	0.328	0.0533	15.4

Table 4.2: Fluorescence lifetime kinetic values for polymer micelles in mixtures of THF and H2O measured at λ_{em} = 425 nm and λ_{em} = 600 nm. Values are derived from third-order exponential decay fitting of raw decay curves.

In conjunction with DLS characterization, we measured each of the five samples with time-resolved fluorescence spectroscopy which we hypothesized would provide complementary information about local environmental differences near each end group. First, we confirmed the presence of both fluorescent end groups by measuring steady-state fluorescence spectra, exciting the 0% v/v THF sample at 345 nm and 450 nm, corresponding to the HDA and CA chain ends, respectively. Two independent emission peaks emerged, dependent on excitation wavelength, confirming dual-color fluorescent end group presence (**Figure 4.4D**). Next, we excited all five THF/water mixture samples at 390 nm with a picosecond pulsed diode laser and recorded their fluorescence lifetimes at two different emission wavelengths, 425 nm and 600 nm, corresponding to the HDA and CA chain ends, respectively. A trend analogous, but inverse, to the diameter data emerged for both end groups, with average fluorescence lifetimes remaining relatively constant from 0 to 50% v/v THF, transitioning to longer lifetimes at 75% v/v THF, and slightly decreasing from there at 100% v/v THF (**Figure 4.4E**).

Despite following the general diameter trend, the HDA end group's average fluorescence lifetime only fluctuates across a range of approximately 0.34 ns, while the CA end group's lifetime fluctuates across a considerably larger range of 5.5 ns. From 0 to 50% v/v THF, **P8** exists in a

micellar state, regardless of swelling and size differences, and thus the phenylethyl dithiomaleimide CA end group is hidden in the hydrophobic core of the micelle. Since the end group itself is hydrophobic we posit that, despite being buried in the core, it is better solvated and more freely rotating than when the micelle disassembles and the system enters a unimeric state at 75% v/v THF. Upon disassembly, the end group is no longer hidden from the polar THF/water environment, resulting in poorer solvation and a longer fluorescence lifetime. When the system oligomerizes at 100% v/v THF, the CA chain ends aggregate with each other and the hydrophobic **P8** blocks, decreasing its fluorescence lifetime. The **5**-functionalized HDA end group experiences significantly less perturbation across the THF/water paradigm due to its presence on the surface of the micelle. From 0 to 50% v/v THF in the micellar state, the end group exists at the interface of the micelle and solvent, either interacting with solvent molecules or nearby PEGMA chains and τ_{av} falls between 2.71 and 2.92 ns (**Figure 4.4E**, **Table 4.2**). When the micelle disassembles into unimers at 75% v/v THF, the HDA end group experiences a very modest increase in τ_{av} to 3.05 ns, possibly indicating that solvent shielding may be occurring, with one possible reason being proximity-related interactions with hydrophobic **P8** blocks. By 100% v/v THF, however, the τ_{av} returned back to the original range at 2.88 ns, potentially due to reorganization into a slightly more ordered oligomeric state.

The ability for time-resolved fluorescence spectroscopy to both corroborate physical characterization data (i.e. DLS) and provide added information about the assembly state of heterobifunctional **P8** encouraged us to explore if it could also be used to discern the micelle system's interaction with exogenous species. Nanosilver has been widely deployed as an antibacterial polymer additive and surface coating for medical device applications. However, it has recently come under scrutiny regarding its toxicity profile, bioaccumulation, and impact on

microbe populations. New methods of nanosilver detection are thus required. The proximity of a plasmonic species to a fluorophore is known to both enhance the intensity of fluorescence, while simultaneously decreasing the lifetime of emission, due to so-called metal-enhanced fluorescence (MEF).[234–236] We hypothesized that a hydrophobically-modified nanosilver species, like the kind that is doped into an antibacterial polymer, would be readily internalized into the hydrophobic core of the **P8** micelle and decrease the fluorescence lifetime of the core-localized dithiomaleimide fluorophore. Additionally, a hydrophillically-modified nanosilver species, would interact with the hydrophilic shell of the **P8** micelle and not interact with the core-localized dithiomaleimide fluorophore.

To test this hypothesis, we incubated a suspension of **P8** micelles in water at a constant 1 mg/mL concentration with increasing amounts of both hydrophobically-coated silver nanoparticles (C_{12} Ag NPs) and hydrophilically-coated silver nanoparticles (PVP Ag NPs) (**Figure 4.5A**, **C**) and measured the fluorescence lifetime of the system at both 425 nm and 600 nm to probe the shell and core emissive ends of the composite polymer. With regard to C_{12} Ag NP incubation, τ_1 and τ_2 values from lifetime measurements acquired at 425 nm did not change appreciably over the measurement range and the slight increase in α_1 from 0.9 to 1.0 was the main factor driving the decrease in τ_{av} (**Figure 4.7C**, **D**). **P8** incubation with PVP Ag NPs resulted in a similar trend when measured at 425 nm (**Figure 4.7E**, **F**), indicating that regardless of surface chemistry, Ag NPs do not have a large MEF effect on the shell fluorescent polymer end group.

Considerably more information can be drawn about this system through the consideration of the fluorescence lifetime measurements of the core dithiomaleimide-functionalized end group of the **P8** micelles. In the case of incubation with C_{12} Ag NPs, the lifetime decay curves measured at 600 nm exhibited a transition to shorter decays as C_{12} Ag NP concentration increased from 0-

250 ug/mL (**Figure 4.5B**). τ_1 decreased from 0.666 ns to 0.243 ns and α_1 increased from 0.780 to 0.991 (**Figure 4.5C**, **Table 4.3**), suggesting an increasing amount of plasmon-active Ag NPs in the micelle core which significantly decreased the fluorescence lifetime of core-localized fluorophore in a concentration-dependent manner via MEF. In the case of incubation with PVP Ag NPs, the lifetime decay curves measured at 600 nm did not change significantly as PVP Ag NP concentration increased (**Figure 4.5E**). τ_1 decreased from 0.831 ns to 0.578 and α_1 only increased from 0.727 to 0.833 (**Figure 4.5F**, **Table 4.3**). In both silver nanoparticle cases, τ_2, τ_3, α_2, and α_3 did not significantly contribute to τ_{av}. The observed significant differences in fluorescence lifetime behavior with increasing concentrations of C_{12} and PVP Ag NPs validated our hypothesis and suggests that time-resolved fluorescence spectroscopy is a practical, straightforward instrumental technique that provides characterization data about complex nanomaterial-environment interactions inaccessible to state-of-the-art techniques like DLS.

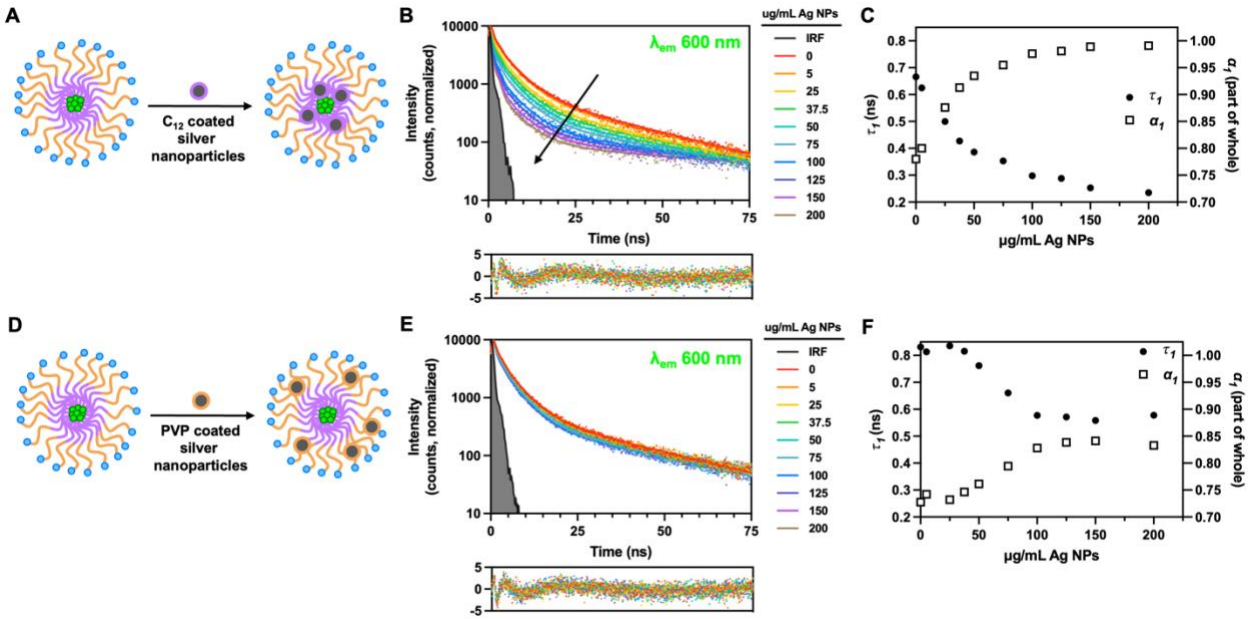

Figure 4.5: (A) **P8** polymer micelles mixed with C_{12}-coated hydrophobic silver nanoparticles, (B) fluorescence lifetime decays of polymer micelles mixed with increasing amounts of C_{12}-coated hydrophobic silver nanoparticles measured at λ_{em} = 600 nm, (C) τ_1 and α_1 of polymer micelles as a function of C_{12}-coated hydrophobic silver nanoparticle concentration measured at λ_{em} = 600 nm, (D) polymer micelles mixed with PVP-coated hydrophilic silver nanoparticles, (E) fluorescence lifetime decays of polymer micelles mixed with increasing amounts of PVP-coated hydrophilic silver nanoparticles measured at λ_{em} = 600 nm, and (F) τ_1 and α_1 of polymer micelles as a function of PVP-coated hydrophilic silver nanoparticle concentration measured at λ_{em} = 600 nm.

Ag NP coating	µg/mL Ag NPs	τ_1 (ns)	τ_2 (ns)	τ_3 (ns)	α_1	α_2	α_3	τ_{av} (ns)
C_{12}	0	0.666	5.26	29.7	0.780	0.193	0.0273	12.7
	5	0.625	5.25	30.0	0.800	0.177	0.0236	12.4
	25	0.500	5.20	32.3	0.876	0.111	0.0134	11.9
	37.5	0.427	5.28	36.1	0.913	0.0782	0.00850	12.1
	50	0.386	5.23	38.3	0.935	0.0590	0.00606	11.8
	75	0.353	5.36	43.5	0.955	0.0405	0.00406	12.3
	100	0.298	5.46	55.7	0.976	0.0219	0.00220	14.2
	125	0.288	5.26	61.4	0.981	0.0174	0.00176	15.0
	150	0.253	5.62	84.3	0.989	0.0103	0.00112	20.7
	200	0.235	5.45	91.1	0.991	0.00806	0.000873	21.1
PVP	0	0.831	4.95	30.1	0.727	0.248	0.0250	11.3
	5	0.814	5.00	31.4	0.742	0.236	0.0222	11.4
	25	0.836	4.99	32.2	0.732	0.245	0.0225	11.7
	37.5	0.816	4.97	32.0	0.747	0.232	0.0213	11.5
	50	0.762	4.92	32.2	0.761	0.220	0.0189	11.2
	75	0.660	4.81	32.7	0.794	0.190	0.0159	11.1
	100	0.578	4.71	33.2	0.828	0.159	0.0129	10.9
	125	0.571	4.73	33.5	0.838	0.149	0.0123	10.9
	150	0.559	4.75	35.7	0.841	0.147	0.0115	11.5
	200	0.578	4.81	40.2	0.833	0.155	0.0118	13.5

Table 4.3: Fluorescence lifetime kinetic values for polymer micelles incubated with increasing amounts of C12 and PVP coated silver nanoparticles measured at λ_{em} = 600 nm. Values are derived from third-order exponential decay fitting of raw decay curves.

4.6 Conclusions

We developed a heterobifunctional RAFT system to synthesize linear methacrylate-based polymers that can undergo HDA and CA reactions at their respective chain ends, via a thiocarbonyl (hetero-dienophile) and dibromomaleimide, respectively. CTA **4** was synthesized in three straightforward steps from 4,4-azobiscyanovaleric acid, a commonly used water-soluble radical initiator, and employed to polymerize hydrophobic, hydrophilic, and fluorinated methacrylic monomers, all of which exhibit low polydispersities approaching 1 and polymerize according to pseudo first-order kinetics. A homopolymer of triethylene glycol methyl ether methacrylate was used as a model substrate for orthogonal end group reactions, characterized by ^{1}H NMR and a dual-color fluorescence spectroscopic approach through the HDA cycloaddition of a fluorescent diene to the thiocarbonyl polymer end and the fluorogenic transformation of the

dibromomaleimide polymer end to a dithiomaleimide with a primary thiol. Amphiphilic, diblock copolymer **P7** was synthesized with chain transfer agent **4**, and functionalized with emissive moieties at both chain ends to yield P8. The dual-color end group labelling strategy provided insight into block copolymer assembly state across five binary THF/water solutions of varying volume ratios via time-resolved fluorescence spectroscopy, complementary to dynamic light scattering characterization. Finally, we used time-resolved fluorescence spectroscopy to detect the core internalization and shell association of hydrophobic and hydrophilic silver nanoparticles, respectively, with dual-color end group functionalized P8 micelles.

4.7 Supplementary Figures and Tables

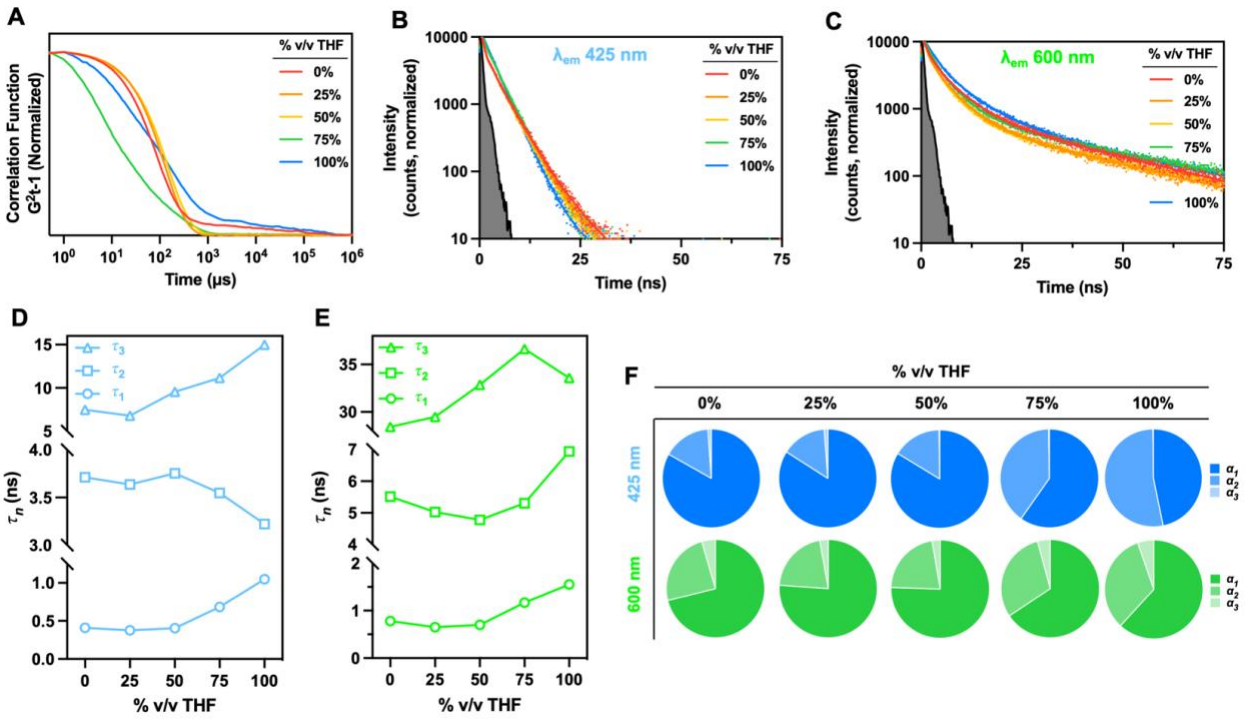

Figure 4.6: Supplemental to **Figure 4.3**. (A) DLS correlation functions of **P8** polymer micelles in varying % v/v THF/H_2O, (B) fluorescence lifetime decays of polymer micelles in varying % v/v THF/H_2O measured at λem 425 nm, (C) fluorescence lifetime decays of polymer micelles in varying % v/v THF/H_2O measured at λ_{em} = 600 nm, (D) τ_1, τ_2, and τ_3 component lifetimes of polymer micelles in varying % v/v THF/H_2O measured at λ_{em} = 425 nm, (E) τ_1, τ_2, and τ_3 component lifetimes of polymer micelles in varying % v/v THF/H_2O measured at λ_{em} = 600 nm, and (F) α_1, α_2, and α_3 lifetime weights of polymer micelles in varying % v/v THF/H_2O plotted as parts of a whole.

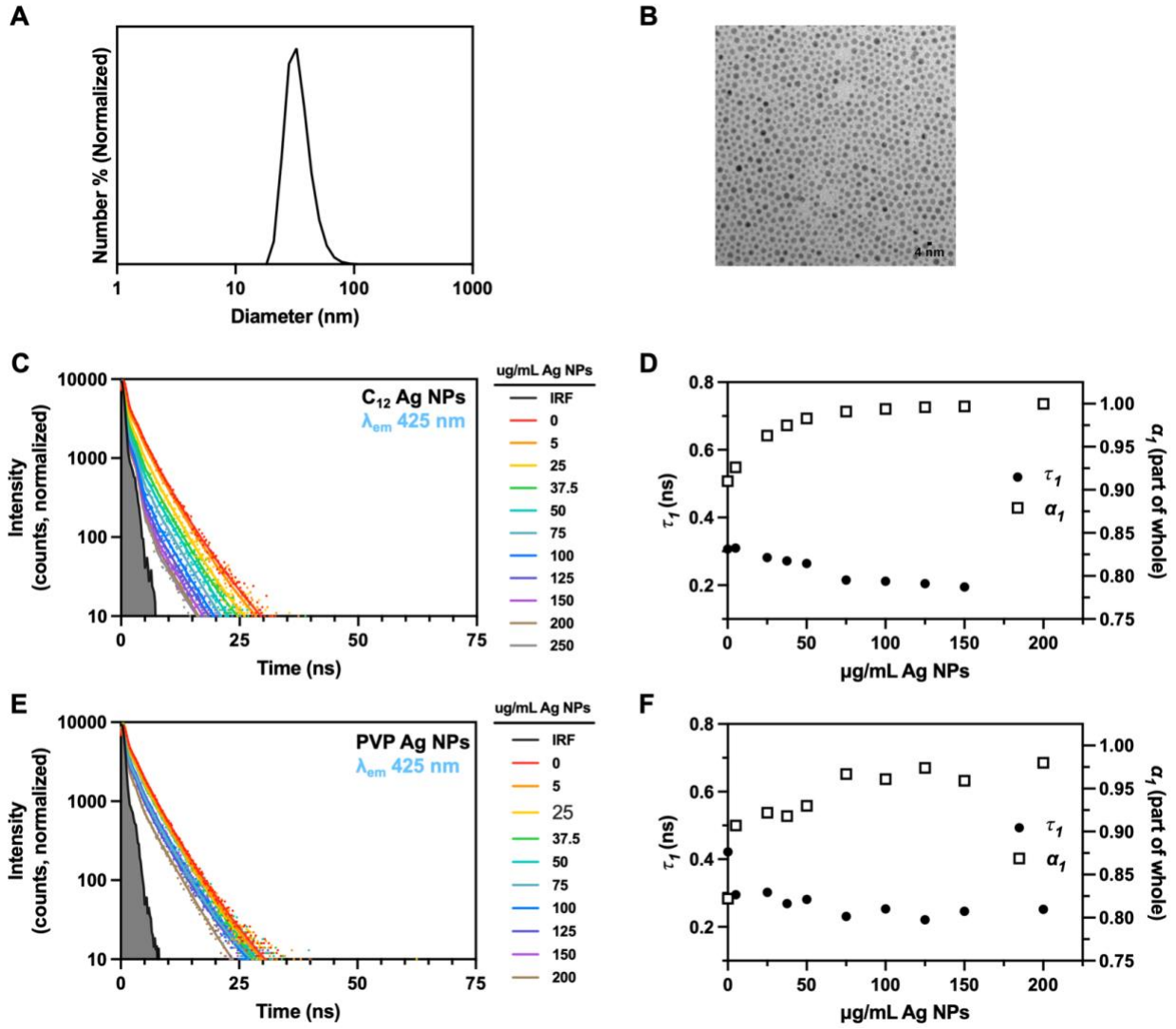

Figure 4.7: Supplemental to **Figure 4.4**. (A) DLS trace of **P8** polymer micelles in H_2O prior to silver nanoparticle addition, (B) TEM image of 4 nm C_{12} silver nanoparticles, (C) fluorescence lifetime decays of polymer micelles mixed with increasing amounts of C12 Ag NPs measured at λ_{em} = 425 nm, (D) τ_1 and α_1 of polymer micelles as a function of C_{12} Ag NP concentration measured at λ_{em} = 425 nm, (E) fluorescence lifetime decays of polymer micelles mixed with increasing amounts of PVP Ag NPs measured at λ_{em} = 425 nm, (F) τ_1 and α_1 of polymer micelles as a function of PVP Ag NP concentration measured at λ_{em} = 425 nm.

Chapter 5 – Summary

Over thirty years and billions of dollars in research and development expenditure later, the nanomedicine field has produced only three FDA approved nanoformulated gene therapies, all for very rare diseases with narrow clinical impact. Each of the three approved therapies are standard lipid nanoparticle formulations that do not employ active targeting mechanisms. The multifunctional, overengineered nanoparticle systems that pervade the scientific literature provide very little information to address the major obstacles the nanomedicine must overcome in order for widespread clinical adoption to occur. Several major questions in the nanomedicine field remain unanswered or under-answered, including but not limited to: Which chemical motifs and materials properties result in nanoparticle systems that target specific tissues and cell types? What type of nanomaterial should be chosen for a given application? How much of the injected dose actually accumulates at the target site? Is the enhanced permeability and retention (EPR) effect real or just theory? How reproducible are obtained biological results? Can the nanomaterial being studied be produced in a scalable manner?

These questions have failed to be answered due to the highly complex nature of nanomedicine formulations (across many orders of magnitude of length scales) and the biological interactions and barriers that must be overcome for successful payload delivery to a target site. Three major technical barriers previously mentioned in the abstract of this dissertation stand in the way of the successful clinical translation of nanomedicines: 1) the chemical and materials design space for the rational engineering of nanoparticle delivery systems is highly complex and multidimensional so the design specifics of an appropriate nanoparticle for a given therapeutic

application is unclear, 2) after administration, the successful delivery of a nanoparticle's therapeutic payload to the target physiological site requires a coordinated spatiotemporal interaction and negotiation with complex biological environments and barriers, and 3) state-of-the-art analytical tools and methods provide limited insight into how the chemical and materials properties of a nanoparticle delivery system interact with those complex biological environments. In this dissertation, time-resolved fluorescence spectroscopy (TRFS) is presented as a readily accessible, cheap, and high-throughput method for the study of nanoparticle formulations, providing insight into nanoparticle formulation design, nanoparticle-environment interactions, nanoparticle architecture, and nanoparticle assembly inaccessible to characterization methods like dynamic light scattering and electron microscopy, which only provide information about physical properties like hydrodynamic diameter and morphology.

In Chapter 1, an overview of the nanomedicine field was discussed, focused on the main variables that one must consider when designing a nanoparticle delivery system. These variables include the chemistry used to synthesize nanomaterials, the four main categories of nanomaterials commonly employed in delivery applications, gene therapeutic payloads, biological barriers that nanomaterials must overcome for successful payload delivery, and the experimental methods available for the study of nanoparticle properties – with a focus on TRFS and how it complements state-of-the-art techniques.

In Chapter 2, a new, scalable method for the production of protein nanoparticles via photoreactive electrohydrodynamic jetting was introduced, which represents a four order of magnitude improvement in processing and purification time compared to previous methods. These production and processing improvements were enabled by designing a fluorescent small molecule

photocrosslinker that both stabilizes protein nanoparticles and reports on the stability, crosslinking density, and size of protein nanoparticle formulations via TRFS.

In Chapter 3, the reactive valency of the fluorescent photocrosslinker developed in Chapter 2 was increased and other reactive variants were synthesized which enabled the production of polymer nanoparticles, in addition to protein nanoparticles. TRFS was used to probe how both protein and polymer nanoparticles responded to different chemical environments and it was found that protein nanoparticles, in particular, exhibit order of magnitude differences in fluorescence lifetime across chemical environments of an orientation polarizability range of 0.307. Additionally, protein nanoparticles stabilized with the fluorescent photocrosslinker developed in this chapter sensed differences in loading configuration of small molecule cancer therapeutic paclitaxel.

In Chapter 4, a heterobifunctional linear RAFT polymer system was developed that could undergo orthogonal end group conjugations via a Hetero-Diels–Alder reaction or a nucleophilic conjugate addition at the ends of the polymer. Several linear, monodisperse polymers were prepared from methacrylic monomers of diverse chemistries were synthesized and the kinetics of polymerization were characterized, indicating that all monomers polymerized according to pseudo-first order kinetics. Two different color fluorescent probes were conjugated to the functional ends of an 18 kDa poly(triethylene glycol methyl ether methacrylate) polymer to confirm end group reactivity, confirmed by TRFS. An amphiphilic block copolymer was synthesized, end group conjugated with the two different color probes, and the assembly state of the polymer was characterized with TRFS across selective and non-selective solvents. Finally, TRFS was used to probe the interaction of the amphiphilic block copolymer assembled into a micelle with hydrophilic and hydrophobic exogenous nanosilver.

A variety of nanoparticle properties inaccessible to state-of-the-art methods were probed using TRFS in this dissertation in an *ex vitro* setting, laying the foundation for *in vitro* and *in vivo* studies of nanoparticle-biology interactions in the future. TRFS can be coupled with microscopy to provide lifetime mapping in a spatial context via fluorescence lifetime imaging microscopy (FLIM) and the nanoparticles studied in this dissertation in an *ex vitro* context can easily be studied in an *in vitro* context. TRFS was used to measure the fluorescence lifetime of nanoparticles in diverse chemical environments and assembly states in this dissertation and order of magnitude differences in lifetime were recorded. In a biological setting, the range of lifetimes measured, for instance, in a single microscope image, will most likely not measure across an order of magnitude. However, we do expect to observe lifetime differences in biochemically distinct inter- and extracellular locations. The fluorescence lifetime of a nanoparticle in the extracellular matrix will certainly be different than in an endosome or in the cytosol due to differences in pH, viscosity, and polarity. We anticipate that studying nanoparticle uptake with FLIM will provide nuanced information regarding how certain materials interact with different stages of barrier interaction and transport, not accessible to typical microscopic assays.

Furthermore, because FLIM images can be acquired in well plates, we anticipate that libraries of chemically diverse nanoparticles stabilized with fluorescent crosslinkers can be screened in parallel in a straightforward manner. The data obtained from these images will be more complex, more multidimensional, and more informative than typical biological well plate assays, which generally use the average fluorescence emission intensity in a single well as the readout to study attributes of the nanoparticle delivery process, like nucleic acid transfection efficiency. The considerably larger amount of data obtained from FLIM measurements unlocks the potential to employ deep learning and artificial intelligence methods for analysis. Overall, the approaches to

nanoparticle formulation detailed in this dissertation enabled through the rational design of fluorescent crosslinkers to suit specific preparation methods, coupled with measurement via TRFS, provide a new framework for the study and development of therapeutically relevant nanomaterials.

Appendices

Appendix A: Synthesis of Stimuli-Responsive, Fluorescent Crosslinkers for Material Crosslinking

Introduction

In addition to the tetravalent fluorescent photocrosslinkers developed in Chapter 3 (denoted as **4a** and **4b**), two analogous compounds were synthesized that contain stimuli-responsive bridge moieties instead of the previously reported non-degradable propyl bridge. These structures will not be published in a peer reviewed journal article, but they are novel and have never been reported before. In this appendix I will discuss the synthesis of both crosslinkers. **Figure AA1**, below, illustrates the two alternative crosslinkers to be discussed. One contains benzophenone reactive groups and a disulfide bridge moiety, degradable under reducing conditions (**3**), and the other contains methacrylate reactive groups and a ketal bridge moiety, degradable under acidic conditions (**6**).

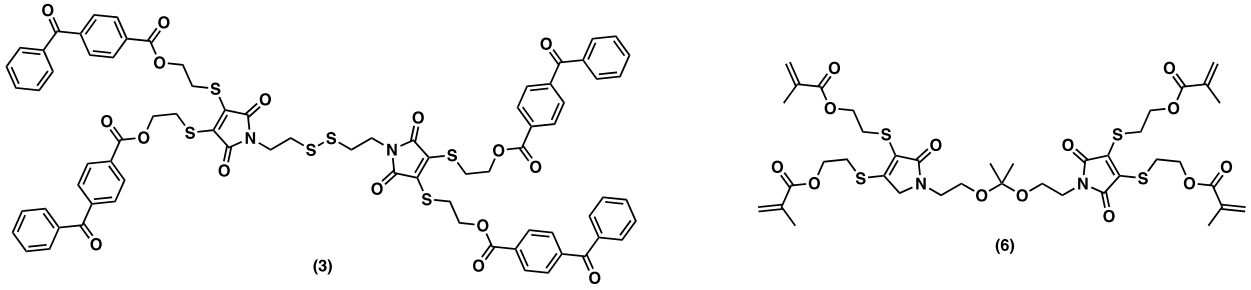

Figure A.1: Structures of stimuli-responsive, fluorescent crosslinkers synthesized in this appendix.

Disulfide-containing, reducible photocrosslinker

The synthesis of the disulfide-containing, reducible photocrosslinker was accomplished in a three-step process, starting from 2,3-dibromomaleimide. **1** and **2** were synthesized as described

in Chapter 3. Finally, **2** was coupled to itself through the disubstitution reaction of bis(2-bromoethyl) disulfide to give tetravalent, disulfide-containing photocrosslinker **3**.

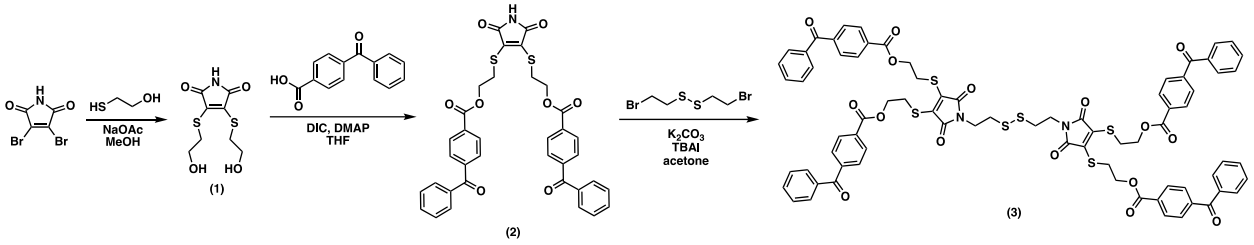

Figure A.2: Synthetic strategy to prepare disulfide-containing, reducible photocrosslinker **3**.

The synthetic protocol to synthesize **3** from **2** is as follows:

Bis(2-bromoethyl) disulfide (0.30 g, 1.8 mmol) was added to a stirring solution of **2** (0.6 g, 0.90 mmol), potassium carbonate (0.24 g, 1.8 mmol), and tetrabutylammonium iodide (0.033 g, 0.090 mmol) in acetone. Following overnight reaction at room temperature, insoluble salts were filtered off, acetone was removed by rotary evaporation, and the resulting brown oil was purified via normal-phase silica gel flash chromatography in 5% ethyl acetate in toluene to isolate the product.

HRMS (ESI-TOF): calc'd for $[M+K]^+$ 1488.63, found 1488.19

^{1}H NMR (500 MHz, $CDCl_3$):

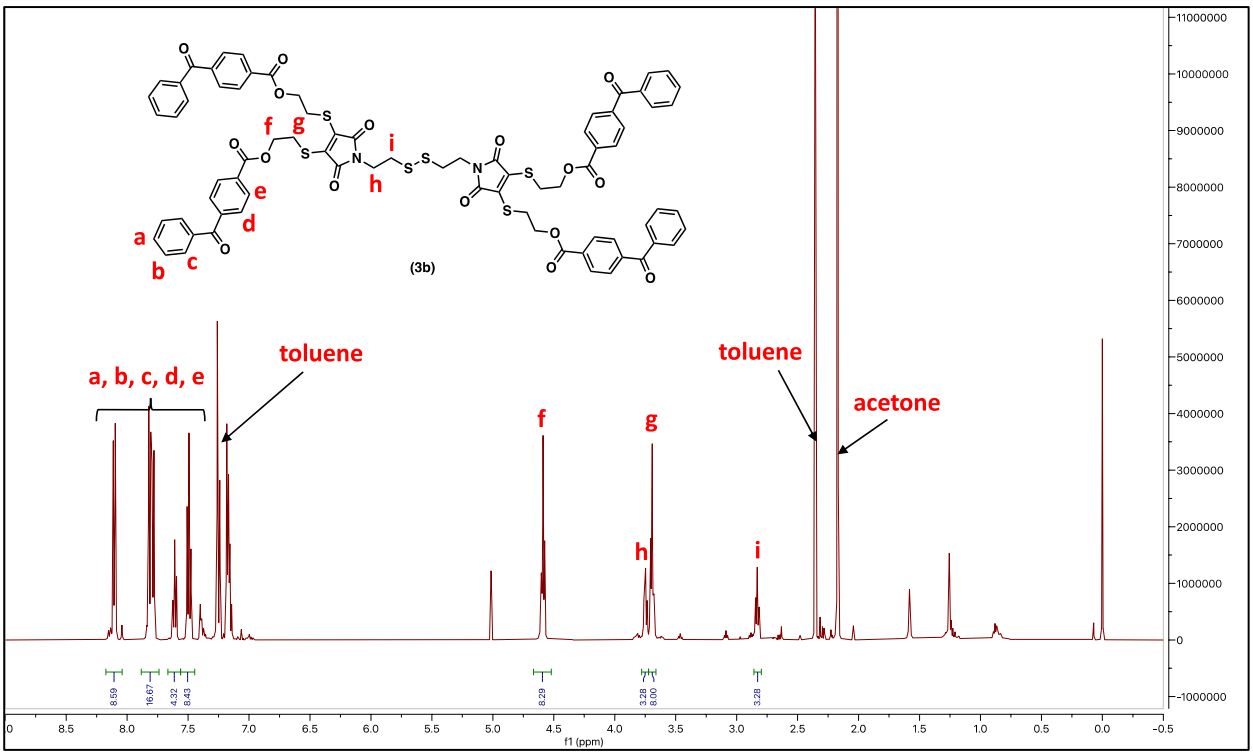

Figure A.3: 1H NMR spectrum of reducible photocrosslinker.

Optical spectroscopy:

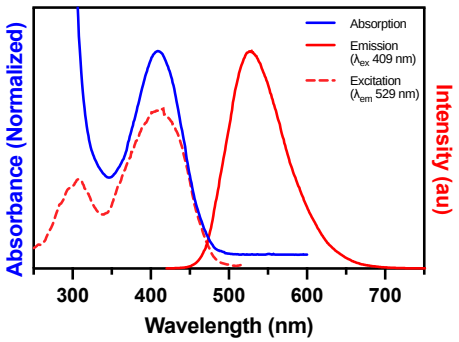

Figure A.4: Optical spectra of reducible photocrosslinker.

Ketal-containing, acid-degradable crosslinker

The synthesis of the ketal-containing, acid degradable crosslinker was accomplished in a four-step process, starting from 2,3-dibromomaleimide. **1**, **4**, and **5** were synthesized as described in Chapter 3.

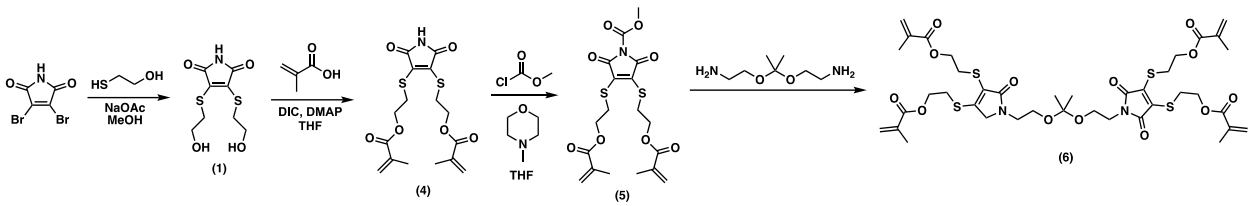

Figure A.5: Synthetic strategy to prepare ketal-containing, acid-degradable crosslinker **6**.

The synthetic protocol to synthesize **6** from **5** is as follows:

2,2-bis(aminoethoxy)propane (0.040 mL, 0.25 mmol) was added to a stirring solution of **5** (0.22 g, 0.50 mmol) dissolved in dichloromethane. The reaction mixture was allowed to stir overnight at room temperature. Dichloromethane was removed via rotary evaporation and the resulting oil was purified via normal-phase silica gel flash chromatography in 1:3 ethyl acetate:toluene to isolate the product.

HRMS (ESI-TOF): calc'd for $[M+Na]^+$ 921.20, found 921.20

^{1}H NMR (500 MHz, $CDCl_3$):

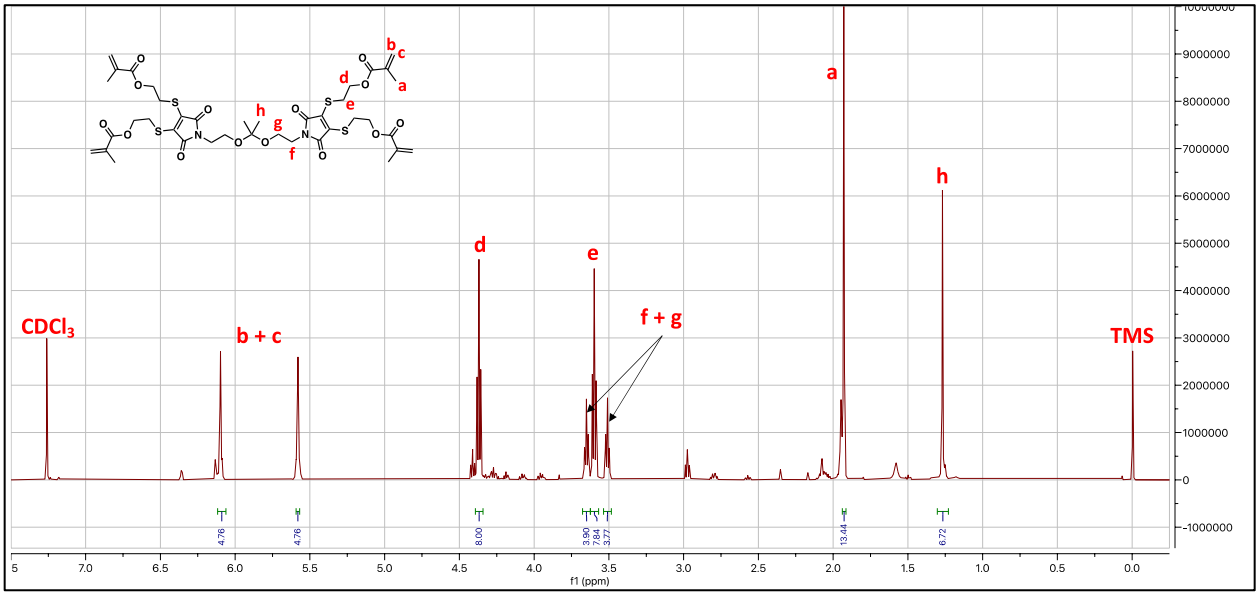

Figure A.6: 1H NMR spectrum of acid-degradable methacrylate crosslinker.

Optical spectroscopy:

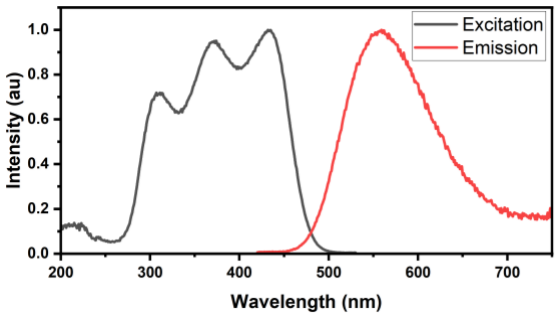

Figure A.7: Optical spectra of acid-degradable methacrylate crosslinker.

The presence of three excitation bands is a result of a sample that was too concentrated. At more dilute concentrations, the excitation spectrum resembles the excitation spectrum reported for **3**.

Appendix B: Failed Approaches and Alternative Strategies to Heterobifunctional RAFT Polymer Design and Synthesis

Several strategies for the synthesis of heterobifunctional RAFT agents (chain transfer agents, CTAs), and therefore, polymers, were pursued prior to the synthesis of CTA **4** reported in Chapter 4 of this dissertation. While the synthesis of several heterobifuntional CTAs were successful, following polymerization with methacrylic monomers and purification, these CTAs proved difficult to end group functionalize via their chosen end group chemistries. In this appendix, I will summarize these systems and provide some commentary regarding the challenges I faced in their end group functionalization. All CTAs synthesized contained the diethoxyphosphoryl moiety adjacent to a dithioester reported in Chapter 4 which activates the thiocarbonyl group as a dienophile in Hetero-Diels–Alder (HDA) reactions with dienes.

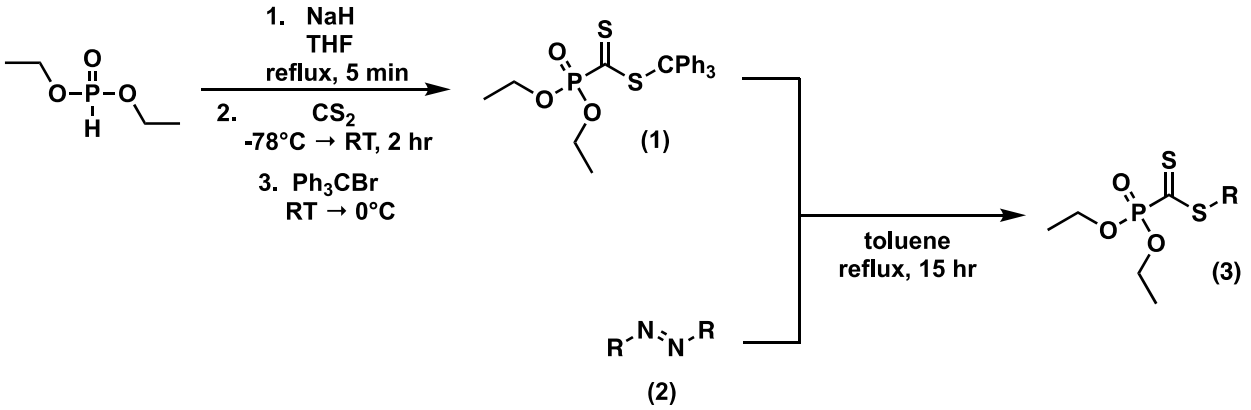

Figure B.1: General scheme for the synthesis of heterobifunctional CTAs.

Generally, the synthesis of heterobifunctional CTAs followed the strategy illustrated in **Figure AB1**, based on previously published radical exchange chemistry.[232] Triphenylmethyl diethoxyphosphoryldithioformate **1** was first synthesized in a three-step, one-pot reaction from

diethyl phosphite. General diazo-containing compound **2** was either purchased from a commercially available source or synthesized to contain the desired R functional group. **1** and **2** were refluxed in toluene to yield general heterobifunctional CTA **3** via a radical exchange reaction.

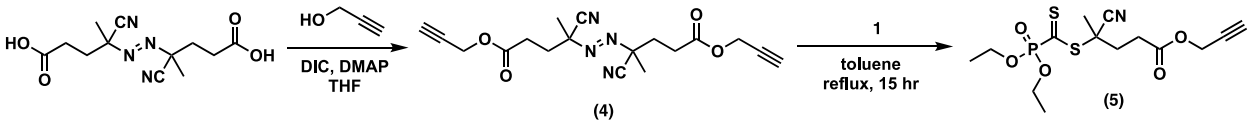

Figure B.2: Synthesis of heterobifunctional CTA **5**.

The first heterobifunctional CTA screened was **5** (**Figure AB2**), synthesized by first functionalizing 4,4-azobiscyanovaleric acid (ACVA) with linear alkyne-containing propargyl alcohol via a carbodiimide-mediated esterification to yield **4**, and finally through the radical exchange reaction with **1** to give **5**. **5** can perform HDA reactions via the left side of the compound through its thiocarbonyl dienophile and copper-catalyzed azide-alkyne click (CuAAC) reactions with azides via the right side of the compound. Preliminary experimentation showed that this molecule could successfully RAFT polymerize a variety of methacrylic monomers (**Figure AB3A**, **Table 12**). The kinetics of the RAFT polymerization of three monomers (n-butyl methacrylate (nBMA), triethylene glycol methyl ether methacrylate (TEGMA), and dimethylaminoethyl methacrylate (DMAEMA)) were characterized and each followed pseudo-first order kinetics, characteristic of RAFT polymerization (**Figure AB3B**, **C**).

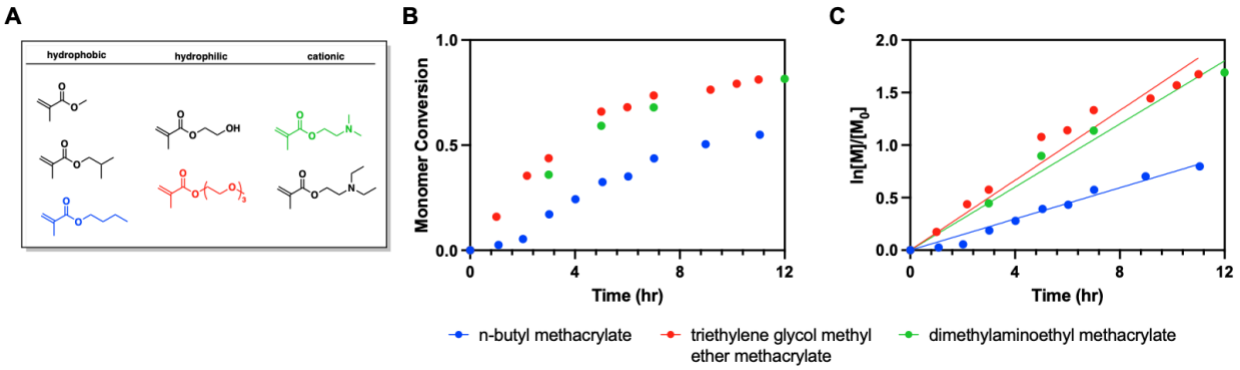

Figure B.3: (A) Methacrylic monomers synthesized with **5** via RAFT polymerization, (B) plot of monomer conversion vs. time, and (C) first-order kinetic plot of $\ln[M]/[M_0]$ vs. time.

Monomer	Conv. (%)	$M_{n,\ theo}$	$M_{n,\ GPC}$	$M_{w,\ GPC}$	$Đ_{GPC}$
n-butyl methacrylate	81	14,597	26,366	30,979	1.17
methyl methacrylate	76	10,389	13,427	14,995	1.12
iso-butyl methacrylate	76	14,597	24,051	29,355	1.22
triethylene glycol methyl ether methacrylate	87	20,377	13,820	16,357	1.18
dimethylaminoethyl methacrylate	85	13,722	-	-	-

Table B.1: Size exclusion chromatographic characterization data for methacrylic monomers polymerized via RAFT polymerization.

Following polymerization, the TEGMA polymer (**pTEGMA**) was subjected to end group reactions to demonstrate polymer heterobifunctionality. First, **pTEGMA** and acid-terminated diene **A** were reacted via HDA reaction to yield **A-pTEGMA** (**Figure AB4A**, middle polymer conjugate). Reaction success was monitored by the disappearance of the UV-vis band at 325 nm (**Figure AB4B**) and the appearance of ^{1}H NMR alkene peaks at 5.8 ppm (**Figure AB4D**). Finally, **A-pTEGMA** HDA conjugate and 3-azido-7-hydroxycoumarin (**B**), a fluorogenic dye that emits following reaction with an alkyne, were reacted via CuAAC reaction to yield fluorescent product **A-pTEGMA-B**. Successful click conjugation was monitored by the appearance of the emission band around 470 nm (**Figure AB4C**) and the appearance of ^{1}H NMR aromatic peaks (**Figure AB4D**).

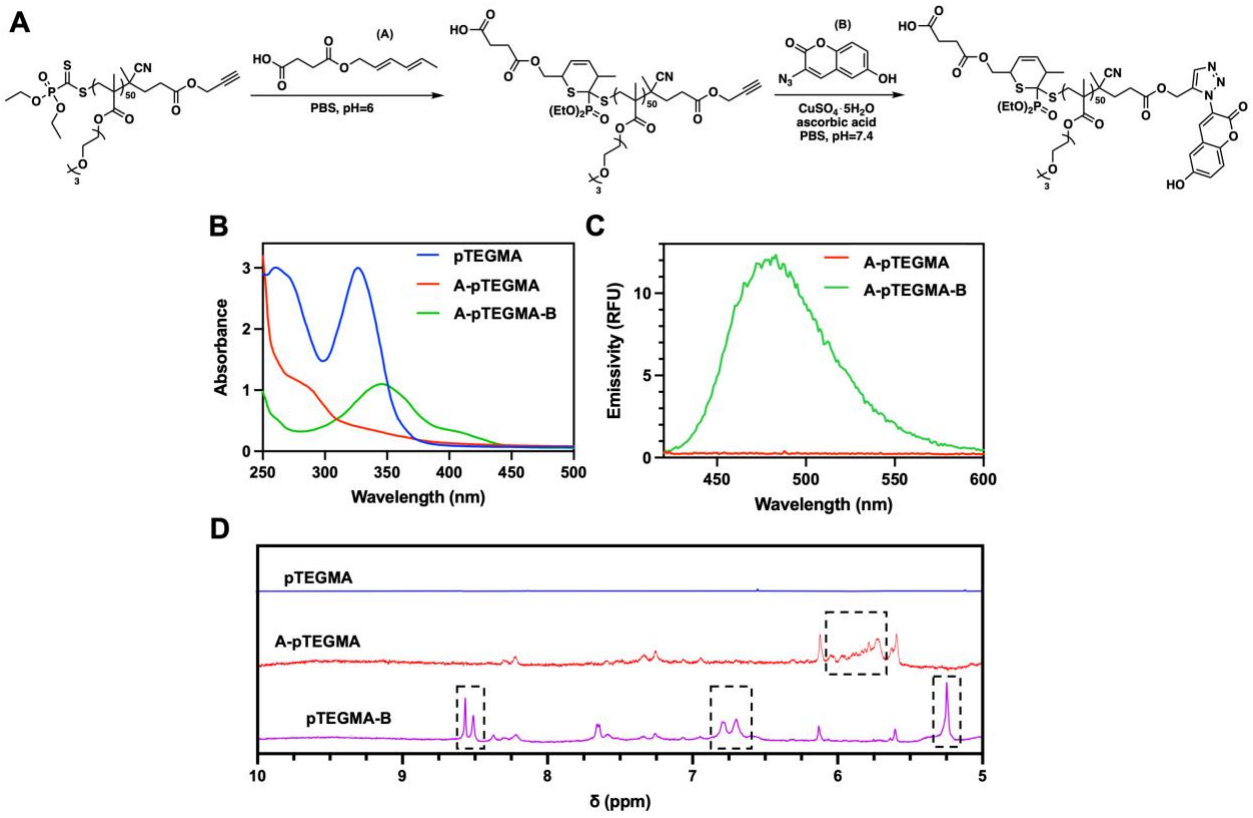

Figure B.4: (A) Scheme for the end group functionalization of heterobifunctional **pTEGMA** prepared from **5**, (B) UV-vis spectra of starting materials and products, (C) emission spectra for starting materials and products (λ_{ex} = 400 nm), and (D) ^{1}H NMR spectra of starting materials and products.

Unfortunately, however, these results could never be replicated, specifically regarding the click reaction. I tried a variety of copper-ligand and copper-reducing agent systems, including CuBr/PMDETA, CuBr/bipyridine, $CuSO_4 \cdot H_2O$/ascorbic acid, in a variety of solvents, including DMF, THF, DMSO, and water, and under dry and inert conditions, to no avail. The inability to perform CuAAC reactions with the **pTEGMA** synthesized from CTA **5** prompted me to redesign the CTA to include a functional group that can undergo click reactions and does not require a copper catalyst, which I suspected to be the culprit.

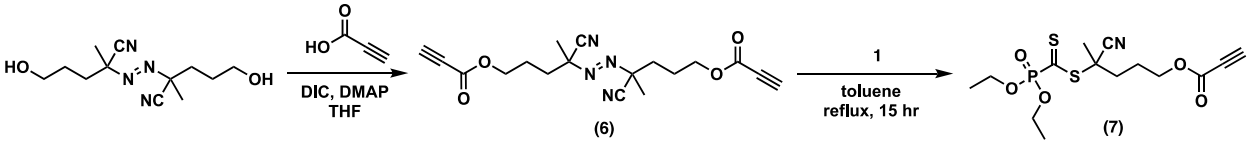

Figure B.5: Synthesis of heterobifunctional CTA **7**.

To mitigate this issue, I pursued an electron-deficient alkyne as the functional group additional to the thiocarbonyl dienophile. Electron-deficient alkynes have been shown to undergo copper-free click reactions and are considerably easier and cheaper to synthesize and ligate to macromolecular systems than dibenzocyclooctyne (DBCO) and bicyclononyne (BCN) groups and the Lahann Lab has experience implementing these functional groups in chemical vapor deposition polymerization-prepared functionalized paracyclophanes.[237–240] First, 4,4-azobis(4-cyano-1-pentanol) was reacted with propiolic acid via a carbodiimide-mediated esterification to yield **6**, which was refluxed with 1 to yield heterobifunctional CTA **7**. Despite the fact that the electron deficient alkyne does not require the use of a copper catalyst to click react with azides, I was not able to successfully perform click reactions with polymers synthesized from this CTA, despite troubleshooting across several solvents, reactant stoichiometries, and dry/inert conditions.

Next, I turned to the synthesis of an azide-containing CTA, assuming that maybe there was something intrinsic to the chemistry of **7** that might be interfering with its ability to click. First I synthesized **8** by reacting 3-azido-1-propanol with ACVA (**Figure AB5**). The radical exchange of **8** with **1** to yield target CTA **10** proved not successful. For the previous two CTAs synthesized, **5** and **7**, both products were a magenta color and a color change was observed over the course of the reaction as the royal blue color of **1** dissolved in toluene changed. In the case of this reaction, the blue color of **1** disappeared to a light-yellow color. TLC analysis showed a several products in the reaction mixture, none of which were identifiable after column chromatographic separation. An alternative approach to synthesize **10** was pursued, first by reacting ACVA with **1** to yield acid-terminated **9** and then functionalizing **9** with 3-azido-1-propanol to yield **10**. **9** was successfully synthesized and isolated according to a previously published report, but when reacted with 3-

azido-1-propanol, the same color change to a light-yellow was observed and target **10** could not be isolated.

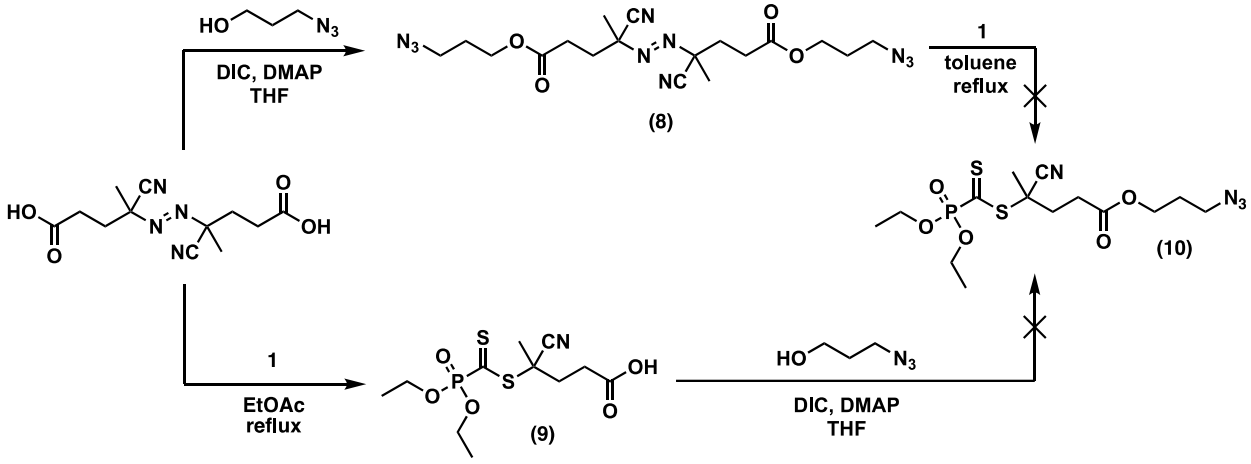

Figure B.6: Unsuccessful strategies for the synthesis of azide-containing heterobifunctional CTA **10**.

Finally, the synthesis of alcohol-terminated CTAs were attempted by reacting **1** with both 4,4-azobis(4-cyano-1-pentanol) and 2,2'-azobis(2-methyl-N-(2-hydroxyethyl)propionamide). Both reactions were unsuccessful, resulting in the color change of **1** from blue to light-yellow, similar to what was observed for the attempted synthesis of **10**. A summary of the structures of the successfully and unsuccessfully synthesized heterobifunctional CTAs is shown in **Figure AB6**.

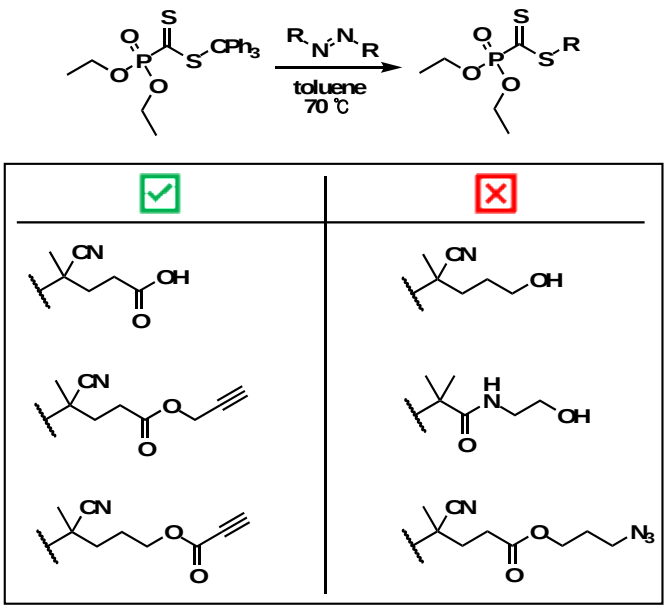

Figure B.7: Summary of heterobifunctional CTAs synthesized successfully and unsuccessfully.

The heterobifunctional CTA synthesized for the work performed in Chapter 4 of this dissertation was developed after screening the failed approaches outlined in this appendix.

Appendix C: Supplementary Figures Not Referenced in Chapter 3

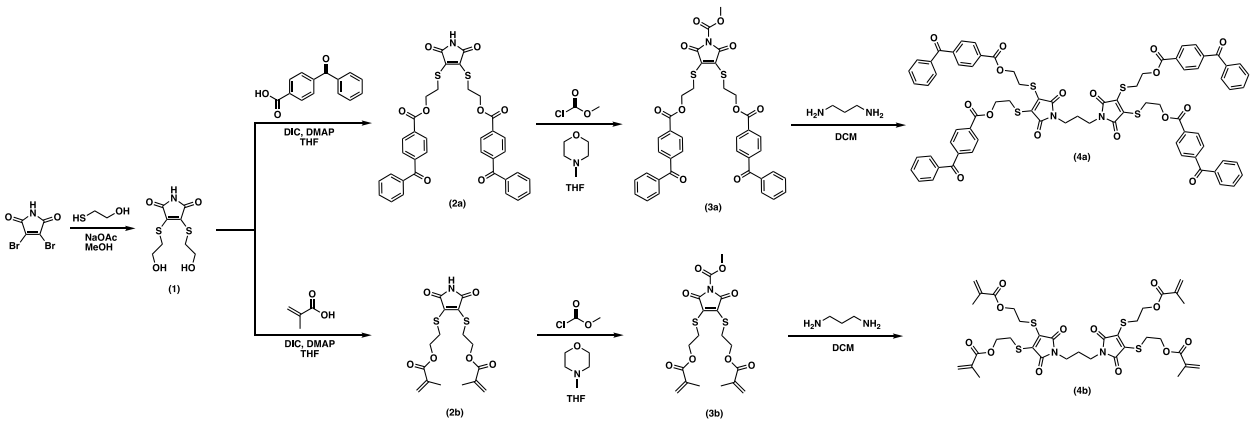

Figure C.1: Detailed reactive molecular reporter synthetic strategy.

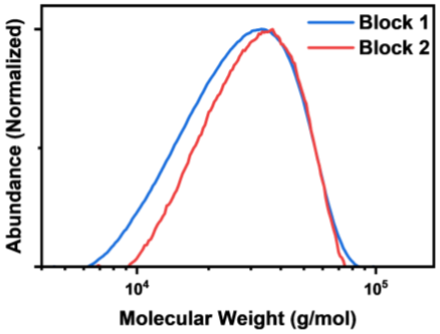

Figure C.2: Block copolymer characterization: SEC. Molecular weight distributions of poly(PEGMA) homopolymer (block 1, blue) and poly(BMA-b-PEGMA) diblock copolymer (block 2, red) calculated from SEC chromatograms.

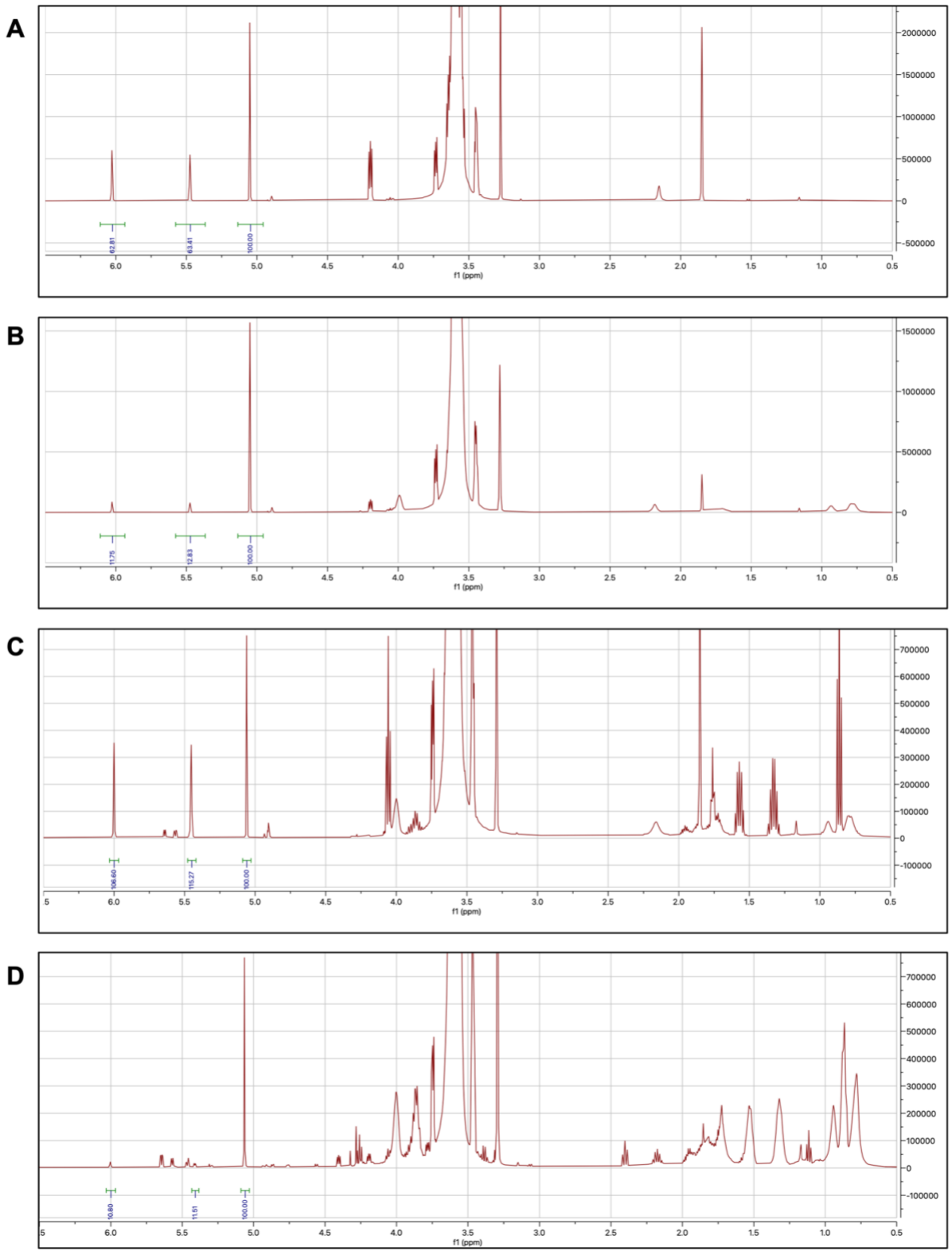

Figure C.3: Block copolymer characterization: ^{1}H NMR. (A) t_0 – pPEGMA homopolymer, (B) t_f – pPEGMA homopolymer, (C) t_0 – pPEGMA-pBMA diblock copolymer, and (D) t_f – pPEGMA-pBMA diblock copolymer. Methacrylate peaks are integrated relative to a trioxane internal standard (~5.1 ppm).

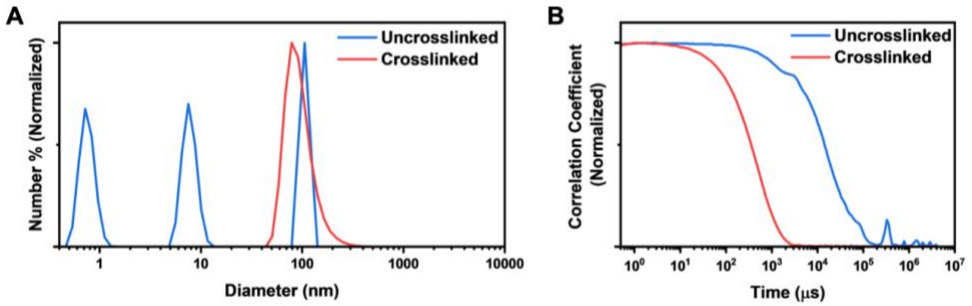

Figure C.4: Confirmation of **MC** core crosslinking. (A) DLS traces and (B) correlation functions of uncrosslinked and crosslinked BCPs. Samples were redispersed in DMSO following self-assembly in selective solvent (water) and subsequent evaporation of water. As expected, the uncrosslinked samples disaggregate in the non-selective solvent of DMSO, evidenced by a trimodal DLS distribution with peaks at 1 nm, 10 nm, and 100 nm, and a poor-quality correlation function. Crosslinked samples in DMSO are identical to the same sample measured in water (see **Figure 3.2 I**).

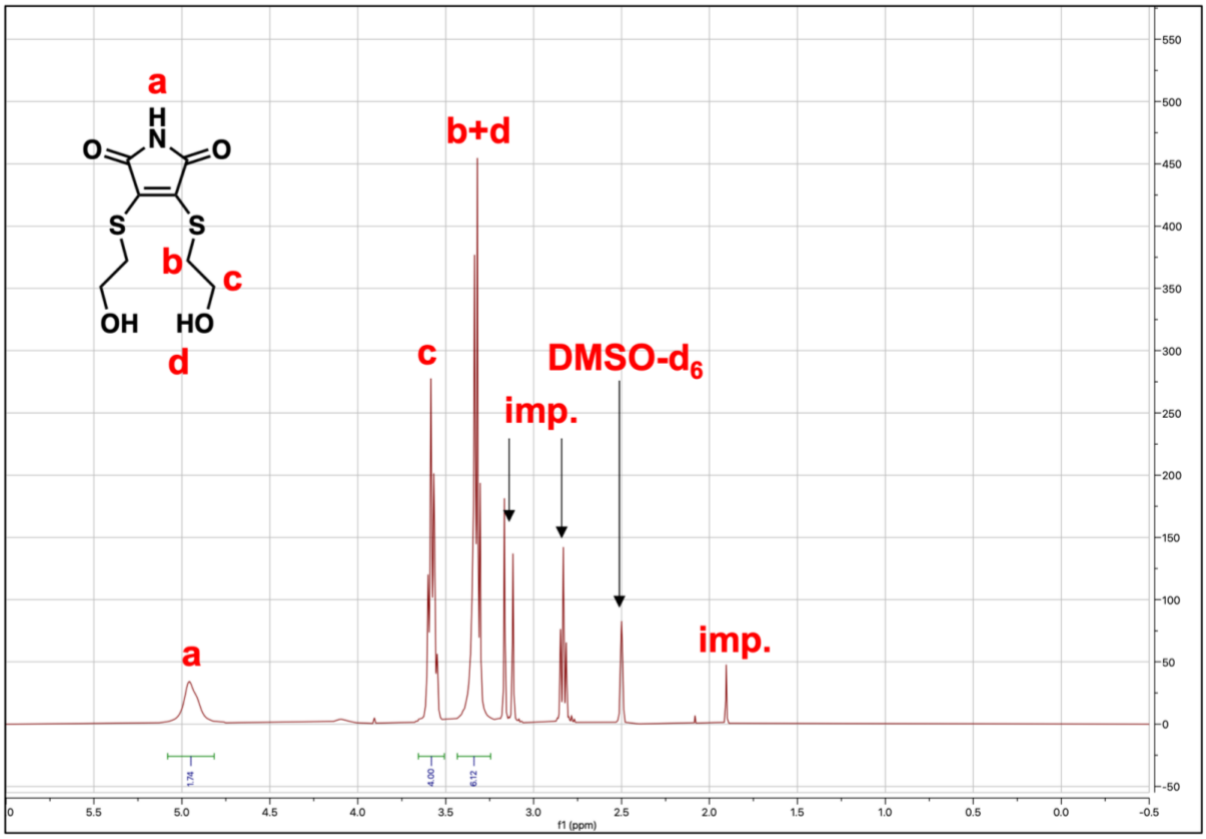

Figure C.5: ^{1}H NMR spectrum of **1** in DMSO-d_6.

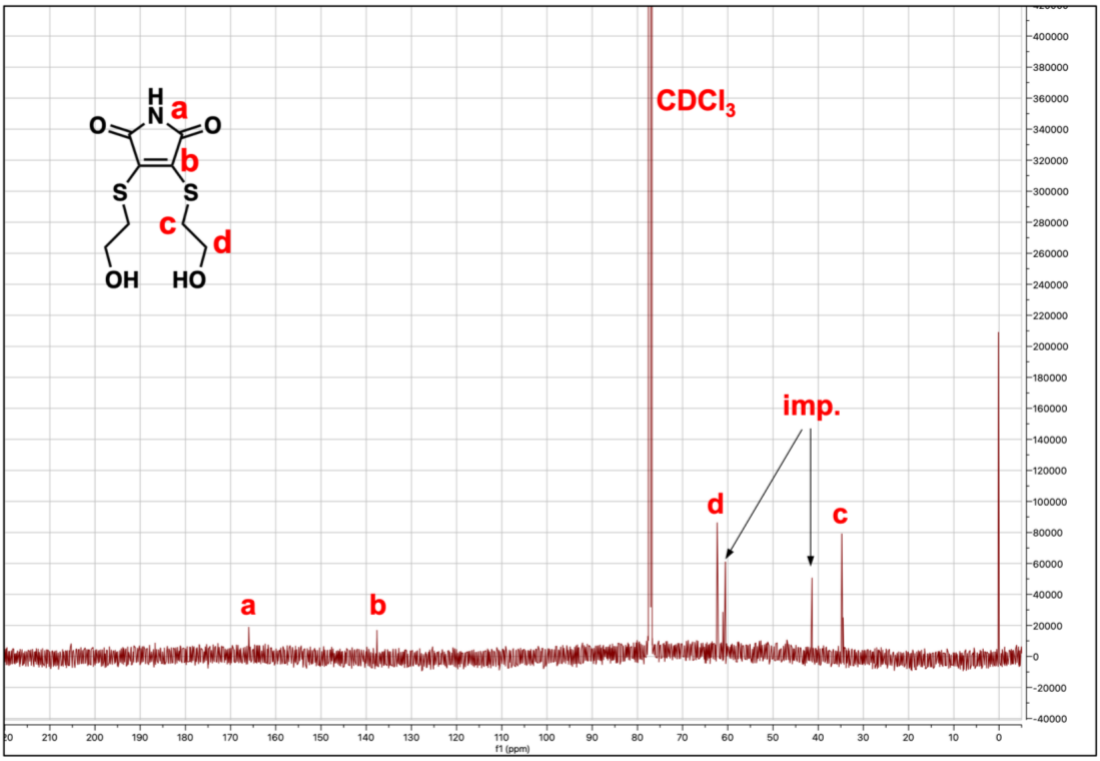

Figure C.6: ^{13}C NMR spectrum of **1** in $CDCl_3$.

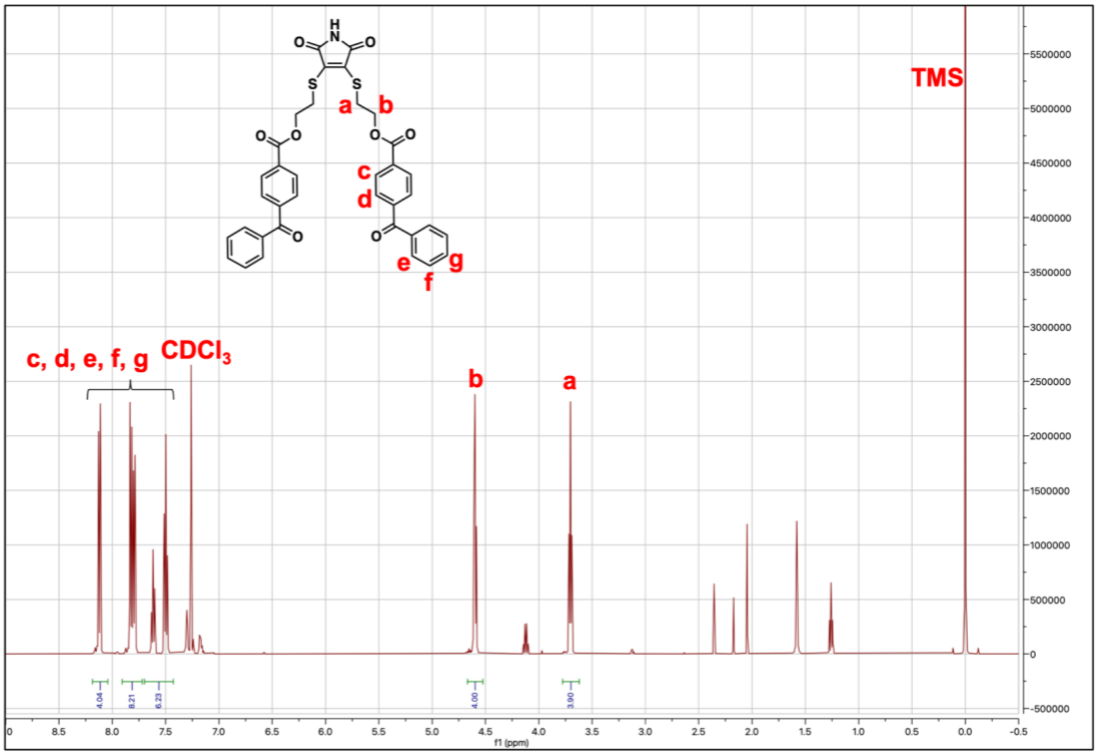

Figure C.7: ^{1}H NMR spectrum of **2a** in $CDCl_3$.

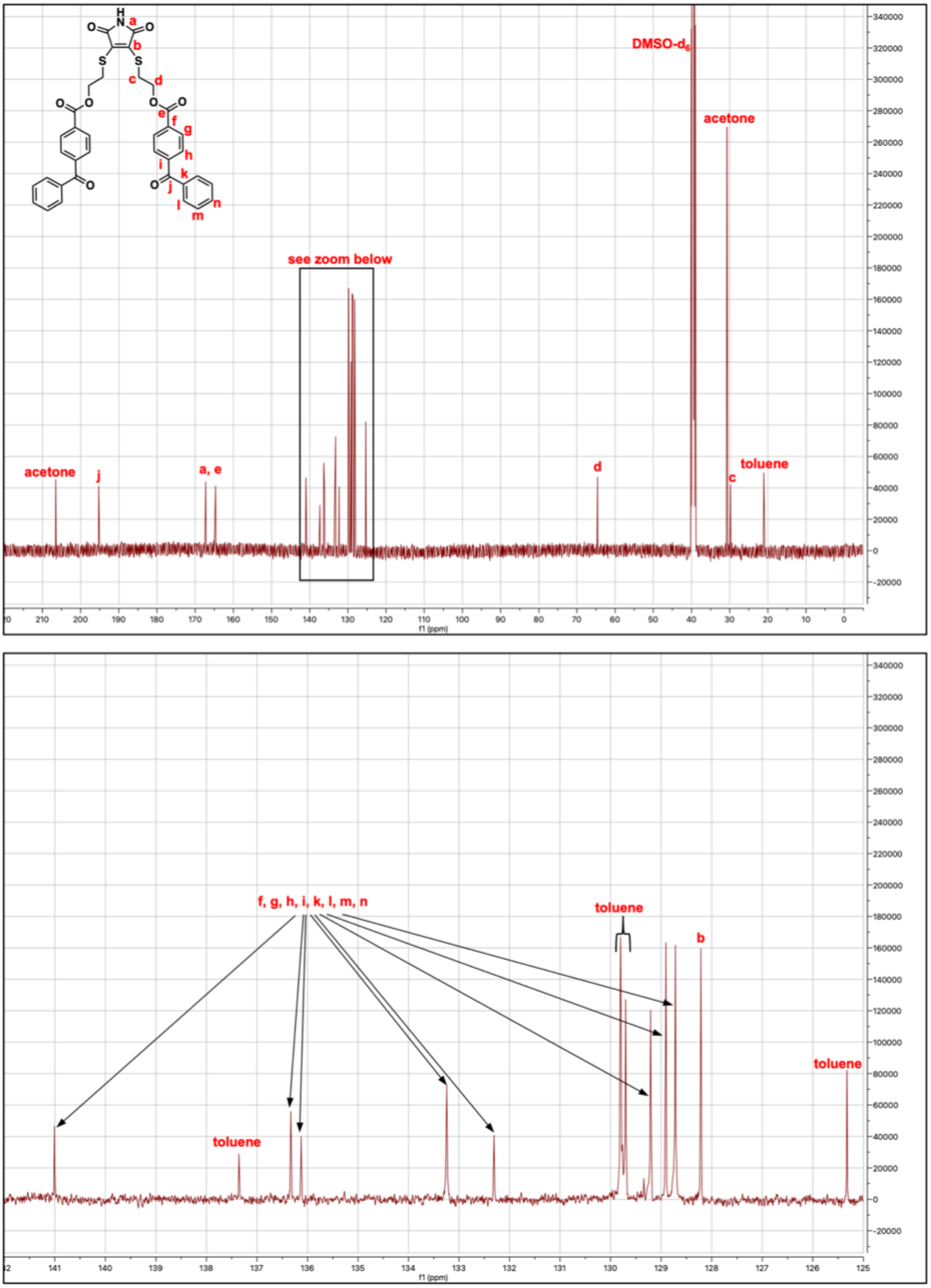

Figure C.8: ^{13}C NMR spectrum of **2a** in DMSO-d_6.

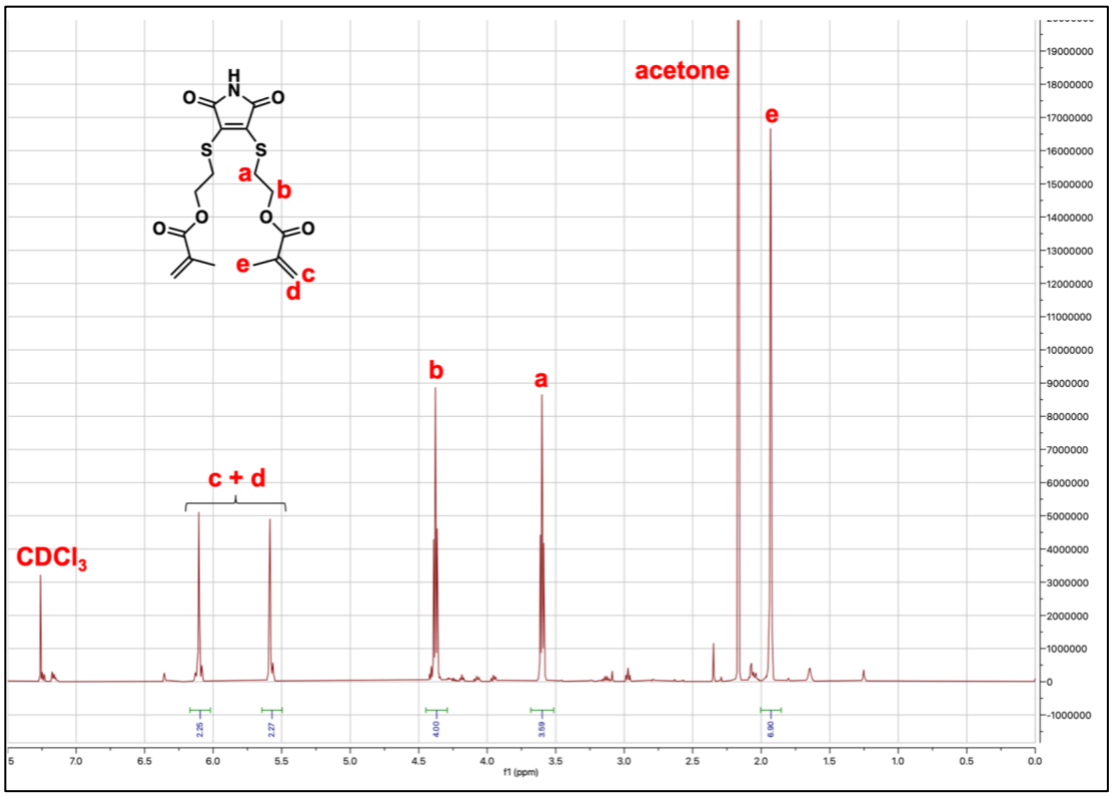

Figure C.9: ^{1}H NMR spectrum of **2b** in $CDCl_3$.

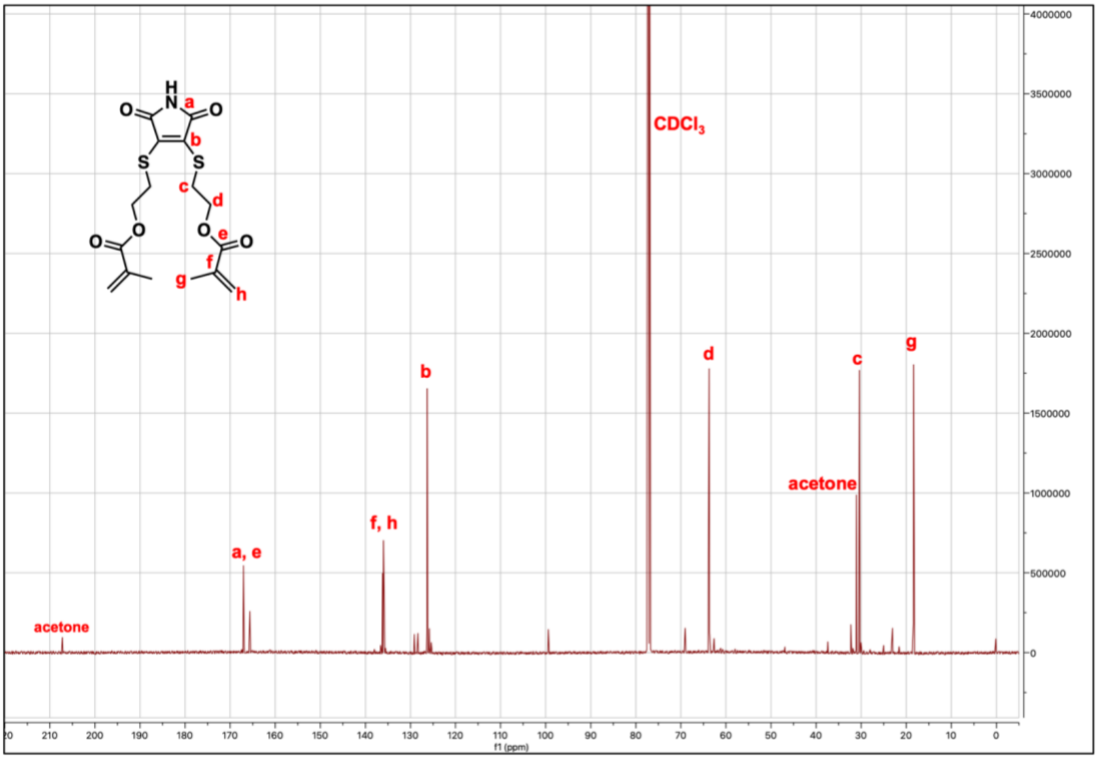

Figure C.10: ^{13}C NMR spectrum of **2b** in $CDCl_3$.

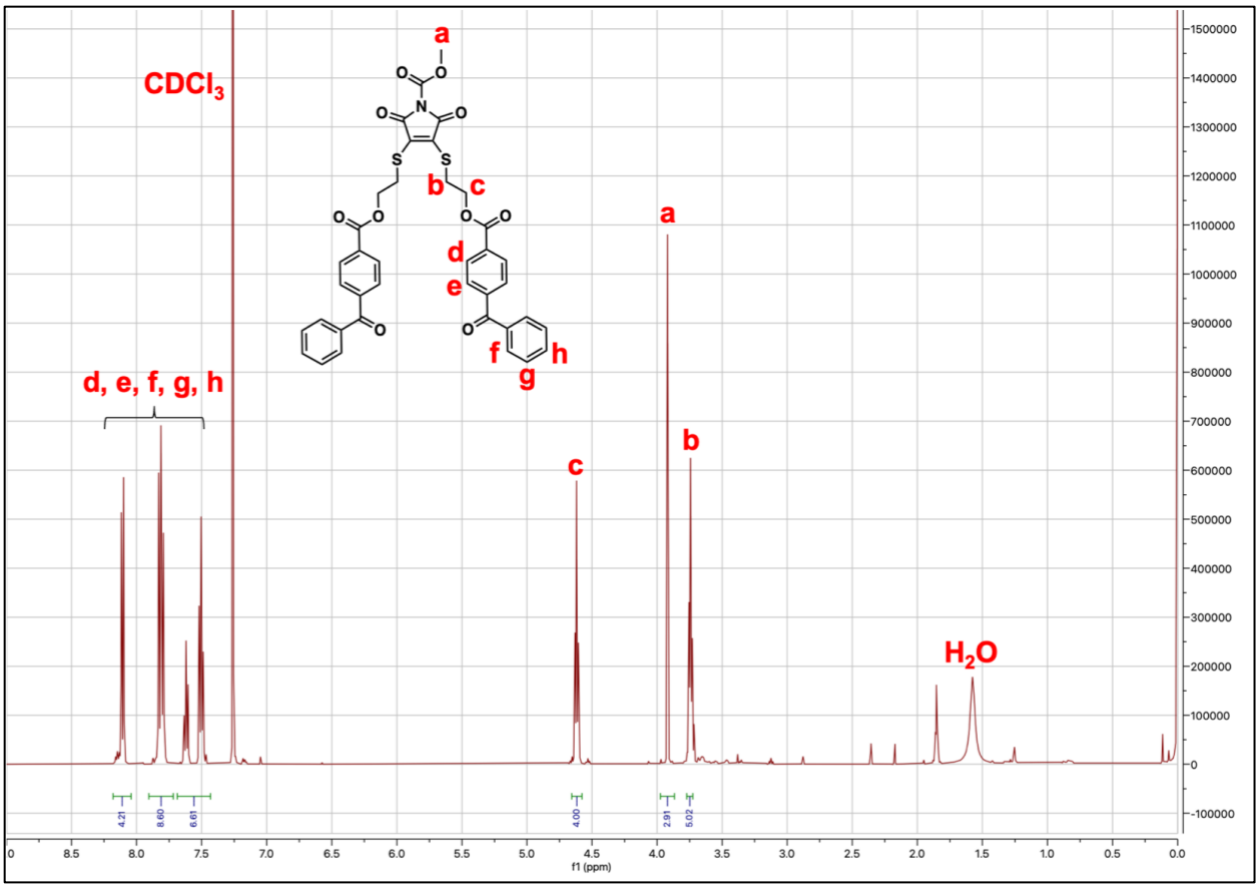

Figure C.11: ^{1}H NMR spectrum of **3a** in $CDCl_3$.

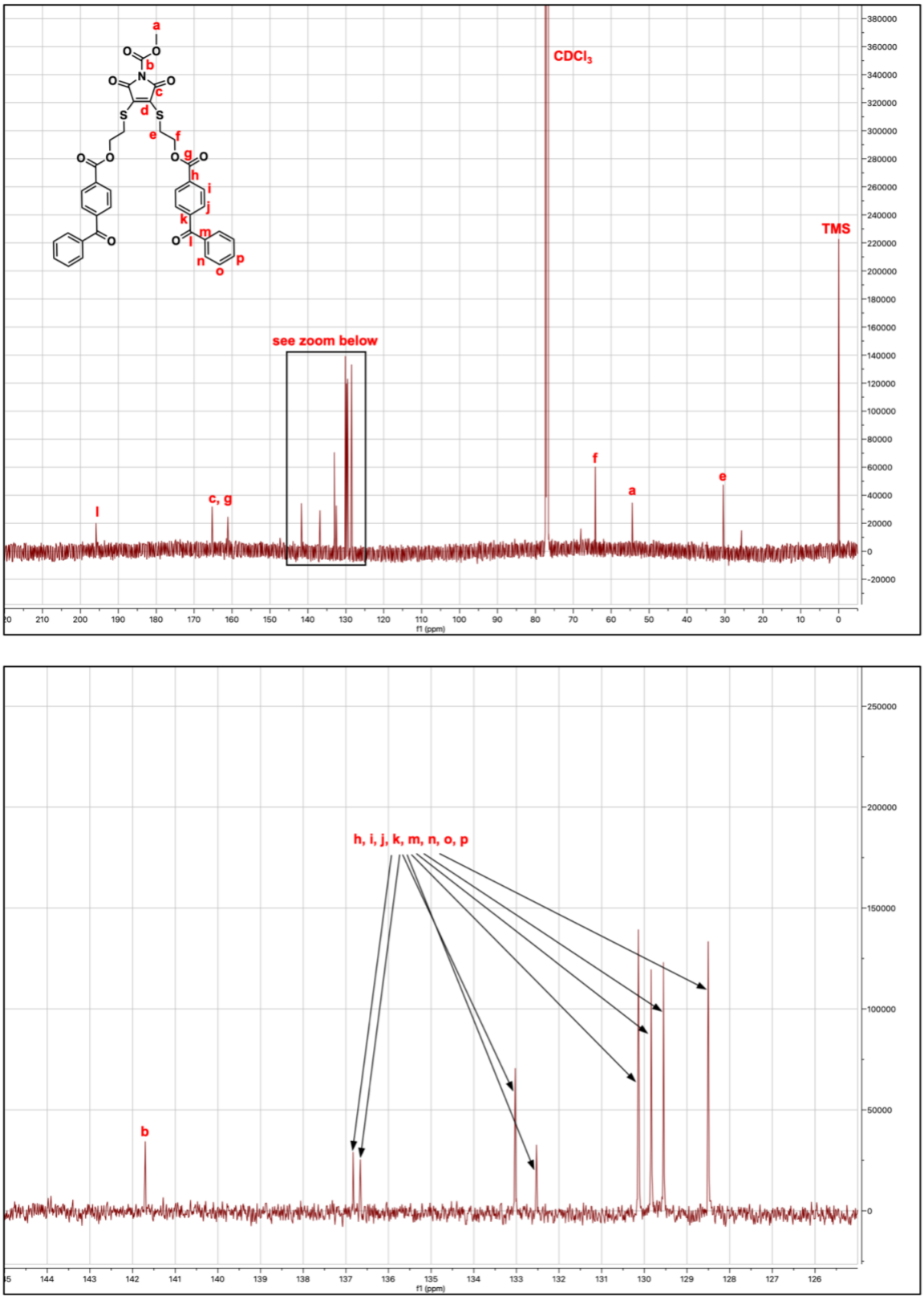

Figure C.12: ^{13}C NMR spectrum of **3a** in $CDCl_3$.

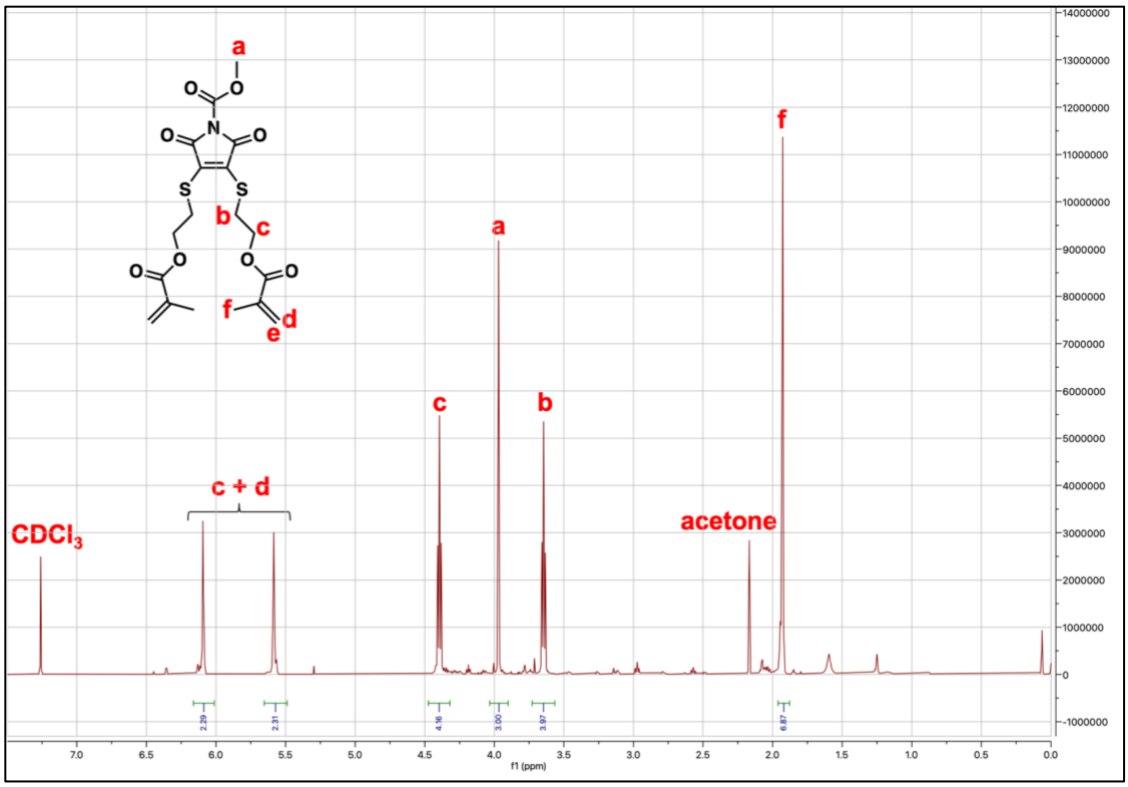

Figure C.13: ^{1}H NMR spectrum of **3b** in $CDCl_3$.

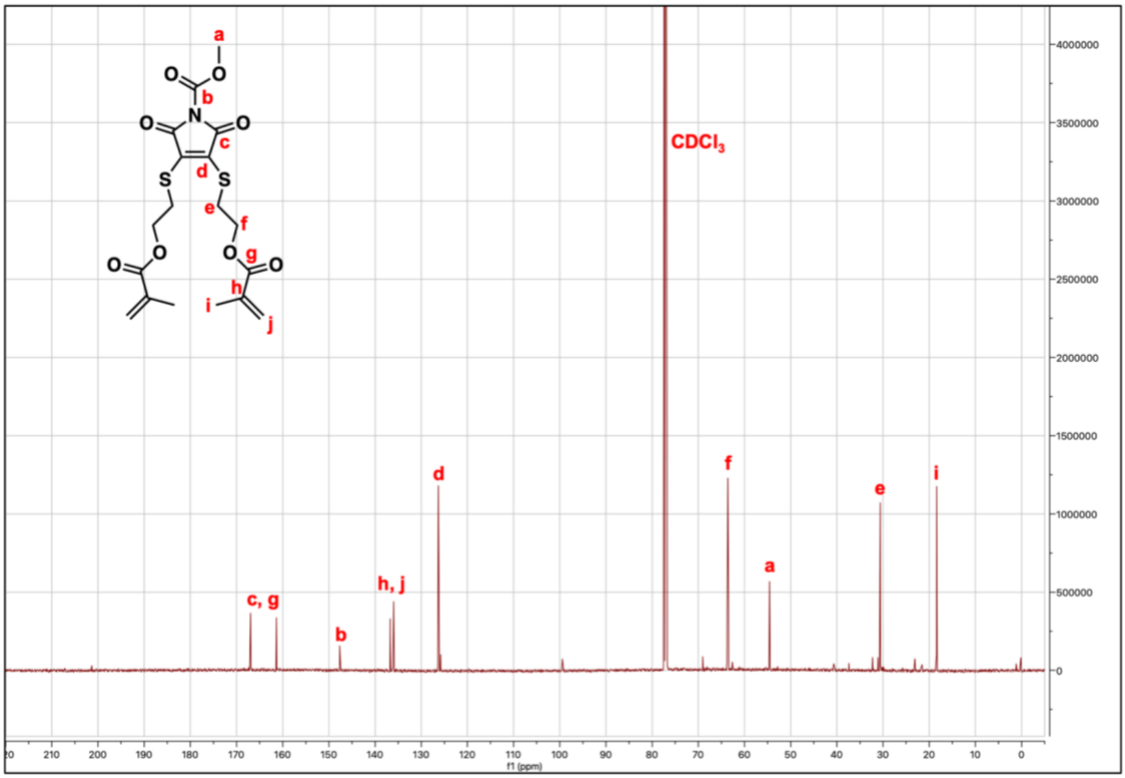

Figure C.14: ^{13}C NMR spectrum of **3b** in $CDCl_3$.

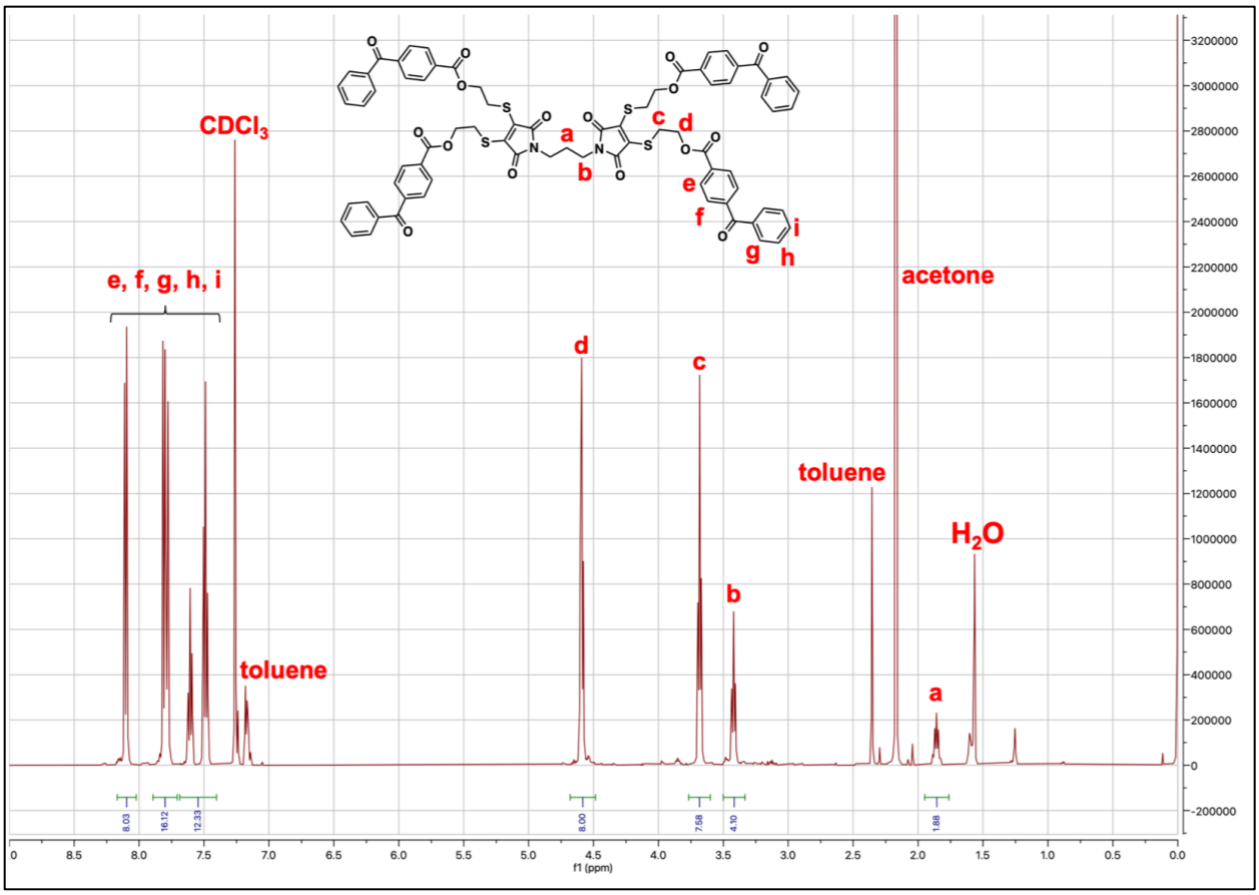

Figure C.15: ^{1}H NMR spectrum of **4a** in $CDCl_3$.

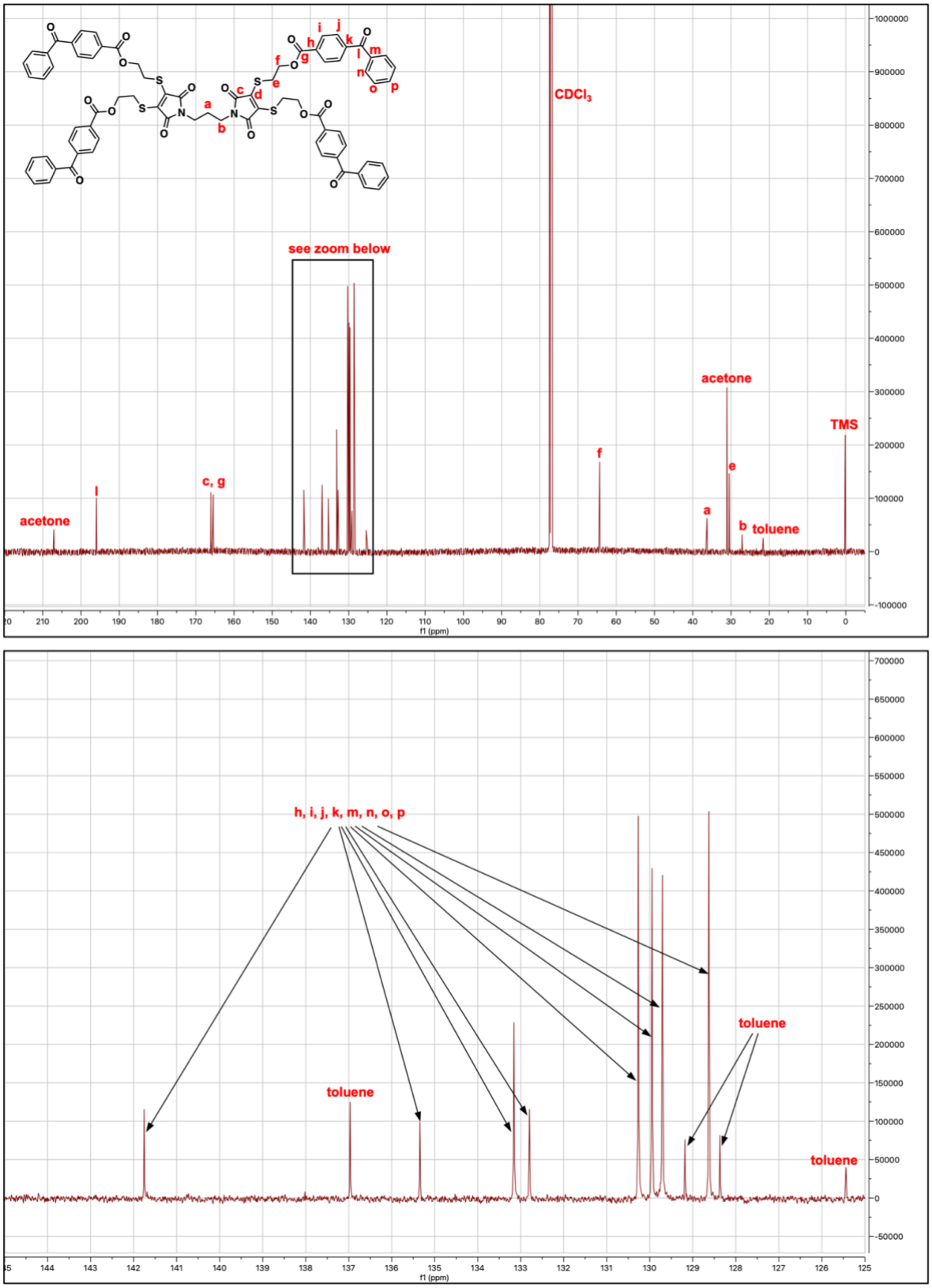

Figure C.16: ^{13}C NMR spectrum of **4a** in $CDCl_3$.

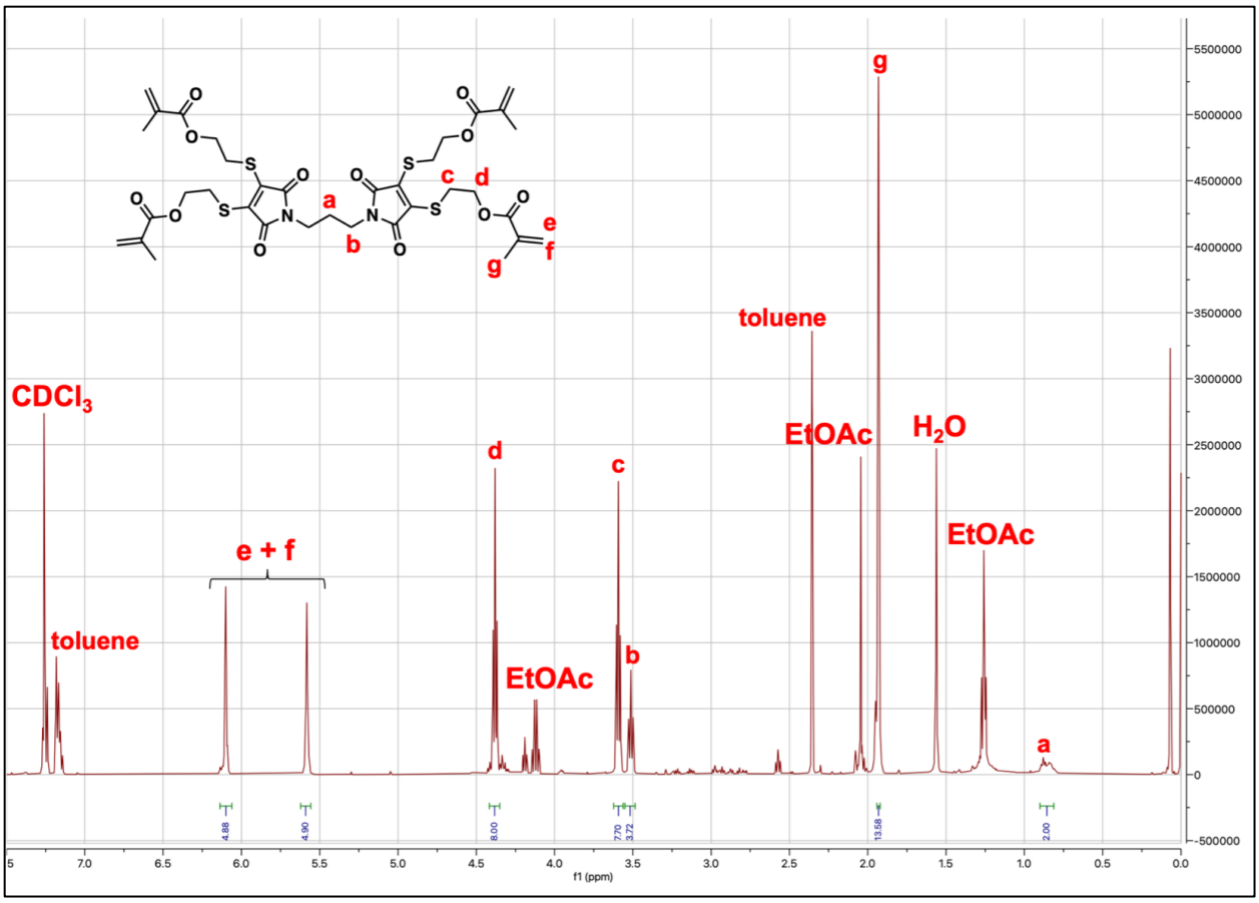

Figure C.17: ^{1}H NMR spectrum of **4b** in $CDCl_3$.

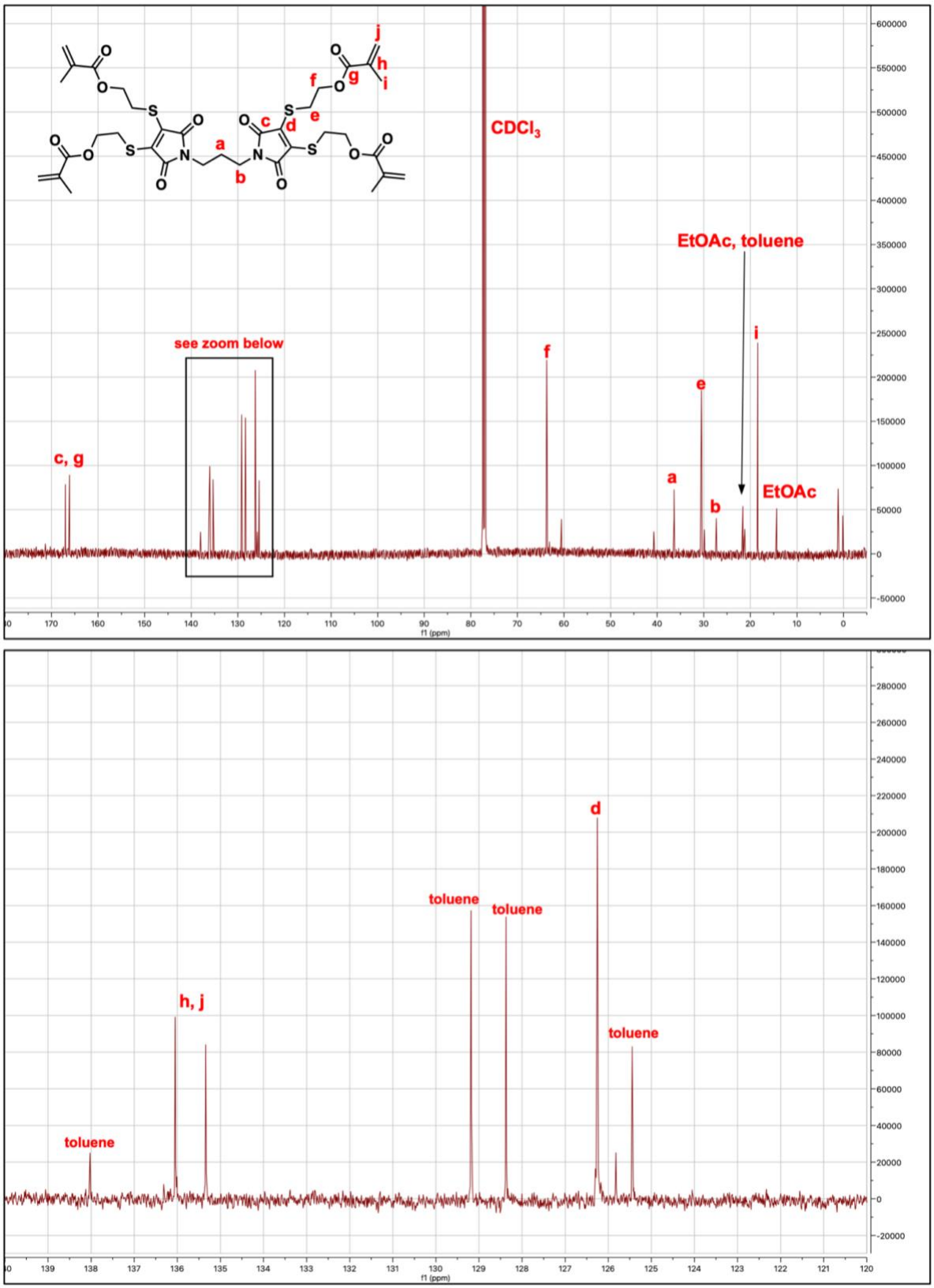

Figure C.18: ^{13}C NMR spectrum of **4b** in $CDCl_3$.

References

(1) Strebhardt, K.; Ullrich, A. Paul Ehrlich's Magic Bullet Concept: 100 Years of Progress. *Nat Rev Cancer* **2008**, *8* (6), 473–480. https://doi.org/10.1038/nrc2394.

(2) Wiesenthal, A.; Hunter, L.; Wang, S.; Wickliffe, J.; Wilkerson, M. Nanoparticles: Small and Mighty. *Int J Dermatology* **2011**, *50* (3), 247–254. https://doi.org/10.1111/j.1365-4632.2010.04815.x.

(3) Pelaz, B.; Alexiou, C.; Alvarez-Puebla, R. A.; Alves, F.; Andrews, A. M.; Ashraf, S.; Balogh, L. P.; Ballerini, L.; Bestetti, A.; Brendel, C.; Bosi, S.; Carril, M.; Chan, W. C. W.; Chen, C.; Chen, X.; Chen, X.; Cheng, Z.; Cui, D.; Du, J.; Dullin, C.; Escudero, A.; Feliu, N.; Gao, M.; George, M.; Gogotsi, Y.; Grünweller, A.; Gu, Z.; Halas, N. J.; Hampp, N.; Hartmann, R. K.; Hersam, M. C.; Hunziker, P.; Jian, J.; Jiang, X.; Jungebluth, P.; Kadhiresan, P.; Kataoka, K.; Khademhosseini, A.; Kopeček, J.; Kotov, N. A.; Krug, H. F.; Lee, D. S.; Lehr, C.-M.; Leong, K. W.; Liang, X.-J.; Ling Lim, M.; Liz-Marzán, L. M.; Ma, X.; Macchiarini, P.; Meng, H.; Möhwald, H.; Mulvaney, P.; Nel, A. E.; Nie, S.; Nordlander, P.; Okano, T.; Oliveira, J.; Park, T. H.; Penner, R. M.; Prato, M.; Puntes, V.; Rotello, V. M.; Samarakoon, A.; Schaak, R. E.; Shen, Y.; Sjöqvist, S.; Skirtach, A. G.; Soliman, M. G.; Stevens, M. M.; Sung, H.-W.; Tang, B. Z.; Tietze, R.; Udugama, B. N.; VanEpps, J. S.; Weil, T.; Weiss, P. S.; Willner, I.; Wu, Y.; Yang, L.; Yue, Z.; Zhang, Q.; Zhang, Q.; Zhang, X.-E.; Zhao, Y.; Zhou, X.; Parak, W. J. Diverse Applications of Nanomedicine. *ACS Nano* **2017**, *11* (3), 2313–2381. https://doi.org/10.1021/acsnano.6b06040.

(4) Leroux, J.-C. Editorial: Drug Delivery: Too Much Complexity, Not Enough Reproducibility? *Angew. Chem. Int. Ed.* **2017**, *56* (48), 15170–15171. https://doi.org/10.1002/anie.201709002.

(5) Time to Deliver. *Nat Biotechnol* **2014**, *32* (10), 961–961. https://doi.org/10.1038/nbt.3045.

(6) Anselmo, A. C.; Mitragotri, S. Nanoparticles in the Clinic. *Bioengineering & Translational Medicine* **2016**, *1* (1), 10–29. https://doi.org/10.1002/btm2.10003.

(7) Anselmo, A. C.; Mitragotri, S. Nanoparticles in the Clinic: An Update. *Bioeng Transl Med* **2019**, *4* (3). https://doi.org/10.1002/btm2.10143.

(8) Anselmo, A. C.; Mitragotri, S. Nanoparticles in the Clinic: An Update Post COVID -19 Vaccines. *Bioengineering & Transla Med* **2021**, *6* (3), e10246. https://doi.org/10.1002/btm2.10246.

(9) Li, S.; Huang, L. Nonviral Gene Therapy: Promises and Challenges. *Gene Ther* **2000**, *7* (1), 31–34. https://doi.org/10.1038/sj.gt.3301110.

(10) Lostalé-Seijo, I.; Montenegro, J. Synthetic Materials at the Forefront of Gene Delivery. *Nat Rev Chem* **2018**, *2* (10), 258–277. https://doi.org/10.1038/s41570-018-0039-1.

(11) Yin, H.; Kanasty, R. L.; Eltoukhy, A. A.; Vegas, A. J.; Dorkin, J. R.; Anderson, D. G. Non-Viral Vectors for Gene-Based Therapy. *Nat Rev Genet* **2014**, *15* (8), 541–555. https://doi.org/10.1038/nrg3763.

(12) Nelson, D. L.; Cox, M. M. *Lehninger Principles of Biochemistry*, Seventh.; W. H. Freeman and Company: New York, 2017.

(13) Shi, J.; Kantoff, P. W.; Wooster, R.; Farokhzad, O. C. Cancer Nanomedicine: Progress, Challenges and Opportunities. *Nat Rev Cancer* **2017**, *17* (1), 20–37. https://doi.org/10.1038/nrc.2016.108.
(14) Lundstrom, K. Viral Vectors in Gene Therapy. *Diseases* **2018**, *6* (2), 42. https://doi.org/10.3390/diseases6020042.
(15) Bulcha, J. T.; Wang, Y.; Ma, H.; Tai, P. W. L.; Gao, G. Viral Vector Platforms within the Gene Therapy Landscape. *Sig Transduct Target Ther* **2021**, *6* (1), 53. https://doi.org/10.1038/s41392-021-00487-6.
(16) Manchefio-Corvo, P.; Martin-Duque, P. Viral Gene Therapy. *Clinical and Translational Oncology* **2006**, *8* (12), 858–867.
(17) Shirley, J. L.; De Jong, Y. P.; Terhorst, C.; Herzog, R. W. Immune Responses to Viral Gene Therapy Vectors. *Molecular Therapy* **2020**, *28* (3), 709–722. https://doi.org/10.1016/j.ymthe.2020.01.001.
(18) PubMed Search for "Gene Therapy."
(19) Hoy, S. M. Patisiran: First Global Approval. *Drugs* **2018**, *78*, 1625–1631. https://doi.org/10.1007/s40265-018-0983-6.
(20) Urits, I.; Swanson, D.; Swett, M. C.; Patel, A.; Berardino, K.; Amgalan, A.; Berger, A. A.; Kassem, H.; Kaye, A. D.; Viswanath, O. A Review of Patisiran (ONPATTRO®) for the Treatment of Polyneuropathy in People with Hereditary Trahsthyretin Amyloidosis. *Neurology and Therapy* **2020**, *9*, 301–315. https://doi.org/10.1007/s40120-020-00208-1.
(21) Scott, L. J. Givosiran: First Approcal. *Drugs* **2020**, *80*, 335–339. https://doi.org/10.1007/s40265-020-01269-0.
(22) Behzadi, S.; Serpooshan, V.; Tao, W.; Hamaly, M. A.; Alkawareek, M. Y.; Dreaden, E. C.; Brown, D.; Alkilany, A. M.; Farokhzad, O. C.; Mahmoudi, M. Cellular Uptake of Nanoparticles: Journey inside the Cell. *Chem. Soc. Rev.* **2017**, *46* (14), 4218–4244. https://doi.org/10.1039/C6CS00636A.
(23) Rennick, J. J.; Johnston, A. P. R.; Parton, R. G. Key Principles and Methods for Studying the Endocytosis of Biological and Nanoparticle Therapeutics. *Nat. Nanotechnol.* **2021**, *16* (3), 266–276. https://doi.org/10.1038/s41565-021-00858-8.
(24) Poon, W.; Kingston, B. R.; Ouyang, B.; Ngo, W.; Chan, W. C. W. A Framework for Designing Delivery Systems. *Nat. Nanotechnol.* **2020**, *15* (10), 819–829. https://doi.org/10.1038/s41565-020-0759-5.
(25) Mitchell, M. J.; Billingsley, M. M.; Haley, R. M.; Wechsler, M. E.; Peppas, N. A.; Langer, R. Engineering Precision Nanoparticles for Drug Delivery. *Nat Rev Drug Discov* **2021**, *20* (2), 101–124. https://doi.org/10.1038/s41573-020-0090-8.
(26) Hoshyar, N.; Gray, S.; Han, H.; Bao, G. The Effect of Nanoparticle Size on *in Vivo* Pharmacokinetics and Cellular Interaction. *Nanomedicine* **2016**, *11* (6), 673–692. https://doi.org/10.2217/nnm.16.5.
(27) Blanco, E.; Shen, H.; Ferrari, M. Principles of Nanoparticle Design for Overcoming Biological Barriers to Drug Delivery. *Nat Biotechnol* **2015**, *33* (9), 941–951. https://doi.org/10.1038/nbt.3330.
(28) Suk, J. S.; Xu, Q.; Kim, N.; Hanes, J.; Ensign, L. M. PEGylation as a Strategy for Improving Nanoparticle-Based Drug and Gene Delivery. *Advanced Drug Delivery Reviews* **2016**, *99*, 28–51. https://doi.org/10.1016/j.addr.2015.09.012.
(29) Verma, A.; Stellacci, F. Effect of Surface Properties on Nanoparticle–Cell Interactions. *Small* **2010**, *6* (1), 12–21. https://doi.org/10.1002/smll.200901158.

(30) Geng, Y.; Dalhaimer, P.; Cai, S.; Tsai, R.; Tewari, M.; Minko, T.; Discher, D. E. Shape Effects of Filaments versus Spherical Particles in Flow and Drug Delivery. *Nature Nanotech* **2007**, *2* (4), 249–255. https://doi.org/10.1038/nnano.2007.70.

(31) Champion, J. A.; Mitragotri, S. Role of Target Geometry in Phagocytosis. *Proc. Natl. Acad. Sci. U.S.A.* **2006**, *103* (13), 4930–4934. https://doi.org/10.1073/pnas.0600997103.

(32) Miller, C. R.; Bondurant, B.; McLean, S. D.; McGovern, K. A.; O'Brien, D. F. Liposome−Cell Interactions in Vitro: Effect of Liposome Surface Charge on the Binding and Endocytosis of Conventional and Sterically Stabilized Liposomes. *Biochemistry* **1998**, *37* (37), 12875–12883. https://doi.org/10.1021/bi980096y.

(33) Arvizo, R. R.; Miranda, O. R.; Thompson, M. A.; Pabelick, C. M.; Bhattacharya, R.; Robertson, J. D.; Rotello, V. M.; Prakash, Y. S.; Mukherjee, P. Effect of Nanoparticle Surface Charge at the Plasma Membrane and Beyond. *Nano Lett.* **2010**, *10* (7), 2543–2548. https://doi.org/10.1021/nl101140t.

(34) Gratton, S. E. A.; Ropp, P. A.; Pohlhaus, P. D.; Luft, J. C.; Madden, V. J.; Napier, M. E.; DeSimone, J. M. The Effect of Particle Design on Cellular Internalization Pathways. *Proc. Natl. Acad. Sci. U.S.A.* **2008**, *105* (33), 11613–11618. https://doi.org/10.1073/pnas.0801763105.

(35) Mendes, B. B.; Conniot, J.; Avital, A.; Yao, D.; Jiang, X.; Zhou, X.; Sharf-Pauker, N.; Xiao, Y.; Adir, O.; Liang, H.; Shi, J.; Schroeder, A.; Conde, J. Nanodelivery of Nucleic Acids. *Nat Rev Methods Primers* **2022**, *2* (1), 24. https://doi.org/10.1038/s43586-022-00104-y.

(36) Maeda, H.; Nakamura, H.; Fang, J. The EPR Effect for Macromolecular Drug Delivery to Solid Tumors: Improvement of Tumor Uptake, Lowering of Systemic Toxicity, and Distinct Tumor Imaging in Vivo. *Advanced Drug Delivery Reviews* **2013**, *65* (1), 71–79. https://doi.org/10.1016/j.addr.2012.10.002.

(37) Wilhelm, S.; Tavares, A. J.; Dai, Q.; Ohta, S.; Audet, J.; Dvorak, H. F.; Chan, W. C. W. Analysis of Nanoparticle Delivery to Tumours. *Nat Rev Mater* **2016**, *1* (5), 16014. https://doi.org/10.1038/natrevmats.2016.14.

(38) Friedman, A.; Claypool, S.; Liu, R. The Smart Targeting of Nanoparticles. *CPD* **2013**, *19* (35), 6315–6329. https://doi.org/10.2174/13816128113199990375.

(39) Tietjen, G. T.; Bracaglia, L. G.; Saltzman, W. M.; Pober, J. S. Focus on Fundamentals: Achieving Effective Nanoparticle Targeting. *Trends in Molecular Medicine* **2018**, *24* (7), 598–606. https://doi.org/10.1016/j.molmed.2018.05.003.

(40) Peng, L.; Wagner, E. Polymeric Carriers for Nucleic Acid Delivery: Current Designs and Future Directions. *Biomacromolecules* **2019**, *20* (10), 3613–3626. https://doi.org/10.1021/acs.biomac.9b00999.

(41) Bai, H.; Lester, G. M. S.; Petishnok, L. C.; Dean, D. A. Cytoplasmic Transport and Nuclear Import of Plasmid DNA. *Bioscience Reports* **2017**, *37* (6), BSR20160616. https://doi.org/10.1042/BSR20160616.

(42) Islam, M. A.; Reesor, E. K. G.; Xu, Y.; Zope, H. R.; Zetter, B. R.; Shi, J. Biomaterials for mRNA Delivery. *Biomater. Sci.* **2015**, *3* (12), 1519–1533. https://doi.org/10.1039/C5BM00198F.

(43) Hou, X.; Zaks, T.; Langer, R.; Dong, Y. Lipid Nanoparticles for mRNA Delivery. *Nat Rev Mater* **2021**, *6* (12), 1078–1094. https://doi.org/10.1038/s41578-021-00358-0.

(44) Hajj, K. A.; Whitehead, K. A. Tools for Translation: Non-Viral Materials for Therapeutic mRNA Delivery. *Nat Rev Mater* **2017**, *2* (10), 17056. https://doi.org/10.1038/natrevmats.2017.56.

(45) Wang, Y.; Yu, C. Emerging Concepts of Nanobiotechnology in mRNA Delivery. *Angew. Chem. Int. Ed.* **2020**, *59* (52), 23374–23385. https://doi.org/10.1002/anie.202003545.
(46) Mout, R.; Ray, M.; Lee, Y.-W.; Scaletti, F.; Rotello, V. M. In Vivo Delivery of CRISPR/Cas9 for Therapeutic Gene Editing: Progress and Challenges. *Bioconjugate Chem.* **2017**, *28* (4), 880–884. https://doi.org/10.1021/acs.bioconjchem.7b00057.
(47) Wilbie, D.; Walther, J.; Mastrobattista, E. Delivery Aspects of CRISPR/Cas for in Vivo Genome Editing. *Acc. Chem. Res.* **2019**, *52* (6), 1555–1564. https://doi.org/10.1021/acs.accounts.9b00106.
(48) Liu, C.; Zhang, L.; Liu, H.; Cheng, K. Delivery Strategies of the CRISPR-Cas9 Gene-Editing System for Therapeutic Applications. *Journal of Controlled Release* **2017**, *266*, 17–26. https://doi.org/10.1016/j.jconrel.2017.09.012.
(49) Anzalone, A. V.; Koblan, L. W.; Liu, D. R. Genome Editing with CRISPR–Cas Nucleases, Base Editors, Transposases and Prime Editors. *Nat Biotechnol* **2020**, *38* (7), 824–844. https://doi.org/10.1038/s41587-020-0561-9.
(50) Porto, E. M.; Komor, A. C.; Slaymaker, I. M.; Yeo, G. W. Base Editing: Advances and Therapeutic Opportunities. *Nat Rev Drug Discov* **2020**, *19* (12), 839–859. https://doi.org/10.1038/s41573-020-0084-6.
(51) Kanasty, R.; Dorkin, J. R.; Vegas, A.; Anderson, D. Delivery Materials for siRNA Therapeutics. *Nature Mater* **2013**, *12* (11), 967–977. https://doi.org/10.1038/nmat3765.
(52) Miller, J. B.; Siegwart, D. J. Design of Synthetic Materials for Intracellular Delivery of RNAs: From siRNA-Mediated Gene Silencing to CRISPR/Cas Gene Editing. *Nano Res.* **2018**, *11* (10), 5310–5337. https://doi.org/10.1007/s12274-018-2099-4.
(53) Whitehead, K. A.; Langer, R.; Anderson, D. G. Knocking down Barriers: Advances in siRNA Delivery. *Nat Rev Drug Discov* **2009**, *8* (2), 129–138. https://doi.org/10.1038/nrd2742.
(54) Habibi, N.; Mauser, A.; Ko, Y.; Lahann, J. Protein Nanoparticles: Uniting the Power of Proteins with Engineering Design Approaches. *Advanced Science* **2022**, *9* (8), 2104012. https://doi.org/10.1002/advs.202104012.
(55) Begines, B.; Ortiz, T.; Pérez-Aranda, M.; Martínez, G.; Merinero, M.; Argüelles-Arias, F.; Alcudia, A. Polymeric Nanoparticles for Drug Delivery: Recent Developments and Future Prospects. *Nanomaterials* **2020**, *10* (7), 1403. https://doi.org/10.3390/nano10071403.
(56) Rai, R.; Alwani, S.; Badea, I. Polymeric Nanoparticles in Gene Therapy: New Avenues of Design and Optimization for Delivery Applications. *Polymers* **2019**, *11* (4), 745. https://doi.org/10.3390/polym11040745.
(57) Xu, L.; Wang, X.; Liu, Y.; Yang, G.; Falconer, R. J.; Zhao, C.-X. Lipid Nanoparticles for Drug Delivery. *Advanced NanoBiomed Research* **2022**, *2* (2), 2100109. https://doi.org/10.1002/anbr.202100109.
(58) Mehnert, W.; Mäder, K. Solid Lipid Nanoparticles. *Advanced Drug Delivery Reviews* **2012**, *64*, 83–101. https://doi.org/10.1016/j.addr.2012.09.021.
(59) Ferhan, A. R.; Park, S.; Park, H.; Tae, H.; Jackman, J. A.; Cho, N. Lipid Nanoparticle Technologies for Nucleic Acid Delivery: A Nanoarchitectonics Perspective. *Adv Funct Materials* **2022**, *32* (37), 2203669. https://doi.org/10.1002/adfm.202203669.
(60) Dahlman, J. E.; Kauffman, K. J.; Xing, Y.; Shaw, T. E.; Mir, F. F.; Dlott, C. C.; Langer, R.; Anderson, D. G.; Wang, E. T. Barcoded Nanoparticles for High Throughput in Vivo Discovery of Targeted Therapeutics. *Proc. Natl. Acad. Sci. U.S.A.* **2017**, *114* (8), 2060–2065. https://doi.org/10.1073/pnas.1620874114.

(61) Paunovska, K.; Sago, C. D.; Monaco, C. M.; Hudson, W. H.; Castro, M. G.; Rudoltz, T. G.; Kalathoor, S.; Vanover, D. A.; Santangelo, P. J.; Ahmed, R.; Bryksin, A. V.; Dahlman, J. E. A Direct Comparison of in Vitro and in Vivo Nucleic Acid Delivery Mediated by Hundreds of Nanoparticles Reveals a Weak Correlation. *Nano Lett.* **2018**, *18* (3), 2148–2157. https://doi.org/10.1021/acs.nanolett.8b00432.

(62) Sago, C. D.; Lokugamage, M. P.; Paunovska, K.; Vanover, D. A.; Monaco, C. M.; Shah, N. N.; Gamboa Castro, M.; Anderson, S. E.; Rudoltz, T. G.; Lando, G. N.; Munnilal Tiwari, P.; Kirschman, J. L.; Willett, N.; Jang, Y. C.; Santangelo, P. J.; Bryksin, A. V.; Dahlman, J. E. High-Throughput in Vivo Screen of Functional mRNA Delivery Identifies Nanoparticles for Endothelial Cell Gene Editing. *Proc. Natl. Acad. Sci. U.S.A.* **2018**, *115* (42). https://doi.org/10.1073/pnas.1811276115.

(63) Paunovska, K.; Gil, C. J.; Lokugamage, M. P.; Sago, C. D.; Sato, M.; Lando, G. N.; Gamboa Castro, M.; Bryksin, A. V.; Dahlman, J. E. Analyzing 2000 *in Vivo* Drug Delivery Data Points Reveals Cholesterol Structure Impacts Nanoparticle Delivery. *ACS Nano* **2018**, *12* (8), 8341–8349. https://doi.org/10.1021/acsnano.8b03640.

(64) Banik, B. L.; Fattahi, P.; Brown, J. L. Polymeric Nanoparticles: The Future of Nanomedicine. *WIREs Nanomed Nanobiotechnol* **2016**, *8* (2), 271–299. https://doi.org/10.1002/wnan.1364.

(65) Elsabahy, M.; Wooley, K. L. Design of Polymeric Nanoparticles for Biomedical Delivery Applications. *Chem. Soc. Rev.* **2012**, *41* (7), 2545. https://doi.org/10.1039/c2cs15327k.

(66) Danhier, F.; Ansorena, E.; Silva, J. M.; Coco, R.; Le Breton, A.; Préat, V. PLGA-Based Nanoparticles: An Overview of Biomedical Applications. *Journal of Controlled Release* **2012**, *161* (2), 505–522. https://doi.org/10.1016/j.jconrel.2012.01.043.

(67) Rezvantalab, S.; Drude, N. I.; Moraveji, M. K.; Güvener, N.; Koons, E. K.; Shi, Y.; Lammers, T.; Kiessling, F. PLGA-Based Nanoparticles in Cancer Treatment. *Front. Pharmacol.* **2018**, *9*, 1260. https://doi.org/10.3389/fphar.2018.01260.

(68) Kapoor, D. N.; Bhatia, A.; Kaur, R.; Sharma, R.; Kaur, G.; Dhawan, S. PLGA: A Unique Polymer for Drug Delivery. *Ther. Deliv.* **2015**, *6* (1), 41–58. https://doi.org/10.4155/tde.14.91.

(69) Suhail, M.; Rosenholm, J. M.; Minhas, M. U.; Badshah, S. F.; Naeem, A.; Khan, K. U.; Fahad, M. Nanogels As Drug-Delivery Systems: A Comprehensive Overview. *Ther. Deliv.* **2019**, *10* (11), 697–717. https://doi.org/10.4155/tde-2019-0010.

(70) Oh, J. K.; Drumright, R.; Siegwart, D. J.; Matyjaszewski, K. The Development of Microgels/Nanogels for Drug Delivery Applications. *Progress in Polymer Science* **2008**, *33* (4), 448–477. https://doi.org/10.1016/j.progpolymsci.2008.01.002.

(71) Chacko, R. T.; Ventura, J.; Zhuang, J.; Thayumanavan, S. Polymer Nanogels: A Versatile Nanoscopic Drug Delivery Platform. *Advanced Drug Delivery Reviews* **2012**, *64* (9), 836–851. https://doi.org/10.1016/j.addr.2012.02.002.

(72) Molina, M.; Asadian-Birjand, M.; Balach, J.; Bergueiro, J.; Miceli, E.; Calderón, M. Stimuli-Responsive Nanogel Composites and Their Application in Nanomedicine. *Chem. Soc. Rev.* **2015**, *44* (17), 6161–6186. https://doi.org/10.1039/C5CS00199D.

(73) Fu, R.; Fu, G.-D. Polymeric Nanomaterials from Combined Click Chemistry and Controlled Radical Polymerization. *Polym. Chem.* **2011**, *2* (3), 465–475. https://doi.org/10.1039/C0PY00174K.

(74) Zetterlund, P. B.; Thickett, S. C.; Perrier, S.; Bourgeat-Lami, E.; Lansalot, M. Controlled/Living Radical Polymerization in Dispersed Systems: An Update. *Chem. Rev.* **2015**, *115* (18), 9745–9800. https://doi.org/10.1021/cr500625k.

(75) Wang, C. E.; Stayton, P. S.; Pun, S. H.; Convertine, A. J. Polymer Nanostructures Synthesized by Controlled Living Polymerization for Tumor-Targeted Drug Delivery. *Journal of Controlled Release* **2015**, *219*, 345–354. https://doi.org/10.1016/j.jconrel.2015.08.054.
(76) Gonçalves, S. D. Á.; Vieira, R. P. Current Status of ATRP-Based Materials for Gene Therapy. *Reactive and Functional Polymers* **2020**, *147*, 104453. https://doi.org/10.1016/j.reactfunctpolym.2019.104453.
(77) Boyer, C.; Bulmus, V.; Davis, T. P.; Ladmiral, V.; Liu, J.; Perrier, S. Bioapplications of RAFT Polymerization. *Chem. Rev.* **2009**, *109* (11), 5402–5436. https://doi.org/10.1021/cr9001403.
(78) Moad, G.; Rizzardo, E.; Thang, S. H. Living Radical Polymerization by the RAFT Process. *Aust. J. Chem.* **2005**, *58* (6), 379. https://doi.org/10.1071/CH05072.
(79) Braunecker, W. A.; Matyjaszewski, K. Controlled/Living Radical Polymerization: Features, Developments, and Perspectives. *Progress in Polymer Science* **2007**, *32* (1), 93–146. https://doi.org/10.1016/j.progpolymsci.2006.11.002.
(80) Matyjaszewski, K. Advanced Materials by Atom Transfer Radical Polymerization. *Advanced Materials* **2018**, *30* (23), 1706441. https://doi.org/10.1002/adma.201706441.
(81) Siegwart, D. J.; Oh, J. K.; Matyjaszewski, K. ATRP in the Design of Functional Materials for Biomedical Applications. *Progress in Polymer Science* **2012**, *37* (1), 18–37. https://doi.org/10.1016/j.progpolymsci.2011.08.001.
(82) Matyjaszewski, K. Atom Transfer Radical Polymerization: From Mechanisms to Applications. *Israel Journal of Chemistry* **2012**, *52* (3–4), 206–220. https://doi.org/10.1002/ijch.201100101.
(83) Matyjaszewski, K.; Tsarevsky, N. V. Nanostructured Functional Materials Prepared by Atom Transfer Radical Polymerization. *Nature Chem* **2009**, *1* (4), 276–288. https://doi.org/10.1038/nchem.257.
(84) Cabral, H.; Miyata, K.; Osada, K.; Kataoka, K. Block Copolymer Micelles in Nanomedicine Applications. *Chem. Rev.* **2018**, *118* (14), 6844–6892. https://doi.org/10.1021/acs.chemrev.8b00199.
(85) Kataoka, K.; Harada, A.; Nagasaki, Y. Block Copolymer Micelles for Drug Delivery: Design, Characterization and Biological Significance. *Advanced Drug Delivery Reviews* **2012**, *64*, 37–48. https://doi.org/10.1016/j.addr.2012.09.013.
(86) Letchford, K.; Burt, H. A Review of the Formation and Classification of Amphiphilic Block Copolymer Nanoparticulate Structures: Micelles, Nanospheres, Nanocapsules and Polymersomes. *European Journal of Pharmaceutics and Biopharmaceutics* **2007**, *65* (3), 259–269. https://doi.org/10.1016/j.ejpb.2006.11.009.
(87) Tan, Z.; Jiang, Y.; Ganewatta, M. S.; Kumar, R.; Keith, A.; Twaroski, K.; Pengo, T.; Tolar, J.; Lodge, T. P.; Reineke, T. M. Block Polymer Micelles Enable CRISPR/Cas9 Ribonucleoprotein Delivery: Physicochemical Properties Affect Packaging Mechanisms and Gene Editing Efficiency. *Macromolecules* **2019**, *52* (21), 8197–8206. https://doi.org/10.1021/acs.macromol.9b01645.
(88) Kumar, R.; Le, N.; Tan, Z.; Brown, M. E.; Jiang, S.; Reineke, T. M. Efficient Polymer-Mediated Delivery of Gene-Editing Ribonucleoprotein Payloads through Combinatorial Design, Parallelized Experimentation, and Machine Learning. *ACS Nano* **2020**, *14* (12), 17626–17639. https://doi.org/10.1021/acsnano.0c08549.
(89) Farshbaf, M.; Davaran, S.; Zarebkohan, A.; Annabi, N.; Akbarzadeh, A.; Salehi, R. Significant Role of Cationic Polymers in Drug Delivery Systems. *Artificial Cells,*

Nanomedicine, and Biotechnology **2017**, 1–20. https://doi.org/10.1080/21691401.2017.1395344.
(90) Samal, S. K.; Dash, M.; Van Vlierberghe, S.; Kaplan, D. L.; Chiellini, E.; Van Blitterswijk, C.; Moroni, L.; Dubruel, P. Cationic Polymers and Their Therapeutic Potential. *Chem. Soc. Rev.* **2012**, *41* (21), 7147. https://doi.org/10.1039/c2cs35094g.
(91) Lungwitz, U.; Breunig, M.; Blunk, T.; Göpferich, A. Polyethylenimine-Based Non-Viral Gene Delivery Systems. *European Journal of Pharmaceutics and Biopharmaceutics* **2005**, *60* (2), 247–266. https://doi.org/10.1016/j.ejpb.2004.11.011.
(92) Akinc, A.; Thomas, M.; Klibanov, A. M.; Langer, R. Exploring Polyethylenimine-Mediated DNA Transfection and the Proton Sponge Hypothesis. *J. Gene Med.* **2005**, *7* (5), 657–663. https://doi.org/10.1002/jgm.696.
(93) Karlsson, J.; Rhodes, K. R.; Green, J. J.; Tzeng, S. Y. Poly(Beta-Amino Ester)s as Gene Delivery Vehicles: Challenges and Opportunities. *Expert Opinion on Drug Delivery* **2020**, *17* (10), 1395–1410. https://doi.org/10.1080/17425247.2020.1796628.
(94) Liu, Y.; Li, Y.; Keskin, D.; Shi, L. Poly(β-Amino Esters): Synthesis, Formulations, and Their Biomedical Applications. *Adv Healthcare Materials* **2019**, *8* (2), 1801359. https://doi.org/10.1002/adhm.201801359.
(95) Green, J. J.; Langer, R.; Anderson, D. G. A Combinatorial Polymer Library Approach Yields Insight into Nonviral Gene Delivery. *Acc. Chem. Res.* **2008**, *41* (6), 749–759. https://doi.org/10.1021/ar7002336.
(96) McKinlay, C. J.; Vargas, J. R.; Blake, T. R.; Hardy, J. W.; Kanada, M.; Contag, C. H.; Wender, P. A.; Waymouth, R. M. Charge-Altering Releasable Transporters (CARTs) for the Delivery and Release of mRNA in Living Animals. *Proc. Natl. Acad. Sci. U.S.A.* **2017**, *114* (4). https://doi.org/10.1073/pnas.1614193114.
(97) Jain, A.; Singh, S. K.; Arya, S. K.; Kundu, S. C.; Kapoor, S. Protein Nanoparticles: Promising Platforms for Drug Delivery Applications. *ACS Biomater. Sci. Eng.* **2018**, *4* (12), 3939–3961. https://doi.org/10.1021/acsbiomaterials.8b01098.
(98) Hong, S.; Choi, D. W.; Kim, H. N.; Park, C. G.; Lee, W.; Park, H. H. Protein-Based Nanoparticles as Drug Delivery Systems. *Pharmaceutics* **2020**, *12* (7), 604. https://doi.org/10.3390/pharmaceutics12070604.
(99) Gradishar, W. J. Albumin-Bound Paclitaxel: A next-Generation Taxane. *Expert Opinion on Pharmacotherapy* **2006**, *7* (8), 1041–1053. https://doi.org/10.1517/14656566.7.8.1041.
(100) Weber, C.; Coester, C.; Kreuter, J.; Langer, K. Desolvation Process and Surface Characterisation of Protein Nanoparticles. *International Journal of Pharmaceutics* **2000**, *194* (1), 91–102. https://doi.org/10.1016/S0378-5173(99)00370-1.
(101) Langer, K.; Balthasar, S.; Vogel, V.; Dinauer, N.; Von Briesen, H.; Schubert, D. Optimization of the Preparation Process for Human Serum Albumin (HSA) Nanoparticles. *International Journal of Pharmaceutics* **2003**, *257* (1–2), 169–180. https://doi.org/10.1016/S0378-5173(03)00134-0.
(102) King, N. P.; Sheffler, W.; Sawaya, M. R.; Vollmar, B. S.; Sumida, J. P.; André, I.; Gonen, T.; Yeates, T. O.; Baker, D. Computational Design of Self-Assembling Protein Nanomaterials with Atomic Level Accuracy. *Science* **2012**, *336* (6085), 1171–1174. https://doi.org/10.1126/science.1219364.
(103) Walls, A. C.; Fiala, B.; Schäfer, A.; Wrenn, S.; Pham, M. N.; Murphy, M.; Tse, L. V.; Shehata, L.; O'Connor, M. A.; Chen, C.; Navarro, M. J.; Miranda, M. C.; Pettie, D.; Ravichandran, R.; Kraft, J. C.; Ogohara, C.; Palser, A.; Chalk, S.; Lee, E.-C.; Guerriero, K.;

Kepl, E.; Chow, C. M.; Sydeman, C.; Hodge, E. A.; Brown, B.; Fuller, J. T.; Dinnon, K. H.; Gralinski, L. E.; Leist, S. R.; Gully, K. L.; Lewis, T. B.; Guttman, M.; Chu, H. Y.; Lee, K. K.; Fuller, D. H.; Baric, R. S.; Kellam, P.; Carter, L.; Pepper, M.; Sheahan, T. P.; Veesler, D.; King, N. P. Elicitation of Potent Neutralizing Antibody Responses by Designed Protein Nanoparticle Vaccines for SARS-CoV-2. *Cell* **2020**, *183* (5), 1367-1382.e17. https://doi.org/10.1016/j.cell.2020.10.043.

(104) Lahann, J. Recent Progress in Nano-biotechnology: Compartmentalized Micro- and Nanoparticles via Electrohydrodynamic Co-jetting. *Small* **2011**, *7* (9), 1149–1156. https://doi.org/10.1002/smll.201002002.

(105) Rahmani, S.; Ashraf, S.; Hartmann, R.; Dishman, A. F.; Zyuzin, M. V.; Yu, C. K. J.; Parak, W. J.; Lahann, J. Engineering of Nanoparticle Size via Electrohydrodynamic Jetting. *Bioengineering & Translational Medicine* **2016**, *1* (1), 82–93. https://doi.org/10.1002/btm2.10010.

(106) Quevedo, D. F.; Habibi, N.; Gregory, J. V.; Hernandez, Y.; Brown, T. D.; Miki, R.; Plummer, B. N.; Rahmani, S.; Raymond, J. E.; Mitragotri, S.; Lahann, J. Multifunctional Synthetic Protein Nanoparticles via Reactive Electrojetting. *Macromol. Rapid Commun.* **2020**, *41* (23), 2000425. https://doi.org/10.1002/marc.202000425.

(107) Habibi, N.; Quevedo, D. F.; Gregory, J. V.; Lahann, J. Emerging Methods in Therapeutics Using Multifunctional Nanoparticles. *WIREs Nanomed Nanobiotechnol* **2020**, *12* (4). https://doi.org/10.1002/wnan.1625.

(108) Rahmani, S.; Saha, S.; Durmaz, H.; Donini, A.; Misra, A. C.; Yoon, J.; Lahann, J. Chemically Orthogonal Three-Patch Microparticles. *Angew. Chem.* **2014**, *126* (9), 2364–2370. https://doi.org/10.1002/ange.201310727.

(109) Misra, A. C.; Lahann, J. Progress of Multicompartmental Particles for Medical Applications. *Adv. Healthcare Mater.* **2018**, *7* (9), 1701319. https://doi.org/10.1002/adhm.201701319.

(110) Hermanson, G. T. *Bioconjugate Techniques*, Third.; Elsevier, 2013.

(111) Binder, W. H.; Sachsenhofer, R. 'Click' Chemistry in Polymer and Materials Science. *Macromol. Rapid Commun.* **2007**, *28* (1), 15–54. https://doi.org/10.1002/marc.200600625.

(112) Moses, J. E.; Moorhouse, A. D. The Growing Applications of Click Chemistry. *Chem. Soc. Rev.* **2007**, *36* (8), 1249–1262. https://doi.org/10.1039/B613014N.

(113) Kim, E.; Koo, H. Biomedical Applications of Copper-Free Click Chemistry: *In Vitro* , *in Vivo* , and *Ex Vivo*. *Chem. Sci.* **2019**, *10* (34), 7835–7851. https://doi.org/10.1039/C9SC03368H.

(114) Gregoritza, M.; Brandl, F. P. The Diels–Alder Reaction: A Powerful Tool for the Design of Drug Delivery Systems and Biomaterials. *European Journal of Pharmaceutics and Biopharmaceutics* **2015**, *97*, 438–453. https://doi.org/10.1016/j.ejpb.2015.06.007.

(115) Dorman, G.; Prestwich, G. D. Benzophenone Photophores in Biochemistry. *Biochemistry* **1994**, *33* (19), 5661–5673. https://doi.org/10.1021/bi00185a001.

(116) Dubinsky, L.; Krom, B. P.; Meijler, M. M. Diazirine Based Photoaffinity Labeling. *Bioorganic & Medicinal Chemistry* **2012**, *20* (2), 554–570. https://doi.org/10.1016/j.bmc.2011.06.066.

(117) Staros, J. V. Aryl Azide Photolabels in Biochemistry. *Trends in Biochemical Sciences* **1980**, *5* (12), 320–322. https://doi.org/10.1016/0968-0004(80)90140-1.

(118) Bargh, J. D.; Isidro-Llobet, A.; Parker, J. S.; Spring, D. R. Cleavable Linkers in Antibody–Drug Conjugates. *Chem. Soc. Rev.* **2019**, *48* (16), 4361–4374. https://doi.org/10.1039/C8CS00676H.
(119) Mura, S.; Nicolas, J.; Couvreur, P. Stimuli-Responsive Nanocarriers for Drug Delivery. *Nature Mater* **2013**, *12* (11), 991–1003. https://doi.org/10.1038/nmat3776.
(120) López-Mirabal, H. R.; Winther, J. R. Redox Characteristics of the Eukaryotic Cytosol. *Biochimica et Biophysica Acta (BBA) - Molecular Cell Research* **2008**, *1783* (4), 629–640. https://doi.org/10.1016/j.bbamcr.2007.10.013.
(121) Gao, W.; Chan, J. M.; Farokhzad, O. C. pH-Responsive Nanoparticles for Drug Delivery. *Mol. Pharmaceutics* **2010**, *7* (6), 1913–1920. https://doi.org/10.1021/mp100253e.
(122) Sonawane, S. J.; Kalhapure, R. S.; Govender, T. Hydrazone Linkages in pH Responsive Drug Delivery Systems. *European Journal of Pharmaceutical Sciences* **2017**, *99*, 45–65. https://doi.org/10.1016/j.ejps.2016.12.011.
(123) Dal Corso, A.; Pignataro, L.; Belvisi, L.; Gennari, C. Innovative Linker Strategies for Tumor-Targeted Drug Conjugates. *Chemistry A European J* **2019**, *25* (65), 14740–14757. https://doi.org/10.1002/chem.201903127.
(124) Modena, M. M.; Rühle, B.; Burg, T. P.; Wuttke, S. Nanoparticle Characterization: What to Measure? *Advanced Materials* **2019**, *31* (32), 1901556. https://doi.org/10.1002/adma.201901556.
(125) Gallego-Urrea, J. A.; Tuoriniemi, J.; Hassellöv, M. Applications of Particle-Tracking Analysis to the Determination of Size Distributions and Concentrations of Nanoparticles in Environmental, Biological and Food Samples. *TrAC Trends in Analytical Chemistry* **2011**, *30* (3), 473–483. https://doi.org/10.1016/j.trac.2011.01.005.
(126) Stetefeld, J.; McKenna; Patel, T. R. Dynamic Light Scattering: A Practical Guide and Applications in Biomedical Sciences. *Biophysical Reviews* **2016**, *8*, 409–427. https://doi.org/10.1007/s12551-016-0218-6.
(127) Mohammed, A.; Abdullah, A. SCANNING ELECTRON MICROSCOPY (SEM): A REVIEW.
(128) Wang, Z. L. New Developments in Transmission Electron Microscopy for Nanotechnology. *Advanced Materials* **2003**, *15* (18), 1497–1514. https://doi.org/10.1002/adma.200300384.
(129) Winey, M.; Meehl, J. B.; O'Toole, E. T.; Giddings, T. H. Conventional Transmission Electron Microscopy. *MBoC* **2014**, *25* (3), 319–323. https://doi.org/10.1091/mbc.e12-12-0863.
(130) Klang, V.; Valenta, C.; Matsko, N. B. Electron Microscopy of Pharmaceutical Systems. *Micron* **2013**, *44*, 45–74. https://doi.org/10.1016/j.micron.2012.07.008.
(131) Cardell, C.; Guerra, I. An Overview of Emerging Hyphenated SEM-EDX and Raman Spectroscopy Systems: Applications in Life, Environmental and Materials Sciences. *TrAC Trends in Analytical Chemistry* **2016**, *77*, 156–166. https://doi.org/10.1016/j.trac.2015.12.001.
(132) Baer, D. R.; Gaspar, D. J.; Nachimuthu, P.; Techane, S. D.; Castner, D. G. Application of Surface Chemical Analysis Tools for Characterization of Nanoparticles. *Analytical and Bioanalytical Chemistry* **2010**, No. 396, 983–1002. https://doi.org/10.1007/s00216-009-3360-1.
(133) Roy, D.; Fendler, J. Reflection and Absorption Techniques for Optical Characterization of Chemically Assembled Nanomaterials. *Advanced Materials* **2004**, *16* (6), 479–508. https://doi.org/10.1002/adma.200306195.

(134) López-Lorente, Á. I.; Mizaikoff, B. Recent Advances on the Characterization of Nanoparticles Using Infrared Spectroscopy. *TrAC Trends in Analytical Chemistry* **2016**, *84*, 97–106. https://doi.org/10.1016/j.trac.2016.01.012.
(135) Bandyopadhyay, S.; Peralta-Videa, J. R.; Hernandez-Viezcas, J. A.; Montes, M. O.; Keller, A. A.; Gardea-Torresdey, J. L. Microscopic and Spectroscopic Methods Applied to the Measurements of Nanoparticles in the Environment. *Applied Spectroscopy Reviews* **2012**, *47* (3), 180–206. https://doi.org/10.1080/05704928.2011.637186.
(136) Lakowicz, J. R. *Principles of Fluorescence Spectroscopy*, Third.; Springer, 2006.
(137) Grimm, J. B.; Lavis, L. D. Caveat Fluorophore: An Insiders' Guide to Small-Molecule Fluorescent Labels. *Nat Methods* **2022**, *19* (2), 149–158. https://doi.org/10.1038/s41592-021-01338-6.
(138) Berezin, M. Y.; Achilefu, S. Fluorescence Lifetime Measurements and Biological Imaging. *Chem. Rev.* **2010**, *110* (5), 2641–2684. https://doi.org/10.1021/cr900343z.
(139) Berezin, M. Y.; Lee, H.; Akers, W.; Achilefu, S. Near Infrared Dyes as Lifetime Solvatochromic Probes for Micropolarity Measurements of Biological Systems. *Biophysical Journal* **2007**, *93* (8), 2892–2899. https://doi.org/10.1529/biophysj.107.111609.
(140) Robin, M. P.; Raymond, J. E.; O'Reilly, R. K. One-Pot Synthesis of Super-Bright Fluorescent Nanogel Contrast Agents Containing a Dithiomaleimide Fluorophore. *Mater. Horiz.* **2015**, *2* (1), 54–59. https://doi.org/10.1039/C4MH00167B.
(141) Altınoglu, S.; Wang, M.; Xu, Q. Combinatorial Library Strategies for Synthesis of Cationic Lipid-Like Nanoparticles and Their Potential Medical Applications. *Nanomedicine (Lond.)* **2015**, *10* (4), 643–657. https://doi.org/10.2217/nnm.14.192.
(142) Tomé, I.; Francisco, V.; Fernandes, H.; Ferreira, L. High-Throughput Screening of Nanoparticles in Drug Delivery. *APL Bioengineering* **2021**, *5* (3), 031511. https://doi.org/10.1063/5.0057204.
(143) Upadhya, R.; Kosuri, S.; Tamasi, M.; Meyer, T. A.; Atta, S.; Webb, M. A.; Gormley, A. J. Automation and Data-Driven Design of Polymer Therapeutics. *Advanced Drug Delivery Reviews* **2021**, *171*, 1–28. https://doi.org/10.1016/j.addr.2020.11.009.
(144) Akinc, A.; Zumbuehl, A.; Goldberg, M.; Leshchiner, E. S.; Busini, V.; Hossain, N.; Bacallado, S. A.; Nguyen, D. N.; Fuller, J.; Alvarez, R.; Borodovsky, A.; Borland, T.; Constien, R.; De Fougerolles, A.; Dorkin, J. R.; Narayanannair Jayaprakash, K.; Jayaraman, M.; John, M.; Koteliansky, V.; Manoharan, M.; Nechev, L.; Qin, J.; Racie, T.; Raitcheva, D.; Rajeev, K. G.; Sah, D. W. Y.; Soutschek, J.; Toudjarska, I.; Vornlocher, H.-P.; Zimmermann, T. S.; Langer, R.; Anderson, D. G. A Combinatorial Library of Lipid-like Materials for Delivery of RNAi Therapeutics. *Nat Biotechnol* **2008**, *26* (5), 561–569. https://doi.org/10.1038/nbt1402.
(145) Love, K. T.; Mahon, K. P.; Levins, C. G.; Whitehead, K. A.; Querbes, W.; Dorkin, J. R.; Qin, J.; Cantley, W.; Qin, L. L.; Racie, T.; Frank-Kamenetsky, M.; Yip, K. N.; Alvarez, R.; Sah, D. W. Y.; De Fougerolles, A.; Fitzgerald, K.; Koteliansky, V.; Akinc, A.; Langer, R.; Anderson, D. G. Lipid-like Materials for Low-Dose, in Vivo Gene Silencing. *Proc. Natl. Acad. Sci. U.S.A.* **2010**, *107* (5), 1864–1869. https://doi.org/10.1073/pnas.0910603106.
(146) Mahon, K. P.; Love, K. T.; Whitehead, K. A.; Qin, J.; Akinc, A.; Leshchiner, E.; Leshchiner, I.; Langer, R.; Anderson, D. G. Combinatorial Approach to Determine Functional Group Effects on Lipidoid-Mediated siRNA Delivery. *Bioconjugate Chem.* **2010**, *21* (8), 1448–1454. https://doi.org/10.1021/bc100041r.

(147) Whitehead, K. A.; Dorkin, J. R.; Vegas, A. J.; Chang, P. H.; Veiseh, O.; Matthews, J.; Fenton, O. S.; Zhang, Y.; Olejnik, K. T.; Yesilyurt, V.; Chen, D.; Barros, S.; Klebanov, B.; Novobrantseva, T.; Langer, R.; Anderson, D. G. Degradable Lipid Nanoparticles with Predictable in Vivo siRNA Delivery Activity. *Nat Commun* **2014**, *5* (1), 4277. https://doi.org/10.1038/ncomms5277.

(148) Yamankurt, G.; Berns, E. J.; Xue, A.; Lee, A.; Bagheri, N.; Mrksich, M.; Mirkin, C. A. Exploration of the Nanomedicine-Design Space with High-Throughput Screening and Machine Learning. *Nat Biomed Eng* **2019**, *3* (4), 318–327. https://doi.org/10.1038/s41551-019-0351-1.

(149) Reis, M.; Gusev, F.; Taylor, N. G.; Chung, S. H.; Verber, M. D.; Lee, Y. Z.; Isayev, O.; Leibfarth, F. A. Machine-Learning-Guided Discovery of ^{19}F MRI Agents Enabled by Automated Copolymer Synthesis. *J. Am. Chem. Soc.* **2021**, *143* (42), 17677–17689. https://doi.org/10.1021/jacs.1c08181.

(150) Perez, H. L.; Cardarelli, P. M.; Deshpande, S.; Gangwar, S.; Schroeder, G. M.; Vite, G. D.; Borzilleri, R. M. Antibody–Drug Conjugates: Current Status and Future Directions. *Drug Discovery Today* **2014**, *19* (7), 869–881. https://doi.org/10.1016/j.drudis.2013.11.004.

(151) Casi, G.; Neri, D. Antibody–Drug Conjugates: Basic Concepts, Examples and Future Perspectives. *Journal of Controlled Release* **2012**, *161* (2), 422–428. https://doi.org/10.1016/j.jconrel.2012.01.026.

(152) Gregory, J. V.; Kadiyala, P.; Doherty, R.; Cadena, M.; Habeel, S.; Ruoslahti, E.; Lowenstein, P. R.; Castro, M. G.; Lahann, J. Systemic Brain Tumor Delivery of Synthetic Protein Nanoparticles for Glioblastoma Therapy. *Nat Commun* **2020**, *11* (1), 5687. https://doi.org/10.1038/s41467-020-19225-7.

(153) Hawkins, M. J.; Soon-Shiong, P.; Desai, N. Protein Nanoparticles as Drug Carriers in Clinical Medicine. *Advanced Drug Delivery Reviews* **2008**, *60* (8), 876–885. https://doi.org/10.1016/j.addr.2007.08.044.

(154) Zhang, T.; Xu, J.; Chen, J.; Wang, Z.; Wang, X.; Zhong, J. Protein Nanoparticles for Pickering Emulsions: A Comprehensive Review on Their Shapes, Preparation Methods, and Modification Methods. *Trends in Food Science & Technology* **2021**, *113*, 26–41. https://doi.org/10.1016/j.tifs.2021.04.054.

(155) Elzoghby, A. O.; Samy, W. M.; Elgindy, N. A. Albumin-Based Nanoparticles as Potential Controlled Release Drug Delivery Systems. *Journal of Controlled Release* **2012**, *157* (2), 168–182. https://doi.org/10.1016/j.jconrel.2011.07.031.

(156) Huang, P.-S.; Boyken, S. E.; Baker, D. The Coming of Age of de Novo Protein Design. *Nature* **2016**, *537* (7620), 320–327. https://doi.org/10.1038/nature19946.

(157) Chevalier, A.; Silva, D.-A.; Rocklin, G. J.; Hicks, D. R.; Vergara, R.; Murapa, P.; Bernard, S. M.; Zhang, L.; Lam, K.-H.; Yao, G.; Bahl, C. D.; Miyashita, S.-I.; Goreshnik, I.; Fuller, J. T.; Koday, M. T.; Jenkins, C. M.; Colvin, T.; Carter, L.; Bohn, A.; Bryan, C. M.; Fernández-Velasco, D. A.; Stewart, L.; Dong, M.; Huang, X.; Jin, R.; Wilson, I. A.; Fuller, D. H.; Baker, D. Massively Parallel de Novo Protein Design for Targeted Therapeutics. *Nature* **2017**, *550* (7674), 74–79. https://doi.org/10.1038/nature23912.

(158) Ingraham, J. B.; Baranov, M.; Costello, Z.; Barber, K. W.; Wang, W.; Ismail, A.; Frappier, V.; Lord, D. M.; Ng-Thow-Hing, C.; Van Vlack, E. R.; Tie, S.; Xue, V.; Cowles, S. C.; Leung, A.; Rodrigues, J. V.; Morales-Perez, C. L.; Ayoub, A. M.; Green, R.; Puentes, K.; Oplinger, F.; Panwar, N. V.; Obermeyer, F.; Root, A. R.; Beam, A. L.; Poelwijk, F. J.; Grigoryan, G.

Illuminating Protein Space with a Programmable Generative Model. *Nature* **2023**, *623* (7989), 1070–1078. https://doi.org/10.1038/s41586-023-06728-8.
(159) Habibi, N.; Mauser, A.; Raymond, J. E.; Lahann, J. Systematic Studies into Uniform Synthetic Protein Nanoparticles. *Beilstein J. Nanotechnol.* **2022**, *13*, 274–283. https://doi.org/10.3762/bjnano.13.22.
(160) Habibi, N.; Christau, S.; Ochyl, L. J.; Fan, Z.; Hassani Najafabadi, A.; Kuehnhammer, M.; Zhang, M.; Helgeson, M.; Klitzing, R.; Moon, J. J.; Lahann, J. Engineered Ovalbumin Nanoparticles for Cancer Immunotherapy. *Adv. Therap.* **2020**, *3* (10), 2000100. https://doi.org/10.1002/adtp.202000100.
(161) Myerson, J. W.; Patel, P. N.; Rubey, K. M.; Zamora, M. E.; Zaleski, M. H.; Habibi, N.; Walsh, L. R.; Lee, Y.-W.; Luther, D. C.; Ferguson, L. T.; Marcos-Contreras, O. A.; Glassman, P. M.; Mazaleuskaya, L. L.; Johnston, I.; Hood, E. D.; Shuvaeva, T.; Wu, J.; Zhang, H.-Y.; Gregory, J. V.; Kiseleva, R. Y.; Nong, J.; Grosser, T.; Greineder, C. F.; Mitragotri, S.; Worthen, G. S.; Rotello, V. M.; Lahann, J.; Muzykantov, V. R.; Brenner, J. S. Supramolecular Arrangement of Protein in Nanoparticle Structures Predicts Nanoparticle Tropism for Neutrophils in Acute Lung Inflammation. *Nat. Nanotechnol.* **2022**, *17* (1), 86–97. https://doi.org/10.1038/s41565-021-00997-y.
(162) Alghamri, M. S.; Banerjee, K.; Mujeeb, A. A.; Mauser, A.; Taher, A.; Thalla, R.; McClellan, B. L.; Varela, M. L.; Stamatovic, S. M.; Martinez-Revollar, G.; Andjelkovic, A. V.; Gregory, J. V.; Kadiyala, P.; Calinescu, A.; Jiménez, J. A.; Apfelbaum, A. A.; Lawlor, E. R.; Carney, S.; Comba, A.; Faisal, S. M.; Barissi, M.; Edwards, M. B.; Appelman, H.; Sun, Y.; Gan, J.; Ackermann, R.; Schwendeman, A.; Candolfi, M.; Olin, M. R.; Lahann, J.; Lowenstein, P. R.; Castro, M. G. Systemic Delivery of an Adjuvant CXCR4–CXCL12 Signaling Inhibitor Encapsulated in Synthetic Protein Nanoparticles for Glioma Immunotherapy. *ACS Nano* **2022**, *16* (6), 8729–8750. https://doi.org/10.1021/acsnano.1c07492.
(163) Robin, M. P.; Wilson, P.; Mabire, A. B.; Kiviaho, J. K.; Raymond, J. E.; Haddleton, D. M.; O'Reilly, R. K. Conjugation-Induced Fluorescent Labeling of Proteins and Polymers Using Dithiomaleimides. *J. Am. Chem. Soc.* **2013**, *135* (8), 2875–2878. https://doi.org/10.1021/ja3105494.
(164) Farrell, I. S.; Toroney, R.; Hazen, J. L.; Mehl, R. A.; Chin, J. W. Photo-Cross-Linking Interacting Proteins with a Genetically Encoded Benzophenone. *Nat Methods* **2005**, *2* (5), 377–384. https://doi.org/10.1038/nmeth0505-377.
(165) Robin, M. P.; Mabire, A. B.; Damborsky, J. C.; Thom, E. S.; Winzer-Serhan, U. H.; Raymond, J. E.; O'Reilly, R. K. New Functional Handle for Use as a Self-Reporting Contrast and Delivery Agent in Nanomedicine. *J. Am. Chem. Soc.* **2013**, *135* (25), 9518–9524. https://doi.org/10.1021/ja403587c.
(166) Xie, Y.; Arno, M. C.; Husband, J. T.; Torrent-Sucarrat, M.; O'Reilly, R. K. Manipulating the Fluorescence Lifetime at the Sub-Cellular Scale via Photo-Switchable Barcoding. *Nat Commun* **2020**, *11* (1), 2460. https://doi.org/10.1038/s41467-020-16297-3.
(167) Robin, M. P.; Osborne, S. A. M.; Pikramenou, Z.; Raymond, J. E.; O'Reilly, R. K. Fluorescent Block Copolymer Micelles That Can Self-Report on Their Assembly and Small Molecule Encapsulation. *Macromolecules* **2016**, *49* (2), 653–662. https://doi.org/10.1021/acs.macromol.5b02152.
(168) Pearce, A. K.; Parkinson, S. J.; Akar, I.; Derry, M. J.; Topham, P. D.; Mathers, R. T.; Stavros, V. G.; O'Reilly, R. K. Mechanistic Insights into Polymerization-Induced Self-

Assembly Using Maleimide-Based Fluorophores. *Macromolecules* **2023**, *56* (23), 9443–9454. https://doi.org/10.1021/acs.macromol.3c01451.
(169) Hench, L. L.; West, J. K. The Sol-Gel Process. *Chem. Rev.* **1990**, *90* (1), 33–72. https://doi.org/10.1021/cr00099a003.
(170) Chen, G.; Roy, I.; Yang, C.; Prasad, P. N. Nanochemistry and Nanomedicine for Nanoparticle-Based Diagnostics and Therapy. *Chem. Rev.* **2016**, *116* (5), 2826–2885. https://doi.org/10.1021/acs.chemrev.5b00148.
(171) Shamay, Y.; Shah, J.; Işık, M.; Mizrachi, A.; Leibold, J.; Tschaharganeh, D. F.; Roxbury, D.; Budhathoki-Uprety, J.; Nawaly, K.; Sugarman, J. L.; Baut, E.; Neiman, M. R.; Dacek, M.; Ganesh, K. S.; Johnson, D. C.; Sridharan, R.; Chu, K. L.; Rajasekhar, V. K.; Lowe, S. W.; Chodera, J. D.; Heller, D. A. Quantitative Self-Assembly Prediction Yields Targeted Nanomedicines. *Nature Mater* **2018**, *17* (4), 361–368. https://doi.org/10.1038/s41563-017-0007-z.
(172) Schmitt, S.; Renzer, G.; Benrath, J.; Best, A.; Jiang, S.; Landfester, K.; Butt, H.-J.; Simonutti, R.; Crespy, D.; Koynov, K. Monitoring the Formation of Polymer Nanoparticles with Fluorescent Molecular Rotors. *Macromolecules* **2022**, *55* (16), 7284–7293. https://doi.org/10.1021/acs.macromol.2c01132.
(173) Shang, L.; Yang, L.; Wang, H.; Nienhaus, G. U. In Situ Monitoring of the Intracellular Stability of Nanoparticles by Using Fluorescence Lifetime Imaging. *Small* **2016**, *12* (7), 868–873. https://doi.org/10.1002/smll.201503316.
(174) Degors, I. M. S.; Wang, C.; Rehman, Z. U.; Zuhorn, I. S. Carriers Break Barriers in Drug Delivery: Endocytosis and Endosomal Escape of Gene Delivery Vectors. *Acc. Chem. Res.* **2019**, *52* (7), 1750–1760. https://doi.org/10.1021/acs.accounts.9b00177.
(175) Wei, T.; Cheng, Q.; Farbiak, L.; Anderson, D. G.; Langer, R.; Siegwart, D. J. Delivery of Tissue-Targeted Scalpels: Opportunities and Challenges for *In Vivo* CRISPR/Cas-Based Genome Editing. *ACS Nano* **2020**, *14* (8), 9243–9262. https://doi.org/10.1021/acsnano.0c04707.
(176) Smith, S. A.; Selby, L. I.; Johnston, A. P. R.; Such, G. K. The Endosomal Escape of Nanoparticles: Toward More Efficient Cellular Delivery. *Bioconjugate Chem.* **2019**, *30* (2), 263–272. https://doi.org/10.1021/acs.bioconjchem.8b00732.
(177) Paunovska, K.; Loughrey, D.; Sago, C. D.; Langer, R.; Dahlman, J. E. Using Large Datasets to Understand Nanotechnology. *Adv. Mater.* **2019**, *31* (43), 1902798. https://doi.org/10.1002/adma.201902798.
(178) Lokugamage, M. P.; Sago, C. D.; Dahlman, J. E. Testing Thousands of Nanoparticles in Vivo Using DNA Barcodes. *Current Opinion in Biomedical Engineering* **2018**, *7*, 1–8. https://doi.org/10.1016/j.cobme.2018.08.001.
(179) Algar, W. R.; Hildebrandt, N.; Vogel, S. S.; Medintz, I. L. FRET as a Biomolecular Research Tool — Understanding Its Potential While Avoiding Pitfalls. *Nat Methods* **2019**, *16* (9), 815–829. https://doi.org/10.1038/s41592-019-0530-8.
(180) Han, J.; Burgess, K. Fluorescent Indicators for Intracellular pH. *Chem. Rev.* **2010**, *110* (5), 2709–2728. https://doi.org/10.1021/cr900249z.
(181) Kaur, A.; Kolanowski, J. L.; New, E. J. Reversible Fluorescent Probes for Biological Redox States. *Angew Chem Int Ed* **2016**, *55* (5), 1602–1613. https://doi.org/10.1002/anie.201506353.

(182) Zhang, X.-F.; Zhang, Y.; Liu, L. Fluorescence Lifetimes and Quantum Yields of Ten Rhodamine Derivatives: Structural Effect on Emission Mechanism in Different Solvents. *Journal of Luminescence* **2014**, *145*, 448–453. https://doi.org/10.1016/j.jlumin.2013.07.066.
(183) Magde, D.; Rojas, G. E.; Seybold, P. G. Solvent Dependence of the Fluorescence Lifetimes of Xanthene Dyes. *Photochem & Photobiology* **1999**, *70* (5), 737–744. https://doi.org/10.1111/j.1751-1097.1999.tb08277.x.
(184) Sarder, P.; Maji, D.; Achilefu, S. Molecular Probes for Fluorescence Lifetime Imaging. *Bioconjugate Chem.* **2015**, *26* (6), 963–974. https://doi.org/10.1021/acs.bioconjchem.5b00167.
(185) Kuimova, M. K.; Yahioglu, G.; Levitt, J. A.; Suhling, K. Molecular Rotor Measures Viscosity of Live Cells via Fluorescence Lifetime Imaging. *J. Am. Chem. Soc.* **2008**, *130* (21), 6672–6673. https://doi.org/10.1021/ja800570d.
(186) Mabire, A. B.; Robin, M. P.; Quan, W.-D.; Willcock, H.; Stavros, V. G.; O'Reilly, R. K. Aminomaleimide Fluorophores: A Simple Functional Group with Bright, Solvent Dependent Emission. *Chem. Commun.* **2015**, *51* (47), 9733–9736. https://doi.org/10.1039/C5CC02908B.
(187) Pervez, M.; Pearce, A. K.; Husband, J. T.; Male, L.; Torrent-Sucarrat, M.; O'Reilly, R. K. Enhancing Dual-State Emission in Maleimide Fluorophores through Fluorocarbon Functionalisation. *Chemistry A European J* **2022**, *28* (58). https://doi.org/10.1002/chem.202201877.
(188) Xie, Y.; Husband, J. T.; Torrent-Sucarrat, M.; Yang, H.; Liu, W.; O'Reilly, R. K. Rational Design of Substituted Maleimide Dyes with Tunable Fluorescence and Solvafluorochromism. *Chem. Commun.* **2018**, *54* (27), 3339–3342. https://doi.org/10.1039/C8CC00772A.
(189) Staniforth, M.; Quan, W.-D.; Karsili, T. N. V.; Baker, L. A.; O'Reilly, R. K.; Stavros, V. G. First Step toward a Universal Fluorescent Probe: Unravelling the Photodynamics of an Amino–Maleimide Fluorophore. *J. Phys. Chem. A* **2017**, *121* (34), 6357–6365. https://doi.org/10.1021/acs.jpca.7b04702.
(190) Hull, E. A.; Livanos, M.; Miranda, E.; Smith, M. E. B.; Chester, K. A.; Baker, J. R. Homogeneous Bispecifics by Disulfide Bridging. *Bioconjugate Chem.* **2014**, *25* (8), 1395–1401. https://doi.org/10.1021/bc5002467.
(191) Forte, N.; Livanos, M.; Miranda, E.; Morais, M.; Yang, X.; Rajkumar, V. S.; Chester, K. A.; Chudasama, V.; Baker, J. R. Tuning the Hydrolytic Stability of Next Generation Maleimide Cross-Linkers Enables Access to Albumin-Antibody Fragment Conjugates and Tri-scFvs. *Bioconjugate Chem.* **2018**, *29* (2), 486–492. https://doi.org/10.1021/acs.bioconjchem.7b00795.
(192) Chen, Z.; Boyd, S. D.; Calvo, J. S.; Murray, K. W.; Mejia, G. L.; Benjamin, C. E.; Welch, R. P.; Winkler, D. D.; Meloni, G.; D'Arcy, S.; Gassensmith, J. J. Fluorescent Functionalization across Quaternary Structure in a Virus-like Particle. *Bioconjugate Chem.* **2017**, *28* (9), 2277–2283. https://doi.org/10.1021/acs.bioconjchem.7b00305.
(193) Robin, M. P.; Jones, M. W.; Haddleton, D. M.; O'Reilly, R. K. Dibromomaleimide End Functional Polymers by RAFT Polymerization Without the Need of Protecting Groups. *ACS Macro Lett.* **2012**, *1* (1), 222–226. https://doi.org/10.1021/mz200164x.
(194) Robin, M. P.; O'Reilly, R. K. Fluorescent and Chemico-Fluorescent Responsive Polymers from Dithiomaleimide and Dibromomaleimide Functional Monomers. *Chem. Sci.* **2014**, *5* (7), 2717. https://doi.org/10.1039/c4sc00753k.

(195) Sillen, A.; Engelborghs, Y. The Correct Use of "Average" Fluorescence Parameters. *Photochem Photobiol* **1998**, *67* (5), 475–486. https://doi.org/10.1111/j.1751-1097.1998.tb09082.x.
(196) Hwang, S.; Lahann, J. Differentially Degradable Janus Particles for Controlled Release Applications. *Macromol. Rapid Commun.* **2012**, *33* (14), 1178–1183. https://doi.org/10.1002/marc.201200054.
(197) Roh, K.-H.; Martin, D. C.; Lahann, J. Biphasic Janus Particles with Nanoscale Anisotropy. *Nature Mater* **2005**, *4* (10), 759–763. https://doi.org/10.1038/nmat1486.
(198) Chan, Y.; Wong, T.; Byrne, F.; Kavallaris, M.; Bulmus, V. Acid-Labile Core Cross-Linked Micelles for pH-Triggered Release of Antitumor Drugs. *Biomacromolecules* **2008**, *9* (7), 1826–1836. https://doi.org/10.1021/bm800043n.
(199) Giugliarelli, A.; Paolantoni, M.; Morresi, A.; Sassi, P. Denaturation and Preservation of Globular Proteins: The Role of DMSO. *J. Phys. Chem. B* **2012**, *116* (45), 13361–13367. https://doi.org/10.1021/jp308655p.
(200) Batista, A. N. L.; Batista, J. M.; Ashton, L.; Bolzani, V. S.; Furlan, M.; Blanch, E. W. Investigation of DMSO-Induced Conformational Transitions in Human Serum Albumin Using Two-Dimensional Raman Optical Activity Spectroscopy. *Chirality* **2014**, *26* (9), 497–501. https://doi.org/10.1002/chir.22351.
(201) Mauser, A. Engineered Protein Nanoparticles as Therapeutics for Gliomas. Doctoral Thesis, University of Michigan, 2024.
(202) Parkatzidis, K.; Wang, H. S.; Truong, N. P.; Anastasaki, A. Recent Developments and Future Challenges in Controlled Radical Polymerization: A 2020 Update. *Chem* **2020**, *6* (7), 1575–1588. https://doi.org/10.1016/j.chempr.2020.06.014.
(203) Nicolas, J.; Guillaneuf, Y.; Lefay, C.; Bertin, D.; Gigmes, D.; Charleux, B. Nitroxide-Mediated Polymerization. *Progress in Polymer Science* **2013**, *38* (1), 63–235. https://doi.org/10.1016/j.progpolymsci.2012.06.002.
(204) Anastasaki, A.; Willenbacher, J.; Fleischmann, C.; Gutekunst, W. R.; Hawker, C. J. End Group Modification of Poly(Acrylates) Obtained via ATRP: A User Guide. *Polym. Chem.* **2017**, *8* (4), 689–697. https://doi.org/10.1039/C6PY01993E.
(205) Hawker, C. J.; Bosman, A. W.; Harth, E. New Polymer Synthesis by Nitroxide Mediated Living Radical Polymerizations. *Chem. Rev.* **2001**, *101* (12), 3661–3688. https://doi.org/10.1021/cr990119u.
(206) Grubbs, R. B. Nitroxide-Mediated Radical Polymerization: Limitations and Versatility. *Polymer Reviews* **2011**, *51* (2), 104–137. https://doi.org/10.1080/15583724.2011.566405.
(207) Boyer, C.; Liu, J.; Bulmus, V.; Davis, T. P.; Barner-Kowollik, C.; Stenzel, M. H. Direct Synthesis of Well-Defined Heterotelechelic Polymers for Bioconjugations. *Macromolecules* **2008**, *41* (15), 5641–5650. https://doi.org/10.1021/ma800289u.
(208) Roth, P. J.; Haase, M.; Basché, T.; Theato, P.; Zentel, R. Synthesis of Heterotelechelic α,ω Dye-Functionalized Polymer by the RAFT Process and Energy Transfer between the End Groups. *Macromolecules* **2010**, *43* (2), 895–902. https://doi.org/10.1021/ma902391b.
(209) Perrier, S. *50th Anniversary Perspective* : RAFT Polymerization—A User Guide. *Macromolecules* **2017**, *50* (19), 7433–7447. https://doi.org/10.1021/acs.macromol.7b00767.
(210) Willcock, H.; O'Reilly, R. K. End Group Removal and Modification of RAFT Polymers. *Polym. Chem.* **2010**, *1* (2), 149–157. https://doi.org/10.1039/B9PY00340A.

(211) Boyer, C.; Bulmus, V.; Priyanto, P.; Teoh, W. Y.; Amal, R.; Davis, T. P. The Stabilization and Bio-Functionalization of Iron Oxide Nanoparticles Using Heterotelechelic Polymers. *J. Mater. Chem.* **2009**, *19* (1), 111–123. https://doi.org/10.1039/B815202K.
(212) Heredia, K. L.; Grover, G. N.; Tao, L.; Maynard, H. D. Synthesis of Heterotelechelic Polymers for Conjugation of Two Different Proteins. *Macromolecules* **2009**, *42* (7), 2360–2367. https://doi.org/10.1021/ma8022712.
(213) Heredia, K. L.; Tao, L.; Grover, G. N.; Maynard, H. D. Heterotelechelic Polymers for Capture and Release of Protein–Polymer Conjugates. *Polym. Chem.* **2010**, *1* (2), 168. https://doi.org/10.1039/b9py00369j.
(214) Liu, J.; Liu, H.; Bulmus, V.; Tao, L.; Boyer, C.; Davis, T. P. A Simple Methodology for the Synthesis of Heterotelechelic Protein-Polymer-Biomolecule Conjugates. *J. Polym. Sci. A Polym. Chem.* **2010**, *48* (6), 1399–1405. https://doi.org/10.1002/pola.23902.
(215) Roth, P. J.; Jochum, F. D.; Zentel, R.; Theato, P. Synthesis of Hetero-Telechelic α,ω Bio-Functionalized Polymers. *Biomacromolecules* **2010**, *11* (1), 238–244. https://doi.org/10.1021/bm901095j.
(216) Huang, X.; Boyer, C.; Davis, T. P.; Bulmus, V. Synthesis of Heterotelechelic Polymers with Affinity to Glutathione-S-Transferase and Biotin-Tagged Proteins by RAFT Polymerization and Thiol–Ene Reactions. *Polym. Chem.* **2011**, *2* (7), 1505. https://doi.org/10.1039/c1py00049g.
(217) Wallyn, S.; Zhang, Z.; Driessen, F.; Pietrasik, J.; De Geest, B. G.; Hoogenboom, R.; Du Prez, F. E. Straightforward RAFT Procedure for the Synthesis of Heterotelechelic Poly(Acrylamide)s. *Macromol. Rapid Commun.* **2014**, *35* (4), 405–411. https://doi.org/10.1002/marc.201300690.
(218) Iha, R. K.; Wooley, K. L.; Nyström, A. M.; Burke, D. J.; Kade, M. J.; Hawker, C. J. Applications of Orthogonal "Click" Chemistries in the Synthesis of Functional Soft Materials. *Chem. Rev.* **2009**, *109* (11), 5620–5686. https://doi.org/10.1021/cr900138t.
(219) Vinciguerra, D.; Tran, J.; Nicolas, J. Telechelic Polymers from Reversible-Deactivation Radical Polymerization for Biomedical Applications. *Chem. Commun.* **2018**, *54* (3), 228–240. https://doi.org/10.1039/C7CC08544C.
(220) Tasdelen, M. A.; Kahveci, M. U.; Yagci, Y. Telechelic Polymers by Living and Controlled/Living Polymerization Methods. *Progress in Polymer Science* **2011**, *36* (4), 455–567. https://doi.org/10.1016/j.progpolymsci.2010.10.002.
(221) Hua, L.; Zhang, Q.; Zhu, X.; Wang, R.; You, Q.; Wang, L. Beyond Proteolysis-Targeting Chimeric Molecules: Designing Heterobifunctional Molecules Based on Functional Effectors. *J. Med. Chem.* **2022**, *65* (12), 8091–8112. https://doi.org/10.1021/acs.jmedchem.2c00316.
(222) Dale, B.; Cheng, M.; Park, K.-S.; Kaniskan, H. Ü.; Xiong, Y.; Jin, J. Advancing Targeted Protein Degradation for Cancer Therapy. *Nat Rev Cancer* **2021**, *21* (10), 638–654. https://doi.org/10.1038/s41568-021-00365-x.
(223) Nebhani, L.; Sinnwell, S.; Inglis, A. J.; Stenzel, M. H.; Barner-Kowollik, C.; Barner, L. Efficient Surface Modification of Divinylbenzene Microspheres via a Combination of RAFT and Hetero Diels-Alder Chemistry. *Macromol. Rapid Commun.* **2008**, *29* (17), 1431–1437. https://doi.org/10.1002/marc.200800244.
(224) Sinnwell, S.; Inglis, A. J.; Davis, T. P.; Stenzel, M. H.; Barner-Kowollik, C. An Atom-Efficient Conjugation Approach to Well-Defined Block Copolymers Using RAFT Chemistry and Hetero Diels–Alder Cycloaddition. *Chem. Commun.* **2008**, No. 17, 2052. https://doi.org/10.1039/b718180a.

(225) Inglis, A. J.; Sinnwell, S.; Stenzel, M. H.; Barner-Kowollik, C. Ultrafast Click Conjugation of Macromolecular Building Blocks at Ambient Temperature. *Angewandte Chemie International Edition* **2009**, *48* (13), 2411–2414. https://doi.org/10.1002/anie.200805993.
(226) Nebhani, L.; Sinnwell, S.; Lin, C. Y.; Coote, M. L.; Stenzel, M. H.; Barner-Kowollik, C. Strongly Electron Deficient Sulfonyldithioformate Based RAFT Agents for Hetero Diels-Alder Conjugation: Computational Design and Experimental Evaluation: Sulfonyldithioformate Based RAFT Agents. *J. Polym. Sci. A Polym. Chem.* **2009**, *47* (22), 6053–6071. https://doi.org/10.1002/pola.23647.
(227) Glassner, M.; Delaittre, G.; Kaupp, M.; Blinco, J. P.; Barner-Kowollik, C. (Ultra)Fast Catalyst-Free Macromolecular Conjugation in Aqueous Environment at Ambient Temperature. *J. Am. Chem. Soc.* **2012**, *134* (17), 7274–7277. https://doi.org/10.1021/ja301762y.
(228) Beloqui, A.; Mane, S. R.; Langer, M.; Glassner, M.; Bauer, D. M.; Fruk, L.; Barner-Kowollik, C.; Delaittre, G. Hetero-Diels–Alder Cycloaddition with RAFT Polymers as Bioconjugation Platform. *Angew. Chem. Int. Ed.* **2020**, *59* (45), 19951–19955. https://doi.org/10.1002/anie.202005747.
(229) Renault, K.; Fredy, J. W.; Renard, P.-Y.; Sabot, C. Covalent Modification of Biomolecules through Maleimide-Based Labeling Strategies. *Bioconjugate Chem.* **2018**, *29* (8), 2497–2513. https://doi.org/10.1021/acs.bioconjchem.8b00252.
(230) Langer, M.; Brandt, J.; Lederer, A.; Goldmann, A. S.; Schacher, F. H.; Barner-Kowollik, C. Amphiphilic Block Copolymers Featuring a Reversible Hetero Diels-Alder Linkage. *Polym. Chem.* **2014**, *5* (18), 5330–5338. https://doi.org/10.1039/C4PY00644E.
(231) Tang, Z.; Wilson, P.; Kempe, K.; Chen, H.; Haddleton, D. M. Reversible Regulation of Thermoresponsive Property of Dithiomaleimide-Containing Copolymers via Sequential Thiol Exchange Reactions. *ACS Macro Lett.* **2016**, *5* (6), 709–713. https://doi.org/10.1021/acsmacrolett.6b00310.
(232) Alberti, A.; Benaglia, M.; Laus, M.; Sparnacci, K. A New Facile Synthesis of Tertiary Dithioesters. *J. Org. Chem.* **2002**, *67* (22), 7911–7914. https://doi.org/10.1021/jo026162q.
(233) Upadhya, R.; Kanagala, M. J.; Gormley, A. J. Purifying Low-Volume Combinatorial Polymer Libraries with Gel Filtration Columns. *Macromol. Rapid Commun.* **2019**, *40* (24), 1900528. https://doi.org/10.1002/marc.201900528.
(234) Zhang, J.; Fu, Y.; Chowdhury, M. H.; Lakowicz, J. R. Plasmon-Coupled Fluorescence Probes: Effect of Emission Wavelength on Fluorophore-Labeled Silver Particles. *J. Phys. Chem. C* **2008**, *112* (25), 9172–9180. https://doi.org/10.1021/jp8000493.
(235) Ray, K.; Zhang, J.; Lakowicz, J. R. Fluorescence Lifetime Correlation Spectroscopic Study of Fluorophore-Labeled Silver Nanoparticles. *Anal. Chem.* **2008**, *80* (19), 7313–7318. https://doi.org/10.1021/ac8009356.
(236) Xin, L.; Lu, M.; Both, S.; Pfeiffer, M.; Urban, M. J.; Zhou, C.; Yan, H.; Weiss, T.; Liu, N.; Lindfors, K. Watching a Single Fluorophore Molecule Walk into a Plasmonic Hotspot. *ACS Photonics* **2019**, *6* (4), 985–993. https://doi.org/10.1021/acsphotonics.8b01737.
(237) Li, Z.; Seo, T. S.; Ju, J. 1,3-Dipolar Cycloaddition of Azides with Electron-Deficient Alkynes under Mild Condition in Water. *Tetrahedron Letters* **2004**, *45* (15), 3143–3146. https://doi.org/10.1016/j.tetlet.2004.02.089.
(238) Bhaskar, S.; Roh, K.-H.; Jiang, X.; Baker, G. L.; Lahann, J. Spatioselective Modification of Bicompartmental Polymer Particles and Fibers via Huisgen 1,3-Dipolar Cycloaddition:

Spatioselective Modification of Bicompartmental Polymer Particles and …. *Macromol. Rapid Commun.* **2008**, *29* (20), 1655–1660. https://doi.org/10.1002/marc.200800459.
(239) Deng, X.; Lahann, J. Orthogonal Surface Functionalization through Bioactive Vapor-Based Polymer Coatings. *J. Appl. Polym. Sci.* **2014**, *131* (14), n/a-n/a. https://doi.org/10.1002/app.40315.
(240) Deng, X.; Friedmann, C.; Lahann, J. Bio-Orthogonal "Double-Click" Chemistry Based on Multifunctional Coatings. *Angew. Chem. Int. Ed.* **2011**, *50* (29), 6522–6526. https://doi.org/10.1002/anie.201101581.